The vertical distribution of phytoplankton in a turbulent boundary layer

Thesis submitted in accordance with the requirements of the University of Liverpool for the degree of Doctor in Philosophy by

Joseph Siddons

February 2018

Contents

List of symbols

$\langle \cdot \rangle$	Full spatial (equivalently ensemble) average	
$\langle \cdot \rangle_T$	2d (horizontal) and time average	
$\langle \cdot \rangle_I$	Instantaneous 2d (horizontal) average	
a	Wave amplitude	m
$\overline{aA}$	Absorption cross-sectional area	m^2
α	Light attenuation coefficient	m^{-1}
α_{sight}	Predator cone angle	
β_e	Phytoplankton growth efficiency	
$D_{P,Z}$	Phytoplankton/zooplankton diffusion coefficient	$\mathrm{m}^2\,\mathrm{s}^{-1}$
D_N	Molecular diffusivity of nitrate	$\mathrm{m}^2\,\mathrm{s}^{-1}$
δ_E	Ekman depth	m
δ_S	Stokes depth	m
$E(k,t)$	Turbulent energy spectrum	$\mathrm{kg}\,\mathrm{m}^2\,\mathrm{s}^{-1}$
ε	Energy Dissipation rate	$\mathrm{m}^2\,\mathrm{s}^{-3}$
η_K	Kolmogorov length scale	m
$\boldsymbol{f}$	Body force	$\mathrm{kg}\,\mathrm{m}\,\mathrm{s}^{-2}$
f	Coriolis frequency	s^{-1}
f_V	Volume fraction	
$\langle f_V \rangle$	Average volume fraction	
g	Acceleration due to gravity	$\mathrm{m}\,\mathrm{s}^{-2}$
$\overline{\gamma C}$	Chlorophyll absorption spectrum	m^{-1}
I_N	Nitrate intensity measure	
I_P	Phytoplankton intensity measure	
$I(z,\lambda)$	Irradiance	$\mathrm{mol}(q)\,\mathrm{m}^{-2}\,\mathrm{nm}^{-1}\,\mathrm{s}^{-1}$
k	Wavenumber	m^{-1}
K_C	Eddy diffusivity	$\mathrm{m}^2\,\mathrm{s}^{-1}$
$k(z,\lambda)$	Attenuation coefficient	m^{-1}
k_g	Attenuation due to gilvin	m^{-1}
k_w	Attenuation due to water	m^{-1}
κ	Von Karmen constant	
L	Length scale	m
L_e	Large eddy scale	m

La	Langmuir number	
μ	Dynamic viscosity	$\mathrm{kg\,m^{-1}\,s^{-1}}$
$\mu_{Z\,death}$	Zooplankton mortality rate	$\mathrm{s^{-1}}$
$\mu_{P,Z}^{max}$	Maximum phytoplankton/zooplankton growth rate	$\mathrm{s^{-1}}$
N	Buoyancy frequency	$\mathrm{s^{-1}}$
$N = N*/N_0$	Normalised nitrate concentration	
$N*$	Nitrate concentration	$\mathrm{kg\,m^{-3}}$
N_0	Background nitrate concentration	$\mathrm{kg\,m^{-3}}$
p	Thermodynamic pressure	$\mathrm{kg\,m^{-1}\,s^{-2}}$
$P = P^*/P_0$	Normalised phytoplankton population	
P^*	Phytoplankton population	$\mathrm{cells\,m^{-3}}$
P_0	Background phytoplankton population	$\mathrm{cells\,m^{-3}}$
p_{cap}	Capture probability	
Pe	Péclet number	
ρ	Density of water	$\mathrm{kg\,m^{-3}}$
$\rho_{P,Z}$	Phytoplankton/zooplankton cellular density	$\mathrm{kg\,m^{-3}}$
ρ_{prey}	Prey density	$\mathrm{cells\,m^{-3}}$
Q_N	Flux of nitrate into cell	$\mathrm{kg\,s^{-1}}$
$q(t)$, $q(z,t)$	Average stored energy at t, z	$\mathrm{mol(quanta)\,cell^{-1}}$
q^{max}	Maximum energy capacity	$\mathrm{mol(quanta)\,cell^{-1}}$
R_{cont}	Zooplankton contact radius	m
r_{ij}	Anti symmetric stress tensor	$\mathrm{s^{-1}}$
$r_{P,Z}$	Phytoplankton/zooplankton cell radius	m
r_M	Distance of predator prey closest approach	m
R_N	Nitrate storage level at concentration N	$\mathrm{kg\,cell^{-1}}$
R_{N_0}	Nitrate storage at background level N_0	$\mathrm{kg\,cell^{-1}}$
R_N^{max}	Maximum nitrate storage capacity	$\mathrm{kg\,cell^{-1}}$
Re	Reynolds number	
s_{ij}	Rate of strain tensor	$\mathrm{s^{-1}}$
s_I	Energy stoichiometry coefficient	
s_N	Nitrate stoichiometry coefficient	
Sh	Turbulent Sherwood number	
σ	Wave frequency	$\mathrm{s^{-1}}$
$\sigma_{P,Z}$	Phytoplankton/zooplankton swimming speed standard deviation	$\mathrm{m\,s^{-1}}$
σ_U	Variance for U	$\mathrm{m\,s^{-1}}$
$T_{R_{cont}}$	Zooplankton reaction time	s
T_{sim}	Simulation time	s
T_e	Eddy turnover time	s
$t(r_M), t_{r_M}$	Time prey is in contact	s
$\boldsymbol{\tau}$	Stress tensor	$\mathrm{kg\,m^{-1}\,s^{-2}}$
τ_{pred}	Turbulent predictability timescale	s

τ_K	Kolmogorov time scale	s
$\boldsymbol{\tau_S}$	Surface (wind) stress	$\mathrm{kg\,m^{-1}\,s^{-2}}$
$\boldsymbol{u}$	Fluid velocity / resolved fluid velocity	$\mathrm{m\,s^{-1}}$
$\boldsymbol{U}$	Mean flow velocity	$\mathrm{m\,s^{-1}}$
U	Velocity scale	$\mathrm{m\,s^{-1}}$
U_e	Large eddy velocity scale	$\mathrm{m\,s^{-1}}$
U_*	Ocean friction velocity	$\mathrm{m\,s^{-1}}$
U_S	Stokes drift velocity	$\mathrm{m\,s^{-1}}$
$\overline{\boldsymbol{u}}$	Resolved fluid velocity	$\mathrm{m\,s^{-1}}$
$\boldsymbol{u}''$	Fluctuating fluid velocity	$\mathrm{m\,s^{-1}}$
$\boldsymbol{u}'$	Unresolved fluid velocity	$\mathrm{m\,s^{-1}}$
$\boldsymbol{v_{P,Z}}$	Phytoplankton/zooplankton swimming velocity	$\mathrm{m\,s^{-1}}$
$\boldsymbol{V_{P,Z}}$	Total phytoplankton/zooplankton velocity	$\mathrm{m\,s^{-1}}$
v_K	Kolmogorov velocity scale	$\mathrm{m\,s^{-1}}$
ν	Kinematic viscosity	$\mathrm{kg\,m^{-1}\,s^{-1}}$
ν_e	Eddy viscosity	$\mathrm{m^2\,s^{-1}}$
$\boldsymbol{w}(\boldsymbol{x},t)$	Turbulent velocity	$\mathrm{m\,s^{-1}}$
$\boldsymbol{\omega}$	Vorticity	$\mathrm{s^{-1}}$
$\overline{\omega}$	Buoyancy frequency	$\mathrm{s^{-1}}$
Y	Yield	
$Z = Z^*/Z_0$	Normalised zooplankton population	
Z^*	Zooplankton population	$\mathrm{cells\,m^{-3}}$
Z_0	Background zooplankton population	$\mathrm{cells\,m^{-3}}$
z_{ML}	Mixing layer depth	m
z_{opt}	Depth of maximum I_P	m
z_{TD}	Mixed layer/turbulent depth	m
z_S	Simulation/boundary layer depth	m

Chapter 1

Introduction

Over the recent decades an increase in the average global temperatures has been observed. This global warming, and its impacts on the climate and the world's ecosystems, has attracted a significant level of research, with a vast number of studies supporting its existence (Hughes 2000). The rise in temperatures is generally attributed to rises in the levels of atmospheric carbon (CO_2), the concentration of which is now higher than it has been in the last 26 million years (Long et al. 2004). Carbon dioxide levels are 38% higher than they were during the 1000 years before the industrial revolution, and are expected to continue to rise (Prentice et al. 2001). This temperature increase has had a significant effect on the world's ecosystems (Parmesan 2006). In particular, some mountain and polar species have almost disappeared, or gone extinct completely, as regions in which they can survive have reduced in size. Plant life can act as a regulator on carbon dioxide levels through photosynthesis. By absorbing energy from light, plants can convert carbon dioxide and water into carbohydrates (for growth) and O_2. However, recent increases in CO_2 concentrations, combined with deforestation, have outweighed the losses through photosynthesis, which is likely to result in permanently higher average global temperatures. This will have severe consequences for marine ecosystems, in particular planktonic ecosystems are very sensitive to changes in their ocean environment. Rising ocean temperates will bring about changes in salinity, acidity, O_2 content, viscosity, and changes in ocean dynamics. Understanding how small and large scale fluid dynamics influence the planktonic ecosystem is one of the main aims of this thesis.

The marine food web is comprised of organisms on a range of scales, from uni-cellular bacteria (less than 1 μm) to whales ($O(10\text{ m})$). Plankton form part of the first two steps in the food chain, and are (for the purposes of this work) broadly split into two groups. Phytoplankton are microscopic photosynthetic organisms, typically considered as plants. They are typically non-motile, and act as passive tracers within the ocean environment (i.e. they are advected around by the flow, and do not contribute to the flow). Most phytoplankton species are unicellular, despite this they produce over 50% of the world's atmospheric oxygen through photosynthesis, depleting a large amount of the atmospheric CO_2 (Moss 2009, Harris 2012, Sekerci and Petrovskii 2015). For this reason they are a highly important part of the

world's climate and understanding their growth patterns is essential in further understanding climate change.

The second group, known as zooplankton are μm to cm scale organisms that feed on the phytoplankton, making up the second step on the food chain. Whilst phytoplankton are typically non-motile, some zooplankton species are capable of motions over distances of metres at speeds of the order of 10 $\mu\mathrm{m\,s^{-1}}$ – $\mathrm{cm\,s^{-1}}$ (Denman and Gargett 1995, Bundy et al. 1998).

It is widely recognised that the physical processes influencing the dynamics of the ocean have an important impact on the distribution and dynamics of phytoplankton communities Denman and Gargett (1995), Bees et al. (1998), Yamazaki et al. (2002), Gallager et al. (2004), Lewis (2005). One of the greatest difficulties facing researchers seeking to model the interactions between the physical and biological dynamics is the wide range of spatial scales that must be considered. Phytoplankton blooms (rapid increase, or accumulation of phytoplankton populations) form in a range of sizes, from long term kilometre scale aggregations which can discolour the sea-water and are visible from satellite imagery (Martin 2003, Ahn and Shanmugam 2006, Wang and Shi 2008) to short term, millimetre aggregations. Large scale up-welling zones called gyres ($O(1000\ \mathrm{km})$) transport nutrients from the colder waters below into the surface mixed layer, a process which stimulates phytoplankton growth (Franks et al. 1986). Small scale turbulent motions ($O(1\ \mathrm{mm})$) drive the interactions between the species, in particular predator-prey encounters are enhanced by turbulent mixing Rothschild and Osborn (1988), Lewis and Pedley (2000). Accounting for all the biological processes and dynamics across the wide range of physical scales over the biological growth cycles is a colossal challenge.

One of the more ubiquitous features of the ocean boundary layer is the formation of biological aggregations termed deep chlorophyll maxima (DCM) (Cullen 2015). Measurements of chlorophyll a (a compound that acts as a catalyst in the process of photosynthesis and is a 'marker' for the presence of phytoplankton) vertical profiles are rarely uniform, and often exhibit a non-random subsurface maxima. These subsurface maxima are an ecologically significant feature of the planktonic ecosystem. A number of processes are thought to contribute to the formation, and maintenance, of DCM. Their existence is typically explained by the presence of two vertically opposing gradients that contribute to the phytoplankton growth rate, light availability and nutrient resources. It has long been known that turbulence can influence the vertical distribution of plankton. However, it is not fully understood how turbulence influences the formation and characteristics of DCM. Recent evidence has suggested that DCM often form in weakly turbulent regions of the water column (Macías et al. 2013). It has been speculated that Langmuir cells (near surface counter rotating vertical vortices driven by surface water waves) play a significant role in biological production (Bees et al. 1998, Lewis 2005). Large Langmuir circulations will rapidly cycle the phytoplankton throughout the sunlit mixed layer. However, it is unclear how Langmuir turbulence will affect the spatial (lateral and vertical) distribution of the phytoplankton.

The main aim of this thesis is to understand the main drivers of vertical heterogeneity within phytoplankton populations, in particular the formation, development and persistence of deep chlorophyll maxima. In order to do this, it is necessary to formulate both the physical and biological aspects that influence the formation and development of DCM. The physical aspects are captured by the use of large eddy simulations to create dynamic, three dimensional models of the wind driven surface mixed layer. Large eddy simulation (LES) is a technique that can be used to solve the Navier-Stokes equations which underlie the motion of all fluids. Typically LES models the large scale motions ($O(1) - O(100\text{ m})$) of the boundary layer very accurately. The biological aspects are captured by the use of a generic nutrient-phytoplankton-zooplankton (NPZ) model, which summarises the main bio-chemical interactions of the planktonic ecosystem. Typically NPZ models are used to describe the small scale processes ($O(10^{-3}) - O(1\text{ m})$) that underlie the biological dynamics such as nutrient uptake and planktonic predation. The large scale physical and small scale biological processes are coupled together to form a truly multi-scale, bio-physical model of the ocean mixed layer, suitable for use in conjunction with modern high performance computational resources. The coupling of the physical and biological models is achieved both directly (through advection), and indirectly as part of the biological interactions through the turbulent intensity, measured by the energy dissipation rate, $\langle\varepsilon\rangle$ $\text{m}^2\,\text{s}^{-3}$, which acts as a coupling parameter. The main benefits of using a full 3 dimensional model of turbulence is that the model can incorporate 3 dimensional features of real ocean turbulence, in particular Langmuir circulations and Stokes drift (introduced in chapter 2. The full description of these features, coupled with the biological model provides insight into both the horizontal and vertical structure of plankton communities, which would not be achieved with a simple model of the ocean environment. The interplay between the horizontal and vertical features of the environment has been modelled using this coupled LES-NPZ model by Lewis et al. (2017), Brereton et al. (2018), the former building upon some of the results and analysis presented in this thesis. In particular, the horizontal distributions of the biological fields (presented in Lewis et al. (2017)) show a relationship with the up/down-wellings that would not be evident in lower dimensions. Chapters 2 and 3 describe the formulation and coupling of the physical and biological parts of the model respectively. The remaining chapters will look in more detail at some of the drivers of vertical phytoplankton population structure. Chapter 4 will investigate the process of photosynthesis, in particular how phytoplankton capture the light available to them, and how the the population responds to different intensities of light. A new NPZ-q model will be developed to capture the full effects of light capture by phytoplankton, including self-shading, to investigate the effect on the phytoplankton vertical distribution. Chapter 5 will introduce the grazing of zooplankton on the phytoplankton and how it's related to the background turbulence. The impact of predation on the vertical structure of phytoplankton populations is the key new idea that will be investigated by this thesis. The final chapter (chapter 6) brings together the ideas presented in chapters 2–5 in a novel way in order to better understand the drivers and dynamics of DCM formation. Results of numerical simulations will be

studied to investigate some of the important variables, in particular the level of turbulence, the predation rate, nutrient concentration, and light levels.

Chapter 2

The Physical Model

2.1 Navier-Stokes equations

The governing equations of fluid flow are the Navier-Stokes equations, originally formulated by Navier (1823). The equations are derived from Newton's second law of motion, *Force* = *Mass* × *Acceleration*. The following section provides a brief overview of the derivation (see Batchelor (1967), Lesieur (2008)).

2.1.1 Conservation of mass

Consider a fluid particle moving within a flow and let $\delta m = \rho \delta V$ be the mass of the particle, where ρ is the density of the fluid and δV is the volume of the fluid particle. The mass of the particle following the fluid motion is conserved, since the exchanges of mass with the surrounding fluid are zero. The derivative of the particle's mass following fluid motion is

$$\frac{\mathrm{D}(\delta m)}{\mathrm{D}t} = \frac{\partial(\delta m)}{\partial t} + \boldsymbol{u} \cdot \nabla(\delta m) = 0,$$

where $\boldsymbol{u}$ is the fluid velocity. This is called the material, or Lagrangian derivative of the fluid particle. Equivalently this can be written as

$$\frac{\mathrm{D}(\delta m)}{\mathrm{D}t} = \delta V \frac{\mathrm{D}\rho}{\mathrm{D}t} + \rho \frac{\mathrm{D}(\delta V)}{\mathrm{D}t} = 0. \tag{2.1.1}$$

From Lesieur (2008), page 24-25, the divergence of velocity can be related to the volume of the particle by

$$\nabla \cdot \boldsymbol{u} = \frac{1}{\delta V} \frac{\mathrm{D}(\delta V)}{\mathrm{D}t}. \tag{2.1.2}$$

Equation (2.1.1) then becomes

$$\frac{1}{\rho} \frac{\mathrm{D}\rho}{\mathrm{D}t} + \nabla \cdot \boldsymbol{u} = 0. \tag{2.1.3}$$

Assuming that there is also conservation of volume (incompressibility, the volume of the fluid remains constant when subjected to a force), i.e. $\mathrm{D}(\delta V)/\mathrm{D}t = 0$, the conservation of mass,

or continuity equation, becomes

$$\frac{1}{\rho}\frac{\mathrm{D}\rho}{\mathrm{D}t} = 0 \quad \Longrightarrow \quad \nabla \cdot \boldsymbol{u} = 0. \tag{2.1.4}$$

2.1.2 Momentum equation

The momentum equation (or force per unit volume acting on an arbitrary fluid particle of volume V) is derived by applying Newton's second law of motion to the fluid, i.e.

$$\rho\frac{\mathrm{D}\boldsymbol{u}}{\mathrm{D}t} = \rho\left[\frac{\partial \boldsymbol{u}}{\partial t} + \boldsymbol{u}\cdot\nabla\boldsymbol{u}\right] = \textit{(Body forces + Surface forces) per unit volume}, \tag{2.1.5}$$

or in indicial notation

$$\rho\frac{\mathrm{D}u_i}{\mathrm{D}t} = \rho\left[\frac{\partial u_i}{\partial t} + u_j\frac{\partial u_i}{\partial x_j}\right] = \textit{(Body forces + Surface forces) per unit volume}, \tag{2.1.6}$$

Here u_i is the i-th component of velocity, x_i is displacement in direction i $(= 1, 2, 3)$ and t is time. Einstein summation is used for the repeated indicies (j in equation (2.1.6). Examples of body forces are the Coriolis force, or gravity. The elemental surface force $\mathrm{d}f_I^s$ exerted across an elemental area $\mathrm{d}\Sigma$ of a fluid particle is given by Batchelor (1967)

$$\mathrm{d}f_I^s = \sigma_{ij}n_j\mathrm{d}\Sigma. \tag{2.1.7}$$

Here n_j is the j-th component of the outward normal vector from $\mathrm{d}\Sigma$ and σ_{ij} is the stress tensor. In what are termed Newtonian fluids the stress tensor is given by

$$\sigma_{ij} = -p\delta_{ij} + \mu s_{ij}, \tag{2.1.8}$$

where δ_{ij} is the Kronecker delta, μ is the dynamic viscosity, p is the thermodynamic pressure, and s_{ij} is the rate of strain (or deformation) tensor.

$$s_{ij} = \frac{1}{2}\left(\frac{\partial u_i}{\partial x_j} + \frac{\partial u_j}{\partial x_i}\right). \tag{2.1.9}$$

The surface forces are then given by (from equation (2.1.7))

$$f_i^s = \int_\Sigma \sigma_{ij}n_j\,\mathrm{d}\Sigma = \int_V \frac{\partial\sigma_{ij}}{\partial x_j}\,\mathrm{d}V. \tag{2.1.10}$$

Hence the momentum equation for the fluid (including the surface forces) is given by

$$\rho\left[\frac{\partial u_i}{\partial t} + u_j\frac{\partial u_i}{\partial x_j}\right] = -\frac{\partial p}{\partial x_i} + \frac{\partial}{\partial x_j}\mu\left(\frac{\partial u_i}{\partial x_j} + \frac{\partial u_j}{\partial x_i}\right) + f_i, \tag{2.1.11}$$

where f_i is the i-th component of the body force vector. Assuming that the flow is incompressible, the Navier-Stokes equations are then the combination of equations (2.1.4) and

(2.1.11):

$$\frac{\partial u_i}{\partial t} + u_j \frac{\partial u_i}{\partial x_j} = -\frac{1}{\rho}\frac{\partial p}{\partial x_i} + \nu \frac{\partial^2 u_i}{\partial x_j \partial x_j} + F_i, \tag{2.1.12}$$

$$\frac{\partial u_i}{\partial x_i} = 0, \tag{2.1.13}$$

where $\nu = \mu/\rho$ is the kinematic viscosity and F_i are the body forces. These equations are fundamental for studying biological interactions that occur in any fluid environment.

2.1.3 The Reynolds number, *Re*

The Navier-Stokes equations (2.1.12) are extremely complicated, primarily because of the non-linear advection terms $u_j \partial u_i/\partial x_j$, and no general analytical solutions to the system are currently known. Low energy, or laminar, flows characterise situations in which the viscous term dominates the advection term. This contrasts with high energy (turbulent) flows in which the advection term dominates the viscous term. In laminar flows the equations become approximately linear and can sometimes be solved analytically. However, this is atypical and numerical techniques must be utilised, especially for turbulent flows.

Flows, turbulent or laminar, are typically characterised by a non-dimensional Reynolds number.

Non-dimensionalising the Navier-Stokes equations determines which parameters are important in analysing the type of flow that is being studied. Making the substitutions $x = x^* L$, $u = u^* U$, $t = Lt^*/U$, $p = \rho p^*/U^2$ and $F_i = F_i^* U^2/L$ where the asterisk represents a non-dimensional quantity and U and L are velocity and length scales respectively (relevant to the boundary conditions of the problem), the Navier-Stokes equations become

$$\frac{U^2}{L}\frac{\partial u_i^*}{\partial t} + \frac{U^2}{L} u_j^* \frac{\partial u_i^*}{\partial x_j^*} = -\frac{U^2}{L}\frac{\partial p^*}{\partial x_i^*} + \nu \frac{U}{L^2}\frac{\partial^2 u_i^*}{\partial x_j^{*2}} + \frac{U^2}{L} F_i^*.$$

Dividing by U^2/L and removing the asterisks for brevity gives the non-dimensional equations

$$\frac{\partial u_i}{\partial t} + u_j \frac{\partial u_i}{\partial x_j} = -\frac{\partial p}{\partial x_i} + \frac{1}{Re}\frac{\partial^2 u_i}{\partial x_j^2} + F_i, \tag{2.1.14}$$

where $Re = UL/\nu$ is the Reynolds number. From the previous analysis it is clear that laminar flows, which are dominated by the viscous term, will have a low Reynolds number. In high energy flows the advection term dominates the viscous term, in this case the flow is turbulent and the Reynolds number is large.

2.2 Spectral dynamics of turbulence

This section is primarily concerned with the behaviour of the turbulent kinetic energy spectrum, $E(k)$. This quantity represents the amount of energy associated with an eddy of size $L = 2\pi/k$ where k is the wavenumber. The universal properties of $E(k)$ that manifest in any

turbulent flow were first discovered by Richardson (1921). However, it was Kolmogorov (1941) who fully realised the mathematical implications of the observations made by Richardson in what is possibly the most important piece of work in the field of turbulence.

2.2.1 The Kolmogorov microscales

In turbulent flows, different processes dominate at the different scales. Advection is the dominant physical process at the larger scales, where the driving force and scale of motion are the most important parameters. At the smaller scales, the viscosity and dissipation of energy via heat are the most important parameters in determining how the flow acts. Using dimensional analysis Kolmogorov (1941) derived length, time, and velocity scales based solely on the parameters governing the small scale motions. These scales, known as the Kolmogorov length, time, and velocity microscales respectively are defined by

$$\begin{aligned} \eta_K &= \left(\frac{\nu^3}{\varepsilon}\right)^{\frac{1}{4}}, \\ \tau_K &= \left(\frac{\nu}{\varepsilon}\right)^{\frac{1}{2}}, \\ v_K &= (\nu\varepsilon)^{\frac{1}{4}}, \end{aligned} \tag{2.2.1}$$

where ν is the kinematic viscosity and ε is the energy dissipation rate, the rate at which energy is transferred between different length scales. This is a measure of how fast energy inputted to drive the flow is dissipated in the form of heat by the action of viscosity.

These scales, whist not derived from first principles, give an indication of the smallest scales on which the flow acts. For a turbulent flow with a given parameter set (ν, ε), then any eddy cascade that is set up cannot sustain vortical motions below η_K. For the biology this means that any organisms smaller than the Kolmogorov length scale will tend to experience a relatively quiescent flow in its local vicinity, as turbulent features cannot manifest themselves over such small distances.

2.2.2 The turbulent kinetic energy spectrum

One of the most important features of turbulent flows is that the velocity field depends upon position and measurements conducted at two nearby points simultaneously are dependent upon one another. The key measure that reflects this interdependence is the correlation tensor, defined by

$$R_{ij}(\boldsymbol{r}) = \langle u_i(\boldsymbol{x}, t) u_j(\boldsymbol{x} + \boldsymbol{r}, t) \rangle \tag{2.2.2}$$

where the triangular brackets represent a spatial average across all positions $\boldsymbol{x}$ in the flow, or equivalently an ensemble (over many different simulations) average. Assuming the flow is homogeneous, R_{ij} will be a function of $\boldsymbol{r}$ only. It turns out to be easier to bring out the universal behaviour of the energy spectrum by considering wavenumber, $\boldsymbol{k}$, space rather than the physical, $\boldsymbol{r}$, space. Consequently, it is important to define the spectrum tensor, ϕ_{ij}, which

is the Fourier transform of R_{ij}, by

$$\phi_{ij}(\boldsymbol{k}) = \frac{1}{(2\pi)^3}\int_V \mathrm{e}^{-i\boldsymbol{k}\cdot\boldsymbol{r}}\, R_{ij}(\boldsymbol{r})\,\mathrm{d}\boldsymbol{r},$$
$$\iff R_{ij}(\boldsymbol{r}) = \int_{\boldsymbol{k}\ space} \mathrm{e}^{i\boldsymbol{k}\cdot\boldsymbol{r}}\,\phi_{ij}(\boldsymbol{k})\,\mathrm{d}\boldsymbol{k}. \tag{2.2.3}$$

The most important statistic is the trace of the spectrum tensor since this represents twice the kinetic energy at a given wavenumber. This is because

$$u_1^2 + u_2^2 + u_3^2 = 3u^2 = R_{ii}(\boldsymbol{0}) = \int_{\boldsymbol{k}\ space} \phi_{ii}(\boldsymbol{k})\,\mathrm{d}\boldsymbol{k}, \tag{2.2.4}$$

where u is a velocity scale that applies to all three components of $u_i(\boldsymbol{x},t)$. Small scale turbulence is both homogeneous and isotropic which means that a single velocity scale is applicable to all three components of $u_i(\boldsymbol{x},t)$.

The integral in equation (2.2.4) is over a three dimensional shell in $\boldsymbol{k}$-space, so that $\mathrm{d}\boldsymbol{k} = k^2\sin(\theta_k)\mathrm{d}\phi_k\mathrm{d}\theta_k\mathrm{d}k$. The turbulent kinetic energy spectrum is then defined as

$$E(k) = \frac{1}{2}\int_0^{\pi}\int_0^{2\pi} \phi_{ii}(\boldsymbol{k})k^2\sin(\theta_k)\,\mathrm{d}\phi_k\mathrm{d}\theta_k. \tag{2.2.5}$$

The factor of $1/2$ is included so that $E(k)$ is equal to the kinetic energy per unit mass

$$\int_0^{\infty} E(k)\,\mathrm{d}k = \frac{1}{2}\int_0^{\infty}\int_0^{\pi}\int_0^{2\pi}\phi_{ii}(\boldsymbol{k})\,\mathrm{d}\boldsymbol{k} = \frac{1}{2}\langle u_i u_i\rangle = \frac{3u^2}{2}. \tag{2.2.6}$$

2.2.3 One dimensional spectra

One dimensional correlations can give some insight into the behaviour of $E(k)$, and such spectra can be found from Fourier transforms of the easily measurable correlations $R_{11}(r,0,0)$ and $R_{22}(r,0,0)$. These are called the longitudinal and transverse correlations respectively. The corresponding one dimensional spectra are defined by

$$R_{11}(r,0,0) = \int_{-\infty}^{\infty} \mathrm{e}^{ik_1 r}\,F_{11}(k_1)\,\mathrm{d}k_1, \tag{2.2.7}$$
$$R_{22}(r,0,0) = \int_{-\infty}^{\infty} \mathrm{e}^{ik_1 r}\,F_{22}(k_1)\,\mathrm{d}k_1. \tag{2.2.8}$$

F_{11} and F_{22} are longitudinal and transverse spectra respectively. Typical measurements (such as seen in Tennekes and Lumley (1972)) of R_{11} and R_{22} are shown in figure 2.1

Although this is not always the case, measured values of R_{11} are typically positive for all values of r (Tennekes and Lumley (1972) point out that there is no particular reason why they shouldn't go negative), which means that F_{11} has a maximum at the origin and decays parabolically from $k_1 = 0$. F_{11} is symmetric because R_{11} is real.

However, R_{22} often becomes negative for some values of r. This is demonstrated by figure

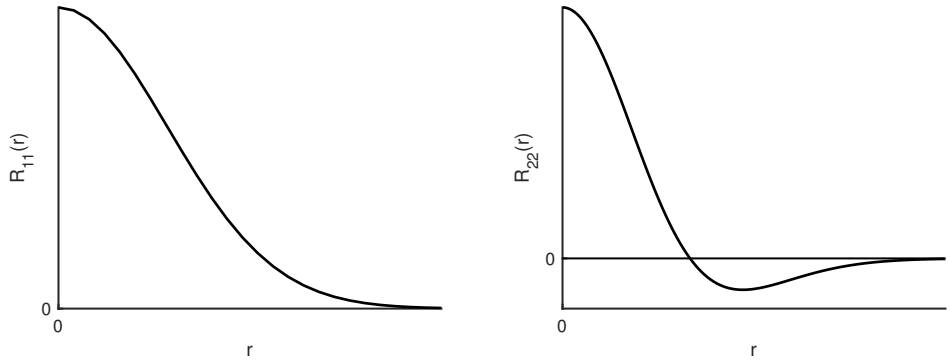

Figure 2.1: The longitudinal, R_{11}, (left) and transverse, R_{22} (right) correlations.

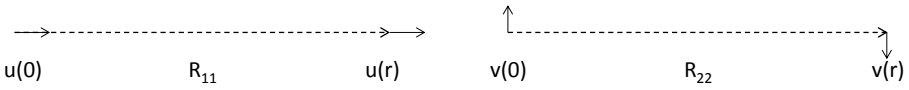

Figure 2.2: Inline (u, left) and perpendicular (v, right) velocities at $x = 0$ and $x = r$.

2.2. $R_{11}(r)$ represents the correlation between the inline velocity, u, at points $(0, 0, 0)$ and $(r, 0, 0)$. In this case, flow along a line does not usually reverse its direction, so $R_{11}(r) > 0$. $R_{22}(r)$ represents the correlation between the perpendicular velocity, v, at points $(0, 0, 0)$ and $(r, 0, 0)$. Flow across a line may, at some point, for example the rotation flow in a vortex. Across a plane perpendicular to the x_2-direction there should be no net mass flux because the average over the perpendicular plane of $u_2 = 0$. The integral of u_2 over the entire x_1-x_3-plane should therefore be zero

$$\int_{-\infty}^{\infty}\int_{-\infty}^{\infty} u_2(x_1, 0, x_3)\,\mathrm{d}x_1\mathrm{d}x_2 = 0, \tag{2.2.9}$$

which implies that

$$\int_{\infty}^{\infty}\int_{\infty}^{\infty} R_{22}(r_1, 0, r_3)\,\mathrm{d}r_1\mathrm{d}r_2 = 0, \tag{2.2.10}$$

so $R_{22}(r_1, 0, r_3) < 0$ somewhere in the x_1-x_3-plane. If the turbulence is isotropic, $R_{22}(r_1, 0, r_3)$ is only a function of $r = \sqrt{r_1^2 + r_3^2}$ and

$$\int_{-\infty}^{\infty} rR_{22}(r, 0, 0)\,\mathrm{d}r = 0, \tag{2.2.11}$$

so $R_{22}(r, 0, 0) < 0$ at some point. Consequently F_{22} is symmetric but with a peak away from the origin.

Understanding the behaviour of R_{11}, R_{22}, F_{11} and F_{22} provides insights into the behaviour of $E(k)$. It is possible to derive relations between F_{11}, F_{22} and $E(k)$, and two of the most useful relations are given by Batchelor (1953), Hinze (1959)

$$E(k) = k^3\frac{\mathrm{d}}{\mathrm{d}k}\left(\frac{1}{k}\frac{\mathrm{d}}{\mathrm{d}k}F_{11}(k)\right), \tag{2.2.12}$$

$$\frac{\mathrm{d}}{\mathrm{d}k}F_{22}(k) = -\frac{k}{2}\frac{\mathrm{d}^2}{\mathrm{d}k^2}F_{11}(k). \tag{2.2.13}$$

Since F_{11} attains its maximum at $k = 0$ and is symmetric, F_{11} is an even function of k such that

$$F_{11} \approx A - Bk^2 + Ck^4 + ... \tag{2.2.14}$$

Substituting this into equations (2.2.12) & (2.2.13) gives

$$E(k) = 8Ck^4 + ... \tag{2.2.15}$$

So $E(k) \propto k^4$ near $k = 0$. By definition there is no energy when $k = 0$. Since $R_{ii} > 0$ and real, ϕ_{ii} must be symmetric and take the form $\phi_{ii} \propto k^2$ near $k = 0$. However, the observation of $E(k) \propto k^4$ is rarely exhibited in practice because the large scale (small k) structure of turbulence is almost never homogeneous and isotropic. Nevertheless this is a useful theoretical observation with regard to the behaviour of $E(k)$.

2.2.4 Vorticity dynamics

The vorticity, $\boldsymbol{\omega}$, equation can be found by taking the curl of the Navier-Stokes equations, (2.1.12). This gives

$$\frac{\partial \boldsymbol{\omega}}{\partial t} + \boldsymbol{u} \cdot \nabla \boldsymbol{\omega} = \boldsymbol{\omega} \cdot \nabla \boldsymbol{u} + \nu \nabla^2 \boldsymbol{\omega}, \tag{2.2.16}$$

The main advantage of looking at dynamics of the flow through the vorticity is the absence of the pressure term in the resultant equation. This is because the curl of the gradient of a scalar function is zero. In equation (2.2.16), the terms on the left hand side represent the rate of change of vorticity with time and advection of vorticity with the flow. On the right hand side the $\nu \nabla^2 \boldsymbol{\omega}$ term is the dissipation of vorticity by viscosity. The interesting term is $\boldsymbol{\omega} \cdot \nabla \boldsymbol{u}$ which has no counterpart in the momentum equation (Batchelor 1967). In indicial notation this term can be written as $\omega_j \partial u_i / \partial x_j$, which can be split up into symmetric, s_{ij}, and anti-symmetric, r_{ij}, parts such that

$$\omega_j \frac{\partial u_i}{\partial x_j} = \omega_j s_{ij} + \omega_j r_{ij}, \tag{2.2.17}$$

where s_{ij} is as previously defined by equation (2.1.9) and

$$r_{ij} = \frac{1}{2}\left(\frac{\partial u_i}{\partial x_j} - \frac{\partial u_j}{\partial x_i}\right). \tag{2.2.18}$$

Using equation 2.2.18 and the definition of vorticity, the anti-symmetric part becomes

$$\omega_j r_{ij} = -\frac{1}{2}\epsilon_{ijk}\omega_j\omega_k \tag{2.2.19}$$

where ϵ_{ijk} is the permutation tensor defined by

$$\epsilon_{ijk} = \begin{cases} 1 & \text{if } (i,j,k) = (1,2,3),\ (3,1,2),\ (2,3,1) \\ -1 & \text{if } (i,j,k) = (1,3,2),\ (3,2,1),\ (2,1,3) \\ 0 & \text{if } i = j,\ j = k,\ \text{or } i = k \end{cases}.$$

Interchanging the dummy indices j and k yields

$$-\frac{1}{2}\epsilon_{ijk}\omega_j\omega_k = -\frac{1}{2}\epsilon_{ikj}\omega_k\omega_j = -\frac{1}{2}\epsilon_{ikj}\omega_j\omega_k = \frac{1}{2}\epsilon_{ijk}\omega_j\omega_k, \tag{2.2.20}$$

which can only be true if this term is zero. Consequently, the vorticity equation (2.2.16) can be written as

$$\frac{\mathrm{D}\omega_i}{\mathrm{D}t} = \frac{\partial\omega_i}{\partial t} + u_j\frac{\partial\omega_i}{\partial x_j} = \omega_j s_{ij} + \nu\frac{\partial^2\omega_i}{\partial x_j^2}. \tag{2.2.21}$$

The $\omega_j s_{ij}$ term is a source/sink term (Tennekes and Lumley 1972), and represents either the amplification or the reduction of the vorticity vector by the strain rate, depending upon the sign of s_{ij}.

In a two dimensional flow $\boldsymbol{\omega}\cdot\nabla\boldsymbol{u} = 0$, resulting in a very simple vorticity equation. This implies that turbulence is inherently "three-dimensional" and analysing its effects in just two dimensions gives an inaccurate description of reality.

Consider a coordinate system such that

$$s_{11} = s > 0,\quad s_{22} = -s,\quad s_{33} = 0,\quad \text{and } s_{ij} = 0 \text{ for } i \neq j. \tag{2.2.22}$$

Assuming that $\left|\nu\nabla^2\boldsymbol{\omega}\right| \ll |\boldsymbol{\omega}\cdot\nabla\boldsymbol{u}|$, then the vorticity equation (2.2.21) becomes

$$\frac{\mathrm{D}\omega_1}{\mathrm{D}t} = \omega_1 s$$
$$\frac{\mathrm{D}\omega_2}{\mathrm{D}t} = -\omega_2 s$$

If the initial conditions are $\omega_1 = \omega_2 = \omega_0$ at $t = 0$ then $\omega_1 = \omega_0\,\mathrm{e}^{st}$ and $\omega_2 = \omega_0\,\mathrm{e}^{-st}$, which implies that

$$\omega_1^2 + \omega_2^2 = 2\omega_0^2\cosh(2st).$$

Since $\cosh(2st) > 1$, there is a net increase in the magnitude of the vorticity. This vorticity creation is brought about by the process of vortex stretching, which usually exceeds the reduction brought about by vortex contraction. Therefore, excluding any viscous dissipation, turbulent flows are characterised by considerable vortex motions.

A simple illustration of this vortex stretching is the accelerated flow in a narrowing pipe, aligned in the x-axis (without loss of generality), shown in figure 2.3. In the coordinate system described by equation (2.2.22), s the flow speeds up through the narrowing pipe, the

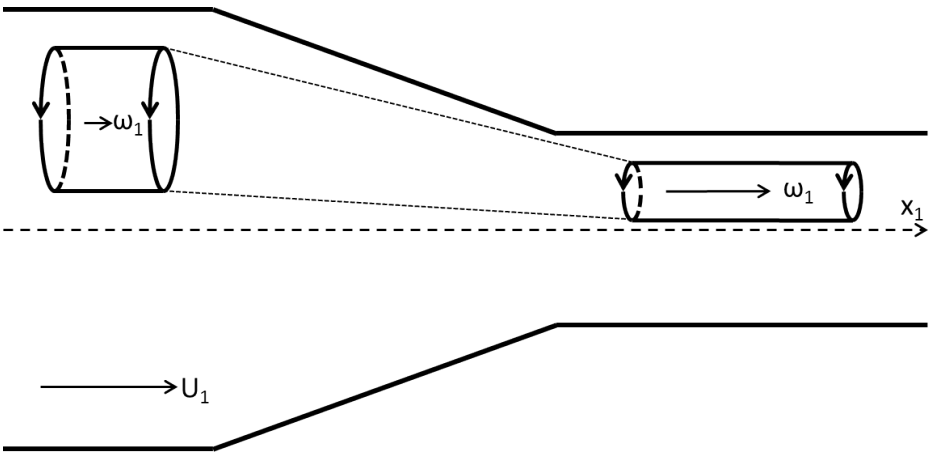

Figure 2.3: Vortex stretching in a narrowing pipe. As the flow speeds up from left to right, the strain rate s_{11} increases, amplifying the vortex component ω_1, because angular momentum must be conserved. Adapted from Tennekes and Lumley (1972).

strain rate in the x-direction, s_{11} increases, which increases the vorticity component ω_1. In order to satisfy the continuity equation ($s_{11} + s_{22} + s_{33} = 0$), the perpendicular strain rate s_{22} must decrease, decreasing the vorticity component ω_2. The stretching (and squeezing) of vortices in this way is a consequence of the conservation of angular momentum.

The stretching of vortex tubes as shown by figure 2.3 requires an exchange of energy as a consequence of the work done by the strain rate. This can be demonstrated by the turbulent energy budget equation, which is found by multiplying the Navier-Stokes equations (2.1.12) by u_i, averaging over 3d space, and then subtracting the kinetic energy of the mean flow (see Tennekes and Lumley (1972), for example). Applying Reynolds decomposition, $u_i = U_i + u_i''$ and $p = P + p''$, under steady conditions the resultant equation is

$$U_j \frac{\partial}{\partial x_j}\left(\frac{1}{2}\langle u_i'' u_i''\rangle\right) = -\frac{\partial}{\partial x_j}\left[\frac{1}{\rho}\langle u_j'' p''\rangle + \frac{1}{2}\langle u_i'^2 u_j''\rangle - 2\nu\langle u_i'' s_{ij}''\rangle\right] - \langle u_i'' u_j''\rangle S_{ij} - 2\nu\langle s_{ij}'' s_{ij}''\rangle, \tag{2.2.23}$$

where U_j and S_{ij} are the velocities and strain rates, respectively, for the mean flow and the double-primed quantities refer to a fluctuation from the mean flow. The first three terms on the right hand side are transport terms, but it is the last two terms are of most interest here. The term $-\langle u_i'' u_j''\rangle S_{ij}$ represents the production of kinetic energy. When a vortex is being stretched energy is transported from the mean flow strain rate to the velocity components u_i'' and u_j''. Energy is also dissipated by viscosity according to

$$\langle \varepsilon \rangle = 2\nu\langle s_{ij}'' s_{ij}''\rangle. \tag{2.2.24}$$

Vortical enhancement requires an exchange of energy from the mean flow into the turbulent fluctuations, which is eventually balanced out by the dissipation term. This exchange of energy is crucial to the behaviour of $E(k)$ at large wavenumbers. The mean flow is usually associated with the large scale features of the flow, such as the domain size etc. The large scale strain rate S_{ij} acts to produce increased small scale $\langle u_i'' u_j''\rangle$ fluctuations. This is achieved

by means of energy transport from large scale disturbances down to small scale disturbances, in an energy cascade from small to large wavenumbers.

It is important to point out that this interpretation is somewhat simplified. Energy is also transported back from small scales to large. However, it is the overall net transport rate that is of interest here. In which case the concept of energy being transported from the large eddies to the small ones is a valid description.

2.2.5 The energy cascade

Eddies

In a turbulent flow, small scale instabilities are common throughout the structure of the flow. Vortical motions, of many length scales, allow particles to move in opposite directions to that of the mean flow. These motions are known as eddies, and are not easy to define. It is often thought that an eddy is a swirling motion of a certain size; Davidson (2015) loosely describes an eddy as a region of vorticity acting as an over-turning process in a fluid. It is better to consider an eddy as a range of disturbances in wavenumber space, with an average length scale. As such, an eddy of wavenumber k can be defined as a disturbance with energy between, say $0.62k$ and $1.62k$. This range centres the energy around k on a logarithmic scale: $\ln(1.62) = \ln(1/0.62) \approx 1/2$. This produces a narrow, but not infinitesimal, band of wavenumbers associated with an eddy of size $L = 2\pi/k$.

Fourier transforming this narrow band results in a fairly localised band of wavelengths in ordinary space. Alternatively, if an eddy was defined as a single wavenumber, k_0, effectively a delta function $\delta(k - k_0)$, then the Fourier transform becomes $\mathrm{e}^{-ik_0 r}$, which is a function over the entire physical space. Hence it is better to consider an eddy as a narrow band of wavenumbers, as previously defined, since it corresponds to a narrow band of wavelengths.

The energy cascade

The strain rate associated with a large eddy of size L_e is given by

$$S(k) \propto \frac{U}{L_e}, \tag{2.2.25}$$

where U_e is the velocity scale associated with the largest eddy and $L_e = 2\pi/k$ is the length scale associated with the largest eddy (Tennekes and Lumley 1972). The strain rate can be expressed in terms of $E(k)$ as follows

$$U_e \propto (kE(k))^{\frac{1}{2}},$$

$$\implies S(k) \propto \frac{k}{2\pi} (kE(k))^{\frac{1}{2}}.$$

This relation can be used to find the strain rate around $k = 0$. In this region $E(k) \propto k^4$ (equation (2.2.15)), which gives

$$S(k) \propto k^{\frac{7}{2}}. \tag{2.2.26}$$

This implies that, at least initially, the strain rate is increasing with k. Assuming that this relation holds for all k, then the timescale defined by

$$T \propto \frac{1}{S(k)} \tag{2.2.27}$$

will decrease as k increases. Kolmogorov referred to this timescale as the 'return to isotropy'. It can be seen that small eddies ($k \to \infty$) return to isotropy faster than larger eddies, effectively making it more difficult for small eddies to create anisotropy in the flow. Hence small scale turbulent features tend to be isotropic, whereas the larger features tend to exhibit distinct directional features.

The inertial subrange

At large scales anisotropic eddies are established which are governed by the boundary conditions and the physical constraints of the flow. At small scales the energy of the flow is dissipated away and converted to heat by viscous effects. In the middle there exists a set of intermediate scale eddies which tend to respond quickly to changes in the mean flow and are in an approximate anisotropic equilibrium.

On small scales, the eddies are independent of the boundary conditions, hence the only parameters which can influence them are the dissipation rate ε and viscosity ν. Kolmogorov (1941) proposed that $E(k)$ should only be a function of k, ε, and ν. This gives a single non-dimensional quantity of the kinetic energy of the form

$$\frac{E(k)}{\nu^{\frac{5}{4}}\varepsilon^{\frac{1}{4}}} = \frac{E(k)}{v_K^2 \eta_K} = f(k\eta_K), \tag{2.2.28}$$

where f is an undetermined non-dimensional function of the non-dimensional parameter $k\eta_K$. As the Reynolds number increases ε increases and $\eta_K \to 0$, so at high Reynolds number this scaling must hold as $k\eta_K \to 0$.

By contrast at the large scales the effects of viscosity are negligible and the key parameter is the strain rate $S(k)$ which acts to introduce kinetic energy into this system via the term $\langle u_i u_j \rangle S_{ij}$ in equation (2.2.23). Along with equation (2.2.25) this leads to

$$\varepsilon \propto \frac{U_e^3}{L_e}. \tag{2.2.29}$$

A similar non-dimensional relation for $E(k)$ at the large scales is given by

$$\frac{E(k)}{S^{-\frac{5}{2}}\varepsilon^{\frac{3}{2}}} = \frac{E(k)}{U_e^2 L_e} = F(kL_e), \tag{2.2.30}$$

where, in this case, $F(kL_e)$ is a non-dimensional function of the non-dimensional parameter kL_e. As the Reynolds number increases the length scale also increases, sot this relation must hold as $kL_e \to \infty$.

It was Kolmogorov's great insight to realise that it was possible to simultaneously take the limits $k\eta_K \to 0$ and $kL_e \to \infty$.This results in a spectrum that is consistent with both the small and large scale motions. As a consequence, this form for $E(k)$ would be expected to be a feature of real turbulent flows.

The methodology proceeds as follows: Kolmogorov took $Re \to \infty$ in such a way that $k\eta_K \to 0$ and $kL_e \to \infty$ at the same time

$$\begin{aligned} k\eta_K &= kL_e\left(\frac{\eta_K}{L_e}\right) = kL_e\left(\left(\frac{\nu^3}{\varepsilon}\right)^{\frac{1}{4}}\frac{1}{L_e}\right) \\ &\approx kL_e\nu^{\frac{3}{4}}\left(\frac{L_e}{U_e^3}\right)^{\frac{1}{4}}\frac{1}{L_e} \\ &= kL_e\left(\frac{1}{Re}\right)^{\frac{3}{4}}. \end{aligned} \tag{2.2.31}$$

Now suppose that $kL_e = Re^n$ for $n > 0$ then taking the limit $Re \to \infty$ is equivalent to $kL_e \to \infty$. But from (2.2.31) it can be seen that

$$k\eta_K = Re^{n-\frac{3}{4}},$$

which means that provided $n < 3/4$, taking the limit $Re \to \infty$ will also be equivalent to $k\eta_K \to 0$. Kolmogorov then matched the two forms for $E(k)$ of equations (2.2.28) & (2.2.30), which are valid at the small and large scales respectively

$$\begin{aligned} E(k) = U_e^2 L_e\, F(kL_e) &= v_K^2 \eta_K\, f(k\eta_K) \\ \implies \frac{U_e^2 L_e}{v_K^2 \eta_K} F\left(Re^n\right) &= f\left(Re^{n-\frac{3}{4}}\right) \\ \implies Re^{\frac{5}{4}} F\left(Re^n\right) &= f\left(Re^{n-\frac{3}{4}}\right), \end{aligned} \tag{2.2.32}$$

using the definitions of v_K, η_K and equation (2.2.29). Kolmogorov then assumed that F and f followed power law style behaviour of the form $F\left(Re^n\right) = \left(Re^n\right)^a$ and $f\left(Re^{n-\frac{3}{4}}\right) = \left(Re^{n-\frac{3}{4}}\right)^b$, in which case

$$\frac{5}{4} + an = b\left(n - \frac{3}{4}\right) \quad \implies \quad \frac{5}{4} + \frac{3}{4}b = n\left(b - a\right),$$

for $a, b \in \mathbb{R}$. Equation (2.2.32) must hold for any $n \in (0, 3/4)$, hence $a = b = -5/3$. This

means that

$$E(k) \propto U_e^2 L_e \, F(kL_e) = U_e^2 L_e (kL_e)^{-\frac{5}{3}} = \frac{U_e^2}{L_e^{\frac{2}{3}}} k^{-\frac{5}{3}}$$
$$\implies E(k) = \alpha \varepsilon^{\frac{2}{3}} k^{-\frac{5}{3}}, \tag{2.2.33}$$

where α is a constant.

This prediction was made in 1941 but was only validated experimentally, for a large variety of turbulent flows for sufficiently high Re, from the 1960's onwards, for example by Grant et al. (1962), Gargett et al. (1984), Maurer et al. (1994) and many others (see Lesieur (2008)). The wavenumber range for which the $-5/3$ law applies is called the inertial subrange.

Richardson (1921)'s experiments with dispersion had hinted that the clouds spread with a scaling law equivalent to equation (2.2.33). However, Richardson failed to predict that this is a universal feature of turbulent flows; consequently he missed out on one of the greatest discoveries in the field, which eventually fell to Kolmogorov.

2.3 Features of Langmuir turbulence and associated ocean boundary layers

2.3.1 Stokes drift

Langmuir turbulence is a term used to describe the effects of surface waves on otherwise ordinary wind driven (Ekman) boundary layers. The first such feature is the generation of an additional drift in the wind direction as a consequence of wave motion. The ocean surface is modelled by assuming that the ocean consists of steady, monochromatic deep water waves (assumed to be propagating in the x-direction) of the form

$$\eta(\boldsymbol{x}, t) = a \cos(kx - \sigma t). \tag{2.3.1}$$

Here η is the position of the free surface, a is the wave amplitude, k is the wavenumber, and $\sigma = \sqrt{(gk)}$ is the wave frequency. To first order, such a wave imposes what is called the "Stokes drift" on passive particles situated close to the ocean surface (Philips 1977). The velocities of such particles are given by

$$\begin{pmatrix} u_S \\ v_S \\ w_S \end{pmatrix} = a^2 \sigma k \, \mathrm{e}^{2kz_0} \begin{pmatrix} 1 - \cos(\sigma t) \\ 0 \\ \sin(\sigma t) \end{pmatrix}. \tag{2.3.2}$$

A schematic of the trajectories of three such particles situated at different depths is shown in figure 2.4. It is readily apparent that the particles exhibit a helical trajectory. Particles initially situated deep in the boundary layer experience a lower net drift over time than those

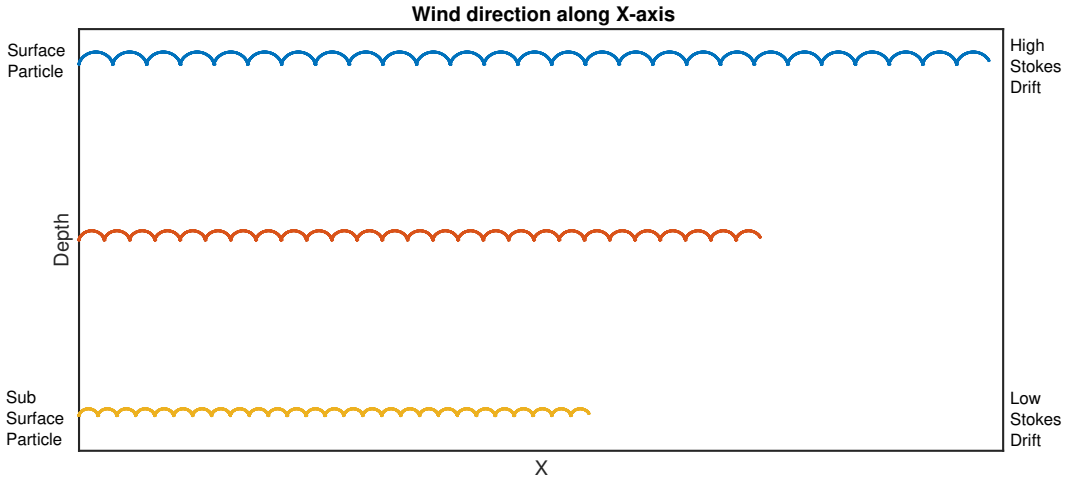

Figure 2.4: Trajectories (2.3.2) of passive particles initially situated at different depths of the water column. Over time the particles experience a net displacement in the wind direction. This displacement is determined by the Stokes drift.

close to the surface. This in turn has has a tilting effect on the vertical vorticity component in the boundary layer (Teixeira and Belcher 2002).

Incorporating the effects of propagating surface waves into a numerical model would require an extremely fine grid, in order to fully capture the dynamics of the surface oscillations. The computation cost of this set-up is very high, and infeasible for the timescales simulated here. However, encapsulating the average effects of the Stoke's drift by considering the time averaged quantities is much easier, especially when considering the overall effect on an Eulerian framework. Since $\overline{\cos(\sigma t)} = \overline{\sin(\sigma t)} = 0$, the Stokes drift is given by

$$\boldsymbol{U_S} = (a^2 \sigma k \, \mathrm{e}^{2kz_0}, 0, 0) = (U_S \, \mathrm{e}^{2kz_0}, 0, 0) \tag{2.3.3}$$

where $U_S = a^2 \sigma k$ is the Stokes drift velocity. However, the effects of surface waves have more subtle and profound effects on the ocean boundary layer than the imposition of a simple drift, as will be seen in section 2.3.3

2.3.2 Currents in the wind driven Ekman boundary layer

Observations of wind-driven oceanic currents show that they are deflected to the right of the prevailing wind in the northern hemisphere. This feature first observed by Norwegian polar explorer Fridtjof Nansen during his attempt to reach the North Pole in 1893-6. Nansen's idea was to trap his specially modified ship, the Fram, into the pack ice and wait for the currents to carry her northwards to the pole. He was unable to reach the pole as the ice moved in response to the wind-driven ocean currents in unpredictable ways. Measurements of current and wind direction taken during the expedition were passed on to the Swedish oceanographer Vagn Walfrid Ekman. Ekman (1905) deduced that the unpredictable current behaviour was due to a momentum balance of the turbulent wind stresses and the Coriolis force. It wasn't until the 1980s that more detailed observations of the structure of the Ekman

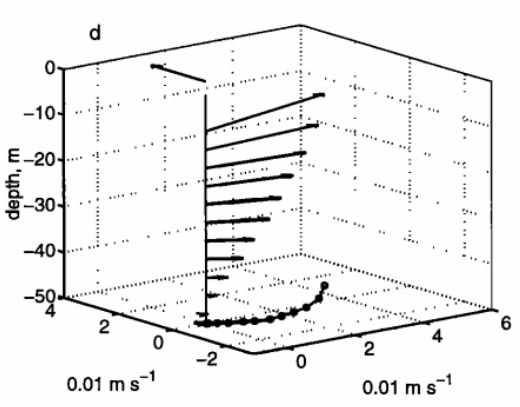

(a) Eastern Boundary Current Experiment (Chereskin 1995)

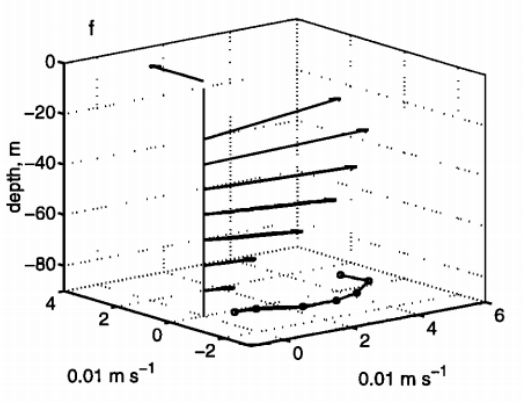

(b) 10°N Pacific (Wijffels et al. 1994)

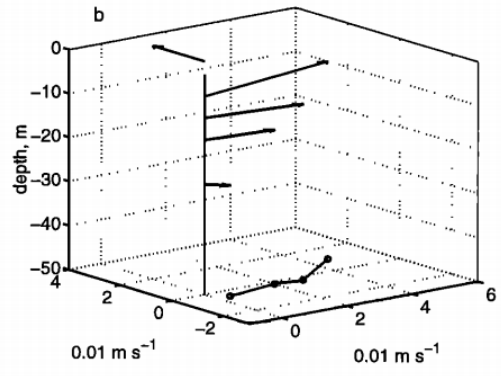

(c) LOTUS - western Sagrasso sea (Price et al. 1987)

Figure 2.5: Experiments showing the magnitude and direction of the ocean current vector forming the famous "Ekman spiral". The wind direction is shown by the topmost arrow (aligned to the north in all three subfigures). From (Price and Sundermeyer 1999).

boundary layer were possible (Price et al. 1987, Wijffels et al. 1994, Chereskin 1995). The Ekman layer has been the subject of considerable theoretical research and modelling (Price and Sundermeyer 1999, Lewis and Belcher 2004, Polton et al. 2005, McWilliams and Huckle 2006, Marlatt et al. 2010, 2011).

Model set-up

The starting point for the modelling of the Ekman boundary layer is the Navier-Stokes equations. Following, for example Lewis and Belcher (2004), the mean current flow $\boldsymbol{U}(\boldsymbol{x}) = (U(\boldsymbol{x}), V(\boldsymbol{x}), W(\boldsymbol{x}))$ satisfies

$$\frac{\partial \boldsymbol{U}}{\partial t} + \boldsymbol{U} \cdot \nabla \boldsymbol{U} = -\frac{1}{\rho}\nabla p + \frac{1}{\rho}\nabla \cdot \boldsymbol{\tau} + \boldsymbol{f}, \tag{2.3.4}$$

where $\boldsymbol{\tau}$ is the stress tensor, $\boldsymbol{f} = f\hat{\boldsymbol{k}} \times \boldsymbol{U}$ represents the Coriolis force with Coriolis frequency f, and $\hat{\boldsymbol{k}}$ is the unit upward vector normal to the surface. For the purposes of studying the Ekman layer, it is assumed that the horizontal gradients are much smaller than the vertical

gradients, so $\partial(U,V,W)/\partial(x,y) = 0$. Furthermore it is also assumed that the vertical velocity component is negligible compared to the horizontal components, hence $W(\boldsymbol{x}) = 0$.

It is convenient to change to a complex notation, rather than vector notation, for the horizontal velocity components. U_O is the east-west horizontal ocean current component and V_O is the north-south component. $\boldsymbol{U_O}(z,t) = U_O + iV_O$, the complex horizontal velocity in the $x-y$ space, is then given by

$$\frac{\partial \boldsymbol{U_O}}{\partial t} + if\boldsymbol{U_O} = \frac{1}{\rho}\frac{\partial \boldsymbol{\tau}}{\partial z} - \frac{1}{\rho}\nabla p + \textit{higher order terms.} \tag{2.3.5}$$

The higher order terms are correlations of the parameters and assumed to be small. It is assumed that the pressure gradient is not influenced by the wind stresses (Price and Sundermeyer 1999), allowing equation (2.3.5) to be decomposed into geostrophic (pressure driven) and Ekman (wind driven) components $\boldsymbol{U_O} = \boldsymbol{U_p} + \boldsymbol{U}$, summarised by the equation

$$\frac{\partial \boldsymbol{U}}{\partial t} + if\boldsymbol{U} = \frac{1}{\rho}\frac{\partial \boldsymbol{\tau}}{\partial z}. \tag{2.3.6}$$

Ekman (1905) used a (constant) eddy viscosity approximation to relate the wind stress to turbulent shear,

$$\boldsymbol{\tau} = \rho\nu_e\frac{\partial \boldsymbol{U}}{\partial z},$$

giving the wind driven boundary layer equations

$$\frac{\partial \boldsymbol{U}}{\partial t} + if\boldsymbol{U} = \nu_e\frac{\partial^2 \boldsymbol{U}}{\partial z^2}. \tag{2.3.7}$$

Infinite depth boundary layer

Equations (2.3.6)–(2.3.7) are subject to the following boundary conditions for an infinite depth boundary layer (with $z \leqslant 0$)

$$\rho\nu_e \left.\frac{\partial \boldsymbol{U}}{\partial z}\right|_{z=0} = \boldsymbol{\tau_S} = \tau_S + i0, \;\; ; \;\; \boldsymbol{U}(z \to -\infty, t) \to 0, \tag{2.3.8}$$

where $\boldsymbol{\tau_S}$ is the wind stress. Most publications, including Ekman's original work, focus on finding the time-independent, or steady state, solutions, as these are of the greatest interest. However, it's perfectly possible to devise (complicated) analytical time-dependent solutions. Lewis and Belcher (2004) solved equation (2.3.7) by applying a Laplace transform

$$\boldsymbol{U}(z,s) = \int_0^\infty \mathrm{e}^{-st}\,\boldsymbol{U}(z,t)\,\mathrm{d}t, \;\; \mathrm{Re}(s) \geqslant 0, \tag{2.3.9}$$

which retains the time-dependence of the solution. The resulting ordinary differential equation

$$\nu_e\frac{\mathrm{d}^2\boldsymbol{U}(z,s)}{\mathrm{d}z^2} = (s+if)\,\boldsymbol{U}(z,s) - \boldsymbol{U}(z,0) \tag{2.3.10}$$

is then solved subject to the transformed surface stress condition

$$\left.\frac{\mathrm{d}\boldsymbol{U}\left(z,s\right)}{\mathrm{d}z}\right|_{z=0} = \frac{\tau_S}{\rho\nu_e s}, \tag{2.3.11}$$

and lower boundary condition. The solution, $\boldsymbol{U}\left(z,t\right)$, to (2.3.7) is then given by the inverse Laplace transform

$$\boldsymbol{U}\left(z,t\right) = \frac{1}{2\pi i}\int_{c-i\infty}^{c+i\infty} \mathrm{e}^{st}\boldsymbol{U}\left(z,s\right)\mathrm{d}s, \quad c \geqslant 0. \tag{2.3.12}$$

The integral in (2.3.12) can usually be established by contour integration.

For a system started from rest, $\boldsymbol{U}(z,0) = 0$, the solution to (2.3.10) is given by

$$\boldsymbol{U}\left(z,s\right) = \frac{\tau_S}{\rho s\sqrt{\nu_e\left(s+\mathrm{i}f\right)}}\exp\left(z\sqrt{\frac{s+\mathrm{i}f}{\nu_e}}\right). \tag{2.3.13}$$

Applying the inverse Laplace transform (2.3.12) and computing the contour integral gives the solution

$$\begin{aligned}\boldsymbol{U}_{rest}\left(z,t\right) = \frac{\tau_S}{\rho\sqrt{2f\nu_e}}\left(1-i\right)\Bigg\{&\exp\left(\left(1+i\right)z\sqrt{\frac{f}{2\nu_e}}\right) - \frac{1}{2}\Bigg[2\cosh\left(\left(1+i\right)z\sqrt{\frac{f}{2\nu_e}}\right) - \\ &\exp\left(-\left(1+i\right)z\sqrt{\frac{f}{2\nu_e}}\right)\operatorname{erf}\left(\sqrt{\frac{ft}{2}}\left(1+i\right) - \frac{z}{2\sqrt{\nu_e t}}\right) - \\ &\exp\left(\left(1+i\right)z\sqrt{\frac{f}{2\nu_e}}\right)\operatorname{erf}\left(\sqrt{\frac{ft}{2}}\left(1+i\right) + \frac{z}{2\sqrt{\nu_e t}}\right)\Bigg]\Bigg\},\end{aligned} \tag{2.3.14}$$

where erf is the complex error function. The first part of the above solution is the steady state solution to equation (2.3.7)

$$\boldsymbol{U}_{steady}\left(z,t\right) = \frac{\tau_S}{\rho\sqrt{2f\nu_e}}\left(1-i\right)\exp\left(\left(1+i\right)z\sqrt{\frac{f}{2\nu_e}}\right) \tag{2.3.15}$$

which exhibits the expected decay in magnitude, and clockwise deflection, of the current. A hodograph of the solution (2.3.14) at different times, for $U_* = 3.5\times10^{-3}\ \mathrm{m\,s^{-1}}$, is show in figure 2.6a. The deflection of the current at the surface is approximately 45° from the prevailing easterly wind arising from the earth's rotation. This was the deflection that Nansen failed to appreciate when planning his polar expedition. The current declines with depth because the viscosity of the water slows down the fluid layers as they slide over each other, causing the current to dissipate. The figure shows that the oscillatory term (erf terms) eventually dies away, although very slowly as $t\to\infty$ over a timescale $z/2\sqrt{\nu_e}$, which is itself infinite since $z\to\infty$. In many ways it is of purely mathematical interest.

For comparison, a hodograph of the horizontal velocities from a full LES simulation of the physical model (also for $U_* = 3.5\times10^{-3}\ \mathrm{m\,s^{-1}}$, in a 33 m boundary layer) described in

this chapter is shown in figure 2.6c. The expected Ekman spiral, with a deflection of 45° is also present, it is important to note that the LES simulation incorporates additional features of ocean turbulence described in this section.

Finite depth boundary layer

For a system starting from rest, with finite lower boundary condition $\boldsymbol{U}(-H,t)=0$, where H is the depth of the boundary layer, the solution to the transformed equation (2.3.10) is given by

$$\boldsymbol{U}_{H,rest}(z,s)=\frac{\tau_S\left[\exp\left(z\sqrt{\frac{s+if}{\nu_e}}\right)-\exp\left(-(z+2H)\sqrt{\frac{s+if}{\nu_e}}\right)\right]}{\rho s\sqrt{\nu_e(s+if)}\left[1+\exp\left(-2H\sqrt{\frac{s+if}{\nu_e}}\right)\right]}. \tag{2.3.16}$$

Computing the inverse Laplace transform, which in this case requires a complicated contour to allow for the infinite series of poles at

$$s=-\frac{(2n+1)^2\pi^2\nu_e}{4H^2}-if,$$

gives the solution

$$\boldsymbol{U}_{H,rest}(z,t)=\frac{\tau_S}{\rho\sqrt{2\nu_e f}}\left\{\frac{(1-i)\sinh\left((1+i)(z+H)\sqrt{\frac{f}{2\nu_e}}\right)}{\cosh\left((1+i)H\sqrt{\frac{f}{2\nu_e}}\right)}+\right.$$
$$\left.\frac{2\sqrt{2\nu_e}\,\mathrm{e}^{-ift}}{H\sqrt{f}}\sum_{n=0}^{\infty}\frac{(-1)^{n+1}\left(\frac{(2n+1)^2\nu_e\pi^2}{4H^2f}-i\right)\sin\left(\frac{(2n+1)\pi(z+H)}{2H}\right)\exp\left(-\frac{(2n+1)^2\nu_e\pi^2}{4H^2}t\right)}{\left(\frac{(2n+1)^2\nu_e\pi^2}{4H^2f}\right)^2+1}\right\}. \tag{2.3.17}$$

The first term on the right hand side is the steady state solution. Similarly to the infinite depth case, the solution exhibits the expected Ekman spiral, and the surface deflection from the prevailing wind is 45°. Figure 2.6b shows a hodograph of the solution (2.3.17) for $U_*=3.5\times10^{-3}\ \mathrm{m\,s^{-1}}$ in a 33 m boundary layer, the result is very similar to the steady-state result (2.3.15). The oscillatory term (the Σ term) represents an inertial oscillation which is transient. It dies off on a timescale $4H^2/\nu_e\pi^2$, much more rapidly than the oscillation term in equation (2.3.14). Imposing a finite boundary layer depth effectively traps the inertial oscillations, allowing them to be damped out by viscosity.

2.3.3 Craik-Leibovich equations

Using perturbation theory Craik and Leibovich (1976) showed that the introduction of a surface wave boundary condition (equation (2.3.1)) into the Navier-Stokes equations leads to a coupling of the Stokes drift and local vorticity, $\boldsymbol{\omega}=\nabla\times\boldsymbol{u}$, giving rise to a vortex force term of the form $\boldsymbol{U_S}\times\boldsymbol{\omega}$. Leibovich (1980) later showed that this term can also

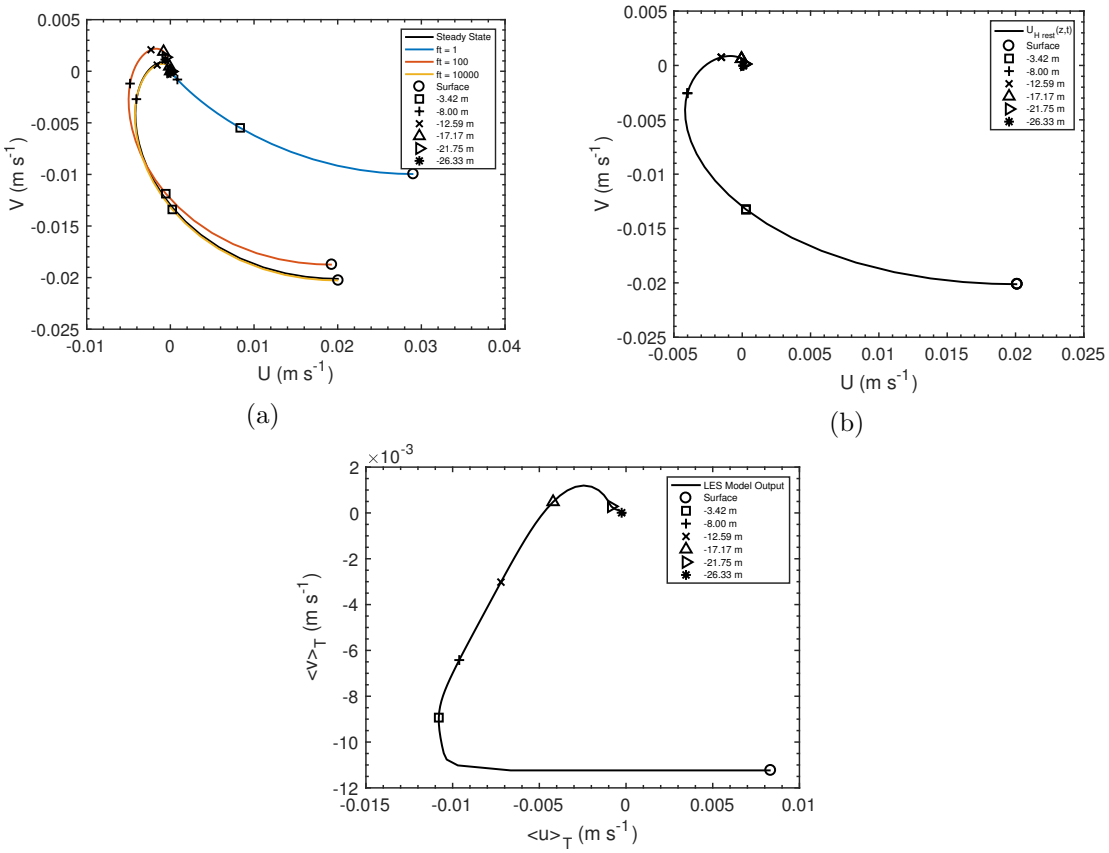

Figure 2.6: Hodographs of the Ekman spiral from (a) equation (2.3.14) at different times and (2.3.15), (b) equation (2.3.17), (c) full LES model, for $U_* = 3.5 \times 10^{-3}$ m s^{-1} . All three cases exhibit the expected decay in the magnitude, and clockwise deflection, of the current.

be derived from generalised Lagrangian mean theory. This term drives the formation of Langmuir circulations. On a voyage from New York to England in 1927 Irving Langmuir noticed large quantities of seaweed aligned in long narrow rows approximately parallel to the wind direction. This indicated the presence of organised three-dimensional flow in the near-surface layer of the ocean. Langmuir (1938) carried out experiments at Lake George, which confirmed the presence of counter-rotating vortex "tunnels" aligned approximately with the wind direction. Flotsam was swept into the convergence zones of these vortices, forming narrow rows which are known as "wind rows". These vortices are known as Langmuir cells, and the associated flow is called Langmuir circulation. Langmuir cells form when vertical eddies are tilted and intensified in the horizontal direction perpendicular to wave propagation. They're important both physically and biologically as they help to increase vertical mixing and advect nutrients into the euphotic zone (Barstow 1983, Hutchings et al. 1995). The Craik-Leibovich equations are defined as

$$\frac{\partial \boldsymbol{u}}{\partial t} + \boldsymbol{u} \cdot \nabla \boldsymbol{u} + f\hat{\boldsymbol{k}} \times (\boldsymbol{u} + \boldsymbol{U_S}) = -\frac{\nabla p_S}{\rho_0} - g\frac{\rho''}{\rho_0}\hat{\boldsymbol{k}} + \boldsymbol{U_S} \times \boldsymbol{\omega} + \nu \Delta \boldsymbol{u} \tag{2.3.18}$$

with continuity

$$\nabla \cdot \boldsymbol{u} = 0. \tag{2.3.19}$$

Here $f = 2\Omega \sin(\phi)$ is the Coriolis frequency (where Ω is the Earth's angular rotation speed & ϕ is the latitude), $\hat{\boldsymbol{k}}$ is the upward vertical unit vector, $\boldsymbol{U_S}$ is the Stokes drift (section 2.3.1). The first part of the term involving the Coriolis frequency, $f\hat{\boldsymbol{k}} \times \boldsymbol{u}$, represents the Coriolis force and leads to the Ekman layer described in section 2.3.2. The second part, $f\hat{\boldsymbol{k}} \times \boldsymbol{U_S}$ is called the Coriolis-Stokes force (Polton et al. 2005) and describes the interaction between the Coriolis effect and wave-induced Stokes drift.

The Craik-Leibovich equations form the basis for the LES physical model that is used in this work to generate the turbulent boundary layers in which the interactions between the plankton populations will be studied.

2.3.4 Langmuir circulation

Wind rows

Wind driven Stokes-Ekman boundary layers exhibit some unique features that arise because of the presence of Langmuir circulations. The LES code can be used to investigate these characteristics further. To begin, the LES can be used to illustrate the presence of wind rows. To do so a number of particles were released at the surface and the trajectories were followed for a short time. The results are shown in figure 2.7. Initially the particles are evenly distributed along the top half of the left boundary. Over time the particles move east in the direction of the wind, and the particles cluster together forming the streaks parallel to the wind direction, as first observed by Langmuir (1938).

Figure 2.8 shows the direction and magnitude of the velocity field in the y and z directions

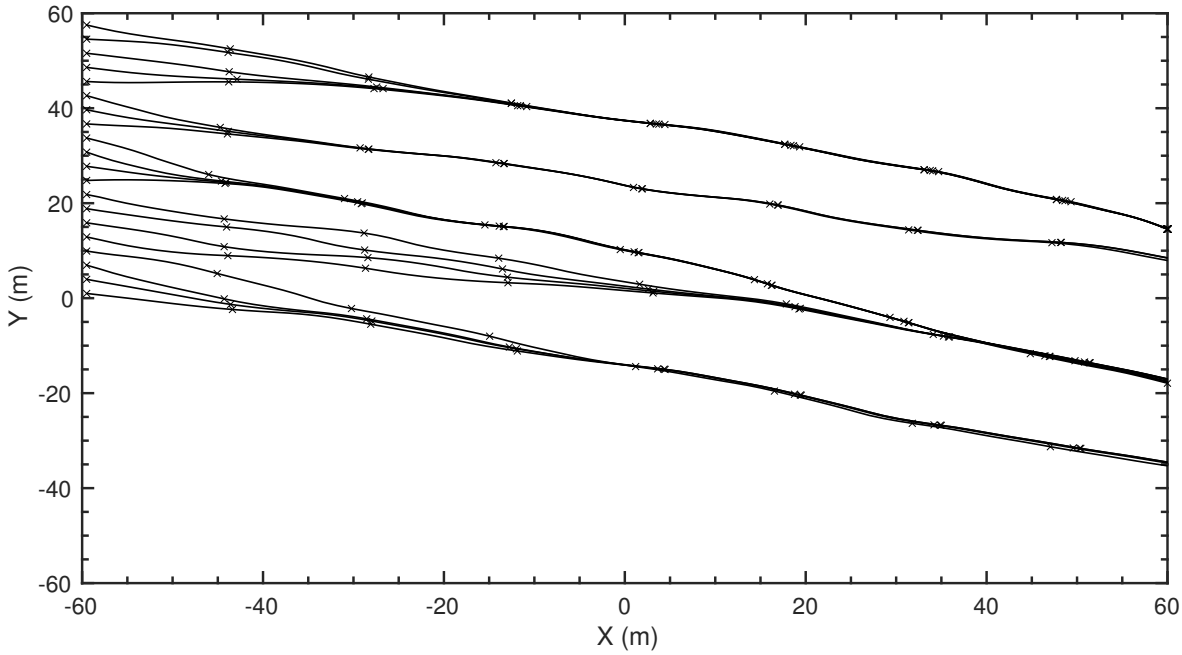

Figure 2.7: A set of 20 particle paths all starting at $X = -60$ m at different $y \in (0, 60)$. The particles are travelling eastwards (increasing X). The crosses indicate intervals of 100 time-steps. These results are from an LES simulation over 30 m, subject to $(U_*, U_S) = (3.0, 3.3)$.

across the simulated boundary layer at $x = 0$. The counter-rotating nature of the Langmuir cells can be seen by the direction of the flow. The background heat-map represents the two dimensional vorticity at each point, with positive vorticity indicating anti-clockwise rotation. As shown most clearly towards the surface, the alternating nature of the positive and negative vorticity indicates the presence of the counter rotating cells.

Langmuir number

By taking the same coordinate transformation as in section 2.1.3, the Craik-Leibovich equations (2.3.18) can be non-dimensionalised giving

$$\frac{\partial \boldsymbol{u}}{\partial t} + \boldsymbol{u} \cdot \nabla \boldsymbol{u} + f\hat{\boldsymbol{k}} \times \left(\boldsymbol{u} + \frac{\boldsymbol{U_S}}{U} \right) = -\nabla p - \frac{L}{U^2} g \hat{\boldsymbol{k}} \frac{\rho''}{\rho_0} + \frac{\boldsymbol{U_S}}{U} \times \boldsymbol{\omega} + \frac{1}{Re} \Delta \boldsymbol{u} + \boldsymbol{F}, \qquad (2.3.20)$$

where $\boldsymbol{\omega}* = \nabla \times \boldsymbol{u}*$ has been used in the vortex force term, and the asterisks removed. Taking $U = cU_*$ where $U_* = (\tau_S/\rho)^{\frac{1}{2}}$ is the oceanic friction velocity (Lewis and Belcher 2004) and c is a constant to be determined, the non-dimensional Langmuir number is defined as $La = \sqrt{(U_*/U_S)}$. Madsen (1977) studied an Ekman layer problem where the eddy viscosity increased linearly with depth (z), and was related to the friction velocity by $\nu_e = \kappa U_* z$, where $\kappa = 0.4$ is von Karmen's constant. From equation (2.3.8)

$$\begin{aligned} \tau_S = \rho U_*^2 &= \rho \nu_e \frac{\partial U}{\partial z} \\ U_*^2 &= \kappa U_* z \frac{\partial U}{\partial z}. \end{aligned} \qquad (2.3.21)$$

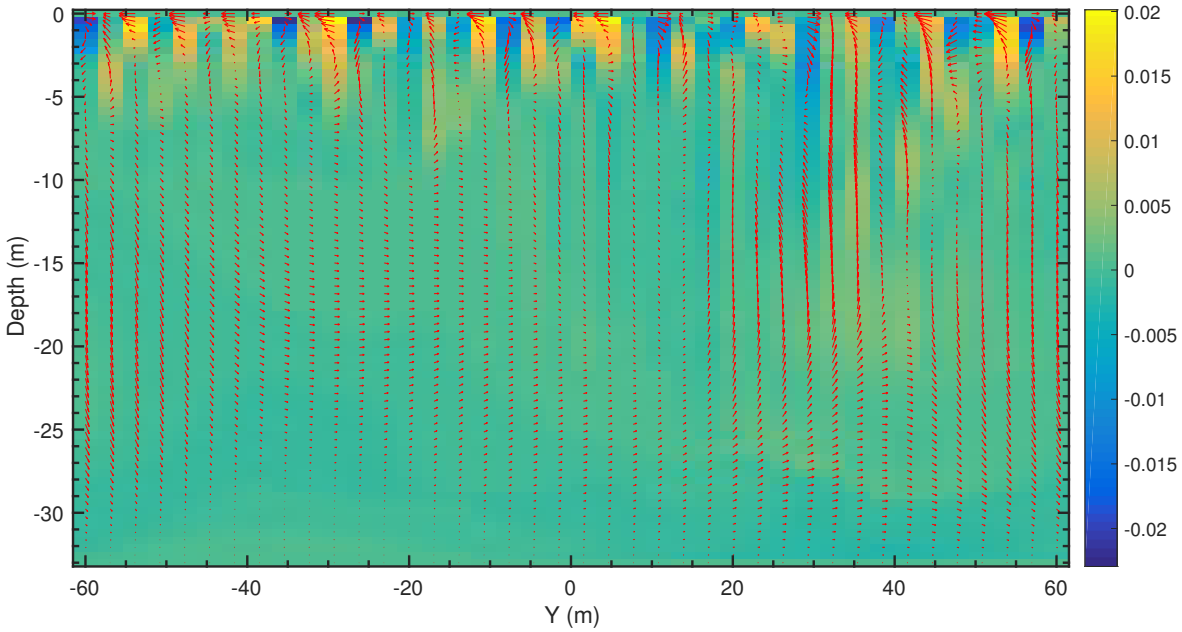

Figure 2.8: →: Instantaneous (v, w) velocities in a vertical $(y-z)$ slice at $x = 0$ m. Heat map represents the 2D vorticity at each point. These results are from an LES simulation over 33 m, subject to $(U_*, U_S) = (3.5, 3.9)$.

On large eddy scales it is assumed that $\partial U_e/\partial z \approx U_e/L_e$, which gives

$$U_* \approx \kappa U_e, \tag{2.3.22}$$

hence $c = 1/\kappa$. The value of the Langmuir number is typically between 0.2 and 0.5 under quasi-equilibrium conditions of wind and waves (Smith 1992). The value of $La = 0.3$ from McWilliams et al. (1997) will be used here and corresponds to a fully developed layer (Komen et al. 1994, Li and Garrett 1995, Grant and Belcher 2009).

2.4 Large eddy simulations (LES)

When numerically solving the Navier-Stokes, or Craik-Leibovich, equations in oceanic boundary layers, it is infeasible to resolve down to the smallest scales. In order to capture both the dynamics of the large scale features that drive the flow and the smallest length scales where energy is dissipated by heat, the resolution scale would ideally be the Kolmogorov length scale, η_K. As the turbulent intensity increases, measured by $\langle\varepsilon\rangle$, a finer resolution is required. Consider a turbulent flow with intensity $\langle\varepsilon\rangle = 1 \times 10^{-7}$ m^2 s^{-3} on a three-dimensional solution grid of size 100 m $\times$ 100 m $\times$ 50 m. For a direct numerical simulation the grid size would need to be $\eta_K = 1.8 \times 10^{-3}$ m, meaning it would require 1×10^{14} calculations for each variable, at each point in time! Even with the most powerful computers available this would not be possible. This highlights a fundamental problem with attempting to solve the Navier-Stokes equations over large scale oceanic boundary layers. As a consequence numerical approximations must be made in order to reduce the resolution scale, yet still

retain the fundamental characteristics of a full boundary layer solution.

There are many methods that can be used to do this, one such example is the $k-\epsilon$ turbulence closure model (Launder and Spalding 1974, Chen and Kim 1987, Mohammadi and Pironneau 1993). This model uses the Reynolds Averaged Navier-Stokes (RANS) (Reynolds 1894) equations to write k (energy) and ε (dissipation rate) equations such as found in Jones and Launder (1972). The RANS are time-averaged equations, however turbulent flows are typically very transient and not stationary so this method will not be used here.

Given the limitation on the resolution, only a portion of the scale range can be explicitly resolved. The obvious choice is to use the scales that are most important to the flow. In the case of an oceanic boundary layer the most important scales are those which contain most of the turbulent kinetic energy, which are the large eddies. Consequently, the model that will be utilised here is one that will capture the dynamics of the large-scale motions, whilst sacrificing the small-scale motion. This method is known as large eddy simulation (LES) (Deardorff 1970, Moeng and Sullivan 2002, Sagaut 2006).

2.4.1 Filtering

The main idea of LES is to split the flow ($\boldsymbol{u},\ p$) into two parts, a large scale flow and a small scale flow, i.e. $\boldsymbol{u}=\overline{\boldsymbol{u}}+\boldsymbol{u}',\ p=\overline{p}+p'$. Here $\overline{\boldsymbol{u}}$ & $\overline{p}$ account for the flow that is larger than the grid scale, the small scale is known as the sub-grid scale. More formally a filter is applied to the equations which "filters" out the sub-grid scales. A Fourier transform of the form

$$\boldsymbol{u}(\boldsymbol{k},t)=\int \boldsymbol{u}(\boldsymbol{x},t)\,\mathrm{e}^{i\boldsymbol{k}\cdot\boldsymbol{x}}\ \mathrm{d}\boldsymbol{x}, \tag{2.4.1}$$

is applied to the flow. A cut-off wavenumber, k_c, which is equivalent to $1/\Delta x$, where Δx is the resolution scale, is introduced. This wavenumber is used to remove the sub-grid scale processes,

$$\overline{\boldsymbol{u}(\boldsymbol{x},t)}=\begin{cases}(1/2\pi)^3\int \boldsymbol{u}(\boldsymbol{k},t)\,\mathrm{e}^{-i\boldsymbol{k}\cdot\boldsymbol{x}}\ \mathrm{d}\boldsymbol{k} & \text{if } k\leqslant k_c,\\ 0 & \text{otherwise.}\end{cases} \tag{2.4.2}$$

As a result the $\boldsymbol{u}'$ contribution is removed. Applying this filter to the Craik-Leibovich equations leads to the equations that govern the large, resolved, scale processes. In Einstein notation the filtered Craik-Leibovich equations are given by

$$\frac{\partial\overline{u}_i}{\partial t}+\frac{\partial\overline{u_iu_j}}{\partial x_j}+\epsilon_{ij3}(\overline{u}_i+U_{Si})=-\frac{1}{\rho}\frac{\partial\overline{p}}{\partial x_i}+\nu\frac{\partial^2\overline{u}_i}{\partial x_j^2}+\epsilon_{ijk}U_{Si}\overline{\omega}_j+F_i, \tag{2.4.3}$$

where ϵ_{ijk} is the 3-dimensional Levi-Civita symbol. The filtering operation removes all linear small scale terms. However, there remains the problem of how to resolve the advection term, $\partial\overline{u_iu_j}/\partial x_j$ since this involves a knowledge of the sub-grid scales. The first step is to define

$\tau_{ij} = \overline{u_i u_j} - \overline{u}_i \overline{u}_j$ rewrite the advection term as

$$\frac{\partial \overline{u}_i \overline{u}_j}{\partial x_j} + \left(\frac{\partial \overline{u_i u_j}}{\partial x_j} - \frac{\partial \overline{u}_i \overline{u}_j}{\partial x_j} \right) = \frac{\partial \overline{u}_i \overline{u}_j}{\partial x_j} + \frac{\partial \tau_{ij}}{\partial x_j}. \tag{2.4.4}$$

The first part of the advection term is the large scale advection, and $\partial \tau_{ij}/\partial x_j$ are the unresolved sub-grid scales (SGS).

Smagorinsky scheme

The problem of resolving the sub-grid scales is termed a closure problem. They cannot be calculated directly or assumed to be negligible. Large eddy simulation is a method which resolves this problem by modelling the non-linear $\partial \tau_{ij}/\partial x_j$ term by means of large-scale processes. The most common way to do this is to use a scheme devised by Smagorinksy (1963), and this will be used here. Smagorinksy (1963) argued that the SGS stress (τ_{ij}) can be related to the resolved strain tensor by

$$\tau_{ij} = -\nu_e(\boldsymbol{x}) S_{ij}. \tag{2.4.5}$$

It was postulated that the eddy viscosity should be a function of the amount of shear in the resolved flow and the size of the largest eddies, since these govern the work done by the flow. The eddy viscosity is related to S_{ij} by

$$\nu_e(\boldsymbol{x}) = C z_S^2 \sqrt{\frac{S_{ij} S_{ij}}{2}}, \tag{2.4.6}$$

where $C = O(1)$ constant, z_S is the depth of the boundary/simulation layer and S_{ij} is the rate of strain tensor, which is a measure of the shear of the resolved flow.

In the rest of this work the overbar will be removed from the filtered scales for brevity, so that $\boldsymbol{u}$ and p will refer to the filtered velocity and pressure respectively.

2.4.2 Energy dissipation rate

As discussed in section 2.2, energy inputted into the boundary layer is ultimately converted into heat due to viscous effects. The amount of energy dissipated in this way gives an indication of the amount of energy that is in the system. The energy dissipation rate is calculated from the (statistically stationary) mean turbulent kinetic energy budget equation given by McWilliams et al. (1997) and Lewis (2005),

$$0 = \frac{1}{2}\frac{\mathrm{d}\langle u_i''^2 \rangle_T}{\mathrm{d}t} = -\frac{1}{2}\frac{\mathrm{d}\langle w'' u_i''^2 \rangle_T}{\mathrm{d}z} - \frac{1}{\rho_0}\frac{\mathrm{d}\langle w'' p'' \rangle_T}{\mathrm{d}z} - \langle u'' w'' \rangle_T \frac{\mathrm{d}\langle u \rangle_T}{\mathrm{d}z} - \langle v'' w'' \rangle_T \frac{\mathrm{d}\langle v \rangle_T}{\mathrm{d}z} - \langle u'' w'' \rangle_T \frac{\mathrm{d}U_S}{\mathrm{d}z} + \alpha g \langle \theta'' \rangle_T - \langle \varepsilon(z) \rangle_T. \tag{2.4.7}$$

Here the angled brackets, $\langle\cdot\rangle_T$, represent a 2d horizontal (x and y) and time average, and the double primed quantities denote a fluctuation from the average of a scalar quantity, i.e.: $q = \langle q\rangle_T + q''$. Equation (2.4.7) can be derived by methods of Reynolds decomposition and horizontal averaging. The terms on the right-hand side represent turbulent transport, pressure work, shear production, Stokes production, buoyancy production and SGS dissipation. In a Stokes-Ekman layer, the Stokes production combines with an increased pressure working term to produced raised levels of turbulent kinetic energy compared to those of shear turbulence (Terray et al. 1996, Lewis 2005). This is an important consequence of including surface waves (2.3.1) in the boundary layer formulation. Mixing levels are increased by Langmuir turbulence, meaning any nutrient sources are advected more rapidly which impacts on the biological dynamics of the system.

2.4.3 Numerical techniques

Solving for the pressure term

One of the main challenges in solving the Navier-Stokes equations numerically is resolving the pressure term and predicting its evolution. In this model, the starting point is to rearrange the Navier-Stokes equations into the form

$$\begin{aligned}\rho\frac{\partial u}{\partial t} &= -\frac{\partial p}{\partial x} + S_u,\\ \rho\frac{\partial v}{\partial t} &= -\frac{\partial p}{\partial y} + S_v,\\ \rho\frac{\partial w}{\partial t} &= -\frac{\partial p}{\partial z} + S_w.\end{aligned} \tag{2.4.8}$$

Here the S_i refer to the source terms, including the advection, for each of the velocities, estimated from the previous numerical iteration. Taking the divergence of the above equation results in the Poisson equation for the pressure (n.b. $\nabla\cdot\boldsymbol{u} = 0$), given by

$$\frac{\partial^2 p}{\partial x_i^2} = \frac{\partial S_i}{\partial x_i} \tag{2.4.9}$$

where Einstein summation notation has been used. In order to solve these equations a two dimensional Fourier transform is applied, across the uniform x-y grid plane. This Fourier transform is given by

$$\tilde{p}(k_x, k_y, z) = \int_{-\infty}^{\infty}\int_{-\infty}^{\infty} p(x, y, z)\, \mathrm{e}^{i(k_x x + k_y y)}\ \mathrm{d}x\mathrm{d}y. \tag{2.4.10}$$

Taking the Fourier transform of equation (2.4.9) gives

$$\frac{\mathrm{d}^2\tilde{p}(k_x, k_y, z)}{\mathrm{d}z^2} - (k_x^2 + k_y^2)\tilde{p} = \int_{-\infty}^{\infty}\int_{-\infty}^{\infty} \nabla\cdot(S_u, S_v, S_w)\, \mathrm{e}^{i(k_x x + k_y y)}\ \mathrm{d}x\mathrm{d}y = G(k_x, k_y, z), \tag{2.4.11}$$

where G represents the (known) Fourier transform of the source terms. This transforms equation (2.4.9) into a relatively simple ODE for $p(k_x, k_y, z)$. Discretising the second derivative in equation (2.4.11), i.e.:

$$\frac{\mathrm{d}^2\tilde{p}(k_x,k_y,z)}{\mathrm{d}z^2} = \frac{\tilde{p}(k_x,k_y,z-\delta z) - 2\tilde{p}(k_x,k_y,z) + \tilde{p}(k_x,k_y,z+\delta z)}{(\delta z)^2} \tag{2.4.12}$$

allows the solution of $\tilde{p}(k_x, k_y, z)$ to be posed as an inverse problem of the form

$$\begin{pmatrix} -\frac{2}{(\delta z)^2} - k_x^2 - k_y^2 & \frac{1}{(\delta z)^2} & 0 & \cdots & 0 \\ \frac{1}{(\delta z)^2} & -\frac{2}{(\delta z)^2} - k_x^2 - k_y^2 & \frac{1}{(\delta z)^2} & \cdots & 0 \\ 0 & \ddots & \ddots & \ddots & \vdots \\ 0 & 0 & \cdots & \frac{1}{(\delta z)^2} & -\frac{2}{(\delta z)^2} - k_x^2 - k_y^2 \end{pmatrix} \begin{pmatrix} \tilde{p}(z_0) \\ \tilde{p}(z_1) \\ \vdots \\ \tilde{p}(z_n) \end{pmatrix} = G. \tag{2.4.13}$$

This can be inverted using standard numerical techniques for tridiagonal matrices (Press 2007). It is then a simple case of using the inverse Fourier transform of $\tilde{p}(k_x, k_y, z)$ to find the pressure.

Time stepping

The velocity and pressure fields are then time-stepped forward by discretising the time derivatives in the Navier-Stokes equations, i.e.:

$$\frac{\partial \boldsymbol{u}}{\partial t} = \frac{\boldsymbol{u}(\boldsymbol{x}, t+\delta t) - \boldsymbol{u}(\boldsymbol{x}, t)}{\delta t}. \tag{2.4.14}$$

In this case a dynamic time-step, δt, is used. As the intensity of the turbulence, $\langle\varepsilon\rangle$, increases the Kolmogorov time-scale τ_K decreases so a higher level of accuracy is required, the time-step is chosen to be dynamic to account for this. The time-step is defined by

$$\delta t = \left(\sqrt{\left|\frac{u}{\delta x}\right|^2 + \left|\frac{v}{\delta y}\right|^2 + \left|\frac{w}{\delta z}\right|^2} + \frac{2\nu}{(\delta x)^2 + (\delta y)^2 + (\delta z)^2} \right)^{-1}. \tag{2.4.15}$$

This can be roughly described as $\delta t = (\text{advection} + \text{diffusion})^{-1}$. If the magnitude of the flow increases then the time-step will decrease to account for the inherent unpredictability of a more turbulent flow.

2.4.4 Boundary conditions

The Craik-Leibovich equations are solved subject to a set of boundary conditions. Periodic lateral boundary conditions are imposed on the solution grid. these take the form

$$\begin{aligned}\Gamma(x_{max}, y, z) &= \Gamma(x_{min}, y, z),\\ \Gamma(x, y_{max}, z) &= \Gamma(x, y_{min}, z),\end{aligned} \tag{2.4.16}$$

where $\Gamma = u, v, w, p$. At the lower boundary $z = z_S$ no-slip, $\Gamma = 0$, boundary conditions are imposed on u and v, a no penetration boundary condition is imposed on w, i.e. $w|_{z=z_S} = 0$. The main driver of the turbulence in the boundary layer is the wind blowing over the surface. This characterises the surface boundary condition for u as

$$\nu_e \left.\frac{\partial u}{\partial z}\right|_{z=0} = \frac{\tau_S}{\rho} = U_*^2. \tag{2.4.17}$$

The surface boundary condition for v is known as a stress free boundary condition, given by

$$\left.\frac{\partial v}{\partial z}\right|_{z=0} = 0. \tag{2.4.18}$$

A no-penetration boundary condition is imposed on w at the surface, $w = 0$ at $z = 0$. Finally, upper and lower boundary conditions on the pressure are determined by the w source terms since $w = 0$ at both boundaries. The boundary conditions on p are then

$$\left.\frac{\partial p}{\partial z}\right|_{z=0} = S_w(z = 0) \;\; ; \;\; \left.\frac{\partial p}{\partial z}\right|_{z=z_S} = S_w(z = z_S), \tag{2.4.19}$$

where S_w is as from equation (2.4.8).

2.4.5 Statistical stability

Lewis (2005) extensively tested the performance of the LES code by comparing the output with that of a similar code used McWilliams et al. (1997), to study Langmuir turbulence in the upper ocean boundary layer. Comparisons of horizontal currents, shear stresses, velocity variances and dissipation rates showed strong agreement across the mixing layer $z \in [-z_{ML}, 0]$. The code of McWilliams et al. (1997) incorporated a stably stratified region below z_{ML} extending to $z \approx -3z_{ML}$. The LES modelled described here does not feature any such stratification, which raises a problem with the terminology "mixing-layer depth", since the hydrographical features regulating its position are absent.

An important feature of the numerics of simulated boundary layers subject to fixed boundary conditions is their associated statistical stability (Lesieur 1997). It is important that key features that characterise the boundary layer structure should remain stable over time. This requires certain ensemble (or equivalently spatial) averages (under the conditions of homo-

geneity and isotropy) to remain approximately constant over a full simulation time. Brereton (2013) discusses the stability of the LES model by considering first and second order stability of the average velocity. Figure 2.9 demonstrates that the first order statistics for $\langle u \rangle_T$ and $\langle v \rangle_T$ are mostly well-behaved, increasingly so for higher values of U_*. The behaviour of the second order statistics for $\langle u''^2 \rangle_T$, $\langle v''^2 \rangle_T$ and $\langle w^2 \rangle_T$, is shown in figure 2.10. The curves shown here have been scaled by their maximum values, i.e.:

$$\frac{\langle u''^2(z,t_i)\rangle_T}{\max_i |\langle u''^2(z,t_i)\rangle_T|}.$$

Except for the low wind-speed case ($(U_*, U_S) = (2.0, 2.2)$), these statistics are all fairly well-behaved, and remain reasonably constant over time, once settled. This demonstrates the reliability of the flow-regime, but illustrates that it has the potential for statistical instabilities to develop at lower levels of turbulence. Furthermore, the evolution of the profiles of the second order statistics, normalised by U_*^2, is shown in figure 2.11. Even in low turbulent regimes there is little variation in the variance profiles. This demonstrates that the flow-regime is likely to be reasonably stable over the timescales that will be considered in the following chapters.

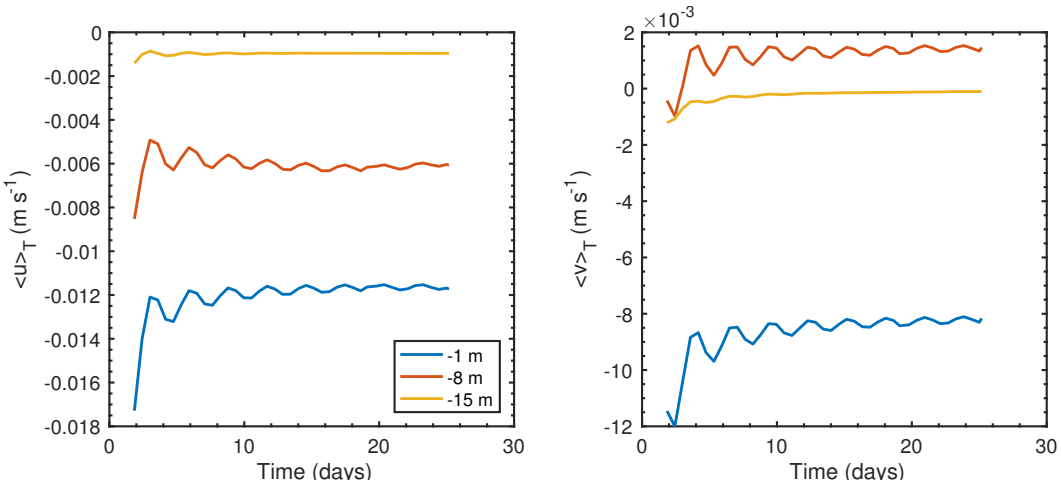

(a)

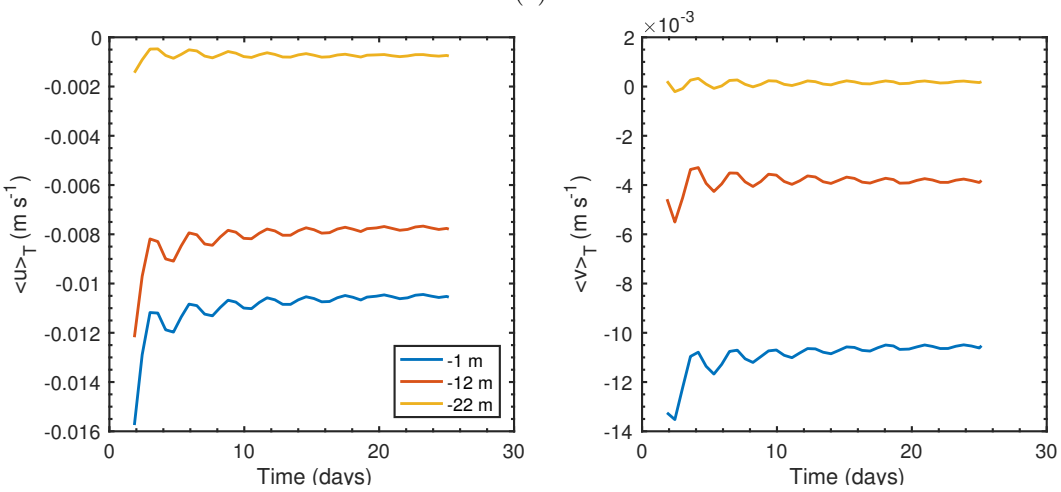

(b)

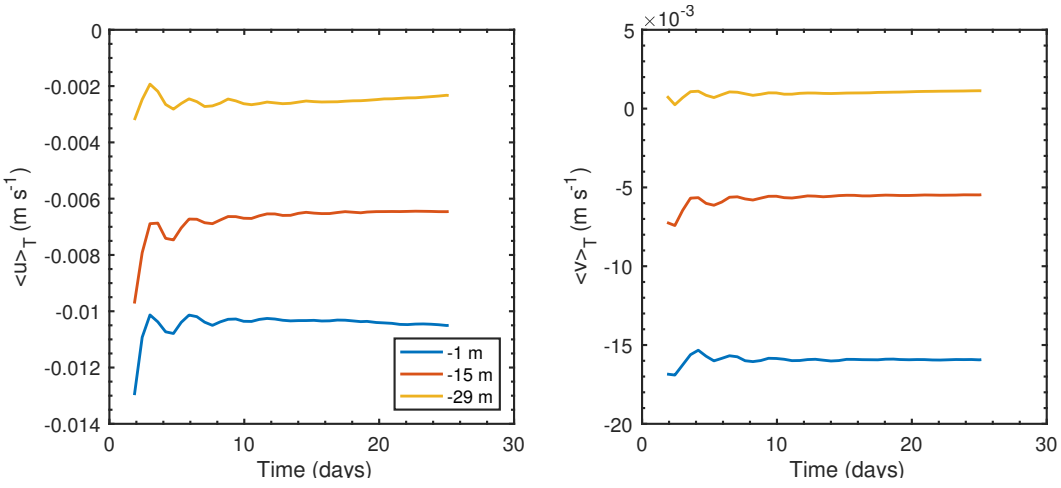

(c)

Figure 2.9: Graphs of the average velocity $\langle u \rangle_T$ (left) and $\langle v \rangle_T$, at three depths, to test for first order statistical stability, taken from LES simulations subject to (U_*, U_S) = (a) $(2.0, 2.2)$, (b) $(3.0, 3.3)$, and (c) $(4.0, 4.4)$.

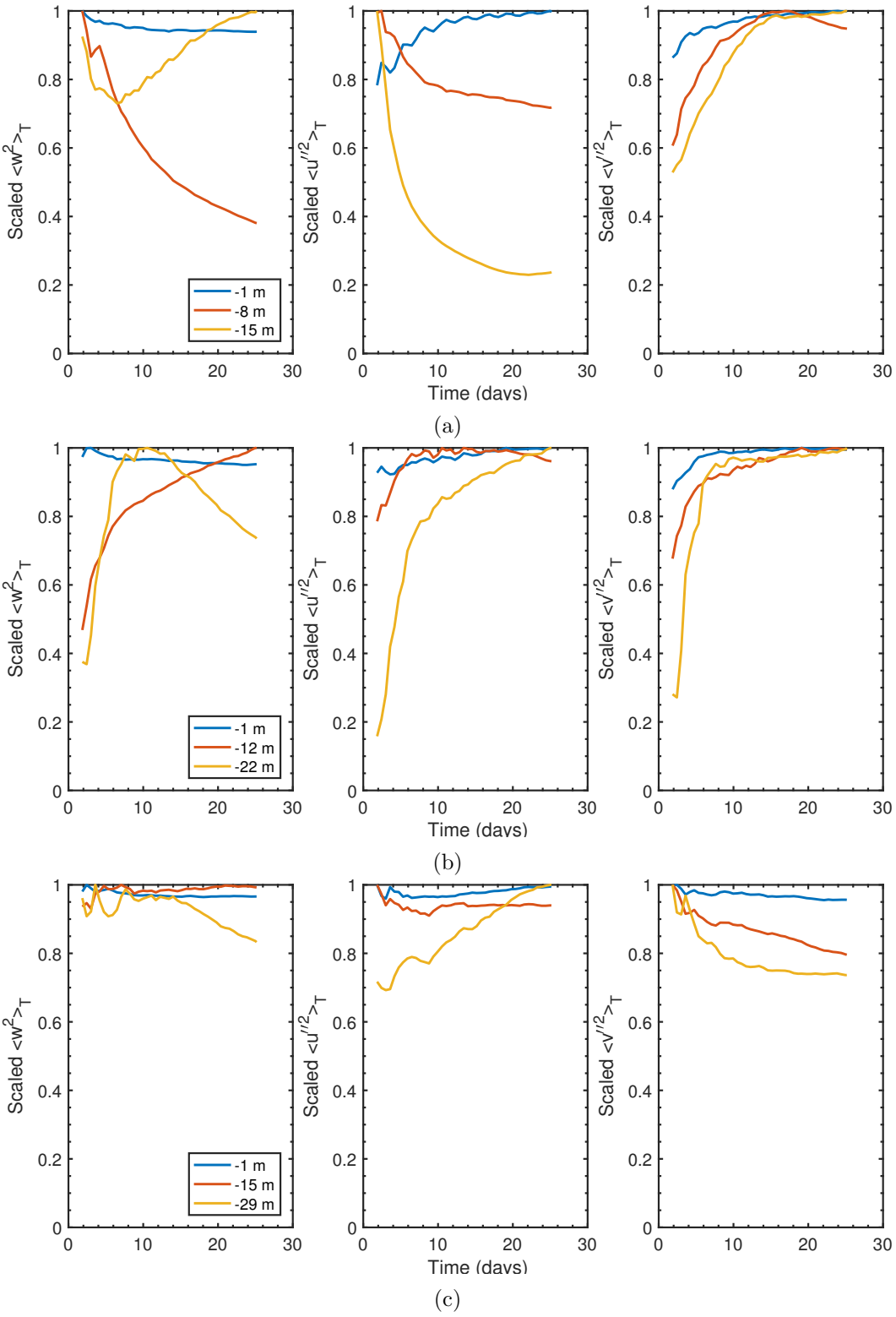

Figure 2.10: Graphs of the scaled variance $\langle w^2 \rangle_T$ (left), $\langle u''^2 \rangle_T$ (centre), and $\langle v''^2 \rangle_T$ (right), at three depths, to test for second order statistical stability, taken from LES simulations subject to (U_*, U_S) = (a) $(2.0, 2.2)$, (b) $(3.0, 3.3)$, and (c) $(4.0, 4.4)$.

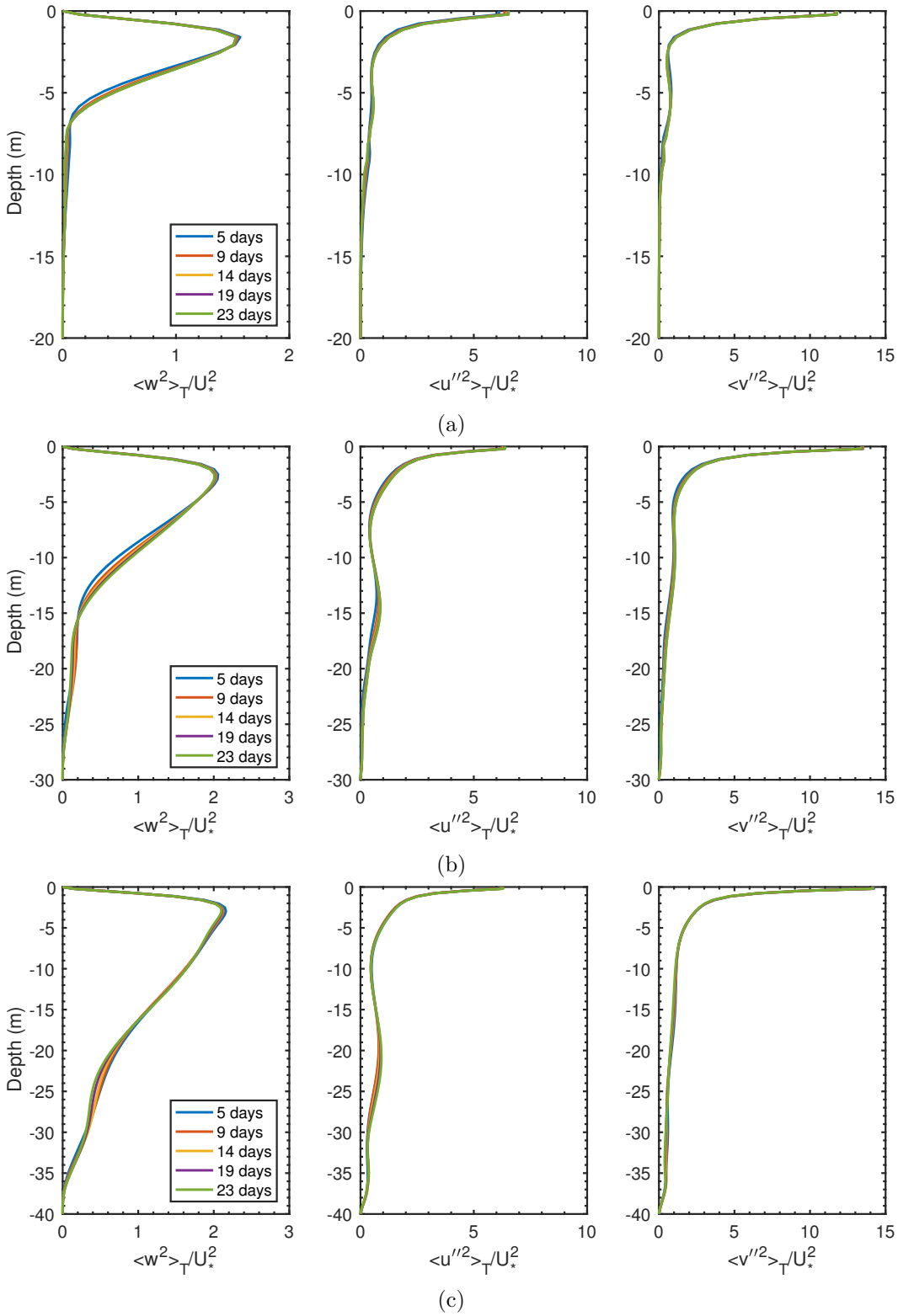

Figure 2.11: Evolution of non-dimensional variance: $\langle w^2 \rangle_T / U_*^2$ (left), $\langle u''^2 \rangle_T / U_*^2$ (centre) and $\langle v''^2 \rangle_T / U_*^2$ (right), taken from LES simulations subject to $(U_*, U_S) =$ (a) $(2.0, 2.2)$, (b) $(3.0, 3.3)$, and (c) $(4.0, 4.4)$.

Chapter 3

The Biological Model

3.1 Nutrient-Phytoplankton-Zooplankton (NPZ) Equations

The biological model that will be studied here is a three-compartment differential equation system which includes compartments for nutrient (N), phytoplankton (P) and zooplankton (Z). Conceptually, each of the three differential equations in this system takes the general form of a Kolmogorov (1936) predator-prey system, $\mathrm{d}\Gamma_i/\mathrm{d}t = f_i(\Gamma_1, ..., \Gamma_n)\Gamma_i$, where in this case $\Gamma_i = (N, P, Z)$. The source and sink terms, f_i, correspond to the various interactions between the different species. For example the phytoplankton are grazed upon by the zooplankton and consequently the phytoplankton equation will have a sink term to reflect that. The NPZ model studied here will take the form

$$\frac{\mathrm{d}N}{\mathrm{d}t} = -N \text{ uptake by } P + N \text{ recycled from } P, \tag{3.1.1}$$

$$\frac{\mathrm{d}P}{\mathrm{d}t} = P \text{ growth from } N - P \text{ grazing loss from } Z, \tag{3.1.2}$$

$$\frac{\mathrm{d}Z}{\mathrm{d}t} = Z \text{ growth from } P - Z \text{ mortality}. \tag{3.1.3}$$

This type of NPZ model is a widely studied model of oceanic and limnic ecosystem dynamics and is used in a variety of forms. The number of state variables in this type of system can range from simple two-compartment models (Huisman et al. 2006, Saha and Bandyopadhyay 2009), through the three-compartment form (Steele and Henderson 1981, Franks et al. 1986, Edwards and Brindley 1996, Kloosterman et al. 2014, Lévy 2015) to many additional compartments (Fasham et al. 1990, Baird and Emsley 1999, Arismendez et al. 2009), for example for additional nutrients or competing plankton species.

In constructing an NPZ type model a balance between complexity and generality must be achieved. In his review on NPZ models, Franks (2002) argues that "there is no compelling reason to reject the NPZ model until it is clear that it cannot describe the system being studied" and that a more complicated model is not necessarily a better model. Indeed a model with many parameters, each of which must be determined probabilistically, or experimentally,

with associated errors, is likely to be of such generality that it can make no specific predictions.

The choice of functional forms of the biological source and sink terms affects the dynamics of the model. These terms can be as simple as linear interactions, for example

$$Z \text{ growth from } P = aPZ, \tag{3.1.4}$$

or include saturation effects, such as a type 2 Holling (1959) predation response,

$$Z \text{ growth from } P = \frac{aP}{1+bP}Z, \tag{3.1.5}$$

where a and b are constants. Similarly growth rates including saturation can be modelled with a Michaelis-Menten uptake rate (Michaelis and Menten 1913, Johnson and Goody 2011) of the form

$$P \text{ growth from } N = \frac{a}{k+N}P. \tag{3.1.6}$$

Many other forms for the individual terms are discussed in the review by Franks (2002).

The main aim of this work is to understand the drivers (both physical and biological) behind the vertical structure of plankton populations in the water column. Consequently the effects of the surrounding fluid must be taken into account. The coupling, both direct (advection-diffusion) and indirect (impact on nutrient uptake, predation etc), of the physical LES model to this biological NPZ model will be described in detail in this chapter.

The construction of this model is undertaken with a mechanistic approach. The choice of this approach over that of simple curve fitting to experimental data is to highlight both the physical and biological explanation of the findings. Whilst a curve fitting strategy may lead to the same theoretical predictions and results it does not provide the same physical and biological insight as the mechanistic approach. This choice is better suited to the aims of this work and will provide insight on each parameter's effects on the structure of the plankton within the water column. Other approaches, such as the experimental fitting, are vital for validation of the parameterisations used here.

3.2 Derivation of source and sink terms

The three non-dimensional scalar fields, denoted $N(\boldsymbol{x},t) = N^*(\boldsymbol{x},t)/N_0$, $P(\boldsymbol{x},t) = P^*(\boldsymbol{x},t)/P_0$ and $Z(\boldsymbol{x},t) = Z^*(\boldsymbol{x},t)/Z_0$ (for suitable reference scales N_0 kg m^{-3}, P_0 cells m^{-3} & Z_0 cells m^{-3}) are determined subject to the differential equations (3.1.1)–(3.1.3) with the following biological interaction source and sink terms.

3.2.1 Nitrate uptake by phytoplankton

Most phytoplankton species are diffusion feeders (Kiørboe 2008), and have evolved to take on soluble nutrients found in the oceanic water column. The most abundant compounds include nitrate (the nutrient considered in this work), ammonia, phosphates, iron, are typ-

ically the focus of nutrient modelling (Fasham et al. 1990). Some of these compounds are formed in the process of the decomposition of plant tissue, including that of phytoplankton (Schulten et al. 1991, Schulten and Schnitzer 1997, Li et al. 2013).

Formulation of the uptake process

Since the process by which phytoplankton absorb nutrients is diffusive, the starting point is Brownian motion. The formulation below will follow the work of Berg (1993) and Kiørboe (2008). Molecules that constitute a solute can move very rapidly but change to a new random direction every time they collide with another molecule, this random motion is known as random walk or Brownian motion.

The starting point is Fick's (1855) first law of diffusion which describes the flux of material across a boundary, relating the diffusive flux J to the concentration C, assuming steady state. A derivation of this term can be found in Berg (1993). Fick's (1855) first law in one dimension is

$$J = -D\frac{\mathrm{d}C(x)}{\mathrm{d}x}, \tag{3.2.1}$$

or in 3 dimensions

$$\boldsymbol{J} = -D\nabla C(\boldsymbol{x}, t),$$

where D m^2 s^{-1} is the coefficient of diffusion. The negative sign indicates that the flux is from high to low concentrations.

The flux of particles, such as nitrate diffusing into a phytoplankton cell, is estimated by integrating the flux over the surface area of the volume of the cell. For simplicity it is initially assumed that the phytoplankton cell is spherical and of radius r_P. In which case the flux of nitrate into the cell is given by

$$Q_N = -D_N \int \nabla N \cdot \boldsymbol{n}\mathrm{d}S, \tag{3.2.2}$$

where D_N is the molecular diffusion coefficient for nitrate, N is the concentration of nitrate, and $\boldsymbol{n}$ is the outward normal directed from the surface S of the spherical cell. For a spherical cell

$$\nabla N = \left(\frac{\mathrm{d}N}{\mathrm{d}r}, 0, 0\right) \implies \nabla N \boldsymbol{n}\mathrm{d}S = \frac{\mathrm{d}N}{\mathrm{d}r} r^2 \sin(\theta)\mathrm{d}\theta\mathrm{d}\phi.$$

Hence

$$Q_N = -D_N \int_0^{\pi}\int_0^{2\pi} \frac{\mathrm{d}N}{\mathrm{d}r} r^2 \sin(\theta)\mathrm{d}\theta\mathrm{d}\phi = -4\pi D_N r^2 \frac{\mathrm{d}N}{\mathrm{d}r}. \tag{3.2.3}$$

Rearranging this result gives a differential equation for N in r

$$\frac{\mathrm{d}N}{\mathrm{d}r} = -\frac{Q_N}{4\pi D_N r^2}. \tag{3.2.4}$$

The concentration of the nitrate a long way from the cell is at its ambient, background level. Close to the cell wall concentration is reduced due to the presence of the cell. Integrating the

differential equation (3.2.4) from ∞ to r_P yields

$$N(\infty) - N(r_P) = \frac{Q_N}{4\pi D_N r_P}. \tag{3.2.5}$$

Rearranging gives the flux of nitrate

$$Q_N = 4\pi r_P D_N (N(\infty) - N(r_P)) = 4\pi r_P D_N (N^* - N_S), \tag{3.2.6}$$

where N^* is the background concentration of nitrate and N_S is the concentration of nitrate at the cell wall. The flux of nutrients into non-spherical cells is studied in Baird and Emsley (1999).

Until now this formulation only considers diffusive uptake and implicitly assumes there is no relative motion of the fluid with respect to the cell wall. Any relative fluid motion, generated by turbulence or cell swimming, has the effect of advecting more solute into the region of the cell wall, with the potential to increase the uptake rate. The details of this process are very complicated (Batchelor 1980), and are too complicated to incorporate into the uptake term of the larger model. Instead, a non-dimensional 'turbulent Sherwood number' is used to model the effects of relative fluid motion. This number $Sh_{turbulent} \geqslant 1$ is a measure of the ratio of the total nutrient flux into a cell in the presence of relative fluid motion, to the flux brought about solely by diffusion. Incorporating the Sherwood number to account for advective transport, the revised uptake rate is then given by

$$Q_N = 4\pi r_P D_N Sh_{turbulent} (N^* - N_S). \tag{3.2.7}$$

Equation (3.2.6) is then a special case of (3.2.7) in the absence of relative fluid flow, i.e. when $Sh = 1$.

The value of the Sherwood number is determined by another dimensionless factor, the Péclet number, Pe, which measures the relative strength of advective transport compared to diffusive transport in a moving solute over a particular length scale R

$$Pe = \frac{UR}{D_N}. \tag{3.2.8}$$

Here U is a velocity scale characterising the relative fluid motion near the cell. For non-motile phytoplankters, as will be assumed here, the fluid motion near the cell is characterised by the turbulent kinetic energy dissipation rate $\langle\varepsilon\rangle$ from section 2.4.2. Furthermore, phytoplankton are relatively small, in particular $r_P < \eta_K$. In summarising the work of Batchelor (1980), Karp-Boss et al. (1996) suggest that the Péclet number under these assumptions can be defined by

$$Pe_{turbulent} = \frac{U_{turbulent} r_P}{D_N}, \tag{3.2.9}$$

where $U_{turbulent} = r_P\sqrt{\langle\varepsilon\rangle/\nu}$. Furthermore Karp-Boss et al. (1996) postulated that the

associated turbulent Sh number can then be estimated by the equation

$$Sh_{turbulent} = \begin{cases} 1 + 0.29Pe_{turbulent}^{1/2}, & Pe_{turbulent} \leqslant 0.01, \\ 0.5(1.969 + 0.15Pe_{turbulent}^{1/2} + 0.344Pe_{turbulent}^{1/3}), & 0.01 < Pe_{turbulent} < 100, \\ 0.55Pe_{turbulent}^{1/3}, & Pe_{turbulent} \geqslant 100. \end{cases} \tag{3.2.10}$$

The above expressions are based on theoretical predictions of nutrient uptake in a pure non-rotating shear flow. Since the approximation of the Sh number depends upon $\langle\varepsilon\rangle$, which is in turn depth-dependent, the flux of nitrate, Q_N is now also a function of the depth, z. For typical phytoplankters modelled in this work, $r_P = 10$ μm, and consequently $Pe < 0.08$ for most $\langle\varepsilon(z)\rangle$ considered in this work ($O(10^{-7}\ \mathrm{m^2\,s^{-3}})$), hence $Sh < 1.1$.

Finally, the physiological state of the cell will play a role in the uptake of nutrients, if the cell is satiated with nutrient, i.e. $N_S/N^* > 1$ then the cell will no longer be able to absorb nutrient and uptake will cease. Consequently the relative nitrate concentration at the cell surface N_S/N^* is important. In a turbulent flow it is very difficult to make estimations of the value of N_S, so instead the extent of the cell's internal nitrate reserves, R_N $\mathrm{kg\,cell^{-1}}$, assuming the local nutrient concentration is N, will be considered. If R_N is currently less than its maximum storage capacity, R_N^{max}, the the cell is able to absorb more nutrient. Baird and Emsley (1999) treated the internal nitrate storage as a fourth independent component to create an NPZ-$\mathrm{R_N}$ model. However, as this would add to the already high computational demands of coupling the NPZ model into the LES code, a fourth scalar field will not be introduced here. Baird et al. (2001) formulated the assumption that R_N and N_S are linearly related, which means that the problem of determining N_S/N^* can be overcome by establishing the relative level of nitrate reserves in the cell, R_N/R_N^{max}. The problem now comes down to estimating R_N/R_N^{max}. Baird et al. (2001) also postulated that storage reserves depend upon their depletion rate when used for cell growth, and that at some point a position of equilibrium would eventually be reached, in which there is a mass balance between the uptake of nutrients from the fluid and the nutrients consumed in the process of growth. Assuming that this balance occurs at a certain background concentration of $N^* = N_0$, then the equation for this mass balance is

$$4\pi r_P Sh_{turbulent}(z) D_N N_0 \left(1 - \frac{R_{N_0}(z)}{R_N^{max}}\right) = \mu_P^{max} \frac{R_{N_0}(z)}{R_N^{max}} \left(s_N + R_{N_0}(z)\right). \tag{3.2.11}$$

Here μ_P^{max} is the maximum phytoplankton growth rate, s_N is a nitrate stoichiometry coefficient, which essentially quantifies the amount of nitrate necessary for a cell to be viable with reproducing. Cell reproduction will only occur if $R_N^{max} > s_N$, the excess being used for the production of the daughter cells. Following Lewis (2005) the value of R_N^{max} will be taken as $3 \times s_N$.

The hypothesis of mass balance by Baird et al. (2001) was made under the assumption that there is an absence of relative fluid motion. It can be argued that no such balance can

be reached for a cell residing in a turbulent flow. However, on small planktonic scales the fluid motion is dominated by viscosity, and is consequently relatively slow moving. This can be seen by considering the Reynolds number at the planktonic scale

$$Re = \frac{U_{turbulent} r_P}{\nu}, \tag{3.2.12}$$

which is $O(10^{-4})$ for $r_P = 10$ μm. Furthermore, the Péclet number is also $O(10^{-2})$ at this scale, supporting this assumption.

The solution to the quadratic equation (3.2.11) is easily found to be

$$\frac{R_{N_0}(z)}{R_N^{max}} \approx 1 - \frac{R_N^{max}\mu_P^{max}}{4\pi r_P D_N Sh_{turbulent}(z) N_0}. \tag{3.2.13}$$

It is then necessary to estimate the value of $R_N(z)/R_N^{max}$ when $N^* \neq N_0$. Changes to background N^* concentrations take place relatively slowly in a boundary layer, in which case it is appropriate to assume that the response to change from N_0 to N^* will be in equation (3.2.13) will be linear. Incorporating such a linear response gives rise to the following expression for R_N/R_N^{max},

$$\frac{R_N(z)}{R_N^{max}} = \begin{cases} \dfrac{R_{N_0}(z)}{R_N^{max}}\left[\dfrac{N^*(\boldsymbol{x},t)}{N_0}\right] = \dfrac{R_{N_0}(z)}{R_N^{max}} N(\boldsymbol{x},t), & \text{assuming this is } \leqslant 1, \\ 1, & \text{otherwise.} \end{cases} \tag{3.2.14}$$

Substituting this into equation (3.2.7) yields the final expression for the flux of nutrients into a cell

$$Q_N = \begin{cases} 4\pi r_P D_N Sh_{turbulent}\left(1 - \dfrac{R_N(z)}{R_N^{max}}\right) N(\boldsymbol{x},t), & \text{if } 0 \leqslant \dfrac{R_N(z)}{R_N^{max}} \leqslant 1 \\ 0, & \text{if } \dfrac{R_N(z)}{R_N^{max}} > 1. \end{cases} \tag{3.2.15}$$

Hence the total nitrate uptake by phytoplankton is

$$N \text{ uptake by } P = \begin{cases} 4\pi r_P D_N Sh_{turbulent}\left(1 - \dfrac{R_N(z)}{R_N^{max}}\right) N(\boldsymbol{x},t) P^*(\boldsymbol{x},t), & \text{if } 0 \leqslant \dfrac{R_N(z)}{R_N^{max}} \leqslant 1 \\ 0, & \text{if } \dfrac{R_N(z)}{R_N^{max}} > 1 \end{cases} \tag{3.2.16}$$

at position $\boldsymbol{x}$ and time t in the flow.

3.2.2 Phytoplankton Growth

Following Baird and Emsley (1999), phytoplankton growth is modelled using methodology employed in the study of chemical kinetics. The reproduction of a phytoplankton species, P, can be described by a chemical reaction, wherein the reactants are the phytoplankton cells themselves (including their constituent molecules), and the molecules required to make

another phytoplankton cell. The process is not entirely efficient, the products of the reaction are two cells, less inefficiencies, and waste molecules that are returned to the system. The balanced chemical reaction describing this process is then

$$P + \underbrace{s_N R_N}_{\text{stored } N} \rightarrow 2\beta_e P + 2(1-\beta_e)\underbrace{s_N R_N}_{\text{recycled}}. \tag{3.2.17}$$

Here $\beta_e \in [0,1]$ (typically $\beta_e \approx 0.75$) is the growth efficiency of the species. Using chemical kinetic methods, assuming first-order reaction rates for each reactant, the phytoplankton growth rate (rate of change of P) can be written as follows

$$P \ \textit{growth} = \beta_e \mu_P^{max} \min\left(1, \frac{R_N(z)}{R_N^{max}}\right) P(\boldsymbol{x}, t), \tag{3.2.18}$$

which incorporates μ_P^{max} the maximum possible growth rate of the phytoplankton species. Furthermore, energy is required for growth, and to obtain this phytoplankton must photosynthesise. Hence growth is regulated by the ambient light levels, which decrease exponentially with depth. Taking this into account, the final form for the phytoplankton growth rate is

$$P \ \textit{growth} = \beta_e \mu_P^{max} \, \mathrm{e}^{\alpha z} \min\left(1, \frac{R_N(z)}{R_N^{max}}\right) P(\boldsymbol{x}, t), \tag{3.2.19}$$

where α m^{-1} is a light attenuation coefficient.

3.2.3 Nitrate recycled

Following the chemical reaction kinetics formulation of the phytoplankton growth rate, a small amount of the nutrient used in the growth process is not used and hence returned to the system. The recycling term is therefore analogous to the phytoplankton growth term and takes the form

$$N \ \textit{recycled} = (1-\beta_e)\frac{s_N P^*(\boldsymbol{x}, t)}{N_0}\left(\mu_P^{max} \, \mathrm{e}^{\alpha z} \min\left(1, \frac{R_N(z)}{R_N^{max}}\right)\right). \tag{3.2.20}$$

It is important to note that this does not include the effects of nutrient regeneration, or remineralisation, from the breakdown of dead phytoplankton cells.

3.2.4 Grazing loss

The predation rate terms are based on the works of Rothschild and Osborn (1988), Lewis and Pedley (2000, 2001), and will be thoroughly discussed in chapter 5 . Briefly, the predation rate is a product of the encounter rate and the probability of capture, $p_{cap}(T_R, t(r_M))$. The encounter rate is a function of the relative velocity scale (σ_U), contact radius (R_{cont}) and the level of turbulence ($\langle\varepsilon\rangle$). The probability of capture is a function of the predator's reaction time ($T_{R_{cont}}$) and the average time the prey is in contact ($t(r_M)$). The capture rate, per

predator, is expressed as

$$I(R_{cont}, T_R, \sigma_Z, \varepsilon) = 4\sqrt{\frac{\pi}{2}} \int_0^{R_{cont}} \left[-\frac{\mathrm{d}p_{cap}}{\mathrm{d}r_M}\right] r_M^2 \left[1 - 0.3\frac{r_M}{R_{cont}}\right] \sigma_U(r_M)\mathrm{d}r_M, \tag{3.2.21}$$

which is in units of $\mathrm{m}^3\,\mathrm{s}^{-1}$. Here r_M is the closest approach distance of the predator to the prey.

The loss of phytoplankton through grazing is then a product of the capture rate, prey density, and the total number of predators

$$Z \text{ grazing loss} = Z^*(\boldsymbol{x}, t)\frac{P^*(\boldsymbol{x}, t)}{P_0} 4\sqrt{\frac{\pi}{2}} \int_0^{R_{cont}} \left[-\frac{\mathrm{d}p_{cap}}{\mathrm{d}r_M}\right] r_M^2 \left[1 - 0.3\frac{r_M}{R_{cont}}\right] \sigma_U(r_M)\mathrm{d}r_M. \tag{3.2.22}$$

3.2.5 Zooplankton growth from grazing

The growth rate of the zooplankton is analogous to the phytoplankton grazing loss term and depends on the number of prey captured. Assuming a yield Y of new zooplankton cells produced per phytoplankton cell captured then the attained growth rate by the predator is a product of the yield by the predation rate (3.2.21). However, in this work it is assumed that the zooplankton growth rate is limited to a maximum value μ_Z^{max}. The zooplankton growth rate is then given by

$$Z \text{ growth from } P = \min\left[\mu_Z^{max}, P^*(\boldsymbol{x}, t) 4\sqrt{\frac{\pi}{2}} \int_0^{R_{cont}} \left[-\frac{\mathrm{d}p_{cap}}{\mathrm{d}r_M}\right] r_M^2 \left[1 - 0.3\frac{r_M}{R_{cont}}\right] \sigma_U(r_M)\mathrm{d}r_M\right] \frac{Z^*(\boldsymbol{x}, t)}{Z_0}. \tag{3.2.23}$$

3.2.6 Zooplankton mortality rate

In order to close the model, since no larger species higher in the food chain are included, a simple linear death rate term is applied to the zooplankton population,

$$Z \text{ mortality} = \mu_{Z\,death}\frac{Z^*(\boldsymbol{x}, t)}{Z_0}. \tag{3.2.24}$$

Here $\mu_{Z\,death}$ s^{-1} is the zooplankton death rate. Typically a value of 4×10^{-6} s^{-1} (Franks et al. 1986), which includes both natural and predator mortality, will be employed in the model. Alternative forms for the death rate, such as quadratic ($\mu_{Z\,death} Z^2$) can be found in many places in the literature such as Edwards and Brindley (1996), Murray and Parslow (1999), Hernández-Carrasco et al. (2014). However, it is most typically modelled as the linear form used here (Franks 2002).

3.3 Model analysis

The coupled LES-NPZ model discussed here is by its very nature complicated, as it describes the many physical and biological drivers that can influence the dynamics of planktonic populations. It depends on a large number of parameters, of which some will be critical in determining the evolution of the biology (Lewis et al. 2017). Since the model does not have any analytical solutions, and is highly non-linear, it makes sense to consider a much simpler dynamical system in order to identify these parameters. To facilitate this, a reduced, non-spatial, version of the NPZ model will be utilised. Due to the non-linear behaviour of the Navier-Stokes equations, the NPZ equations will be stripped of all the physical dynamics (advection and diffusion) and the boundary layer structure. The resulting NPZ model is summarised by equations (3.1.1)–(3.1.3), in which the reduced equations are given by

$$\frac{\mathrm{d}N}{\mathrm{d}t} = -dP(t)N(t)\left(1 - hN(t)\right)H(1 - hN(t)) + ehN(t)P(t), \tag{3.3.1}$$

$$\frac{\mathrm{d}P}{\mathrm{d}t} = ahN(t)P(t) - bP(t)Z(t), \tag{3.3.2}$$

$$\frac{\mathrm{d}Z}{\mathrm{d}t} = cP(t)Z(t) - \mu_{Zdeath}Z(t), \tag{3.3.3}$$

where $H(x)$ is the Heaviside step function ($= 1$ if $x \geqslant 0$ and 0 if $x < 0$). The parameters a–e & h are given by

$$a = \beta_e \mu_P^{max}, \quad b = I(R_{cont}, T_R, \sigma_Z)Z_0, \quad c = YP_0 I(R_{cont}, T_R, \sigma_Z),$$

$$d = 4\pi r_P Sh D_N P_0, \quad e = (1 - \beta_e)\frac{s_N P_0}{N_0}\mu_P^{max}, \quad \& \quad h = \frac{R_{N_0}}{R_N^{max}}. \tag{3.3.4}$$

These parameters no longer exhibit any dependency on depth z or on mixing $\langle\varepsilon(z)\rangle$, which are features of the full LES-NPZ model and the NPZ variables depend solely on t. The equations are now in a much more tractable form for stability analysis. Figure 3.1 sho ws the evolution of the system (3.3.1)–(3.3.3). A key feature of the result is the out of phase oscillations between the interacting predator and prey. It is important to note that there is the lack of nitrate flux into the system. Since the nitrate consumed for growth is not fully replenished by the recycling term, the overall nitrate concentration declines over time. In the fully coupled model the nitrate flux adds to the ambient nitrate concentration. The initial conditions for the simulation shown in figure 3.1 are typical of those used in the full model.

Figure 3.2 shows how P and Z, from figure 3.1, evolve relative to each other. This figure demonstrates how the prey population responds to high (or low) predation pressure. Initially (from the point marked by the X), moving anti-clockwise, the phytoplankton population is declining due to the high predation pressure. The initial population levels are such that there is enough food available for the zooplankton population to increase, until the population of phytoplankton becomes too low for the increased predation pressure to be maintained. This

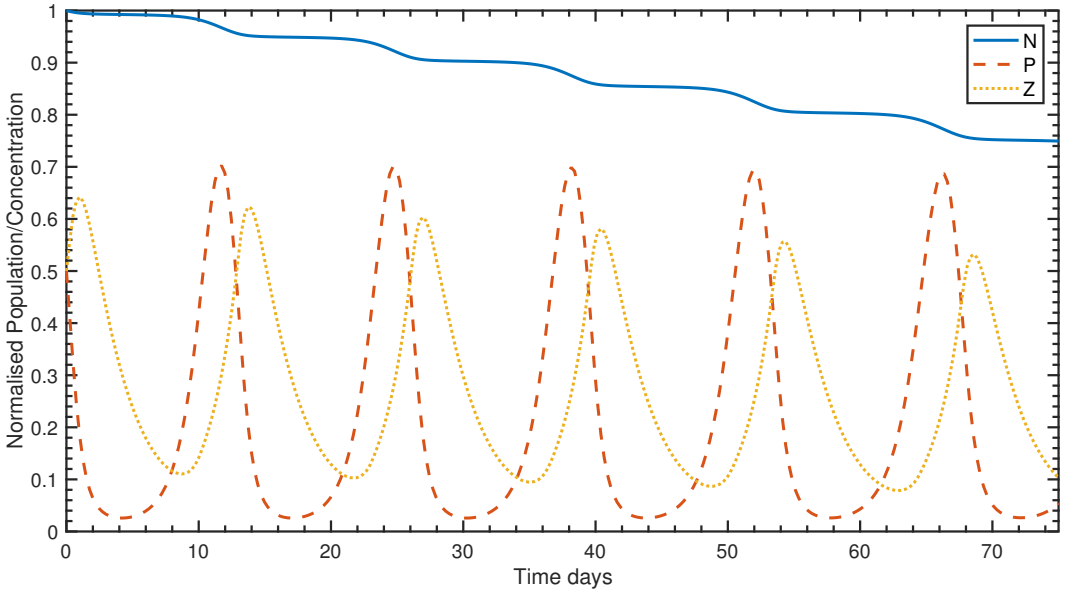

Figure 3.1: Evolution of the non-spatial NPZ model from equations (3.3.1)–(3.3.3) with initial conditions $(N, P, Z) = (1.0, 0.5, 0.5)$.

leads to a decline in the zooplankton population, in absence of enough food. Once the predation pressure is low enough the phytoplankton population can begin to recover. Shortly after the zooplankton population responds to the increased food supply, and the cycle will repeat.

3.3.1 Co-existence equilibrium

Following the ideas of Lotka (1920) and Volterra (1926), stability analysis of a particular system is conducted about the equilibrium points of the system. These equilibria are then analysed to determine if they attract or repel nearby solution trajectories. An equilibrium point, or steady-state, is defined as a solution that does not change with time, i.e. time derivatives at this point are equal to zero. The equilibria of the system (3.3.1)–(3.3.3) are found by considering solutions $(N = N_{eq},\ P = P_{eq},\ Z = Z_{eq})$ of the steady-state set of equations

$$-dP_{eq}N_{eq}\left(1 - hN_{eq}\right) + ehN_{eq}P_{eq} = 0, \tag{3.3.5}$$

$$ahN_{eq}P_{eq} - bP_{eq}Z_{eq} = 0, \tag{3.3.6}$$

$$cP_{eq}Z_{eq} - \mu_{Z death}Z_{eq} = 0. \tag{3.3.7}$$

Here in the paramater values (tables 3.1 & 3.2), it has been assumed that $hN_{eq} < 1$ and $cP_{eq} < \mu_Z^{max}$. This yields a single co-existence $(N, P, Z > 0)$ equilibrium point

$$(N_{eq}, P_{eq}, Z_{eq}) = \left(\left(\frac{1}{h} - \frac{e}{d}\right), \frac{\mu_{Z\,death}}{c}, \frac{ah}{b}\left(\frac{1}{h} - \frac{e}{d}\right)\right). \tag{3.3.8}$$

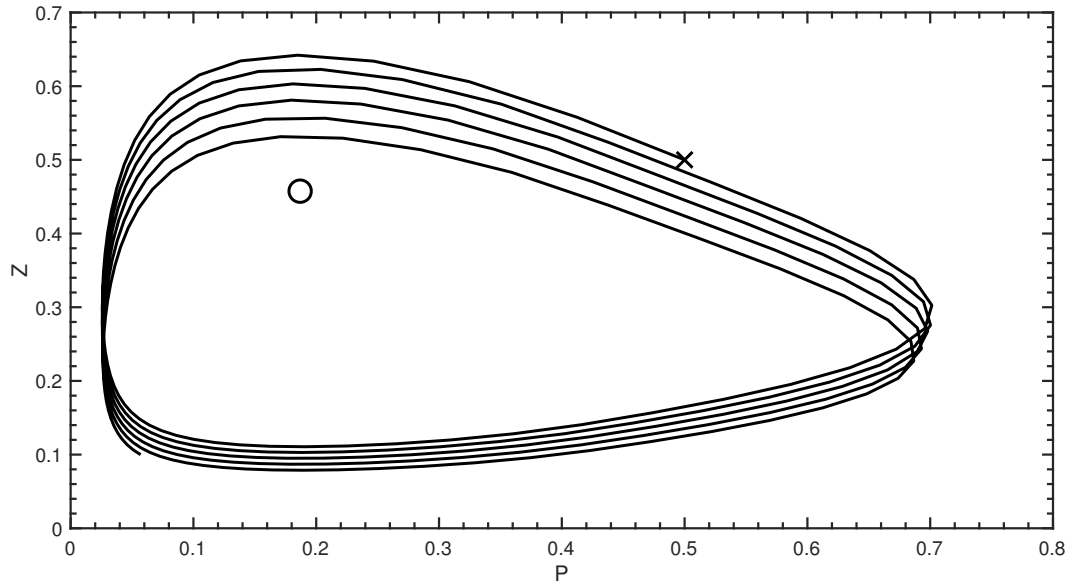

Figure 3.2: Plot of P vs Z trajectories from equations (3.3.1)–(3.3.3) with initial conditions $(N, P, Z) = (1.0, 0.5, 0.5)$, all parameters are the same as those used in figure 3.1. X: Initial condition, O: Equilibrium point (3.3.8).

Employing typical biological parameters, as listed in table 3.1, it is found that $1/h > 10e/d$, hence an approximation to (3.3.8) is

$$(N_{eq}, P_{eq}, Z_{eq}) \approx \left(\frac{1}{h}, \frac{\mu_{Z\,death}}{c}, \frac{a}{b}\right). \tag{3.3.9}$$

To determine the stability properties of this coexistence point can be found using standard equilibrium analysis from the Jacobian matrix. This matrix is composed of the first order partial derivatives of equations (3.3.1)–(3.3.3) with respect to the variables N, P, and Z. The terms of the Jacobian matrix are defined as $J_{ij} = \partial f_i/\partial \Gamma_j$, where $f_i = \mathrm{d}\Gamma_i/\mathrm{d}t$ and $\Gamma = (N, P, Z)$. This is explicitly represented by

$$\hat{J}(N, P, Z) = \begin{bmatrix} ehP - d(1-2hN)P & ehN - d(1-hN)N & 0 \\ ahP & ahN - bZ & -bP \\ 0 & cZ & cP - \mu_{Z\,death} \end{bmatrix}. \tag{3.3.10}$$

The next step is to evaluate this matrix at the equilibrium point,

$$\hat{J}_{eq}(N_{eq}, P_{eq}, Z_{eq}) = \begin{bmatrix} \frac{hd\mu_{Z\,death}}{c}\left(\frac{1}{h} - \frac{e}{d}\right) & 0 & 0 \\ \frac{ah\mu_{Z\,death}}{c} & 0 & -\frac{b\mu_{Z\,death}}{c} \\ 0 & \frac{ahc}{b}\left(\frac{1}{h} - \frac{e}{d}\right) & 0 \end{bmatrix}, \tag{3.3.11}$$

and then to solve the associated characteristic equation $\det(\hat{J}_{eq} - \lambda\hat{I})$ to find the eigenvalues, λ,

$$\begin{aligned}(\lambda_1, \lambda_{2,3}) &= \left(\frac{hd\mu_{Z\,death}}{c}\left(\frac{1}{h} - \frac{e}{d}\right), \pm i\sqrt{ah\mu_{Z\,death}\left(\frac{1}{h} - \frac{e}{d}\right)}\right) \\ &\approx \left(\frac{d\mu_{Z\,death}}{c}, \pm i\sqrt{a\mu_{Z\,death}}\right). \end{aligned} \tag{3.3.12}$$

The stability of any equilibrium point can be determined from the eigenvalues, which correspond to exponential solutions of the form $e^{\lambda_i t}$. If the real part of an eigenvalue is positive then the solution is unstable, and any small perturbation from equilibrium will continue to grow. In this case there are two pure complex eigenvalues, associated with the two phytoplankton species, this indicates oscillatory behaviour on a time-scale of $\tau_{oscil} = 2\pi/\sqrt{ah\mu_{Z\,death}\left(\frac{1}{h} - \frac{e}{d}\right)}$. λ_1 is positive and hence corresponds to a growing exponential solution over the time-scale $\tau_{exp} = 2\pi/\left(\frac{hd\mu_{Z\,death}}{c}\left(\frac{1}{h} - \frac{e}{d}\right)\right)$. The stability of this system changes in the case of $e/d > 1/h$ (an unlikely scenario given typical parameter values), however this yields the impossible case of negative equilibria for N and Z and as a consequence will not be investigated further. The associated eigenvectors corresponding to these eigenvalues are

$$(\boldsymbol{v}_1, \boldsymbol{v}_{2,3}) = \left(\begin{bmatrix} \frac{b}{ah}\left(1 + \frac{hd^2\mu_{Z\,death}}{c^2 a}\left(\frac{1}{h} - \frac{e}{d}\right)\right) \\ \frac{d\mu_{Z\,death}b}{c^2 a} \\ 1 \end{bmatrix}, \begin{bmatrix} 0 \\ \pm i\frac{b}{c}\sqrt{\mu_{Z\,death}/\left(ah\left(\frac{1}{h} - \frac{e}{d}\right)\right)} \\ 1 \end{bmatrix}\right). \tag{3.3.13}$$

This leads to an approximate solution near the coexistence equilibrium point

$$\begin{aligned}\begin{bmatrix} N(t) - N_{eq} \\ P(t) - P_{eq} \\ Z(t) - Z_{eq} \end{bmatrix} = A\begin{bmatrix} \frac{b}{ah}\left(1 + \frac{hd^2\mu_{Z\,death}}{c^2 a}\left(\frac{1}{h} - \frac{e}{d}\right)\right) \\ \frac{d\mu_{Z\,death}b}{c^2 a} \\ 1 \end{bmatrix} \exp\left(\frac{hd\mu_{Z\,death}}{c}\left(\frac{1}{h} - \frac{e}{d}\right)t\right) + \\ B\begin{bmatrix} 0 \\ -\frac{b}{c}\sqrt{\mu_{Z\,death}/\left(ah\left(\frac{1}{h} - \frac{e}{d}\right)\right)}\sin\left(\sqrt{ah\mu_{Z\,death}\left(\frac{1}{h} - \frac{e}{d}\right)}t\right) \\ \cos\left(\sqrt{ah\mu_{Z\,death}\left(\frac{1}{h} - \frac{e}{d}\right)}t\right) \end{bmatrix} + \\ C\begin{bmatrix} 0 \\ \frac{b}{c}\sqrt{\mu_{Z\,death}/\left(ah\left(\frac{1}{h} - \frac{e}{d}\right)\right)}\cos\left(\sqrt{ah\mu_{Z\,death}\left(\frac{1}{h} - \frac{e}{d}\right)}t\right) \\ \sin\left(\sqrt{ah\mu_{Z\,death}\left(\frac{1}{h} - \frac{e}{d}\right)}t\right) \end{bmatrix}, \end{aligned} \tag{3.3.14}$$

where A, B, C are constants that depend on the initial conditions of $\Gamma - \Gamma_{eq}$, for $\Gamma = N, P, Z$. This result confirms that the oscillatory behaviour near equilibrium is associated with the two plankton species only, and additionally that the system will steadily move away from the

equilibrium, declining for $P(0) < P_{eq}$ or growing for $P(0) > P_{eq}$.

A comparison of the solution (3.3.14) to the reduced system (3.3.1)-(3.3.3) is shown in figure 3.3. In both cases the initial conditions are set close to the coexistence equilibrium (3.3.9), using the parameters given in table 3.1. In this case the normalised equilibrium point is given by $(N_{eq}, P_{eq}, Z_{eq}) = (1.50, 0.188, 0.457)$ and the biological timescales are $\tau_{oscil} = 8.38$ days and $\tau_{exp} = 103$ days. While the results are very similar it is important to note the solution (3.3.14) is only valid close to (N_{eq}, P_{eq}, Z_{eq}).

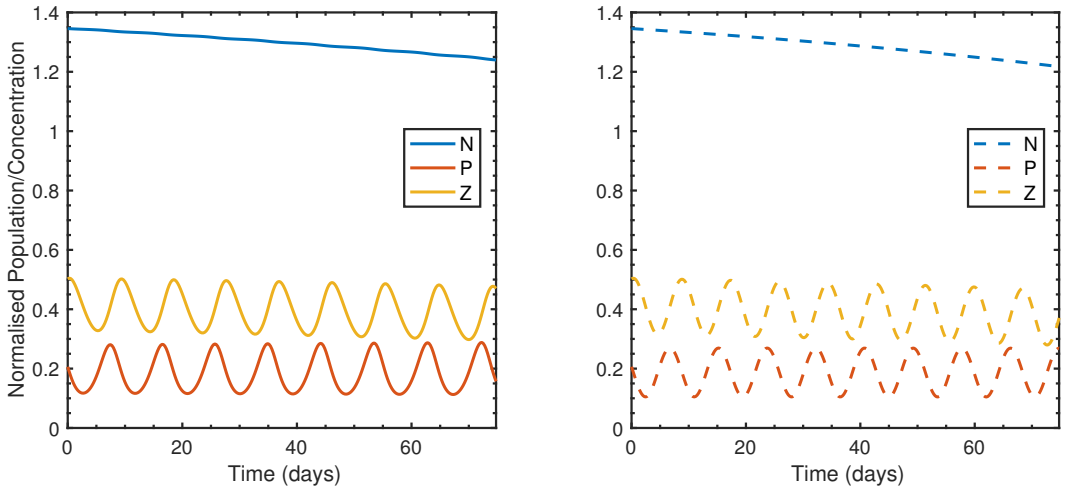

Figure 3.3: Evolution of nitrate, phytoplankton, and zooplankton with initial condition $N = 0.9N_{eq}$, $P = 1.1P_{eq}$, $Z = 1.1Z_{eq}$. Left: numerical solution from the simplified NPZ model (3.3.1)-(3.3.3). Right: Analytic solution (3.3.14).

Parameter	Value
a	1.88×10^{-5} s^{-1} $= 1.63$ day^{-1}
b	4×10^{-5} s^{-1} $= 3.46$ day^{-1}
c	2.13×10^{-5} s^{-1} $= 1.84$ day^{-1}
d	5.27×10^{-7} s^{-1} $= 0.046$ day^{-1}
e	2.42×10^{-8} s^{-1} $= 0.0021$ day^{-1}
$\mu_{Z\,death}$	4×10^{-6} s^{-1} $= 0.35$ day^{-1}
h	0.65

Table 3.1: Approximate values calculated from table 3.2

3.3.2 Extinction equilibrium

There is an additional equilibrium point, with $P, Z = 0$ for any N, called the extinction equilibrium, because associated planktonic population trajectories drive the populations almost out of existence.. The eigenvalues for this equilibrium point are given by

$$(\lambda_1, \lambda_2, \lambda_3) = (0, ahN, -\mu_{Z\,death})\,. \tag{3.3.15}$$

In this case the equilibrium is unstable, meaning that (eventually) the phytoplankton population will always recover, assuming $P > 0$. The eigenvectors for this equilibrium are easily found to be

$$(\boldsymbol{v}_1, \boldsymbol{v}_2, \boldsymbol{v}_3) = \left(\begin{bmatrix} 1 \\ 0 \\ 0 \end{bmatrix}, \begin{bmatrix} 0 \\ 1 \\ 0 \end{bmatrix}, \begin{bmatrix} 0 \\ 0 \\ 1 \end{bmatrix} \right). \tag{3.3.16}$$

This confirms that the phytoplankton population always recovers from a very low base, since the P-field is associated with the unstable eigenvalue. In the absence of any phytoplankton however, the zooplankton population always dies out. The nitrate will remain constant after any small perturbation, assuming absence of phytoplankton. Indeed, the solution for the phytoplankton in this case is given by

$$P(t) = P(0) \exp(ahNt). \tag{3.3.17}$$

If the initial condition $P(0) = 0$ then $P(t) = 0$ for all time. This analysis only applies very close to $(P, Z) = (0, 0)$ as the trajectories move away from this point, control of the population dynamics will be governed by the characteristics of the coexistence equilibrium point.

3.3.3 Parameter analysis

This analysis demonstrates that there are a number of key parameters that determine the behaviour of the biological fields. Primarily the structure changes if $e/d > 1/h$, although as previously discussed this situation is not realistic. When $1/h = e/d$ the only equilibrium point is the extinction equilibrium point. In this section the effects of varying the phytoplankton growth rate, μ_P^{max} and zooplankton predation rate $I(R_{cont}, T_R, \sigma_Z)$ will be examined. A higher growth rate increases the frequency $1/\tau_{oscil}$ of the oscillations, whilst the predation rate affects the amplitude of the oscillations, although in practice it too affects the period of the cycle.

Figure 3.4 shows the phytoplankton evolution for different values of μ_P^{max}. As previously surmised, increasing the growth rate increases the frequency of the oscillations; additionally a lower growth rate results in an increased amplitude. A possible biological reason for this is that a long recovery phase for the phytoplankton results in a lower background zooplankton population, allowing higher phytoplankton growth in relative absence of the predator. The amplitude continues to decline with faster growth rates until the phytoplankton growth rate becomes large enough to compete with predation in the final case, $\mu_P^{max} = 1 \times 10^{-4}\ \mathrm{s}^{-1}$.

Figure 3.5 shows how the phytoplankton population evolves under different predation pressures. For the lowest predation rates, there is little change in the structure of the oscillations, however the frequency does decrease with increasing predation. For higher predation the oscillations change substantially. The phytoplankton are quickly consumed and remain

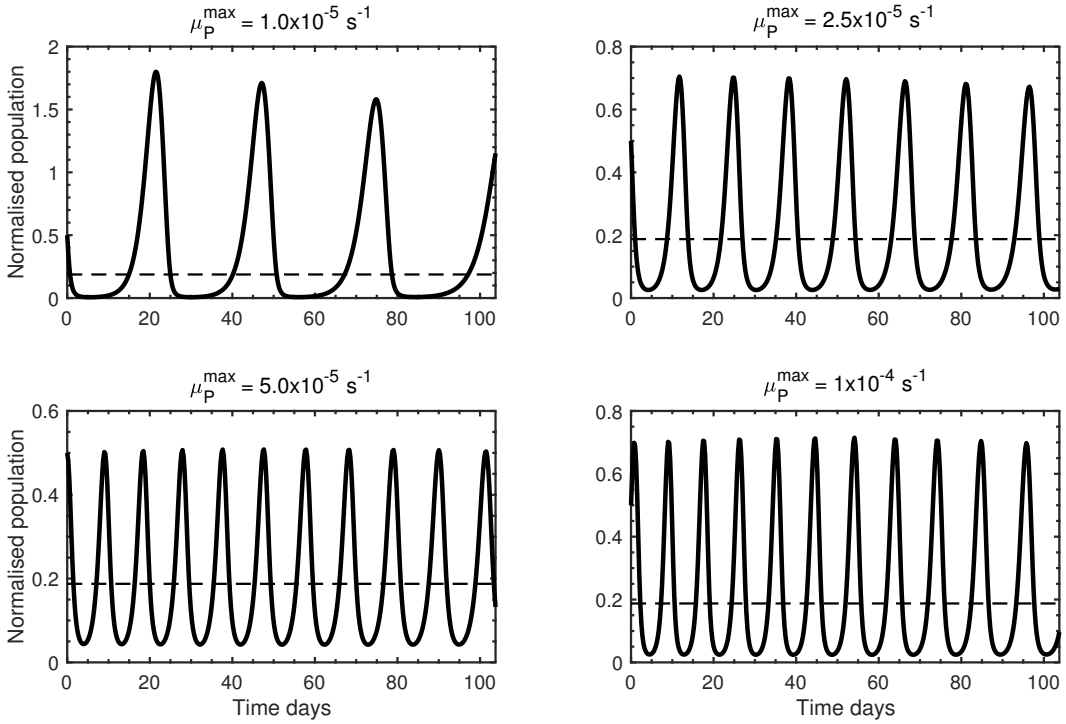

Figure 3.4: Evolution of phytoplankton populations for different values of μ_P^{max}. The dashed line indicates the equilibrium value P_{eq}.

at a very low level for long periods because, even if the zooplankton population falls to a very low level the predation pressure is high enough to prevent the phytoplankton population from recovering. Eventually the phytoplankton population does recover, and, for similar reasons to those of low growth rate, grows to a significantly higher level. Whilst the simple equilibrium mathematical analysis does not show any dependence of predation pressure this analysis is important. Very high zooplankton predation pressure drives the biological fields to a near-extinction regime, significantly changing the dynamics of the system.

3.4 Coupling to the LES model

So far the focus has been on the biological dynamics, the interactions between the species within the model. However, it is also important to consider how the environment, in particular the flow, affects the spatial variability of the biological fields. This will be achieved by coupling the physical dynamics of the LES model to the biological dynamics of the NPZ model. This coupling to the physical model will be captured by the means of an advection-diffusion equation (for example Yeung et al. (2002), Ryabov and Blasius (2008), McKiver and Neufeld (2009), Hsu and Lou (2010))

$$\frac{\partial \Gamma}{\partial t} + \boldsymbol{u} \cdot \nabla \Gamma = \nabla \cdot (D_\Gamma(\boldsymbol{x}) \nabla \Gamma(\boldsymbol{x}, t)) + \textit{Biological terms}, \tag{3.4.1}$$

for $\Gamma = N, P, Z$, where D_Γ is the diffusion coefficient for species Γ and $\boldsymbol{u}$ is the flow as calculated by the LES simulation. The advection term, $\boldsymbol{u} \cdot \nabla \Gamma$, provides the bio-physical

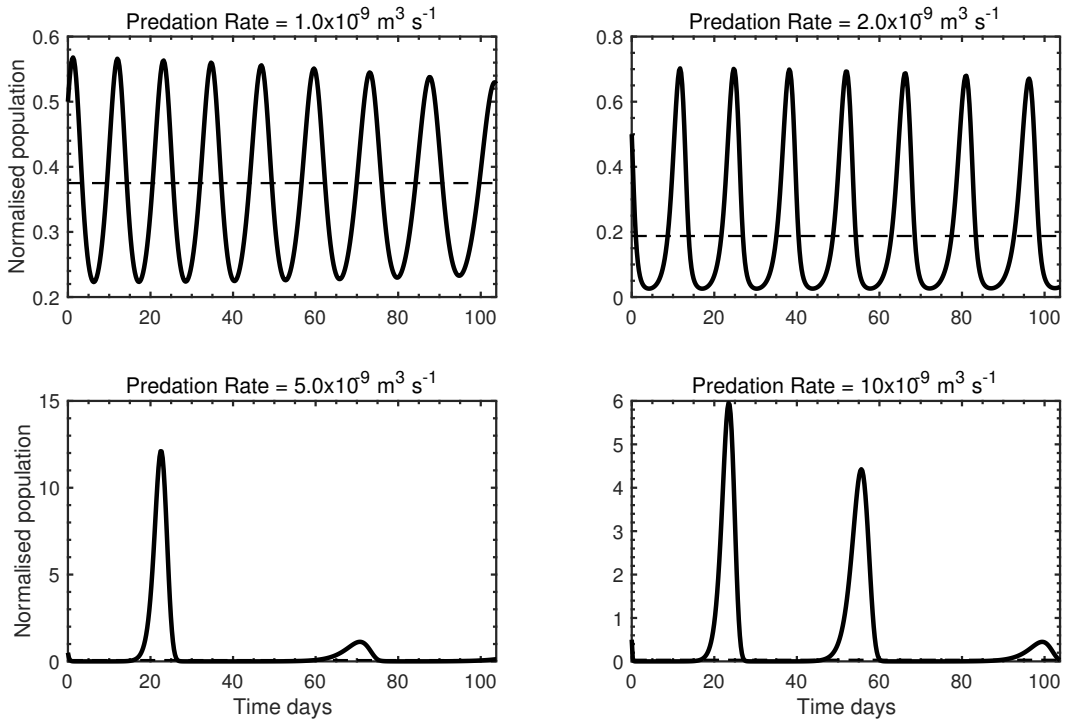

Figure 3.5: Evolution of phytoplankton populations for different predation rates. The dashed line indicates the equilibrium value P_{eq}.

coupling and describes how the flow carries the biological fields in the boundary layer. The velocity field $\boldsymbol{u}$ is calculated by solving the Craik-Leibovich equations (2.3.18) using the LES methodology. The computation of $\boldsymbol{u}$ is discussed in more detail in chapter 2. The implications of adding spatial structure to the biological fields are discussed below.

3.4.1 Diffusive terms

The diffusion term in equation (3.4.1), $\nabla \cdot (D_\Gamma(\boldsymbol{x})\nabla\Gamma(\boldsymbol{x},t))$, is in the standard form of Fick (1855)'s second law, with diffusion coefficient $D_\Gamma(\boldsymbol{x})$. For the case of a constant diffusion coefficient, i.e. the strength of diffusion is homogeneous in space, this simplifies to

$$D_\Gamma \nabla^2 \Gamma(\boldsymbol{x},t). \tag{3.4.2}$$

The problem now is to determine the value of D_Γ. Diffusion is a small-scale process, as a consequence the resolution scales of the LES code are relevant. If the diffusion rate is below a certain size then it implies that the biological fields can be resolved down to scales below that prescribed in the LES, which is unreasonable. This consideration provides a bound on the diffusion coefficients, and a numerical approximation of this small scale behaviour must be used. Diffusion can also be considered as a scalar transport process, and its effectiveness can be compared to that of the molecular momentum transport by the means of a dimensionless

Schmidt number (He et al. 1999, Yeung et al. 2002)

$$Sc = \frac{\nu}{D_\Gamma}, \tag{3.4.3}$$

where ν is the viscosity of water. The Schmidt number can be thought of as the ratio between the levels of physical diffusion to that of biological diffusion. This ratio can provide an indication of the extent of spatial structure at small scales that can be achieved and sustained by the plankton species. High levels of diffusion imply that there is little spatial structure. On the other hand if D_Γ is low, the Schmidt number increases and the spatial scales of formed patterns decreases until any aggregations are too small to be resolved by the numerical simulations. This implies that a limit on the size of Sc should be imposed. Lewis (2005) posits that this limit should be $Sc < 1$. Imposing this restriction ensures that the resolution of the velocity fields is higher than those of the biological fields. A drawback of this restriction is that the diffusion coefficient may be higher than the actual value and in reality there may be more structure at very small scales (which cannot be resolved by the simulations). This may subsequently feed back into the larger scales. However, this is unavoidable because computing power limitations mean that turbulent ocean boundary layers cannot be resolved down to the smallest Kolmogorov microscales.

Sullivan et al. (1994) suggest that D_Γ and the eddy viscosity, $\nu_e(\boldsymbol{x})$, can be related by

$$Sc = \frac{\nu}{D_\Gamma} = \frac{1}{(1 + 2L_0/\Delta)}, \tag{3.4.4}$$

where L_0 is a resolution (or mixing) scale and $\Delta^3 = (3\Delta x/2)(3\Delta y/2)\Delta z$ with $\Delta(x, y, z)$ being the grid spacings in the (x, y, z) directions respectively. In these simulations $L_0 = 1$, $\Delta \approx 2$ which yields $Sc = 1/2$ and consequently $D_\Gamma = 2\nu_e$, which, since ν is known from the LES, gives the diffusion term. The NPZ equations, now coupled with the LES model, are now given by

$$\frac{\partial N}{\partial t} + (\boldsymbol{u} + \boldsymbol{U_S}) \cdot \nabla N = D_{TN}\nabla^2 N - N \text{ uptake by } P + N \text{ recycled from } P, \tag{3.4.5}$$

$$\frac{\partial P}{\partial t} + (\boldsymbol{u} + \boldsymbol{U_S}) \cdot \nabla P = D_{TP}\nabla^2 P + P \text{ growth from } N - Z \text{ grazing loss from } P, \tag{3.4.6}$$

$$\frac{\partial Z}{\partial t} + (\boldsymbol{u} + \boldsymbol{U_S}) \cdot \nabla Z = D_{TZ}\nabla^2 Z + Z \text{ growth from } P - Z \text{ mortality}. \tag{3.4.7}$$

3.4.2 Boundary conditions and sinking rates

Equations (3.4.5)–(3.4.7) can only be solved subject to various boundary conditions. Horizontal periodic boundary conditions are imposed on the simulation domain. A zero flux boundary condition is also imposed at the surface, i.e.

$$\left.\frac{\partial \Gamma}{\partial z}\right|_{z=0} = 0 \; ; \; \Gamma = N, P, Z. \tag{3.4.8}$$

At the lower boundary, $z = z_S < 0$, the equations will be solved subject to prescribed advective-diffusive fluxes into or out of the simulation domain. Nitrate supplies can be replenished from the nutrient rich water of the permanent thermocline (Lewis et al. 1986, Planas et al. 1999). Large vertical gyres ensure that the mixed layer is constantly resupplied with nutrients, which will be used by the phytoplankton in photosynthesis process to generate growth. Williams and Follows (1998) estimate that this vertical flux of nitrate can reach a maximum of 2×10^{-2} μmol $N\,\mathrm{m}^{-2}\,\mathrm{s}^{-1}$. The molar weight of nitrogen is 14 g mol^{-1}, therefore this flux is equivalent to -2.8×10^{-10} kg $\mathrm{m}^{-2}\,\mathrm{s}^{-1}$, which is negative because $z_S < 0$. This value will be used in these simulations, i.e.,

$$\frac{\nu_e}{Sc}\frac{\partial N}{\partial z}\bigg|_{z=z_S} = -2.8 \times 10^{-10}\ \mathrm{kg\,m^{-2}\,s^{-1}} \tag{3.4.9}$$

Following Baird et al. (2001), the phytoplankton and zooplankton are assumed to be more dense than the surrounding fluid, and consequently are subject to a gravitational settling force. In the absence of fluid flow, and assuming non-motility, the micro-organisms will settle at a terminal sinking velocity U_{sink}. This sinking rate can be estimated from a force balance between gravity and the friction from the surrounding fluid. This balance gives

$$gV_\Gamma(\rho_\Gamma - \rho_0) = C_D \mu U_{sink}. \tag{3.4.10}$$

Here V_Γ and ρ_Γ are the cell volume and density respectively for $\Gamma = P, Z$, C_D is a drag coefficient and $\mu = 10^{-3}$ kg $\mathrm{m}^{-1}\,\mathrm{s}^{-1}$ is the viscosity of water. For spherical cells $C_D = 6\pi r_\Gamma$ (Lewis 2005) and

$$U_{sink} = \frac{2gr_\Gamma^2(\rho_\Gamma - \rho_0)}{9\mu}. \tag{3.4.11}$$

In this work it will be assumed that living cells can maintain their relative vertical position in the water column, and hence only a small proportion of cells, ϕ_Γ^{dead}, (dead cells) will settle in this manner. This outward flux of cells is then the product of the number of sinking cells and the sinking speed, i.e.

$$\frac{\nu_e}{Sc}\frac{\partial \Gamma}{\partial z}\bigg|_{z=z_S} = -\frac{2gr_\Gamma^2(\rho_\Gamma - \rho_0)}{9\mu}\Gamma\phi_\Gamma^{dead} \quad ; \quad \Gamma = P, Z. \tag{3.4.12}$$

This settling velocity could be used throughout the layer, and be attributed to live cells too, however experiments by Ruiz et al. (2004) suggest that the settling velocity would be small compared to the vertical fluid velocities at the levels of turbulence studied here. Consequently, settling of living cells throughout the mixed layer will not be considered in this work.

3.5 1d NPZ model

The fully coupled 3d LES-NPZ model is by nature complicated and requires significant computational resources. To help facilitate its application it is very useful to construct a very

much faster, one-dimensional version of the model. This can be done by omitting the direct effects of advection by the flow field. This simplification puts the equations in the form of the diffusion (or heat) equation ($\partial\Gamma/\partial t = \nabla \cdot (D\nabla\Gamma)$) with source and sink terms (Okubo 1980, Okubo and Levin 2013, Chakraborty et al. 2015). In the one spatial (depth z) dimensional case, where $\partial\Gamma/\partial x, y = 0$, the NPZ equations (3.1.1)–(3.1.3) become

$$\frac{\partial N}{\partial t} = \frac{\partial}{\partial z}\left(D_N \frac{\partial N}{\partial z}\right) - N \text{ uptake by } P + N \text{ recycled by } P, \tag{3.5.1}$$

$$\frac{\partial P}{\partial t} = \frac{\partial}{\partial z}\left(D_P \frac{\partial P}{\partial z}\right) + P \text{ growth from } N - Z \text{ grazing loss}, \tag{3.5.2}$$

$$\frac{\partial Z}{\partial t} = \frac{\partial}{\partial z}\left(D_Z \frac{\partial Z}{\partial z}\right) + Z \text{ growth from } P - Z \text{ mortality}, \tag{3.5.3}$$

where D_Γ is the diffusion coefficient for species $\Gamma = N, P, Z$. The above form assumes that the diffusion coefficients may be depth dependent. If they are constant then the diffusion term can be written as $\partial\Gamma/\partial t = D_\Gamma \partial^2\Gamma/\partial z^2$. The boundary conditions are the same as in section 3.4.2.

This model is useful for analysing how depth dependent predation and uptake/growth rates affect the structure of the non-physically-forced biological fields. A proxy for vertical mixing, in the form of an eddy diffusivity K_C, can be easily included in this model by replacing the D_Γ with $D_\Gamma + K_C$. This eddy diffusion has a vertical structure, i.e. $K_C = K_C(z)$, which can influence the plankton depth profiles.

3.5.1 PZ model

One of the strongest features of the NPZ model is the interaction between predator and prey. To focus on these interactions more closely the nitrate levels can be held constant over time, removing the nitrate equation (3.5.1). This results in a two component pde model, similar to that of Huisman et al. (2006), except with P, Z rather than N, P. In this simplified model the equations now become

$$\frac{\partial P}{\partial t} = \frac{\partial}{\partial z}\left(D_P \frac{\partial P}{\partial z}\right) + P \text{ growth} - Z \text{ grazing loss}, \tag{3.5.4}$$

$$\frac{\partial Z}{\partial t} = \frac{\partial}{\partial z}\left(D_Z \frac{\partial Z}{\partial z}\right) + Z \text{ growth from } P - Z \text{ mortality}. \tag{3.5.5}$$

Another major difference of this two compartment model to that of Huisman et al. (2006) is that sinking (settling) is only included at the lower boundary, rather than throughout the domain. The simplicity of this model allows closer investigation into the interactions between the predator and prey. For example, since the predation rate may be depth dependent, through $\langle\varepsilon(z)\rangle$, using such a profile can give predictions of the biological distributions likely to arise in the 3d model.

Since here the nutrient level is fixed, the source and sink terms for the plankton species

are unchanged from the full NPZ model. The fixed nutrient means that the phytoplankton growth term becomes

$$P \ growth = \beta_e \mu_P^{max} \, \mathrm{e}^{\alpha z} \, \frac{R_{N_0}(z)}{R_N^{max}} P(z,t). \tag{3.5.6}$$

Apart from nitrate and predation profiles, the main parameter that will affect the vertical profiles will be the exponential decay in light levels. This will reduce the attained growth rates in the deeper regions of the layer.

Constant K_C

The evolution of this simplified system (3.5.4)-(3.5.5) for constant N and predation pressure is shown in figure 3.6. The phytoplankon and zooplankton oscillate regularly out of phase, with the predator lagging slightly behind the prey. This behaviour is typical of predator-prey systems (Lotka 1920, Volterra 1926, Murray 2002, 2003). The biological interpretation of this is that the prey can grow under low predation pressure, when the predator population level is low. As the food supplies (in this case phytoplankton) increase, the predator reacts and their population levels rise. Under the increasing predation pressure the growth of the prey falls below the death rate and the population declines. Eventually the now declining food source will be insufficient to sustain the higher population of zooplankton and as a consequence its population will decline in response. Finally, when the predation pressure becomes low enough the prey population recovers and the cycle repeats again.

In the figure the growth rate of the phytoplankton is higher at the surface than at lower depths, as a result the "streaks" that represent the growth cycles are time dilated towards the base of the simulation domain at $z = -30$ m. This is a consequence of the lower light levels at this depth meaning that photosynthesis is less effective and the cells are growing more slowly in a light-limited scenario. The diffusion coefficients were set to values $D_{P,Z} =$

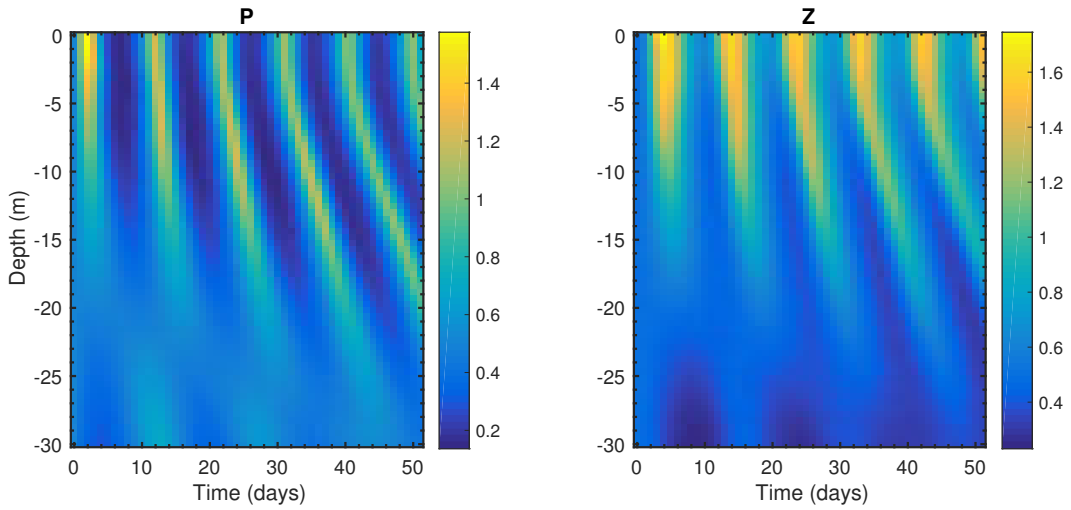

Figure 3.6: Evolution of P (left) and Z (right) for constant (in depth and time) normalised nutrient concentration $N = 1.0$ and predation pressure $= 1 \times 10^{-9}$ m^3 s^{-1} and $K_C = 0$. Initial conditions are $(P, Z) = (0.5, 0.5)$ background level.

2×10^{-6} m^2 s^{-1}. The effects of turbulent mixing were introduced by using an eddy diffusion term (Gargett 1984, Kraichnan 1987, Bataille et al. 2005, Schmitt 2007). This acts in a similar way to molecular diffusion. Typical values of eddy diffusivity in the ocean are between $1\times10^{-5} \rightarrow 1\times10^{-4}$ m^2 s^{-1} (Pacanowski and Philander 1981, Baird and Emsley 1999, Huisman et al. 2006). Figures 3.7 & 3.8 show the evolution of the plankton populations for constant $K_C = 1 \times 10^{-5}$ & 1×10^{-4} m^2 s^{-1} respectively.

As K_C increases, the depth profiles of the phytoplankton become increasingly uniform. In figure 3.7 it is apparent that the diffusion is stronger than the $K_C = 0$ case in figure 3.6, since the time dilation caused by the reduced growth rate is less significant. The reason for this is because the phytoplankton are more "well-mixed" within the layer, phytoplankton at deeper regions will be mixed into shallower regions and consequently the attained growth rate will be higher and more uniform. However, the converse is also true, the plankton residing near the surface in figure 3.6 will be "mixed" into lower regions and experience a lower growth rate, on average. This can be clearly seen in figure 3.6 since the plankton initially residing near the surface oscillate 6 times in 52 days, whereas the equivalent plankton in figure 3.7 oscillate only 4 times in that period. In figure 3.8 the effects of mixing are much more apparent as the time dilation because of the reduced light is removed completely.

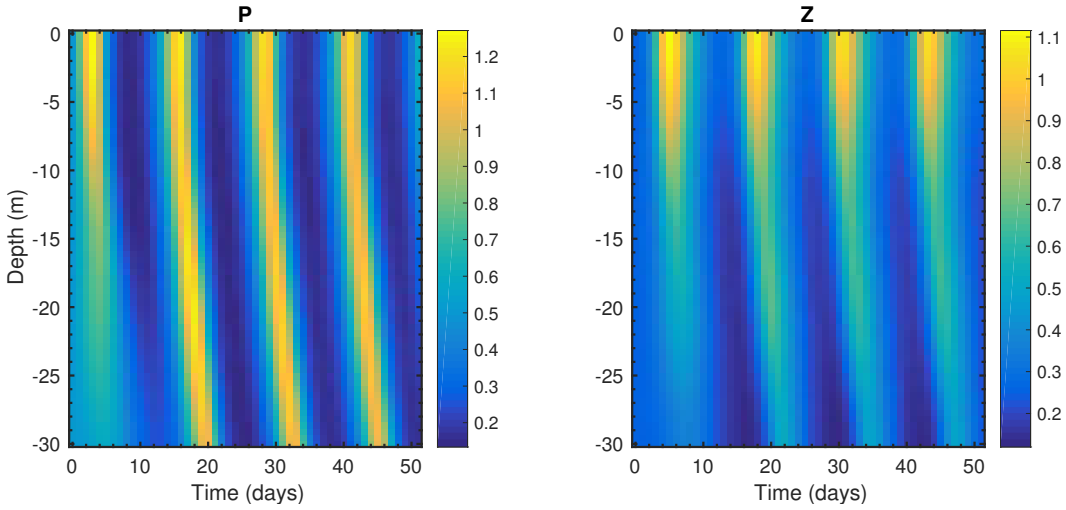

Figure 3.7: Evolution of P (left) and Z (right) for constant (in depth and time) normalised nutrient concentration $N = 1.0$ and predation pressure $= 1 \times 10^{-9}$ m^3 s^{-1} for $K_C = 1 \times 10^{-5}$ m^2 s^{-1}. Initial conditions are $(P, Z) = (0.5, 0.5)$ background level.

Depth dependent $K_C(z)$

So far the mixing has been assumed to be constant over the depth of the domain. However, this may not be the case. In fact it is very likely that the eddy diffusivity may depend on depth. The LES code automatically provides vertical profiles of eddy viscosity and this data can be used in the 1d model. The way this is done is to relate eddy viscosity to eddy

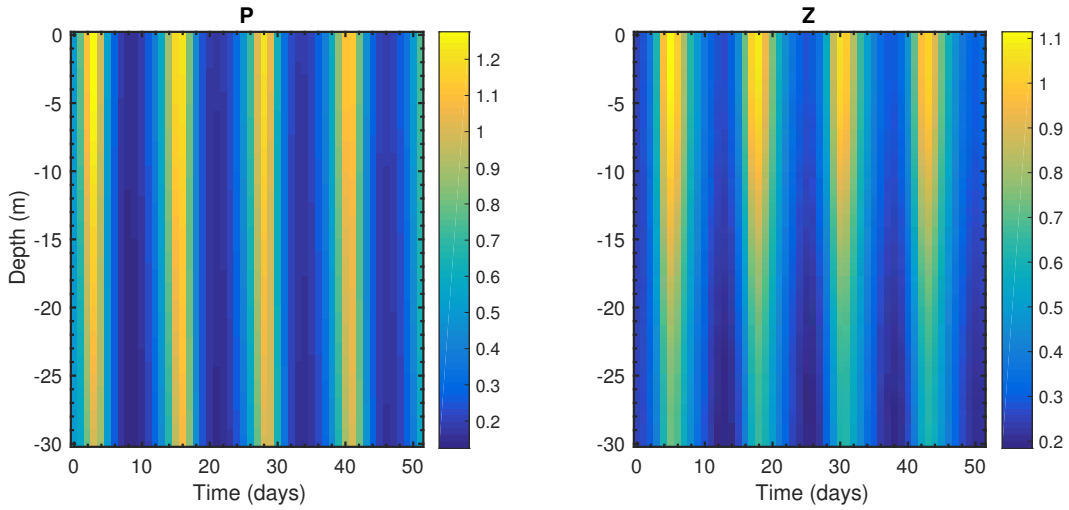

Figure 3.8: Evolution of P (left) and Z (right) for constant (in depth and time) normalised nutrient concentration $N = 1.0$ and predation pressure $= 1 \times 10^{-9}$ m^3 s^{-1} for $K_C = 1 \times 10^{-4}$ m^2 s^{-1}. Initial conditions are $(P, Z) = (0.5, 0.5)$ background level.

diffusivity. The simplest method is to assume a linear model of the form

$$\nu_e = \beta K_C. \tag{3.5.7}$$

The value of β is typically taken to be equal to one, however Lees (1981) postulates that β is related to the size of the particles. Values of eddy viscosity from the LES model are typically $O(10^{-3})$ m^2 s^{-1}, compared to typical ocean eddy diffusivity levels being $O(10^{-4})$ m^2 s^{-1}. Based on this and the analysis of Lees (1981) for particles of similar size to the plankton species, it will be assumed that $\beta = 0.1$ in this work.

Figure 3.9 demonstrates how this change affects the plankton populations. The high level of "mixing" near the surface can be seen by the streaks of growth above 12 m. Below this point the eddy diffusivity becomes low and the mixing effect is reduced, resulting in the time dilated vertical growth profiles similar to those of figure 3.6.

3.6 Simulation set-up (Lewis et al. 2017)

Before looking in more detail at the biological and physical parameters which influence the vertical distribution of phytoplankton it is important to describe how the simulations are set up and some of the generic features common to the LES-NPZ simulations reported here. The first step is to generate a relatively short, purely physical, LES, boundary layer in order to obtain the necessary physical parameters for the biological/physical coupling. Each physical boundary layer is generated by means of wind forcing at the surface boundary, summarised by the friction velocity and Stokes drift, (U_*, U_S), parameters. A boundary layer forced with $U_* = 3.5 \times 10^{-3}$ m s^{-1} and $U_S = 3.9 \times 10^{-2}$ m s^{-1} will be denoted by $(U_*, U_S) = (3.5, 3.9)$. Typically each boundary layer is "spun-up" from rest with a high level of forcing, before the respective (U_*, U_S) boundary condition is applied and the boundary layer relaxes to a state

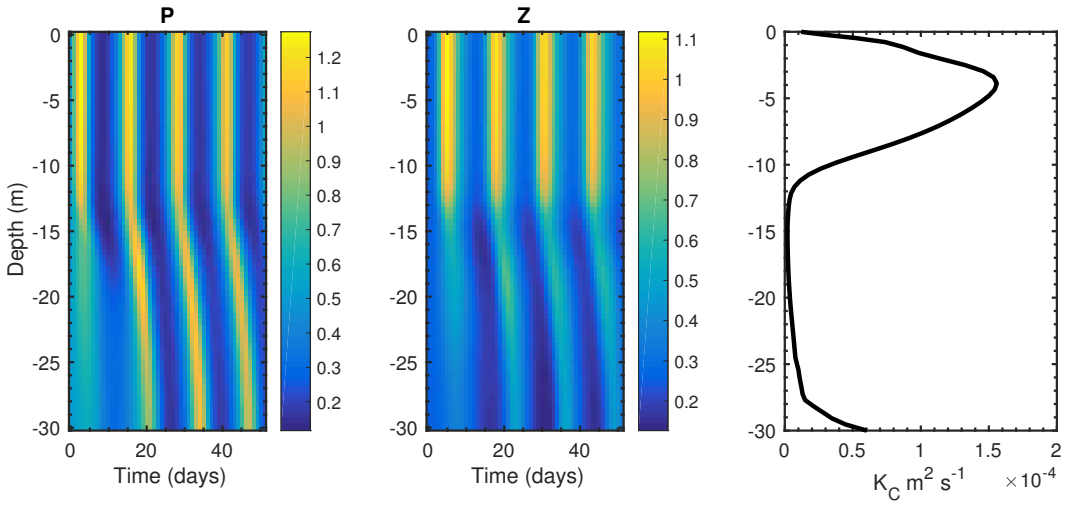

Figure 3.9: Evolution of P (left) and Z (centre) for constant (in depth and time) normalised nutrient concentration $N = 1.0$ and predation pressure $= 1 \times 10^{-9}$ m^3 s^{-1}. Eddy diffusion calculated from an LES simulation (right). Initial conditions are $(P, Z) = (0.5, 0.5)$ background level.

of quasi-equilibrium. This spinning-up and relaxation process takes about $\tau_{spin} = 60,000$ s. After this time the $\langle \varepsilon \rangle_T$ profiles are recorded, from which the predation rate, and other bio-physical coupling terms from section 3.2 are estimated.

Once the physical, Langmuir, simulation has been completed, a full LES-NPZ simulation is initiated in much the same way. In this case the on-set of quasi-equilibrium, τ_{spin}, serves as the signal for the introduction of the biological fields into the boundary layer. Typically, the evolution of the normalised biological fields commences from a spatially uniform initial condition of $(N, P, Z)_{t=0} = (1.0, 0.5, 0.5)$. The biological fields are then allowed to evolve for a period $T_{sim} \approx 20 - 25$ days.

The simulation time $T_{sim} \approx 20-25$ days is chosen primarily as a consequence of biological considerations. It is long enough to allow the biological fields to replicate through at least a couple of reproductive cycles. It is important to point out that T_{sim} is somewhat larger than the predictability timescale, τ_{pred} of the LES (Lesieur 1997). The predictability timescale is the time by which imperfections in the flow, brought about by not resolving down to the smallest scales, begin to propagate through the flow, producing significant large scale motions. Here, $\tau_{pred} \approx 25 T_E = 25 \times$ the large eddy turnover timescale ≈ 1.5 days. However, this does not invalidate the method, since a LES computed over times $T_{sim} > \tau_{pred}$ is still a statistically realistic representation of an actual flow. The statistical stability of the LES is confirmed by the discussion in section 2.4.5.

3.7 Table of parameters

Parameter	Value	Reference
Background N concentration, N_0	2.8×10^{-5} kg m^{-3}	F90
Background P concentration, P_0	4.0×10^{6} cells m^{-3}	L05
Background Z concentration, Z_0	2.0×10^{4} kg m^{-3}	L05
P cell radius, r_P, & volume, V_P	1×10^{-5} m $\implies V_P = 4.2 \times 10^{-15}$ m^3	L05
Z cell radius, r_Z, & volume, V_Z	5×10^{-5} m $\implies V_Z = 5.2 \times 10^{-13}$ m^3	L05
P cell density, ρ_P	$1.002\rho_0$	L05
Z cell density, ρ_Z	$1.02\rho_0$	L05
P maximum growth rate, μ_P^{max}	2.5×10^{-5} s^{-1} $\approx 2.4 \times 10^{-8} V_P^{-0.21}$	H97, BE99
Z maximum growth rate, μ_Z^{max}	1.0×10^{-5} s^{-1} $\approx 2.4 \times 10^{-8} V_Z^{-0.21}$	H97, BE99
Z death rate, $\mu_{Z\,death}$	6.0×10^{-7} or 4.0×10^{-6} s^{-1}	F86, F90
Z swimming speed, σ_Z	5×10^{-5} m s^{-1} $\approx 1.97 \times 10^{-2} V_Z^{0.2}$	H97
Contact radius, R_{cont}	2×10^{-3} m	M94
Yield, Y	$0.003 \approx 0.33 V_P / V_Z$	H97
P growth efficiency, β_e	0.75	BE99
Light attenuation rate, α	0.04 m^{-1}	F90
Proportion of dead P cells, ϕ_P	10^{-3}	L05
Proportion of dead Z cells, ϕ_Z	10^{-5}	L05
Nitrate stoichiometry coefficient, s_N	2.7×10^{-14} kg cell^{-1} $\approx \frac{1.38 \times 10^3 V_P}{3} \times \frac{14}{1000}$	S97, BE99
Nitrate flux, $\langle wN^* \rangle$	-2.8×10^{-10} kg m^{-2} s^{-1}	WF98

Table 3.2: Key biological parameters used to prescribe the NPZ plankton model. F86: Franks et al. (1986), F90: Fasham et al. (1990), M94: Muelbert et al. (1994), H97: Hansen et al. (1997), S97: Straile (1997), WF98: Williams and Follows (1998), BE99: Baird and Emsley (1999), L05: Lewis (2005).

Chapter 4

Light attenuation by phytoplankton

4.1 Introduction

The role of photosynthesis by phytoplankton in climate change is hugely important. It is estimated that O_2 produced in the ocean due to photosynthetic activity by phytoplankton can be attributed to $50 - 75\%$ of the global atmospheric levels (Moss 2009, Harris 2012, Sekerci and Petrovskii 2015). Additionally, this primary production has the effect of regulating the levels of CO_2 in the atmosphere. In absence of phytoplankton it is estimated that CO_2 levels would be up to 50% (200 ppmv) higher (Falkowski et al. 2000). Consequently, it is useful to understand how phytoplankton grow in response to available light within the eutrophic zone.

Firstly, it is important to understand how much light is available, the first part of this chapter will describe how light is depleted within the atmosphere and upper ocean. From there a model of light capture, and energy storage, by phytoplankton will be developed and incorporated into a modified NPZ model. This "NPZ-q" model will then be used to understand how the planktonic growth cycle, and vertical distribution, changes with light levels. Sections 4.1.1–4.3 introduce and build upon the ideas of light attenuation by different media within the ocean to develop a phytoplankton specific attenuation rate. Using this result, the simple and 1 dimensional NPZ models presented in sections 3.3 and 3.5 will be modified to incorporate a new equation for the average stored energy (from captured light) of a phytoplankton cell.

4.1.1 Beer-Lambert-Bouguer Law

As light passes through a medium, such as the atmosphere or upper ocean, some of the radiation is lost as it is absorbed by various chemical, biological or physical components. This reduction in propagating radiation (absorption or scattering of photons) is called attenuation. The Beer-Lambert-Bouguer law relates the attenuation of light through the material which the light travels. The law was first discovered by Pierre Bouguer (1729), it was later cited by Johann Heinrich Lambert (1760) who stated that the absorbance of a medium was directly proportional to the path length. August Beer (1852) later related absorbance to the

concentrations of attenuating components within the medium. The Beer-Lambert-Bouguer law combines these two ideas.

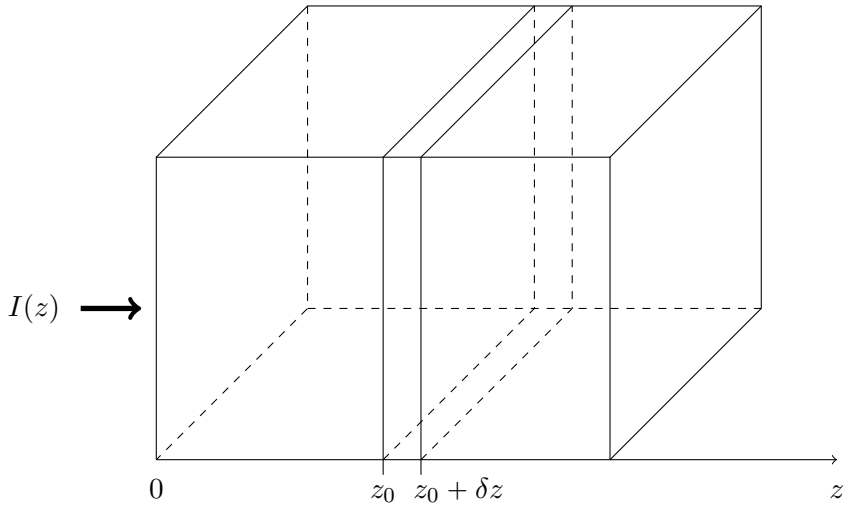

Figure 4.1: Slice, of thickness δz, of sample medium at $z = z_0$. Incident radiation is parallel to the z-axis

Consider a sample through which light passes parallel to the z-axis. Divide the medium into slices, of thickness δz, perpendicular to the beam of light, as in figure 4.1. The size of δz is assumed to be small enough so that the particles within a slice do not obscure, or 'shade' each other from the incident radiation. The amount of light detected at a point on the face $z + \delta z$ can be approximated by

$$I(z + \delta z) = I(z) - k(z)I(z)\delta z. \tag{4.1.1}$$

Here $k(z) > 0$ m^{-1} represents the attenuation coefficient of the medium. Attenuation is a measure of the loss of photons incident at z which fail to reach $z + \delta z$. This loss is due primarily to two mechanisms - absorption and scattering. Scattering is caused by particles within the sample diverting incident radiation to directions no longer parallel to z; in this instance the associated energy is conserved as light. By contrast absorption is the process by which light is transferred to an absorbing molecule in the medium whose internal energy is increased. Usually the absorbed energy is converted to heat. Both of these effects reduce the amount of radiation that reaches the far side of the slice. $I(z)$ is the amount of light radiation incident at depth z. In the limit $\mathrm{d}z \to 0$, equation (4.1.1) can be written as a first-order linear ordinary differential equation of the form

$$\frac{\mathrm{d}I(z)}{\mathrm{d}z} = -k(z)I(z). \tag{4.1.2}$$

This in turn can be modified to account for media that may attenuate different wavelengths of incident radiation by different amounts, such as a coloured light filter (as used in theatre productions etc) which attenuates all light that isn't the colour of the filter, transmitting

only that colour of light. In which case the parameters k and I now become wavelength, λ dependent, giving

$$\frac{\mathrm{d}I(z,\lambda)}{\mathrm{d}z} = -k(z,\lambda)I(z,\lambda). \tag{4.1.3}$$

The solution to either (4.1.2) or (4.1.3), can easily be obtained using the integrating factor method. This yields

$$I(z,\lambda) = I(0,\lambda)\exp\left(-\int_0^z k(z',\lambda)\mathrm{d}z'\right), \tag{4.1.4}$$

where $I(0,\lambda)$ is the incident radiation of wavelength λ at the surface.

For the case of a single, constant, attenuating component ($k(z,\lambda) = k$) we obtain the simple form of the Beer-Lambert-Bouguer law, as used in the phytoplankton growth equation in the NPZ model (3.2.19)

$$I(z) = I(0)\,\mathrm{e}^{-kz}. \tag{4.1.5}$$

This simply states that the amount of light available decays exponentially with depth. The right-hand side of (4.1.5) is the total amount of light transmitted through the medium. Transmission is defined as the amount of light radiation, or total energy flux per second, passing through the medium divided by the amount of light radiation incident on its surface,

$$T := \frac{I(z)}{I(0)}. \tag{4.1.6}$$

If there are n components within the medium that are attenuating light, each with individual attenuation coefficients k_i (for $i = 1, ..., n$), then the overall attenuation coefficient k can be written as a sum of the contributing components (Ciotti et al. 1999)

$$k(z,\lambda) = \sum_{i=1}^{n} k_i(z,\lambda). \tag{4.1.7}$$

For typical values used in the NPZ model, the amount of light radiation at 100 m in the ocean is less than 2% of the light at the ocean surface, see figure 4.2 which shows how light levels decline in the ocean where $k = 0.04\,\mathrm{m}^{-1}$ (Fasham et al. 1990). The value $0.04\,\mathrm{m}^{-1}$ is derived from the Sargasso sea which is one of the clearest bodies of water in the world (Smith and Baker 1981), it only takes into account the attenuation effects of water alone.

4.1.2 Light in the Atmosphere

Solar radiation incident at the top of the atmosphere decays as it passes through the different levels, from the exosphere to the troposphere. Figure 4.3 shows the radiation spectrum incident at the exosphere, which closely matches black body temperature of the Sun (5777 K) (Iqbal 2012), and the radiation at the surface of the earth for air mass coefficient, $m = 1$.

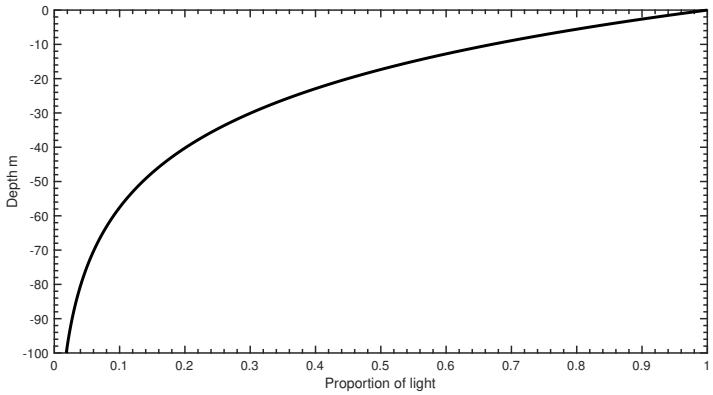

Figure 4.2: Percentage of light radiation available through the water column, using a typical value from the NPZ model for the attenuation coefficient.

The air mass coefficient is given by

$$m = \frac{1}{\cos(\theta)} = \frac{L}{L_0}, \tag{4.1.8}$$

where θ is the Sun's zenith angle (angle from the Sun being directly above), hence for $m = 1$ the Sun is directly above the surface. L is the path length through the atmosphere and L_0 is the zenith path length, i.e. at $\theta = 0$ (Nelson et al. 2003, Iqbal 2012).

The decrease of light in the atmosphere is primarily caused by the scattering by aerosols, such as chloro-fluoro-carbons (CFCs), and broad band absorption by consituent gases in the air, such as water vapour (H_2O), CO_2, and O_2. Some of these absorption bands are shown on figure 4.3.

This is an active area of research of great importance. It has implications firstly on climate change. Many of the aerosols contribute to the greenhouse effect through strong infrared aborption. It also impacts on solar power generation. The amount of radiation available in different regions of the Earth determines how much energy output can be achieved.

The following gives a summary of the review by Horvath (1993), of the roles played by the various chemical constituents of the atmosphere in the absorption of solar radiation.

Ozone (O_3)

Ozone has extremely high absorption values in the ultraviolet spectrum, $\lambda < 300\,\text{nm}$. The ozone layer, located in the lower stratosphere, is of great importance in global warming since its depletion leads to an increase of the dangerous ultraviolet light reaching the troposphere, contributing to the heating of the earth through radiative forcing. The absorption of u.v. light is also important biologically, as much of the important macrobiology are strong absorbers of u.v. radiation and are therefore easily damaged by its presence.

Otherwise, ozone only has a very small absorption band in the region of $\lambda = 600\,\text{nm}$, its absoprtion of visible light is therefore of minor impact.

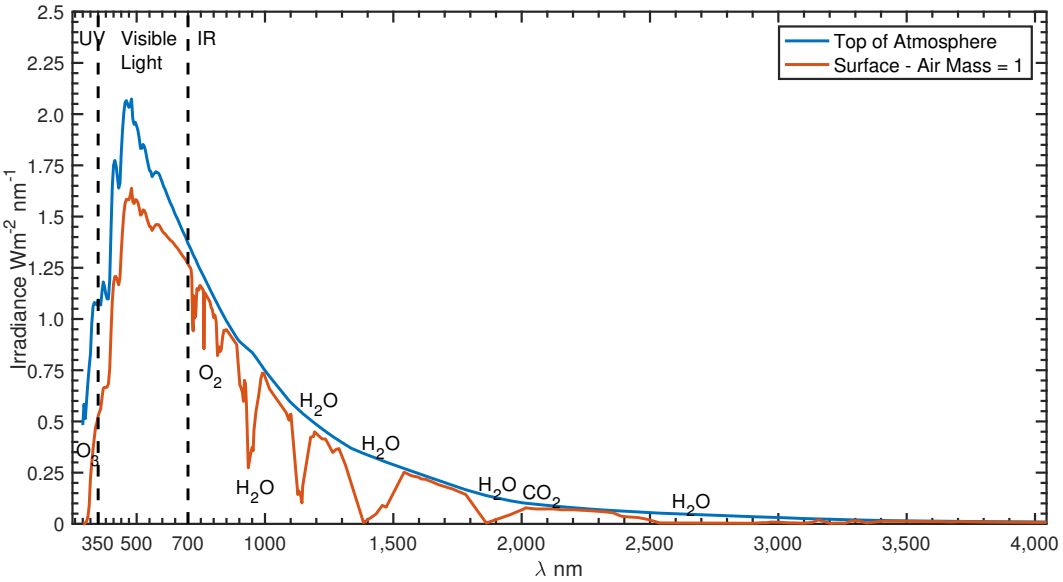

Figure 4.3: Extraterrestrial solar radiation spectrum & global total radiation spectrum incident at sea-level for air mass = 1. Absorption bands for various atmospheric components are shown. Data for spectra from Mecherikunnel and Richmond (1980) table 4, absorption bands from Horvath (1993), Herron et al. (2015).

Water vapour (H_2O)

Several distinct absorption bands for water vapour can be seen in figure 4.3, primarily located in the infrared region of the spectrum, where H_2O absorbs most strongly. There is some weak absorption in the visible spectrum, at about 700 nm.

Carbon dioxide (CO_2), oxygen (O_2) & other gases

Most of the absorbtion for these gases is in the infrared spectrum. Oxygen has a weak absorption peak in the visible region. The absorption by carbon dioxide at $\lambda > 1500$ nm is the main cause of the greenhouse effect. Molecular nitrogen is very unreactive and only has absorption bands in the extreme u.v. region of the spectrum, associated with photodissociation (Juzeniene et al. 2011).

Most of these other gases, primarily the CFCs and halocarbons are of interest because of their detrimental effect on the ozone layer and the ozone cycle.

The total attenuation of solar radiation in the atmosphere can be modelled using a sum of the constituent attenuating components. Following equation (4.1.7),

$$k_{atmos}(\lambda) = k_{O_3}(\lambda) + k_{H_2O}(\lambda) + k_{CO_2}(\lambda) + k_{O_2}(\lambda) + k_{other}(\lambda). \tag{4.1.9}$$

For simplicity however, $I(0, \lambda)$ will be treated as the radiation incident at the surface of the ocean using the data from Mecherikunnel and Richmond (1980) table 4, assuming that the zenith angle is 0°, and hence the air mass coefficient $m = 1$.

4.2 Light in the Ocean

As with the atmosphere, there are many components within the euphotic zone of the upper ocean that contibute to the overall attenuation of light radiation. For simplicity, the only components studied here will be water, gilvin (decaying and dissolved organic matter, also known as yellow substance), and phytoplankton. From equation (4.1.7) the total attenuation coefficient for these is given by

$$k(\lambda) = k_w(\lambda) + k_g(\lambda) + k_P(\lambda), \tag{4.2.1}$$

where k_w, k_g, and k_P are the individual attenuation coefficients for water, gilvin, and phytoplankton respectively. Additional attenuating elements in the upper ocean could include tripton (suspended inorganic particulate matter, also known as brown substance) and other non-photosynthesising microbial biology (Kirk 1994).

4.2.1 Attenuation due to water

Whilst imperceptible in small quantities, water is in fact not colourless but a blue liquid, arising from it's very weak absorption in the blue region of the spectrum (Buiteveld et al. 1994). The absorption in the red and infrared regions is much more significant. The attenuation of visible light due to sea-water can be approximated using an exponential relationship of the form

$$k_w(\lambda) = k_{w0} \exp(S_w \lambda), \tag{4.2.2}$$

for the light attenuation coefficient. Here k_{w0} is equivalent to attenuation at $\lambda = 0$, S_w is the slope of the exponential curve. Applying this approximation to the data from (Kirk 1994) gives best fit values of $k_{w0} = 3.49 \times 10^{-4}\,\mathrm{nm}^{-1}$ and $S_w = 1.1 \times 10^{-2}\,\mathrm{nm}^{-1}$. A comparison of the approximation to the data is given in figure 4.4. Note that the approximation closely matches, but over-estimates, the data in the visible spectrum. It is important to notice that equation (4.2.2) does not accurately model attenuation of infrared or u.v. radiation. Attenuation for larger wavelengths is even stronger, with attenuation levels at $10 - 50\,\mathrm{m}^{-1}$ for $\lambda \in (900, 1000)\,\mathrm{nm}$.

A comparison of attenuation modelled by equation (4.1.5) with $k_w = 0.04\,\mathrm{m}^{-1}\ \forall\ \lambda$ from Fasham et al. (1990), to the decay predicted by equation (4.2.2) for individual wavelengths is shown in figure 4.5.

4.2.2 Attenuation due to gilvin (yellow substance)

Gilvin is a by-product of the decomposition of plant tissue (both in soil or a body of water), the group of compounds that make up gilvin are also referred to as 'humic substances'. These substances are often polymers made up of aromatic rings joined by long-chain alkyl stuctures (Schulten et al. 1991, Schulten and Schnitzer 1997). The colour of gilvin is yellow-brown due

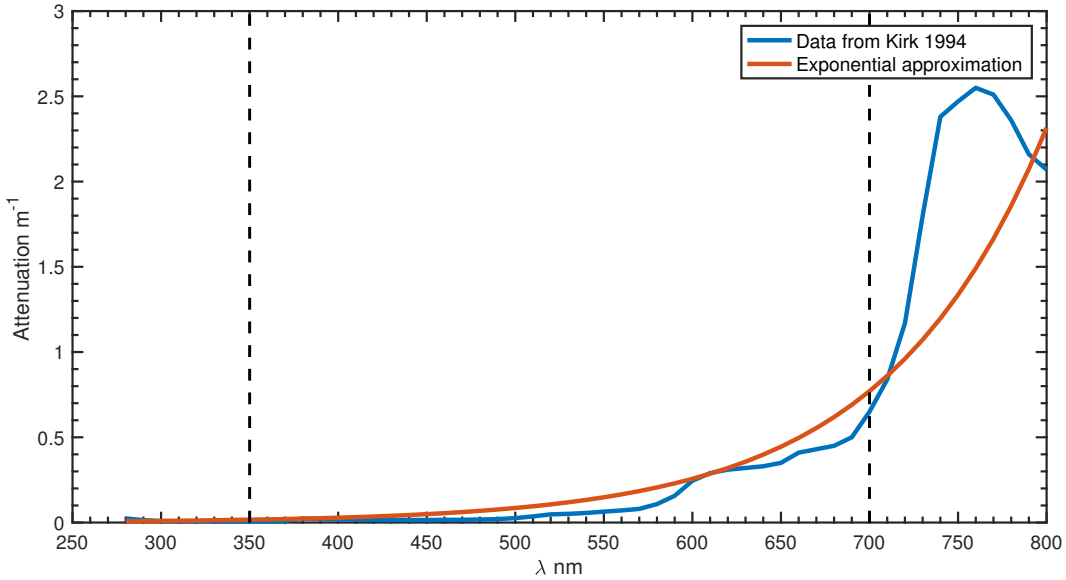

Figure 4.4: Attenuation of visible light by sea-water. Comparison of exponential approximation (4.2.2) to data from Kirk (1994).

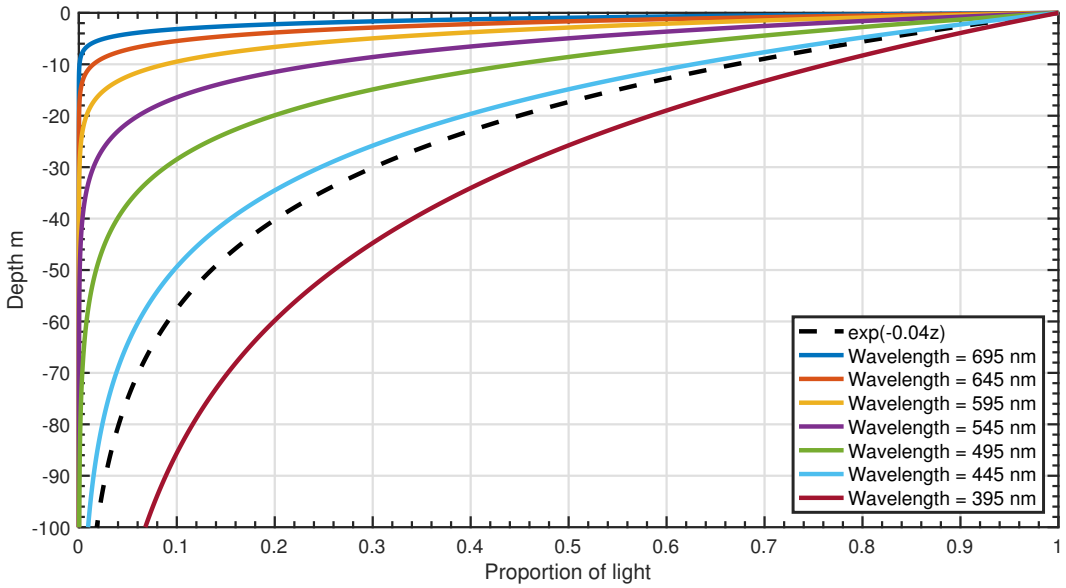

Figure 4.5: Attenuation of visible light by sea-water over depth for different wavelengths compared to the rate from Fasham et al. (1990).

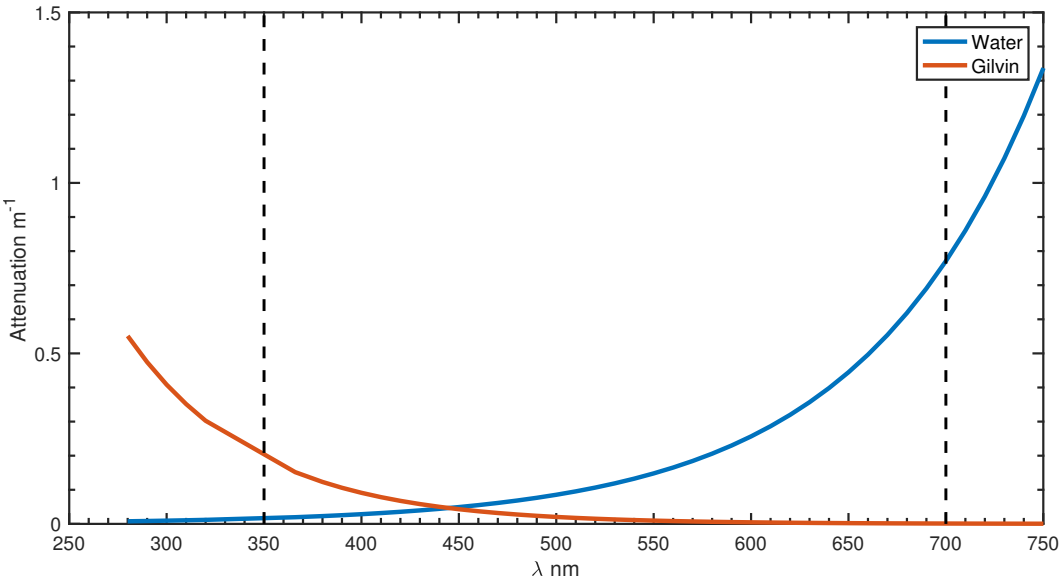

Figure 4.6: Attenuation of visible light by sea-water and gilvin. Equations (4.2.2), (4.2.3). Visible light is shown as the region between the dashed lines at $\lambda \in (350, 700)\,\text{nm}$.

to low absorption in the yellow-red-infrared region of the spectrum. Absorption increases with decreasing wavelength, with high absorption in the blue and ultraviolet. Attenuation due to gilvin is typically modelled using another approximate exponential relationship (Bricaud et al. 1981)

$$k_g(\lambda) = k_{g\lambda_{g0}} \exp(-S_g(\lambda - \lambda_{g0})), \tag{4.2.3}$$

where $k_{\lambda_{g0}}$ is the attenuation at a reference wavelength λ_{g0} and S_g is a coefficent descibing the exponential slope of the absorbtion curve. Here $\lambda_{g0} = 440\,\text{nm}$, $k_{g440\,\text{nm}} = 0.05\,\text{m}^{-1}$ and $S_g = 0.015\,\text{nm}^{-1}$ (Kirk 1994). The wavelength 440 nm is chosen since it gives an indication of the concentration of humic substances in the environment. The value of $k_{g440\,\text{nm}}$ varies greatly with location and type of environment (Kirk 1976*b*). The concentrations of gilvin in freshwater lakes tend to be much higher than in ocean environements and can contribute strongly to the reduction of radiation available for radiation. The value chosen here corresponds to an ocean environment.

The combined effects of water and gilvin on the levels of solar radiation in the ocean are demonstrated in figure 4.7. The high levels of attenuation of infra-red radiation by water and of uv radiation by gilvin means that only light in the visible spectrum, primarily in the blue-green region, is available to the phytoplankton, hence the remainder of this work will focus on the wavelength range $\lambda = 350 \to 700$ nm, i.e. the visible spectrum. In the context of photosynthesis, this range is also known as photosynthetically active radiation (PAR). Radiation below this range (ultraviolet) is damaging to the cells, and radiation above this range is of too little energy to be useful for photosynthesis.

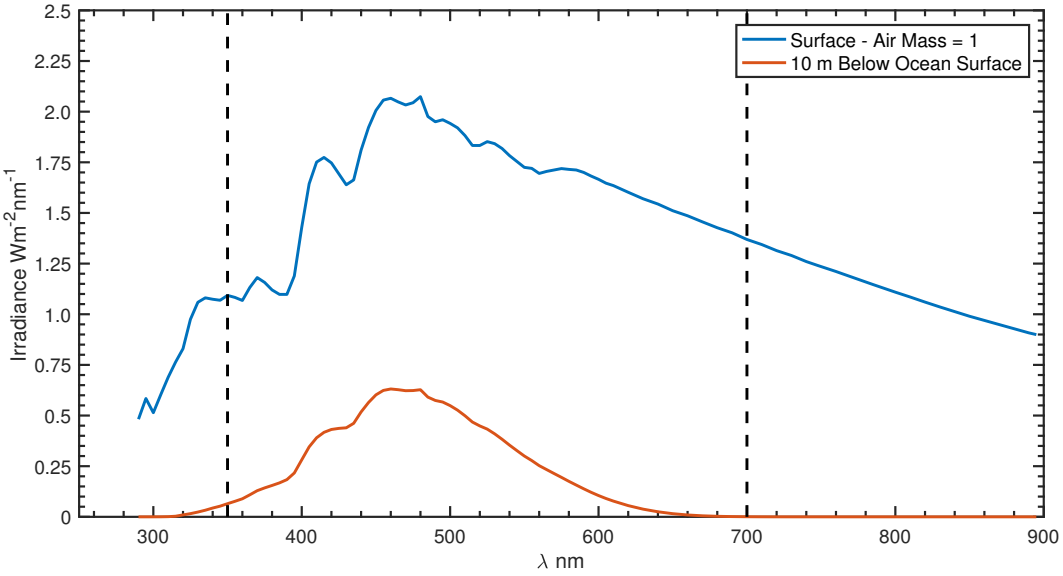

Figure 4.7: Radiation spectrum at ocean surface and at 10 m deep in the ocean due to the combined effects of attenuation by water and gilvin, computed using equations (4.2.2) & (4.2.3).

4.3 Light capture by phytoplankton

The Beer-Lambert-Bouguer law does not strictly apply to a suspension of particles, such as phytoplankton. However, as long as the total volume of the particles is much smaller than the total volume of the suspension then the attenuation can be approximated by equation (4.1.5). This requirement is to ensure that the cells within the volume do not shade each other appreciably.

For a typical model species the cell volume is of the order $10^{-17} - 10^{-14}$ m^3, and the typical population levels are of the order $10^5 - 10^{11}$ cells m^{-3}. The total cellular volume, in 1 m^3, will be typically less than 10^{-3} m^3, even in strong bloom conditions. In this case the Beer-Lambert-Bouguer law can be used as an approximation for light attenuation by phytoplankton.

4.3.1 Pigment absorption

Simply put, photosynthesis is the process that takes CO_2 and converts it to carbohydrates, used for growth, and O_2 following the basic equation

$$CO_2 + 2H_2O \xrightarrow{\sim 8h\nu} (CH_2O) + H_2O + O_2. \tag{4.3.1}$$

This reaction requires energy, in particular eight photons are required for each molecule of O_2 produced, indicated by the $\sim 8h\nu$ in the reaction above. Electrons are 'donated' by a donor molecule to the reaction centre (the site where the photosynthesis reaction occurs). Electrons are first provided by the photosynthetic pigments, in particular chlorophyll *a*. When chlorophyll *a* is excited by photons it is raised to a higher energy state. In this state it can

Peak number ξ	Peak absorpbtion γ_ξ m mg^{-1}	Wavelength λ_ξ nm	Half-width W_ξ nm
1	0.01276	438.4	15.42
2	0.02542	418.5	68.63
3	0.01059	477.9	17.27
4	0.02125	676.2	17.45

Table 4.1: Characteristics of the Gaussian bands, used to model the chlorophyll absorption spectrum.

then transfer an electron to the acceptor molecule in the reaction. Chlorophyll a can return to it's original state by absorbing an electron from the donor molecule, allowing the pigment to catalyse the process again at a later time. The overall photosynthetic process is highly complicated and will not be discussed here. A detailed review can be found in Lambers et al. (2008).

The energy required to reach the required electronic state is achieved by the absorption of red light at 660 nm. Chlorophyll a also has a strong absorption band in the blue region of the spectrum, the energy provided by blue light moves the chlorophyll to a higher electronic state. In this state the chlorophyll cannot provide an electron to the reaction centre. However, some of the excess energy is transferred to heat and the pigment can relax into the required energy state (Sybesma and Olson 1963).

The absorption spectrum for chlorophyll a (Kirk 1975) is shown in figure 4.8. The peaks in the blue and red regions correspond to the energy states described above. This spectrum can be modelled by approximating each of the absorption bands by a series of Gaussian curves, the overall spectrum is then approximated by the sum of the component curves (Hoepffner and Sathyendranath 1991). The focus of this work will be chlorophyll a and it's absorption spectrum will be approximated by

$$\overline{\gamma C}(\lambda) = C \sum_{\xi=1}^{\Xi} \gamma_\xi \exp\left(-\frac{(\lambda-\lambda_\xi)^2}{2W_\xi^2}\right), \tag{4.3.2}$$

where γ_ξ m^{2}mg^{-1} is the peak absorption coefficient for the absorption band defined by wavelength λ_ξ nm and W_ξ nm is the half-width of the ξ-th absorption band. C is the cellular concentration of chlorophyll a mg m^{-3}. (4.3.2) and the curves for each absorption band are shown in figure 4.8 for a cellular chlorophyll a concentration of 10^6 mg m^{-3}. In this case a series of four such curves were used to approximate the absorption spectrum. Table 4.1 shows the values of γ_ξ, λ_ξ and W_ξ that were used.

4.3.2 Absorption cross-section

The proportion of light that is absorbed by a phytoplankton cell is given by the absorption cross-section, $aA(\lambda)$. This quantity is the product of the projected area, A, of a cell in the plane perpendicular to the beam of light and a, the proportion of the beam of light passing

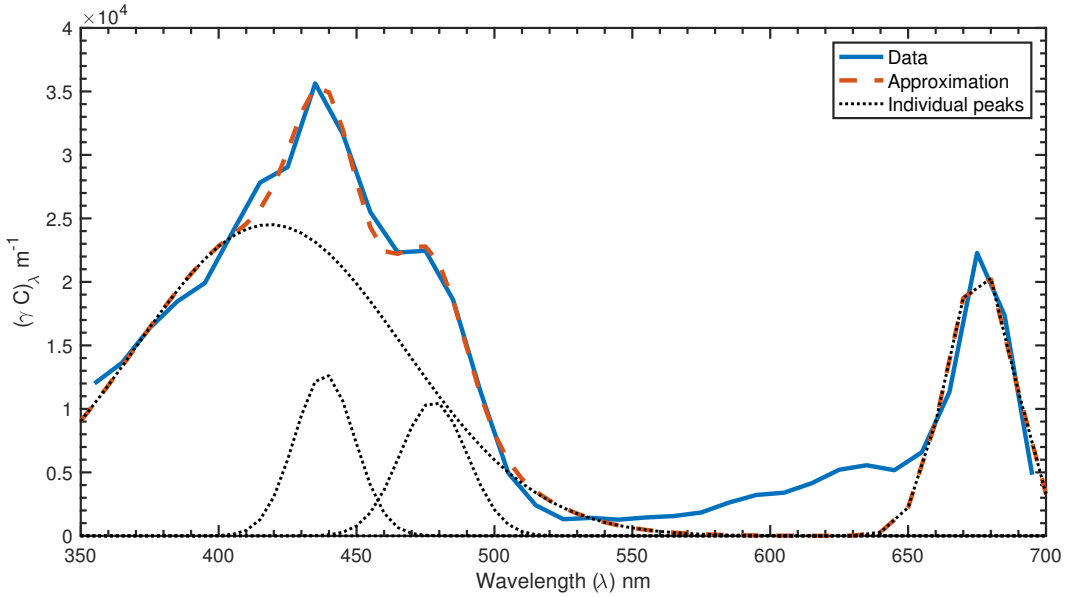

Figure 4.8: Comparison of $10^6\,\mathrm{mg\,m^{-3}cell^{-1}}$ chlorophyll a absorption from Kirk (1975) and the approximation given by (4.3.2) from table 4.1. The individual Gaussian curves are plotted in the finer dotted lines.

through the cell that is absorbed (see figures 4.9 and 4.10). The value of a is a function of the pigment absorbtion coefficent $\overline{\gamma C}(\lambda)$ (4.3.2), and it is assumed that the cell has a uniform distribution of the chlorophyll pigment. For simplicity, all cells will be assumed to have the same value of $aA(\lambda) = \overline{aA}(\lambda)$, where $\overline{aA}(\lambda)$ is the average value of $aA(\lambda)$ and based on the average projected area of a cell.

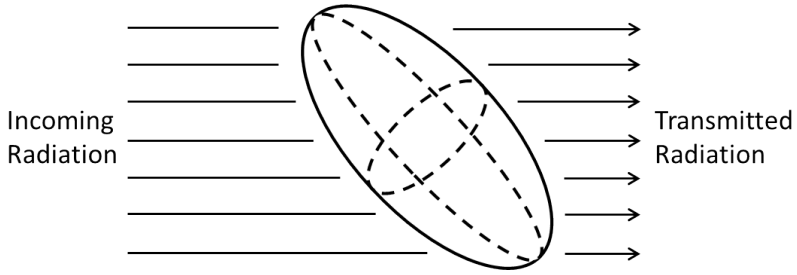

Figure 4.9: Light absorption by a rotated ellipsoidal cell, light absorbed = light incident − light transmitted.

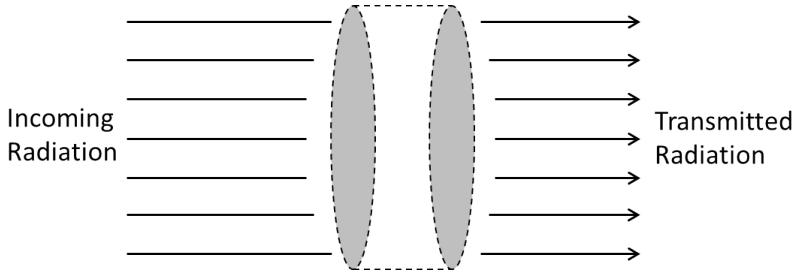

Figure 4.10: Light absorbed by equivalent cell volume defined by the absorption cross-section of the rotated ellipsoid cell from figure 4.9.

The simplest case is of a spherical cell as the projected area remains constant for all

orientations. In this case

$$\overline{aA}(\lambda) = a\left(\overline{\gamma C}(\lambda)\right) \times \pi r^2. \tag{4.3.3}$$

Following the method of Duysens (1956) the absorption is related to the transmission, T, by

$$a\left(\overline{\gamma C}(\lambda)\right) = \left(1 - T\left(\overline{\gamma C}(\lambda)\right)\right). \tag{4.3.4}$$

The transmission of the cell is defined as the total energy flux per second passing through the cell, divided by the energy flux incident on it, $T = I(z)/I(0)$. For a spherical phytoplankton cell, of radius r, with pigment absorption given by (4.3.2), the transmission of light through the centre of the cell is given by

$$T_{cell\,centre}\left(\overline{\gamma C}\right) = \exp\left(-2\overline{\gamma C}r\right). \tag{4.3.5}$$

Since the cell is spherical, the orientation does not matter so integrating the sphere over the cross-section of the cell (using polar coordinates), in the plane perpendicular to the direction of the light, gives the transmission for the entire cell

$$\begin{aligned} T_{cell}\left(\overline{\gamma C}\right) &= \int_0^{2\pi}\int_0^{r} \exp(-2\overline{\gamma C}r')r'\mathrm{d}r'\mathrm{d}\theta, \\ T_{cell}\left(\overline{\gamma C}\right) &= \frac{2\pi}{(2\overline{\gamma C})^2}\left[1 - (2\overline{\gamma C}r + 1)\exp(-2\overline{\gamma C}r)\right]. \end{aligned} \tag{4.3.6}$$

Note the inclusion of r required for integration in polar, and cylindrical coordinates. Dividing (4.3.6) by the cross-sectional area gives the average transmission of light through any point in the cell

$$T\left(\overline{\gamma C}\right) = \frac{2\left[1 - (2\overline{\gamma C}r + 1)\exp(-2\overline{\gamma C}r)\right]}{(2\overline{\gamma C}r)^2}. \tag{4.3.7}$$

Substitution of (4.3.7) into equation (4.3.4) gives the absorption of a beam of light averaged over the entire projected area of the cell

$$a\left(\overline{\gamma C}\right) = 1 - \frac{2\left[1 - (2\overline{\gamma C}r + 1)\exp(-2\overline{\gamma C}r)\right]}{(2\overline{\gamma C}r)^2}. \tag{4.3.8}$$

Multiplying (4.3.8) by the cross-sectional area of the cell gives the total amount absorbed by a single phytoplankton cell

$$\overline{aA} = \pi r^2\left[1 - \frac{2\left[1 - \left(2\overline{\gamma C}r + 1\right)\exp(-2\overline{\gamma C}r)\right]}{(2\overline{\gamma C}r)^2}\right]. \tag{4.3.9}$$

The absorption cross-sections for other typical cell shapes are more complicated since the orientation of the cell needs to be taken into account. Here only the spherical case will be considered, since this simplest of cases is what is assumed in the LES-NPZ model of chapters 2 and 3. Other shapes have been analysed in Duysens (1956), Kirk (1975, 1976*a*) & Baird and Emsley (1999).

Parameter	Value
Cell Radius	1×10^{-5} m
Cell Volume	4.2×10^{-15} m^3
Cellular Chl.a	1.0×10^6 mg m^{-3} $\implies$ 4.2×10^{-9} mg cell^{-1}
Population size	1.0×10^6 $\rightarrow$ 1×10^{10} cells m^{-3}
Background Chl.a	0.0042 $\rightarrow$ 42 mg m^{-3}

Table 4.2: Phytoplankton data from Baird and Emsley (1999) & Lewis (2005).

4.3.3 Light capture by phytoplankton

The attenuation coefficient for the bulk of the phytoplankton population is given by the product of the number of cells and the absorption cross-section for a single cell

$$k_P(\lambda) = \overline{aA}(\lambda)P. \tag{4.3.10}$$

The total attenuation coefficient for the upper ocean is then given by

$$k(\lambda) := k_{ocean}(\lambda) = k_w(\lambda) + k_g(\lambda) + k_P(\lambda). \tag{4.3.11}$$

Figure 4.11 shows the the individual attenuation coefficients for water, gilvin, and various population levels of the model phytoplankton species, see table 4.2. Except for the higher population levels of 10^9 & 10^{10} cells m^{-3}, which would coincide with the winter-spring & summer bloom events respectively (Gallagher 1980), the attenuation level, k_P, is lower than that of both water and gilvin.

The fraction of the total light attenuated, at wavelength λ, which is brought about by the presence of the phytoplankton, through absorption, is

$$\frac{k_P(\lambda)}{k_w(\lambda) + k_g(\lambda) + k_P(\lambda)}. \tag{4.3.12}$$

This fraction is the proportion of attenuated light absorbed by *all* phytoplankton. The light attenuated by a single phytoplankton cell, at a depth z, is then computed by multiplying the above by the total light attenuated at this depth, divided by the total phytoplankton population at this depth (cells m^{-3}). The total light attenuated at depth z is $k(z,\lambda)I(z,\lambda)$ by equations (4.1.1) and (4.1.2). Hence the light attenuated by a phytoplankton cell is

$$\textit{Light Attenuated}(\lambda) = \frac{1}{P}\frac{\overline{aA}(\lambda)P}{k_w(\lambda) + k_g(\lambda) + \overline{aA}(\lambda)P} \times \underbrace{(k_w(\lambda) + k_g(\lambda) + \overline{aA}(\lambda)P)}_{k(z,\lambda)} \times I(z,\lambda), \tag{4.3.13}$$

which simplifies to

$$\textit{Light Attenuated}(\lambda) = \overline{aA}(\lambda)\,(\text{m}^2\,\text{cells}^{-1}) \times I(z,\lambda)\,(\text{photons m}^{-2}\,\text{nm}^{-1}\,\text{s}^{-1}). \tag{4.3.14}$$

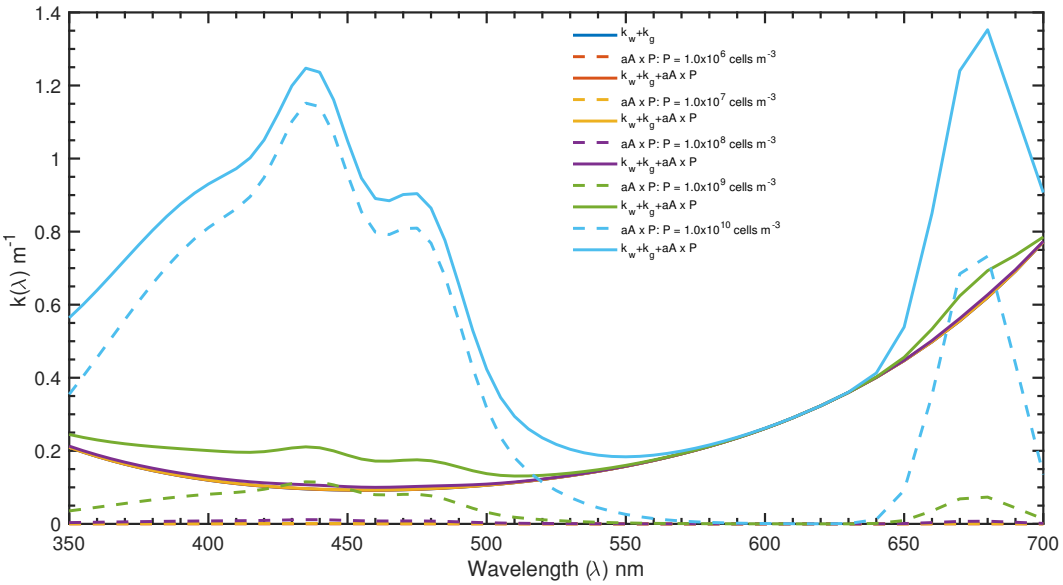

Figure 4.11: Total attenuation rates for different populations of phytoplankton. Data for the model species from Baird and Emsley (1999), Lewis (2005). Individual phytoplankton attenuation coefficients are shown as dashed curves, total attenuation (including water and gilvin) for each population are shown as solid curves.

This is the rate at which photons of wavelength λ are attenuated by a single phytoplankton cell. Integrating over all wavelengths will give the total rate at which photons are attenuated by a cell (for all wavelengths).

A phytoplankton cell has a limited storage capacity for energy, depending on the cellular concentration of chlorophyll *a*. If $q(t)$ is the amount of energy stored by the cell at time t, and the maximum amount of energy that can be stored is q_{max}, then the cell will only actually capture the light if $q(t) < q_{max}$. An analogous situation also pertains for nutrient storage. The amount of light captured by a single phytoplankton cell can be written as *Light Captured* = *Available Energy Storage* × *Total Light Attenuated*. This is given by

$$\textit{Light Captured} = \left(\frac{q_{max} - q(t)}{q_{max}}\right) \int_{350}^{700} \overline{aA}(\lambda) I(z,\lambda) \mathrm{d}\lambda \tag{4.3.15}$$

where $\left(\frac{q_{max}-q(t)}{q_{max}}\right)$ is the amount of energy storage space remaining in the cell, and

$$I(z,\lambda) = I(0,\lambda) \exp\left(-(k_w(\lambda) + k_g(\lambda))z - \overline{aA}(\lambda) \int_z^0 P(z')\,\mathrm{d}z'\right). \tag{4.3.16}$$

is the light available at depth z.

4.4 A modified NPZ model to include light capture

The process of light capture and energy storage can be explicitly incorporated into the biological NPZ system. This can be achieved by including a new equation for the internal energy of a phytoplankton cell, q, to create a new NPZ-q type model. Starting with the simple,

non-spatial, form of the NPZ equations the new system is summarised by the following four equations:

$$\frac{\mathrm{d}N}{\mathrm{d}t} = -N \text{ uptake by } P + N \text{ recycled by } P, \tag{4.4.1}$$

$$\frac{\mathrm{d}P}{\mathrm{d}t} = P \text{ growth from } N \text{ \& light } q - Z \text{ grazing loss}, \tag{4.4.2}$$

$$\frac{\mathrm{d}Z}{\mathrm{d}t} = Z \text{ growth from } P - Z \text{ mortality}, \tag{4.4.3}$$

$$\frac{\mathrm{d}q}{\mathrm{d}t} = \text{light } q \text{ captured by } P - \text{light } q \text{ used in } P \text{ growth}. \tag{4.4.4}$$

The growth term in the phytoplankton equation will now explicitly depend on the internal energy storage for the cell. For simplicity the value $q(t)$ will be an average over the cells at time t, so that all cells will have the same amount of stored energy. One new term must be derived - q *used in* P *growth* - and the phytoplankton growth term needs to be modified to incorporate $q(t)$. In practice the energy storage term behaves in a very similar way to the nutrient storage term.

4.4.1 Phytoplankton growth and energy use

Phytoplankton growth is now explicitly regulated by both the availability and internal storage of energy, in addition to the storage of nutrients. In order to incorporate the use of energy in the growth process Baird and Emsley (1999) modified the growth reaction (3.2.17), the new growth reaction is given by

$$P + \underbrace{s_N R_N}_{\text{stored } N} + \underbrace{s_I q}_{\text{stored } q} \rightarrow 2\beta_e P + 2(1-\beta_e)[\underbrace{s_N R_N}_{\text{recycled}} + \underbrace{s_I q}_{\text{heat}}], \tag{4.4.5}$$

where s_I mol(q) cell^{-1} is an amount (stoichiometry coefficient) of the stored energy going into the process, and a loss of energy through heat (which is not returned to the system). The value of s_I depends on the amount of chlorophyll a, or other photosynthetic pigments, in the cell.

Using chemical kinetics methods, the new growth equation can be written as (see (3.2.19))

$$P \text{ growth} = \beta_e \mu_P^{max} \min\left(1, \frac{R_N(t)}{R_N^{max}}\right) \min\left(1, \frac{q(t)}{q^{max}}\right) P(t). \tag{4.4.6}$$

Here the $\min\left(1, q(t)/q^{max}\right)$ term represents the internally stored energy in the cell. The process of growth now requires an amount of both nutrient and energy. Importantly, the stored energy varies with time as well as depth, whereas the energy was previously modelled as a simple exponential decay with depth in the original NPZ system.

The amount of energy used in growth is an analogue of (4.4.6)

$$q \text{ used in growth} = s_I \mu_P^{max} \min\left(1, \frac{R_N(t)}{R_N^{max}}\right) \min\left(1, \frac{q(t)}{q^{max}}\right). \tag{4.4.7}$$

As growth is also regulated by the stored nutrients, growth will only occur if both light and nutrient are available, hence not all the stored energy will be used up. If the cell is nutrient-limited then only a small amount of energy will be used up in the growth process. The nutrient recycling term (3.2.20) must also be modified to include the effects of light. If the cell is light-limited, then only a small portion of the nutrients will be used up as the energy supplies cannot support additional growth. This leads to a new recycling term of the form

$$N \ recycled = (1-\beta_e)\frac{P(t)}{P_0 N_0}\left[\mu_P^{max}\min\left(1,\frac{R_N(t)}{R_N^{max}}\right)\min\left(1,\frac{q(t)}{q^{max}}\right)\right]. \tag{4.4.8}$$

Finally, since this model is non-spatial, equation (4.3.15) can be modified to improve the modelling of the effects of light attenuation in the boundary layer. The $k(z,\lambda)I(z,\lambda)$ term in equation (4.3.13), which is equivalent to $\mathrm{d}I(z,\lambda)/\mathrm{d}z$, can be replaced by $(I(0,\lambda)-I(z_S,\lambda))/z_S$, where z_S is the depth of the boundary layer. This represents the average attenuation over the boundary layer, giving a better indication of the light levels to be found there. This leads to a modified light capture term

$$Light\ Captured = \left(\frac{q^{max}-q\,(t)}{q^{max}}\right)\int_{350}^{700}\frac{1}{P}\frac{\overline{aA}\,(\lambda)\,P}{k_w\,(\lambda)+k_g\,(\lambda)+\overline{aA}\,(\lambda)\,P}\left[\frac{I(0,\lambda)-I(z_S,\lambda)}{z_S}\right]\mathrm{d}\lambda. \tag{4.4.9}$$

4.4.2 Equilibrium analysis of the NPZ-q model

In order to better understand the behaviour of the model, and it's dependence on the various parameters, it is important to look at the behaviour of near-equilibrium solutions. Using the same methods as in section 3.3, the coexistence equilibrium $(N,P,Z,q>0)$ is found by setting the right-hand side of equations (4.4.1)-(4.4.4) equal to 0 and solving for $N,P,Z,q>0$.

$$\frac{\mathrm{d}N}{\mathrm{d}t} = -dP(t)N(t)\left(1-hN(t)\right)H(1-hN(t)) + e\hat{q}(t)hN(t)P(t) = 0, \tag{4.4.10}$$

$$\frac{\mathrm{d}P}{\mathrm{d}t} = a\hat{q}(t)hN(t)P(t) - bP(t)Z(t) = 0, \tag{4.4.11}$$

$$\frac{\mathrm{d}Z}{\mathrm{d}t} = cP(t)Z(t) - \mu_{Zdeath}Z(t) = 0, \tag{4.4.12}$$

$$\frac{\mathrm{d}q}{\mathrm{d}t} = \left(1-\hat{q}(t)\right)Q - l\hat{q}(t)hN(t) = 0, \tag{4.4.13}$$

where $\hat{q}(t) = q(t)/q^{max}$, $l = s_I\mu_P^{max}$ and Q is the light capture integral from (4.4.9), which is assumed to be approximately constant when P is close to equilibrium. All other terms are as previously defined (equation 3.3.4). Making the assumptions that $hN(t)<1$, $cP(t)<\mu_{Zdeath}$

and $q(t) < q^{max}$, the coexistence equilibrium is found to satisfy:

$$\begin{aligned} N_{eq} &\approx \frac{1}{h} - \frac{eI}{d\,(Q+l)} = \frac{1}{h}\,(1-\epsilon\omega) = \frac{1}{h} + O(\epsilon), \\ P_{eq} &= \frac{\mu_{Zdeath}}{c}, \\ Z_{eq} &\approx \frac{a}{b}\,(1-\epsilon\omega)\,\omega = \frac{a}{b}\omega + O(\epsilon), \\ \hat{q}_{eq} &\approx \frac{Q}{Q+l} + \frac{Q^2 l\epsilon}{2(Q+l)^3} = \omega + O(\epsilon), \end{aligned} \tag{4.4.14}$$

where $\omega = Q/(Q+l)$, and $\epsilon = eh/d$ is a small parameter, approximately linear in μ_P^{max}.

For typical parameter values, from tables 3.2, 4.3 and 4.4, the coexistence equilibrium (to zero-th order in ϵ) for the model phtoplaknton species is calculated to be

$$\begin{aligned} N_{eq} &= 4.32 \times 10^{-5}\ \mathrm{kg\,m^{-3}}, \\ P_{eq} &= 7.50 \times 10^{5}\ \mathrm{cells\,m^{-3}}, \\ Z_{eq} &= 6.57 \times 10^{3}\ \mathrm{cells\,m^{-3}}, \\ \hat{q}_{eq} &= \frac{q_{eq}}{q^{max}} = 0.698. \end{aligned} \tag{4.4.15}$$

In the above calculations, the irradiance $I(\lambda)$, is converted to units of $\mathrm{mol}(q)\,\mathrm{m^{-2}\,nm^{-1}\,s^{-1}}$ by the relation

$$1\ \mathrm{W\,m^{-2}\,nm^{-1}} = 8.3525 \times 10^{-9} \times \lambda\ \mathrm{mol}(q)\,\mathrm{m^{-2}\,nm^{-1}\,s^{-1}}$$

from Koller (1965). The predation rate was calculated to be $2.0 \times 10^{-9}\ \mathrm{m^3\,s^{-1}}$ and the boundary layer depth was chosen to be $z_S = 30$ m. The values of Z_{eq} and $\hat{q}_{eq}$ decrease with increasing boundary layer depth z_S, at the surface (using equation (4.3.15)) $Z_{eq} = 8.50 \times 10^3\ \mathrm{cells\,m^{-3}}$ and $\hat{q}_{eq} = 0.904$. For comparison, the coexistence equilibrium in the non-spatial NPZ model is

$$\begin{aligned} N_{eq} &= 4.32 \times 10^{-5}\ \mathrm{kg\,m^{-3}}, \\ P_{eq} &= 7.5 \times 10^{5}\ \mathrm{cells\,m^{-3}}, \\ Z_{eq} &= 9.41 \times 10^{3}\ \mathrm{cells\,m^{-3}}. \end{aligned} \tag{4.4.16}$$

The reduction in the zooplankton equilibrium in the NPZ-q model reflects the lower attained phytoplankton growth rate caused by the limiting factor q/q^{max}.

In order to establish the stability of the equilibrium points the eigenvalues of the Jacobian

Parameter	Value	Reference
Max internal quota of energy q^{max}	$848/16 \times (1.38 \times 10^3) \times V_P$ mol(q) cell^{-1}	AS94 & BE99
Energy stoichiometry coefficient s_I	q^{max} mol(q) cell^{-1}	BE99

Table 4.3: 848/16 from marine Redfield ratio C:N:P of 106:16:1 from AS94 and 8 quanta per C required, $(1.38 \times 10^3) \times V_P$ is max amount of nitrogen storage in mol(N) cell^{-1}. References: AS94 (Anderson and Sarmiento 1994), BE99 (Baird and Emsley 1999).

matrix are computed. To zero-th order in ϵ

$$\begin{aligned}
\lambda_1 &= i\sqrt{a\mu_{Zdeath}\omega} = i\sqrt{a\mu_{Zdeath}\frac{Q}{Q+l}}, \\
\lambda_2 &= -i\sqrt{a\mu_{Zdeath}\omega} = -i\sqrt{a\mu_{Zdeath}\frac{Q}{Q+l}}, \\
\lambda_3 &= \frac{d\mu_{Zdeath}}{c}, \\
\lambda_4 &= -\frac{Q}{\omega} = -(Q+l).
\end{aligned} \tag{4.4.17}$$

The eigenvalues are very similar to those of the simple NPZ system. The oscillatory timescale $\tau_{oscil} = 2\pi/\sqrt{a\mu_{Zdeath}\omega}$ is now increased, reflecting the lower attained phytoplankton growth rate. There is a new eigenvalue associated with q which has a stabilising effect, although the system remains unstable because of the exponentially increasing solution branch with time scale $\tau_{exp+} = c/d\mu_{Zdeath}$. For the case of the model species over a 30 m boundary layer,

$$\begin{aligned}
\tau_{oscil} &= 10.0 \text{ days}, \\
\tau_{exp+} &= 103.8 \text{ days}.
\end{aligned} \tag{4.4.18}$$

The P & Z fields will slowly oscillate about their equilibrium values over, whilst growing exponentially at a faster rate. However, like with the NPZ system, if N gets too large ($hN > 1$) the unstable branch becomes stable over the same time scale. The time scale associated with q is significantly larger, since $Q, l = O(10^{-14})$ mol(q) cell , so it is an insignificant factor in this analysis. This means that the P & Z populations oscillate regularly whilst the nutrient concentration declines as it funds new P growth, much as before.

4.4.3 Results

Figure 4.12 shows the evolution of the NPZ-q system with initial conditions very close to the equilibrium values for the model (see equation (4.4.16)). As predicted by the analysis of the previous section the P and Z populations oscillate very slowly - out of phase, with the zooplankton oscillations occurring after those of the phytoplankton - over a period of approximately 10 days. The magnitude of these oscillations is small, with the difference in population at maximum and minimum is $O(10^{-1})$ of the background population for each

Parameter	Value
P cell radius, r_P, & volume, V_P	1×10^{-5} m, $V_P = 4.2 \times 10^{-15}$ m^3
P background concentration, P_0	4.0×10^6 cells m^{-3}
P cell density, ρ_P	$1.002\rho_0$
P max growth rate, μ_P^{max}	2.5×10^{-5} s^{-1}
Yield, Y	3×10^{-3}
Proportion of dead P cells, ϕ_P^{dead}	10^{-3}
Nitrate stoichiometry coefficient, s_N	2.70×10^{-14} kg cell^{-1}
Max nitrate storage capacity, R_N^{max}	8.09×10^{-14} kg cell^{-1}
Energy stochiometry coefficient, s_I	3.06×10^{-10} mol(q) cell^{-1}
Max energy storage capacity, q^{max}	3.06×10^{-10} mol(q) cell^{-1}

Table 4.4: Model parameters for phytoplankton, based on the formulae and parameters from table 3.2. All other parameters, for N & Z are the same as previous.

species. The nitrate concentration slowly decreases from it's equilibrium value as it is being used in growth. The light storage fraction, $\hat{q}$, steadily grows from its initial condition. This is because the declining nitrate concentration results in less growth as the simulation progresses, consequently less energy is being used. The effect of this on P and Z is very small, $O(10^{-3})$.

If the initial conditions are set well away from equilibrium, as shown in figure 4.13, everything happens on larger scales. As before the P and Z populations oscillate out of phase, but the magnitude of the oscillations are much higher, $O(10)$ for P and $O(1)$ for Z. The timescale of the oscillations is also longer, taking 40 days to complete one cycle. In this case the nitrate concentration grows from it's initial condition because $N > 1/h$. This means that the nitrate uptake term is set to 0, since the phytoplankton cells are satiated, so the only effect is that of the recycling term which returns nitrate to the system. If the initial condition for N is much $< 1/h$, the nitrate concentration declines rapidly from it's initial condition towards 0 as it is consumed by the phytoplankton. In that case the effect of uptake is larger than that of the recycling term. Since there is no other replenishment of nitrate, such as an inward flux at the base of the boundary layer, the nitrate concentration cannot recover. The light storage is much more interesting, it stays at a fixed level, close to equilibrium, except when energy is being used in the process of growth.

Figures 4.14 and 4.15 show the evolution of the system for initial conditions similar to those used in the NPZ models. In both cases the P and Z populations oscillate over a period of about $12 \rightarrow 15$ days, the magnitude of the oscillations is $O(1)$ times the background population in both cases. In the case of figure 4.14, the initial concentration of nitrate is sufficiently low that the uptake is higher than the recycling term and the concentration declines over time, as energy reserves increase (as per figure 4.12). The decay in concentration occurs alongside phytoplankton growth. Over time the magnitude of the phytoplankton population maxima reduces as a result of the decreasing availability of nitrates. For figure

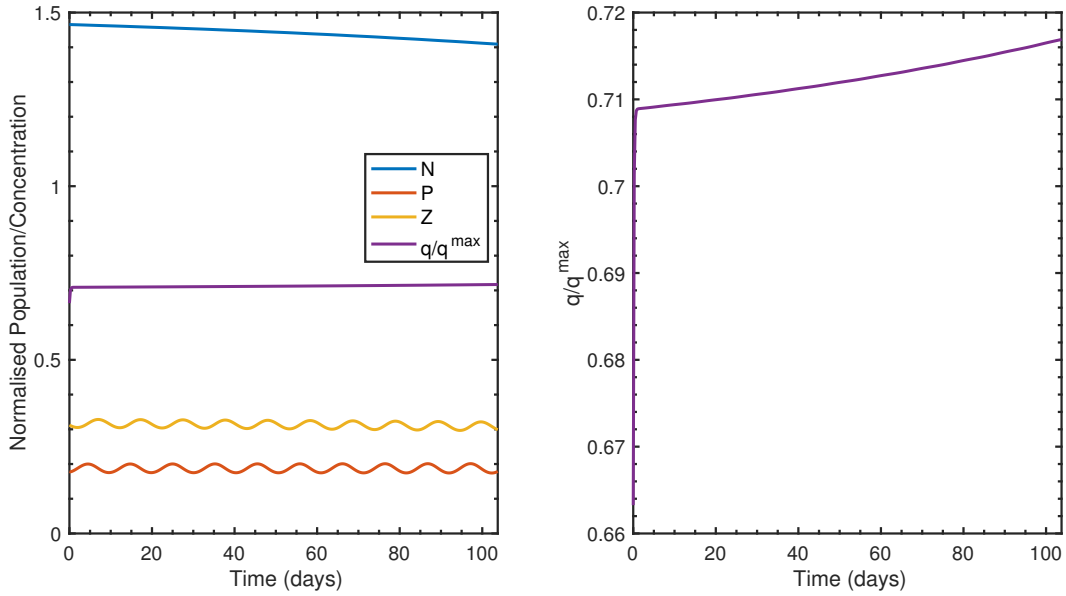

Figure 4.12: Left: Evolution of nitrate, phytoplankton, zooplankton, and light started from close to coexistence equilibrium. Right: Evolution of light q. Values are normalised by background concentrations.

4.15, the initial concentration of nitrate is such that the cells are satiated and hence uptake term is set to 0 which results in the nitrate concentration increasing over time.

In most of the results described here, with the exception of figure 4.13, the amount by which q changes under growth is very low and the overall results are very similar to those from the NPZ model. The change in population levels in these cases corresponds to low growth and hence only a small amount of nitrate and energy is used in the process. During a bloom event, such as figure 4.13, the growth is much more substantial, therefore a more significant proportion of the energy is used in this process.

4.5 1d NPZ-q model

The main difference between the non-spatial and one-dimensional models is the effect of mixing. In this model the mixing is by laminar diffusion. This one-dimensional model is adapted from the one-dimensional NPZ model of section 3.5, however the diffusion term for the average stored energy, $q(z,t)$, presents some difficulty. Since $q(z,t)$ is a property of the phytoplankton cells it would be expected that the diffusion term for $q(z,t)$ would depend on both q and P. The only vertical motion of q occurs with the vertical motion of P.

Baird and Emsley (1999) suggest that the diffusion of q should take the form

$$\frac{\partial}{\partial z}\left(\frac{D_P}{P}\frac{\partial\left(P(z,t)q(z,t)\right)}{\partial z}\right), \tag{4.5.1}$$

where D_P is the diffusion coefficient for phytoplankton. There are a few problems with this formulation, in particular a flux of q could occur from a uniform distribution if there is a gradient in P, as shown by figure 4.16. This figure shows how P and q diffuse subject to

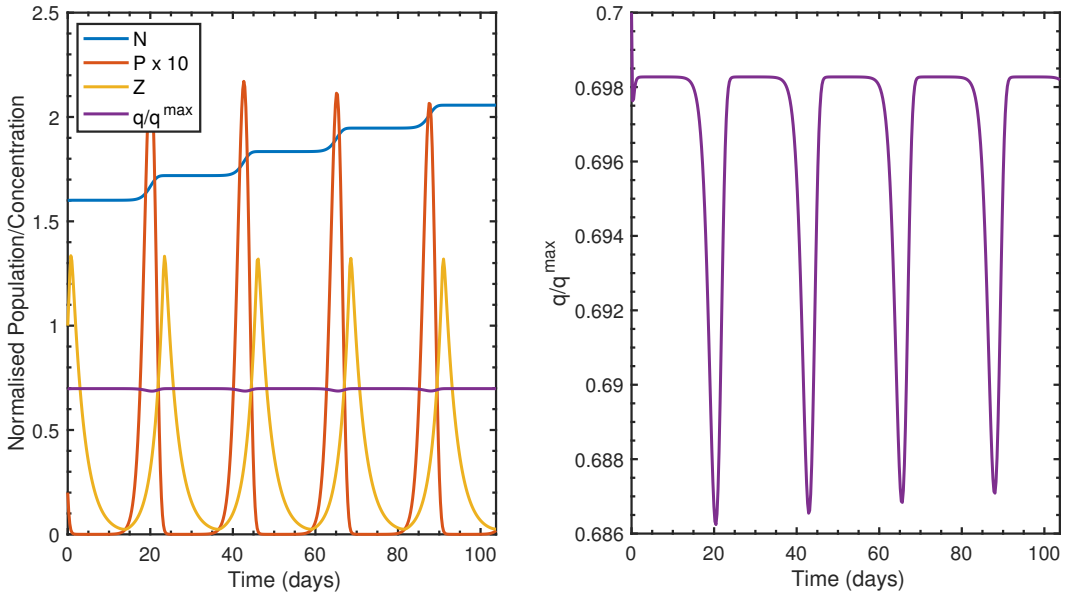

Figure 4.13: Left: Evolution of nitrate, phytoplankton, zooplankton, and light with initial condition far from coexistence equilibrium. Right: Evolution of light q. Values are normalised by background concentrations. Initial conditions: $N = 1.6$, $P = 2$, $Z = 1$, $\hat{q} = 0.7$.

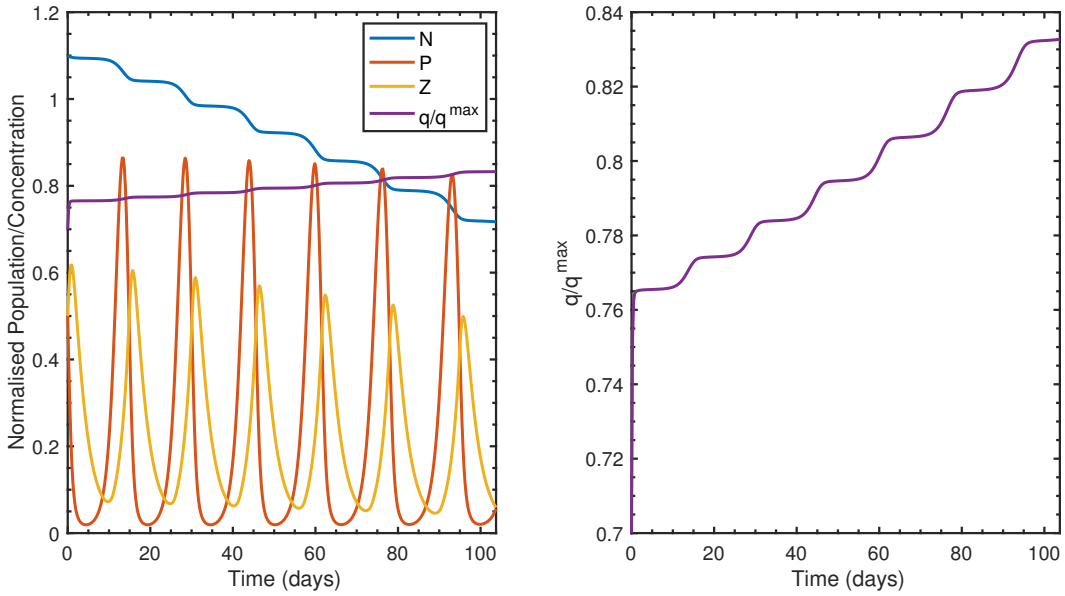

Figure 4.14: Left: Evolution of nitrate, phytoplankton, zooplankton, and light with initial condition $N = 1.1$, $P = 0.5$, $Z = 0.5$, $\hat{q} = 0.7$. Right: Evolution of light q. Values are normalised by background concentrations.

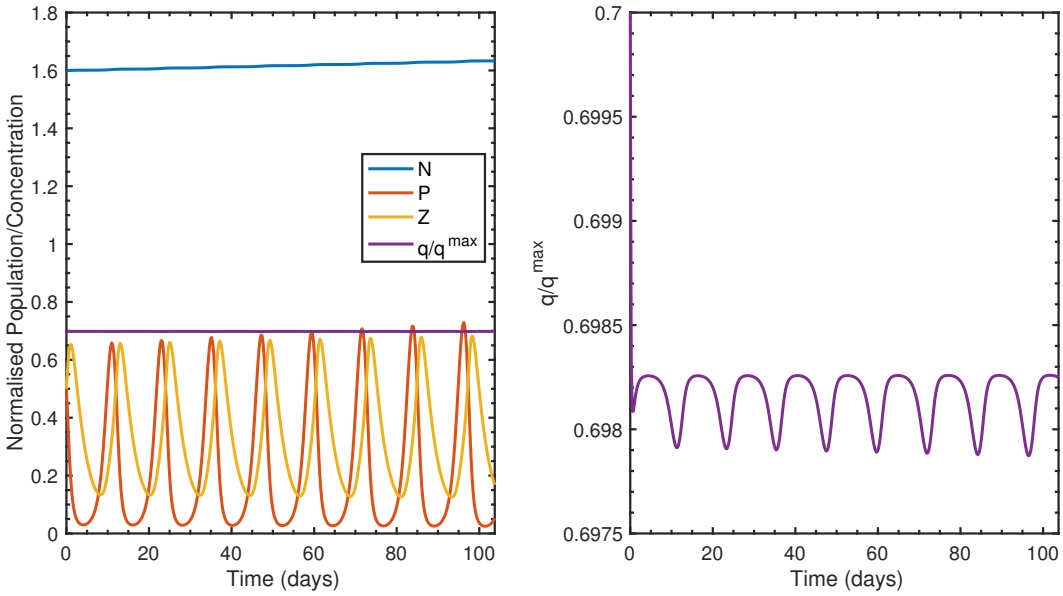

Figure 4.15: Left: Evolution of nitrate, phytoplankton, zooplankton, and light with initial condition $N = 1.6$, $P = 0.5$, $Z = 0.5$, $\hat{q} = 0.7$. Right: Evolution of light q. Values are normalised by background concentrations.

equations (3.4.2) and (4.5.1) respectively, with no source or sink terms. An upwards flux of q occurs as a consequence of the upward flux of P.

4.5.1 Alternative forms for diffusion of $q(z,t)$

To attempt to solve the problem described above, a number of alternative forms for the diffusion of $q(z,t)$ are presented. All forms of q-diffusion described in this section are subject to

$$\left.\frac{\partial q}{\partial z}\right|_{z=0} = 0 \;\; ; \;\; \left.\frac{\partial q}{\partial z}\right|_{z=z_S} = 0. \tag{4.5.2}$$

1. The first, and most simple, proposed method to solve the problems with equation (4.5.1) is to remove the diffusion term altogether.

2. A second option is to apply a factor to the diffusion term that solves the problem described above. The proposed form of this factor is

$$\frac{\partial}{\partial z}\left(\frac{D_P}{P}\frac{\partial\left(P(z,t)q(z,t)\right)}{\partial z}\right)\left(1-\exp\left(-A\left|\frac{\partial q}{\partial z}\right|\right)\right), \tag{4.5.3}$$

   where A is a length scale, chosen to be the inverse of the sum of the attenuation coefficients for water and gilvin. When q is uniform throughout the boundary layer the diffusion of q is effectively switched off since $\exp(-A * 0) = 1$, so equation (4.5.3) returns 0. The diffusion of P and q, with q starting from an initial profile defined by $\exp(-0.04z)$, for different initial P profiles is shown in figure 4.17. In all cases the boundary condition (4.5.2) results in $\partial q/\partial t = 0$ at both the surface and base of the boundary layer. An upwards flux of P containing low q brings about a decrease in the

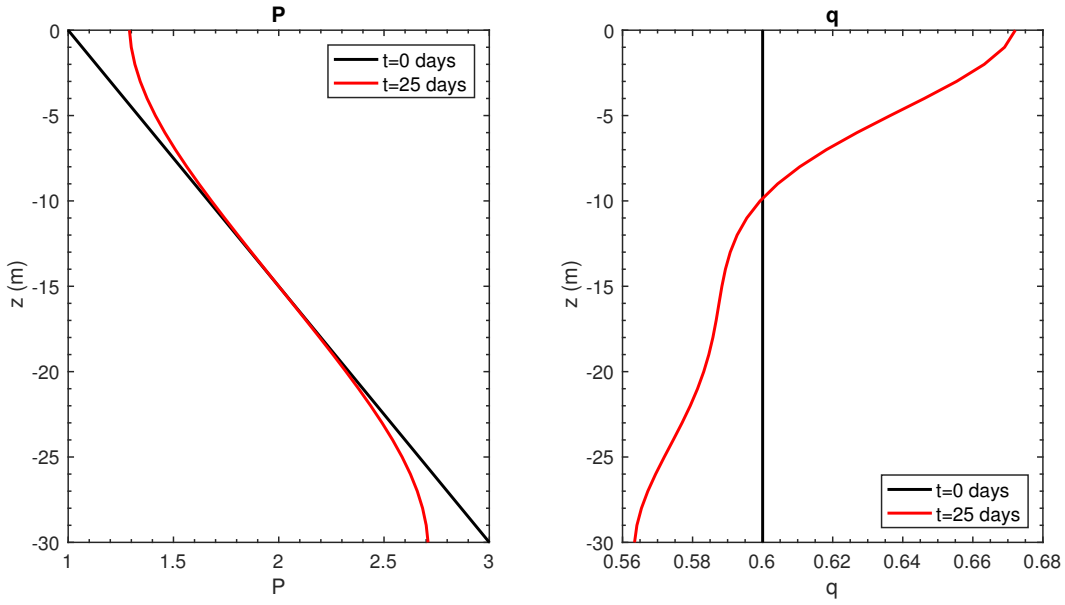

Figure 4.16: Profiles of $P(z,t)$ (left) and $q(z,t)$ (right) initially and after diffusing for 25 days with $D_P = 2 \times 10^{-6}$ m^2 s^{-1} subject to equation (4.5.1) with no-flux boundary conditions applied at both the surface $z = 0$ and base of the simulation layer $z = z_S = -30$ m.

average stored energy above. Similarly, a downward flux of P containing high q results in an increase in q below.

3. Expanding equation (4.5.1) for constant D_P gives

$$D_P \left(\frac{\partial^2 q}{\partial z^2} - \frac{q}{P^2} \left(\frac{\partial P}{\partial z} \right)^2 + \frac{1}{P} \frac{\partial P}{\partial z} \frac{\partial q}{\partial z} + \frac{q}{P} \frac{\partial^2 P}{\partial z^2} \right). \tag{4.5.4}$$

The terms that lead to the problem described above are

$$\frac{q}{P} \frac{\partial^2 P}{\partial z^2} - \frac{q}{P^2} \left(\frac{\partial P}{\partial z} \right)^2,$$

since these terms do not depend on the gradient of q but do depend on the gradient of P. If $\partial q/\partial z = 0$ these terms may not be equal to 0, leading to flux of q. Removing these terms from equation (4.5.1) leads to

$$D_P \left(\frac{1}{P} \frac{\partial P}{\partial z} \frac{\partial q}{\partial z} + \frac{\partial^2 q}{\partial z^2} \right). \tag{4.5.5}$$

This equation is effectively a drift-diffusion equation, where $\frac{1}{P} \frac{\partial P}{\partial z} \frac{\partial q}{\partial z}$ is the 'drift'. The diffusion of P and q, with q starting from an initial profile defined by $\exp(-0.04z)$, for different initial P profiles is shown in figure 4.18. The results are very similar to those in figure 4.17, except that the boundary conditions do not impose the restriction on diffusion at the surface. As before, an upwards flux of P containing low q brings about a decrease in the average stored energy above. Similarly, a downward flux of P

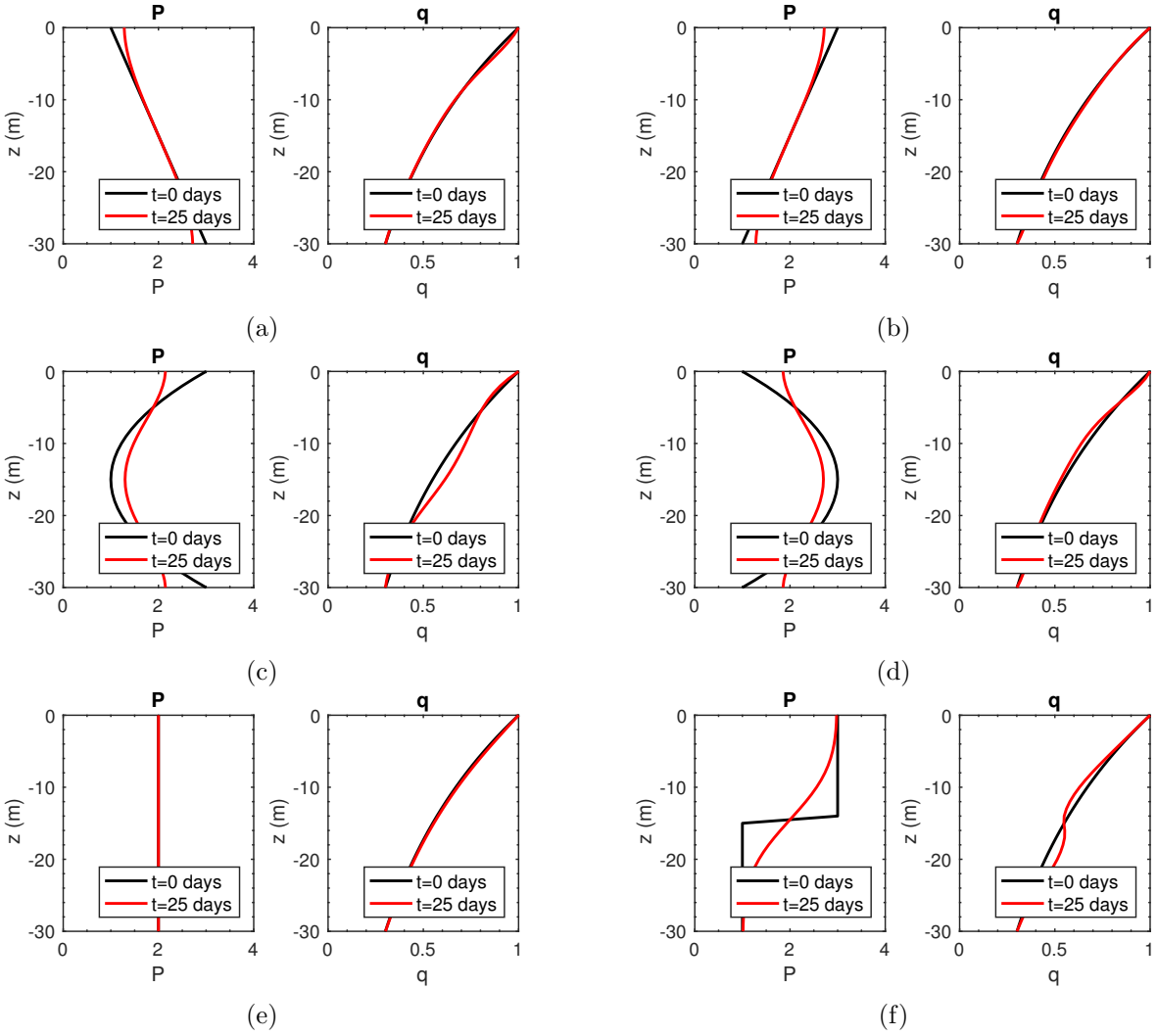

Figure 4.17: Profiles of $P(z,t)$ (left) and $q(z,t)$ (right) initially and after diffusing for 25 days with $D_P = 2 \times 10^{-6}$ m^2 s^{-1} subject to equation (4.5.3) with no-flux boundary conditions applied at both the surface $z = 0$ and base of the simulation layer $z = z_S = -30$ m.

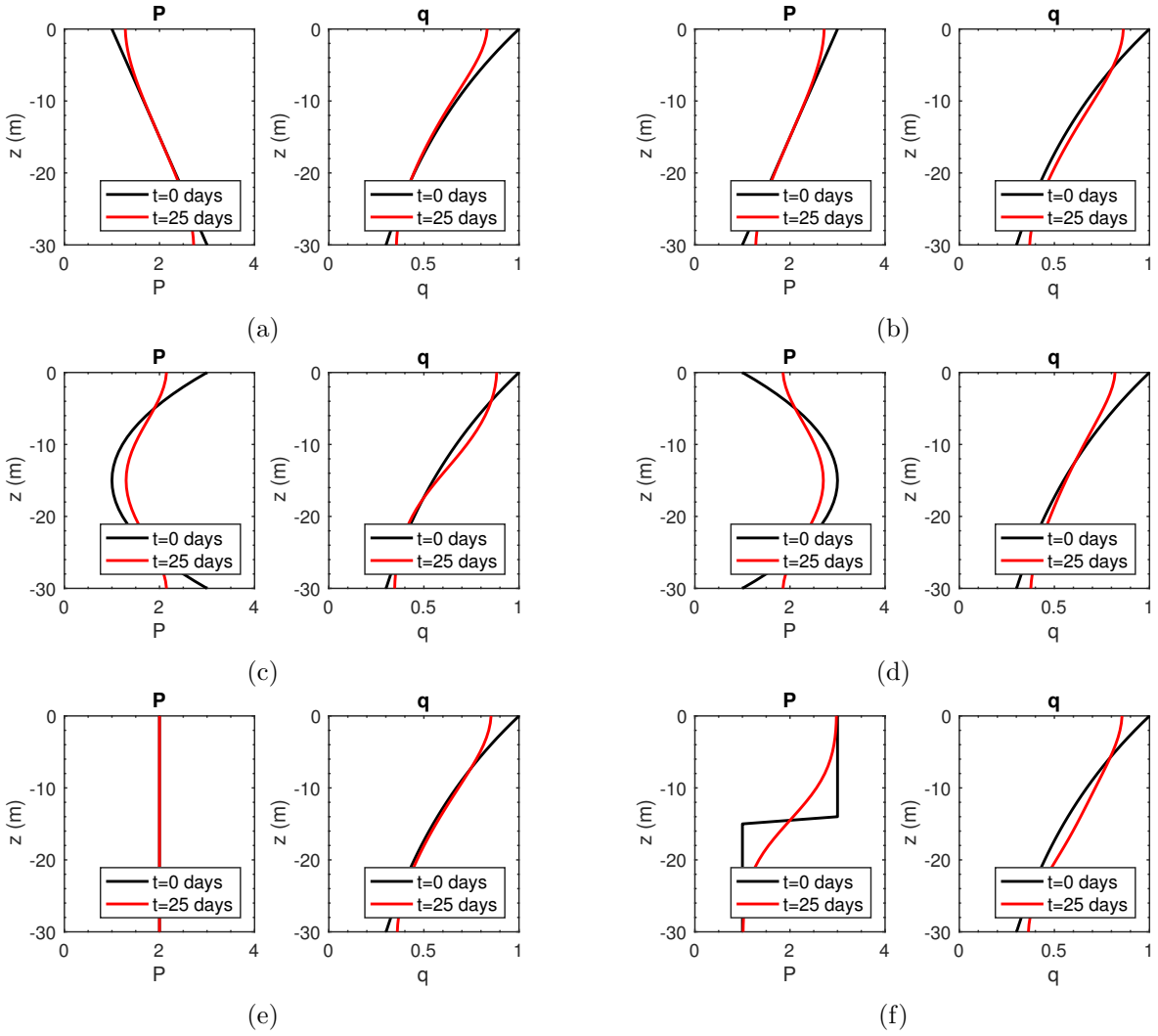

Figure 4.18: Profiles of $P(z,t)$ (left) and $q(z,t)$ (right) initially and after diffusing for 25 days with $D_P = 2 \times 10^{-6}$ m^2 s^{-1} subject to equation (4.5.5) with no-flux boundary conditions applied at both the surface $z = 0$ and base of the simulation layer $z = z_S = -30$ m.

containing high q results in an increase in q below. This can be clearly seen in figure 4.18d where P in the middle of the boundary layer diffuses both towards the surface and base of the boundary layer. This results in q decreasing near the surface, but increasing at $z = -30$ m.

4. The main problem with equations (4.5.3) and (4.5.5) is that the total q over time is not conserved. In order for q to be conserved over the simulated time it is required that

$$\int_{z_S}^{0} \frac{\partial q}{\partial t} \, \mathrm{d}z = 0. \tag{4.5.6}$$

For equation (4.5.1) this is simple to guarantee. Integrating (4.5.1) results in

$$\frac{D_P}{P} \frac{\partial (Pq)}{\partial z}. \tag{4.5.7}$$

In this case the value of equation (4.5.7) at the boundaries need to match for q to be conserved. For equations (4.5.3) and (4.5.5) this is not as simple to resolve, because these formulations do not consist of a single derivative with respect to z. Moving the factor in equation (4.5.5) inside the derivative gives

$$\frac{\partial}{\partial z}\left(\frac{D_P}{P}\frac{\partial\left(P(z,t)q(z,t)\right)}{\partial z}\left(1-\exp\left(-A\left|\frac{\partial q}{\partial z}\right|\right)\right)\right). \tag{4.5.8}$$

The result is that equation (4.5.8) is in the form of a single derivative. For q to be conserved over time the values of

$$\frac{D_P}{P}\frac{\partial\left(P(z,t)q(z,t)\right)}{\partial z}\left(1-\exp\left(A\left|\frac{\partial q}{\partial z}\right|\right)\right) \tag{4.5.9}$$

at $z = 0$ and $z = z_S$ must be equal. This condition is satisfied by the boundary conditions given by equation (4.5.2). The evolution of P and q subject to the diffusion process modelled by equation (4.5.8) for various initial profiles of P is shown in figure 4.19. As in figures 4.17 and 4.18, an upwards flux of P containing low q decreases the average stored energy above. Similarly, a downward flux of P containing high q increases q below.

4.5.2 The 1d NPZ-q Model

The full one-dimensional NPZ-q model is given by

$$\frac{\partial N}{\partial t} = \frac{\partial}{\partial z}\left(D_N\frac{\partial N}{\partial z}\right) - N \text{ uptake by } P + N \text{ recycled by } P, \tag{4.5.10}$$

$$\frac{\partial P}{\partial t} = \frac{\partial}{\partial z}\left(D_P\frac{\partial P}{\partial z}\right) + P \text{ growth from } N - Z \text{ grazing loss}, \tag{4.5.11}$$

$$\frac{\partial Z}{\partial t} = \frac{\partial}{\partial z}\left(D_Z\frac{\partial Z}{\partial z}\right) + Z \text{ growth from } P - Z \text{ mortality}, \tag{4.5.12}$$

$$\frac{\partial q}{\partial t} = D(P,q) + \text{light } q \text{ captured by } P - \text{light } q \text{ used in } P \text{ growth}, \tag{4.5.13}$$

where $D(P,q)$ is the diffusion formulation used. The overall impact of diffusion of q on the one-dimensional model is minimal. This can be seen by figure 4.20, which shows the evolution of P and q subject the the NPZ-q equations above. The results are very similar for all forms of diffusion discussed above. This is because the vertical structure of q is largely determined by the amount of light available. Since these results are so similar, for the remainder of this chapter the q diffusion term will be removed. This choice solves both problems illustrated above: flux of uniform q under P diffusion, and the conservation of q.

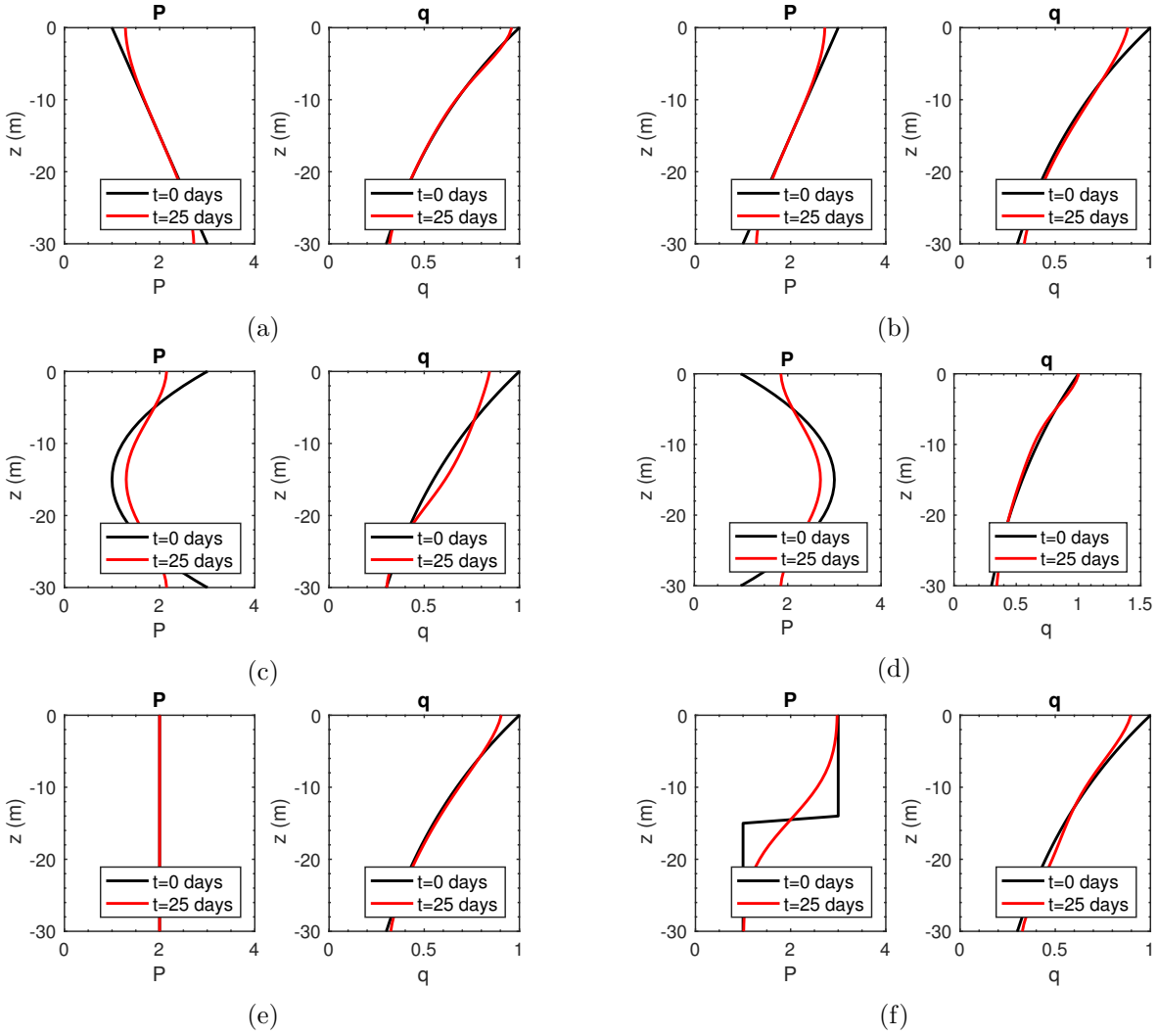

Figure 4.19: Profiles of $P(z,t)$ (left) and $q(z,t)$ (right) initially and after diffusing for 25 days with $D_P = 2 \times 10^{-6}$ m^2 s^{-1} subject to equation (4.5.8) with no-flux boundary conditions applied at both the surface $z = 0$ and base of the simulation layer $z = z_S = -30$ m.

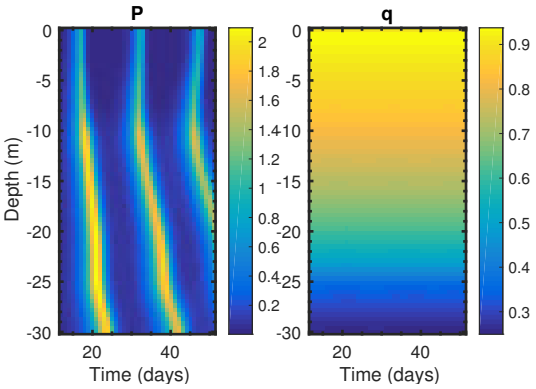

(a) No q diffusion

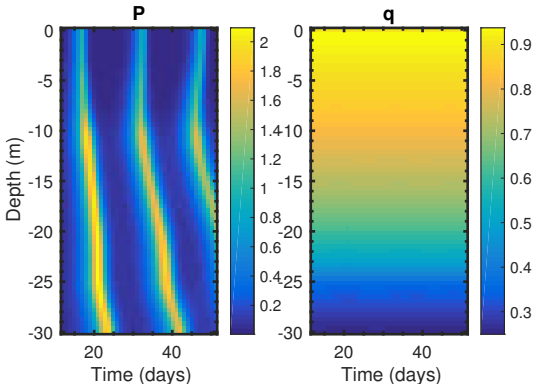

(b) Equation (4.5.3)

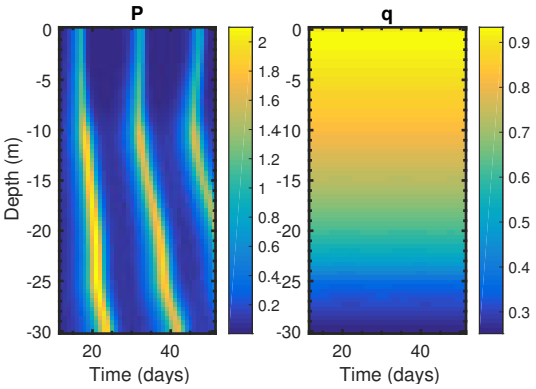

(c) Equation (4.5.5)

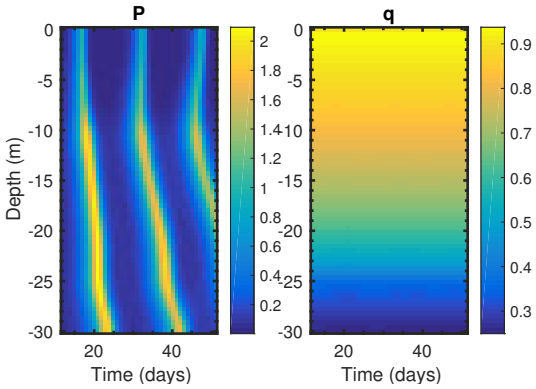

(d) Equation (4.5.8)

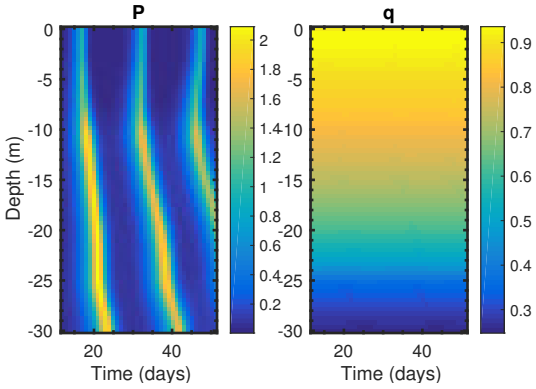

(e) Equation (4.5.1)

Figure 4.20: Evolution of P and q subject to the NPZ-q model described by equations (4.5.10)–(4.5.13), for different methods of diffusion of q.

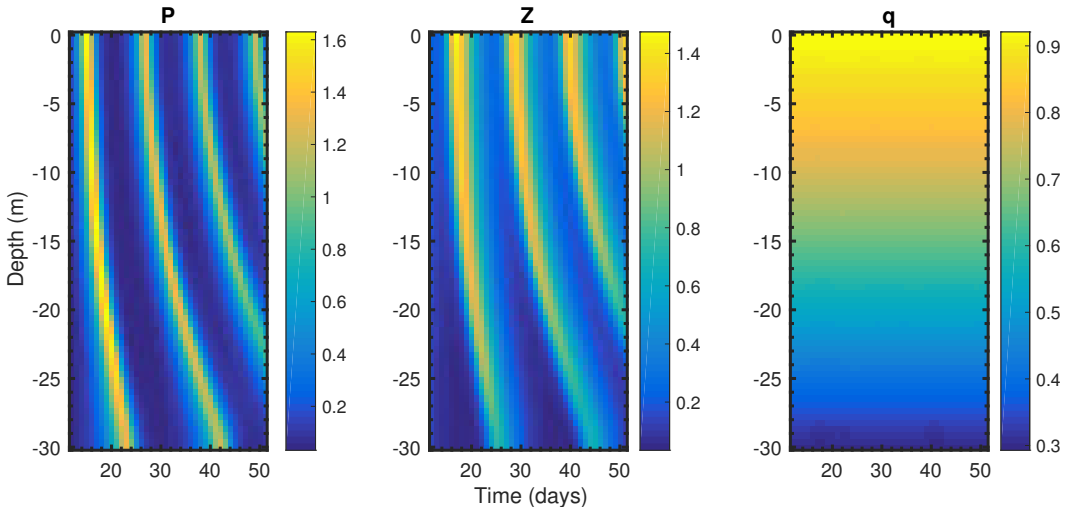

Figure 4.21: Evolution of P, Z and q for constant (in depth and time) N and predation rate.

4.5.3 Results of a simplified 1d PZ-q model

Since the focus of this chapter is on the storage, and use, of internal energy, from light capture, the equation governing the nitrate concentration, equation (4.5.10), is removed and the nitrate is instead held constant in time. This simplified model is called the PZ-q model. The following results are generated from this model, subject to initial conditions These investigations were conducted with initial conditions

$$\begin{aligned} P &= 0.5 \times P_0 = 2 \times 10^6 \text{ cells m}^{-3}, \\ Z &= 0.05 \times Z_0 = 1 \times 10^3 \text{ cells m}^{-3}, \\ q &= 0.8 \times q^{max} \text{ mol}(quanta) \text{ cell}^{-1}. \end{aligned} \tag{4.5.14}$$

Constant N and predation rate

In order to demonstrate how the internal energy changes with depth, and how it affects the growth of the phytoplankton, figure 4.21 shows the evolution of P, Z and q over depth for a constant (in both time and depth) nitrate concentration ($N = 1.3$) and predation rate (calculated as the mean of predation rate with $\sigma_Z = 5.0 \times 10^{-5}$ m s^{-1} & $T_R = 5$ s).

As with the non-spatial model the P and Z populations oscillate, however they oscillate more frequently towards the surface (12-13 days) than at the bottom of the layer (18-20 days). This is because of the reduced light capture, and hence lower q, at depths, the effect of which is to reduce the attained growth rate of the phytoplankton.

Depth dependent N and predation rate

Figure 4.22 shows how the populations evolve applying more realistic, depth dependent, nitrate and predation rate ($\sigma_Z = 5.0 \times 10^{-5}$ m s^{-1} & $T_R = 5$ s) profiles as shown in figure 4.23. The general structure of oscillations of P and Z populations is the same as before,

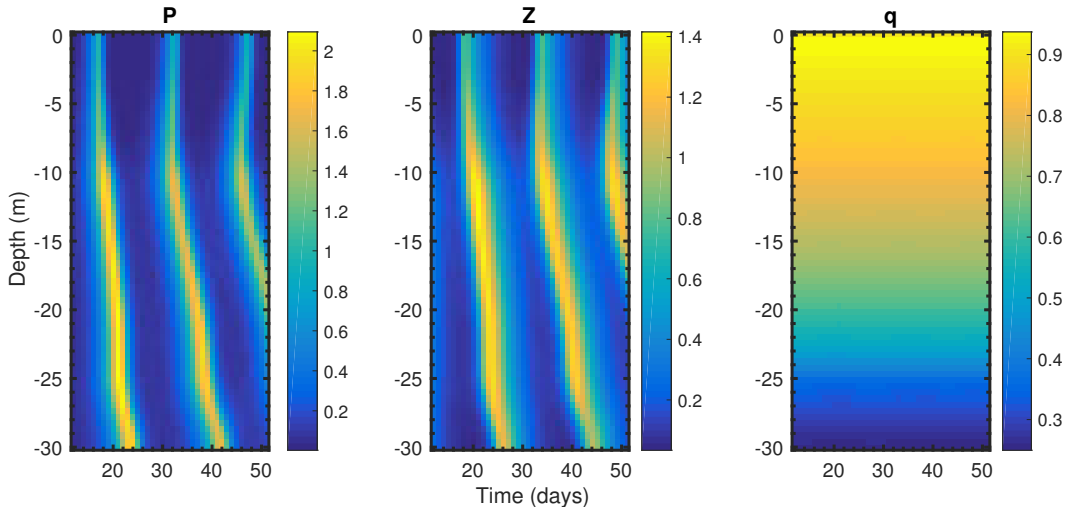

Figure 4.22: Evolution of P, Z and q for nutrient profile and predation rate with $\sigma_Z = 5 \times 10^{-5}\,\mathrm{m\,s^{-1}}$ & $T_R = 5$ s from figure 4.23.

however the periods of these oscillations are now affected by the variation in predation and nitrate levels. The oscillations are less frequent at the surface, where the predation rate is highest. As before the frequency decreases with depth as the light available for capture decreases, although it is slightly faster than figure 4.21 because of the additional nitrate near the bottom of the boundary layer.

Effect of varying k_g on DCM

The focus of this work is the vertical structure of phytoplankton, from the context of deep chlorophyll maxima. To study the effects of light capture on the vertical structure, the depth and magnitude of maximal growth in P was calculated using the PZ-q model for different values of $k_g(440\text{ nm})$. Increasing the reference gilvin attenuation rate effectively darkened the layer, decreasing the amount of light available for capture by phytoplankton. The aim of this study was to investigate how the darkening affects the vertical structure of the phytoplankton populations. Figure 4.24 shows the results of this investigation for the six different predation rates shown in figure 4.23. The red dashed curve shows how the magnitude of maximum phytoplankton population, P, decreases as k_g increases (less light). The solid black curve shows the depth at which this maximal population level occurs. As expected, there is a general trend of the maximal population decreasing and the corresponding depth shallowing as light levels decline. With less light available, phytoplankton will capture and store less energy and hence will not be able to grow as strongly. Equally the depth of maximal growth decreases as light levels fall. Deeper in the boundary layer, there is no longer sufficient light to promote phytoplankton growth.

The structure of the black curves, indicating the DBM (deep biological maxima) depth, particularly in the cases of low and medium predator swimming speeds, is interesting. If light levels are high throughout the boundary layer (k_g small), then a DBM forms towards the base of the simulation layer, below 20 m, where the nutrient concentration is highest.

The maximum phytoplankton population at the DBM (red dashed lines) is also greater than the DBM intensities seen for higher k_g values. In slightly darker water the DBM depth is at 12–15 m (with the exception of figure 4.24f). Although the nutrient concentration is greater, there is insufficient light for significant growth below this depth. Since the DBM is not forming in the high nutrient regions, the question arises as to why the growth is not at the surface in the slightly darker waters. Consider for example the figure 4.24a ($T_R = 5$ s, $\sigma_Z = 2.5 \times 10^{-5}$ m s^{-1}), for $0.1 < k_g < 0.5$ m^{-1}. In the regions above 12 m the predation rate, shown as the solid blue predation curve in figure 4.23, is very high. Here the predation rate acts to restrict growth near the surface. However, the predation pressure is much lower at 12 m, which means the phytoplankton can grow relatively unabated, as the light levels are still sufficient to promote growth. As the water darkens ($k_g > 0.5$ in this example), the light levels fall to a level that are insufficient to allow significant subsurface growth. As a result, the highest phytoplankton population levels are now seen at the surface. Due to the levels of predation, this can only reach a very low (normalised) level of approximately 1 (4) depending upon the predator's reaction capabilities $T_R = 5$ s ($T_R = 15$ s). For the slow reacting, fast swimming, predator with $T_R = 15$ s, $\sigma_Z = 10 \times 10^{-5}$ m s^{-1} shown in figure 4.24f, a DBM only forms in the clearest waters ($k_g < 0.1$), as a consequence of the high light and nutrient levels. As k_g increases, the phytoplankton level shifts rapidly to the surface. This is because the predation rate (dashed yellow curve in figure 4.23) is low throughout, and almost uniform over the depth. This means that predation pressure has limited influence and allows the P population to thrive in waters close to the surface.

Figures 4.25 and 4.26 show the evolution of the phytoplankton for six values of $k_g(440\text{ nm})$, subject to predation pressure characterised by $T_R = 5$ s, $\sigma_Z = 5 \times 10^{-5}$ m s^{-1} and $T_R = 15$ s, $\sigma_Z = 5 \times 10^{-5}$ m s^{-1} respectively. These demonstrate the transition from the formation of a DBM at 12 m in clear waters ($k_g(440\text{ nm}) = 0.01$ m^{-1}, figures 4.25a & 4.26a) to high surface growth when the light levels are very low ($k_g(440\text{ nm}) = 0.7$ m^{-1}, figures 4.25e–4.25f & 4.26e–4.26f). The DBM present when $k_g(440\text{ nm}) = 0.01$ extends to the base of the simulation layer (with decreasing intensity). In slightly darker waters ($k_g(440\text{ nm}) = 0.01$–$0.4$ m^{-1}), the DBM narrows with decreasing light levels. When $k_g(440\text{ nm}) = 0.4$, the light no longer penetrates to below 12 m sufficiently to allow significant growth, the DBM relocates itself towards the surface while its intensity decreases. When k_g is very high, all the growth is concentrated at the surface and no DBM forms.

Comparison with 3d LES-NPZ model

Figure 4.27 shows the evolution of the phytoplankton population from the LES-NPZ model for three attenuation rates based on the analysis of section 4.2. The predation rate used in these simulations is for a predator possessing swimming speed $\sigma_Z = 2.5 \times 10^{-5}$ m s^{-1} and a reaction time $T_R = 5$ s. The lowest attenuation rate ($k = 0.04$ m^{-1}), as used in Fasham et al. (1990), is equivalent to the attenuation of just sea-water at $\lambda = 440$ nm; the two larger

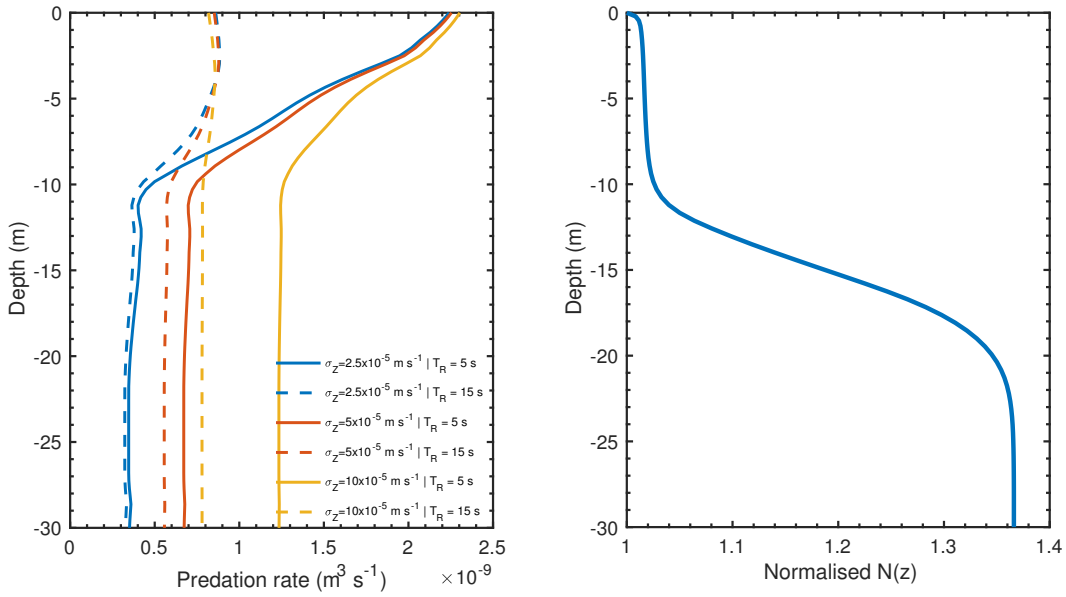

Figure 4.23: Left: profiles of the predation rates. Right: nitrate profile normalised by background concentration, representative of a typical nutricline. Data taken from a full LES-NPZ simulation with $U_* = 3.0 \times 10^{-3}\ \mathrm{m\,s^{-1}}$, $U_S = 3.3 \times 10^{-2}\ \mathrm{m\,s^{-1}}$.

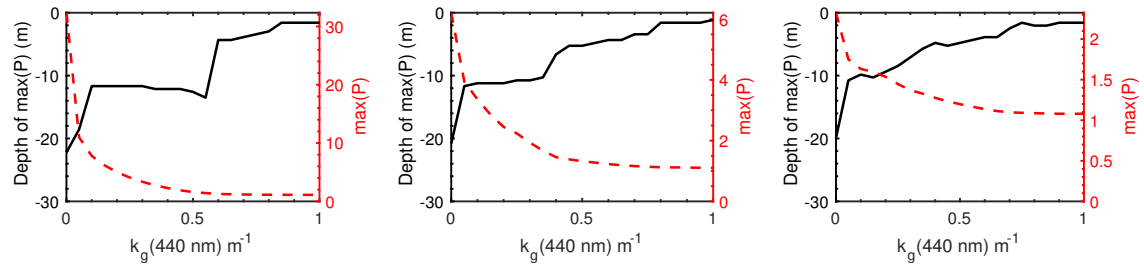

(a) $T_R = 5$ s
$\sigma_Z = 2.5 \times 10^{-5}\ \mathrm{m\,s^{-1}}$

(b) $T_R = 5$ s
$\sigma_Z = 5 \times 10^{-5}\ \mathrm{m\,s^{-1}}$

(c) $T_R = 5$ s
$\sigma_Z = 10 \times 10^{-5}\ \mathrm{m\,s^{-1}}$

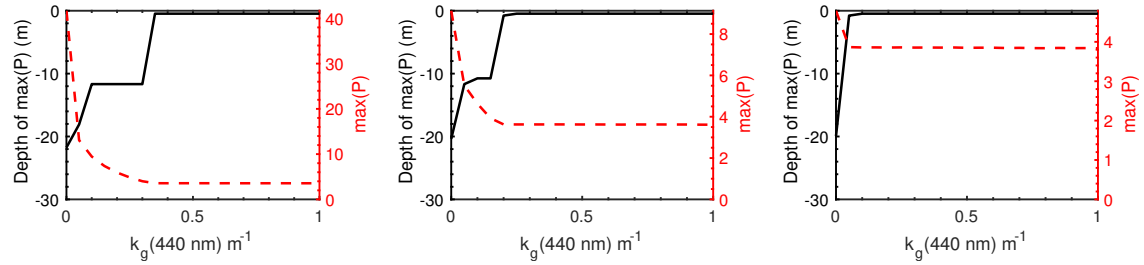

(d) $T_R = 15$ s
$\sigma_Z = 2.5 \times 10^{-5}\ \mathrm{m\,s^{-1}}$

(e) $T_R = 15$ s
$\sigma_Z = 5 \times 10^{-5}\ \mathrm{m\,s^{-1}}$

(f) $T_R = 15$ s
$\sigma_Z = 10 \times 10^{-5}\ \mathrm{m\,s^{-1}}$

Figure 4.24: Maximum value of P (red dashed, right axes) and depth at which the maximum of P occurs (black solid, left axes) against $k_g(440\ \mathrm{nm})$ for six different predation rates from figure 4.23. Reading left to right, top to bottom, the predation pressure is falling.

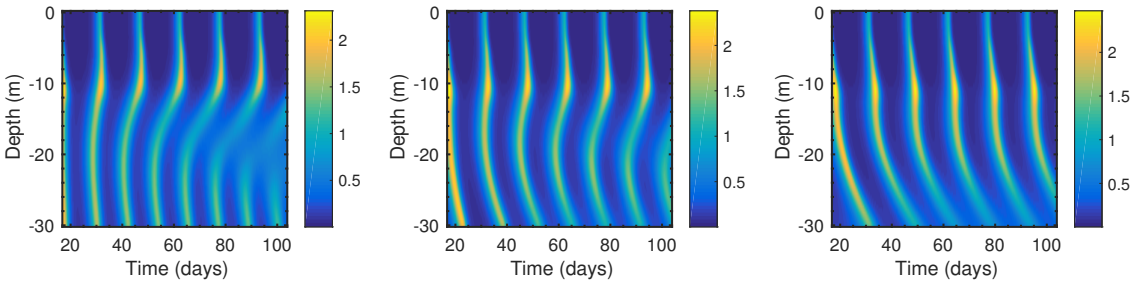

(a) $k_g(440\text{ nm}) = 0.01\text{ m}^{-1}$ (b) $k_g(440\text{ nm}) = 0.05\text{ m}^{-1}$ (c) $k_g(440\text{ nm}) = 0.1\text{ m}^{-1}$

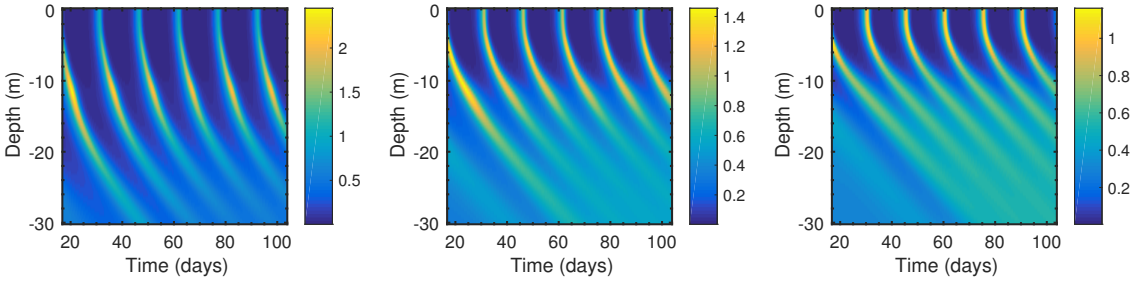

(d) $k_g(440\text{ nm}) = 0.2\text{ m}^{-1}$ (e) $k_g(440\text{ nm}) = 0.4\text{ m}^{-1}$ (f) $k_g(440\text{ nm}) = 0.7\text{ m}^{-1}$

Figure 4.25: Evolution of P for six values of $k_g(440\text{ nm})$ for predation rate with $\sigma_Z = 5 \times 10^{-5}\text{ m s}^{-1}$ & $T_R = 5\text{ s}$ from figure 4.23.

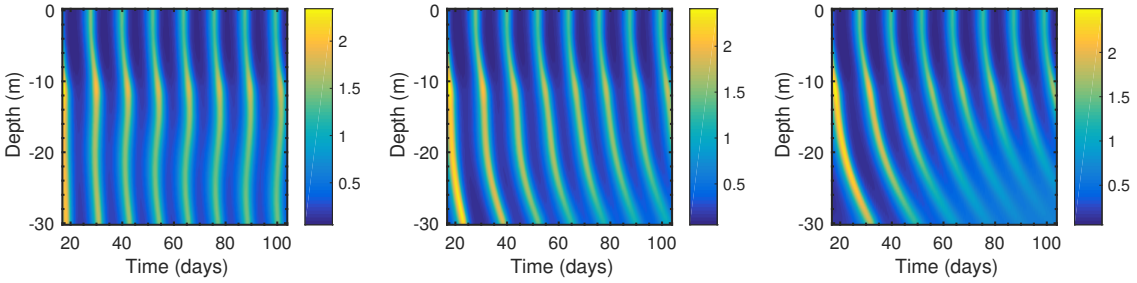

(a) $k_g(440\text{ nm}) = 0.01\text{ m}^{-1}$ (b) $k_g(440\text{ nm}) = 0.05\text{ m}^{-1}$ (c) $k_g(440\text{ nm}) = 0.1\text{ m}^{-1}$

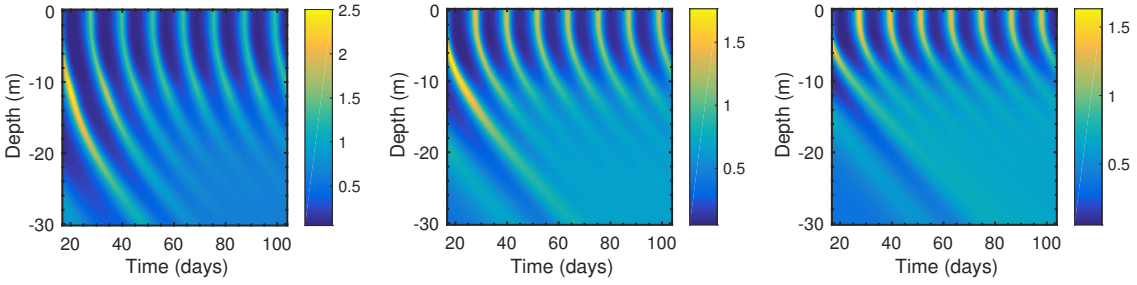

(d) $k_g(440\text{ nm}) = 0.2\text{ m}^{-1}$ (e) $k_g(440\text{ nm}) = 0.4\text{ m}^{-1}$ (f) $k_g(440\text{ nm}) = 0.7\text{ m}^{-1}$

Figure 4.26: Evolution of P for six values of $k_g(440\text{ nm})$ for predation rate with $\sigma_Z = 5 \times 10^{-5}\text{ m s}^{-1}$ & $T_R = 15\text{ s}$ from figure 4.23.

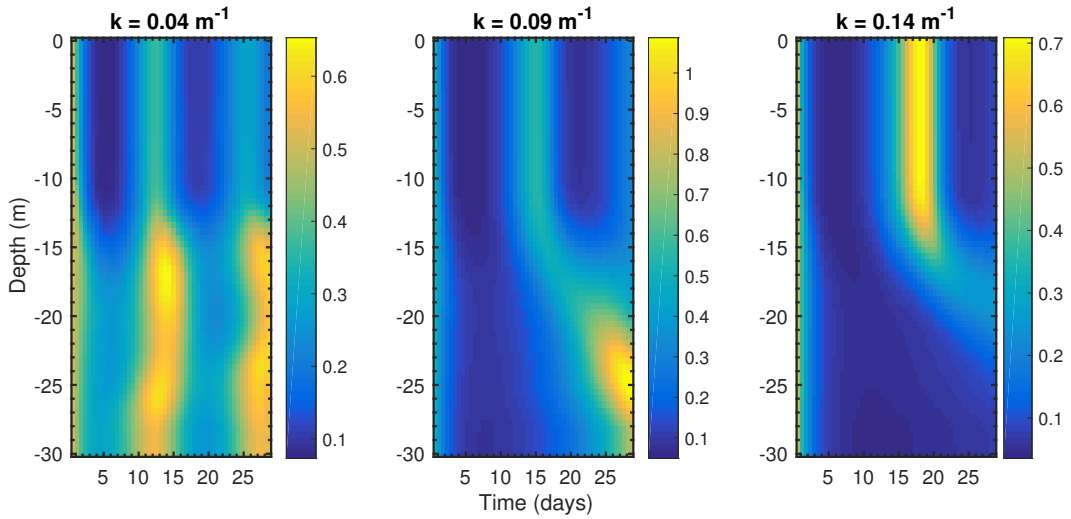

Figure 4.27: Evolution of P from full LES-NPZ model for three different values of k m^{-1}.

attenuation rates, $k = 0.09$ and 0.14 m^{-1}, are equivalent to $k_g(440) = 0.05$ and 0.1 m^{-1} respectively.

These results show a similar pattern to those seen in figures 4.25 and 4.26, wherein the increasing attenuation rates result in the depth of maximum phytoplankton growth moving towards the surface. The growth transitions from a deep chlorophyll maxima, for the lowest attenuation rate, to purely surface growth when $k = 0.14$ m^{-1}. What is interesting is that initially as k increases, the DBM stays much where it is, but its intensity falls. However, as k increases further there is a relocation of the DBM to the surface

The results from the LES-NPZ model with an increased attenuation rate are similar to those of the PZ-q model, the main difference being the effects of mixing. This means that for the highest attenuation rate, the maximal growth of the phytoplankton is spread throughout the well-mixed region, peaking close to the surface, rather than at a specific sub-surface depth.

4.6 Conclusions

The results presented in this chapter demonstrate the importance of light levels on the vertical structure of phytoplankton communities. The interactions between the modified growth rate term with the predation pressure gives some interesting results. In darker waters, the phytoplankton cannot take advantage of low predation pressure below the surface, since they are not able to obtain enough energy through light capture. The analysis of chapters 5 and 6 will highlight the significance of non-uniform predation pressure upon the vertical phytoplankton population structure, particularly for the formation of DBM. However these results show that this is not the full story.

The time evolution of $q(t)$ gives insight into how phytoplankton populations grow. During the phytoplankton growth stages of the cycle, energy is used up. As q decreases, the effective growth rate also declines, and the phytoplankton growth is restricted. This means that the

phytoplankton population will be lower than when the simple attenuation model (equation (4.2)) is used, where the growth rate would remain constant. As the zooplankton respond, and the phytoplankton population begins to decline, the energy stores are able to recover before the next cycle.

The differences in the results of the NPZ-q model and full LES-NPZ model (which incorporates a 'simple' model of light attenuation, as exponential decay) are subtle, and are mainly brought about by the turbulence. The added computational complexity of including the light capture integral, and q, into the LES-NPZ model outweighs the benefit that would be gained. As a consequence, the LES-NPZ will retain the simple Beer-Lambert-Bouguer attenuation model of light capture.

Despite this, the NPZ-q model is a powerful tool for fully understanding the biological interactions. In particular, the light capture integral takes into account a simple form of 'self-shading' and would be useful for modelling the interactions during seasonal blooms. The attenuation brought about by the bloom would radically reduce the availability of light in deeper regions of the boundary layer.

Chapter 5

Plankton predation in homogeneous isotropic turbulence

The predation model used in the full LES-NPZ model described in chapters 2 and 3 is, in simple terms, composed of two components and follows the work of Lewis and Pedley (2000, 2001). The two components comprise an encounter (or contact) rate, which estimates the number of prey particles a predator will "encounter" per unit time, and a capture probability, Combined together the encounter rate and capture probability give the predation rate for use in the LES-NPZ model. What is meant by an "encounter"? Each predator (zooplankton) is assumed to possess have some volume, or perception field, within which it can detect prey (phytoplankton). Figure 5.1 presents some schematics of typical perception fields. Many experimental results, such as Fields and Yen (1997), Bundy et al. (1998), have shown that the orientation of a copepod can influence its ability to detect predator and prey. In particular the results of Bundy et al. (1998) demonstrate that copepods appear to be more sensitive to disturbances in directions closely aligned to their antennae. For simplicity diagrams 5.1b and 5.1c, studied by Lewis (2003*b*), will be considered in most detail here. All prey entering the perception field are assumed to be detected and this is what defines an "encounter". A predator's encounter *rate* (assuming non-swimming prey) is a function of the predator swimming speed v_Z, perception field (given as a contact radius R_{cont}), sight angle α_{sight}, prey density ρ_{prey} and the state of the flow, measured by its turbulent intensity ε.

It is now important to define the probability of capture. Naturally if the prey detected by the predator remains within the perception field for enough time that the predator can react to its presence, then it is likely to be captured, and consumed. Zooplankton often initiate their own distinctive attack behaviours in order to boost their capture probabilities. For instance copepods can increase their capture abilities by generating feeding currents, e.g. Strickler (1982), Emlet (1985), Saiz and Kiørboe (1995), Fields and Yen (1997), Jiang et al. (1999), Malkiel et al. (2003). Another possibility is to employ ambush feeding, where they surprise their prey with fast "jump" attacks Saiz and Kiørboe (1995), Fenchel and Juel Hansen (2006), Kiørboe et al. (2009), Kiørboe (2011). The predation (or capture) rate is then a product of

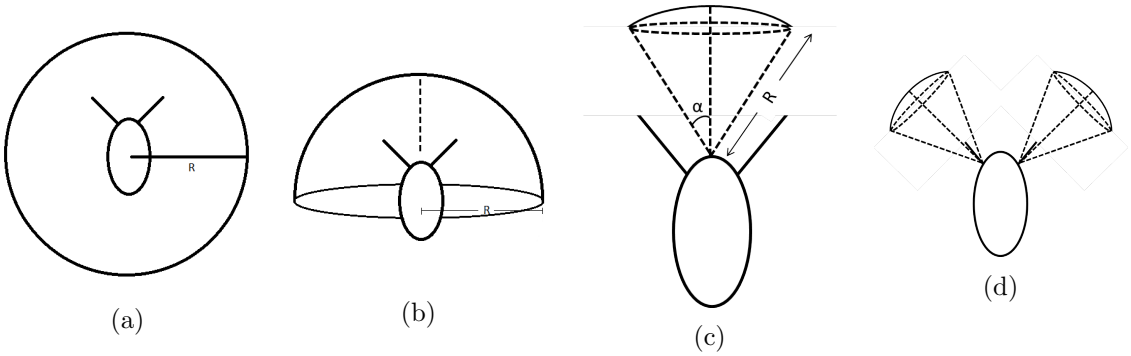

Figure 5.1: Schematic diagram of copepod perception fields. Swimming direction is assumed to lie along its body axis (i.e. upwards in these figures). (a) Spherical perception field of radius R, (b) hemispherical perception field of radius R perpendicular to swimming direction, (c) circular cone of semi-vertex angle α_{sight} perception field with radius R, (d) conical perception fields aligned with antennae, experimental results of Bundy et al. (1998) appear to correlate with this perception field. (a)–(c) will be considered in the model described by in this chapter. Line of sight is assumed to lie in the direction of its swimming motion.

the encounter rate and the probability of capture,

$$\text{Capture rate} = P(\text{capture}) \times \text{Encounter rate}(v_Z, \rho_{prey}, \alpha_{sight}, R_{cont}, \varepsilon). \tag{5.0.1}$$

The objective now is to try to make robust mathematical estimates of capture rates based on all the various parameters. Given all the uncertainties, particularly as the perception and capture events are taking place in a turbulent fluid environment, this is an extremely difficult task. Inevitably to make progress, a number of simplifying assumptions must be made. Sections 5.1–5.2 and 5.4 outline the models of Lewis and Pedley (2000) and Lewis and Pedley (2001) that are used to model planktonic encounter, and capture rates, respectively. Results of numerical experiments to test the ideas presented by Lewis and Pedley (2000), and Lewis and Pedley (2001), in sections 5.3, and 5.5, respecitvely. In each case the first set of results confirms the analysis and numerical experiments presented in these works, before a new investigation into the effect of restricting a predator's field on encounter and capture strategy, in particular swimming style.

5.1 Planktonic encounters

5.1.1 Formulation of the turbulent encounter rate

The importance of small-scale turbulence on planktonic encouter rates has long been established (MacKenzie and Leggett 1991, Sundby and Fossum 1990, Sundby et al. 1994, Saiz et al. 1992, Saiz and Kiørboe 1995, Pécseli et al. 2014). The first expression for the encounter rate between two species of mirco-organisms subject to small-scale turbulence was first postulated by Rothschild and Osborn (1988). Their model was based on the work of Gerritsen and Strickler (1977), who calculated the exact contact rate, CR_S, in still fluid be-

tween a single predator and its prey, swimming with constant speeds v_Z and v_P, respectively, in isotropically random orientations. Their result was

$$CR_S = \frac{\pi \rho_{prey} R_{cont}^2 (v_P^2 + 3v_Z^2)}{3v_Z} \quad ; \quad v_Z \geqslant v_P. \tag{5.1.1}$$

Here ρ_{prey} is the prey density (assumed to be uniform throughout this chapter), and R_{cont} is the contact radius for the spherical perception field of the predator. The derivation goes as follows. The number of phytoplankton prey expected to pass through a small area, defined in spherical coordinates by $\mathrm{d}\theta$ and $\mathrm{d}\phi$, on the surface of the perception sphere is given by

$$\frac{\rho_{prey}}{4\pi} \sin(\theta)\, \mathrm{d}\theta \mathrm{d}\phi. \tag{5.1.2}$$

Without loss of generality, the z-axis of the coordinate system can be directed along the direction of the zooplankton swimming, $\boldsymbol{v_Z}$. The prey therefore has a relative velocity

$$\boldsymbol{v_{PZ}} = \boldsymbol{v_Z} - \boldsymbol{v_P}, \tag{5.1.3}$$

with respect the predator. The relative speed is given by

$$v_{PZ} = \sqrt{v_P^2 + v_Z^2 - 2v_P v_Z \cos(\theta)}, \tag{5.1.4}$$

where θ is the orientation angle of the prey with respect to the predator. To enter the perception field during a time interval t, the prey must be initially in the cylindrical volume that is swept out by the predator's perception sphere, given by $v_{PZ}t \times \pi R_{cont}^2$. The number of prey entering the small area on the sphere per unit time is given by

$$\pi R_{cont}^2 v_{PZ} \frac{\rho_{prey}}{4\pi} \sin(\theta)\, \mathrm{d}\theta \mathrm{d}\phi. \tag{5.1.5}$$

Integrating over the surface area of the perception sphere gives the result (5.1.1).

Rothschild and Osborn (1988) attempted to adapt equation (5.1.1) to take account of the presence of turbulence. They began by estimating the turbulent velocity scale, w_{RO} as the difference between the (spatial) average of the square of the turbulent velocity $\boldsymbol{w}(\boldsymbol{x}, t)$ and its correlation with the velocity at position $\boldsymbol{x} + \boldsymbol{r}$,

$$w_{RO} = \langle \boldsymbol{w}^2(\boldsymbol{x}, t) \rangle - \langle \boldsymbol{w}(\boldsymbol{x}, t) \cdot \boldsymbol{w}(\boldsymbol{x} + \boldsymbol{r}, t) \rangle = \frac{3S_C}{2} \langle \varepsilon \rangle^{2/3} r^{2/3}. \tag{5.1.6}$$

Here S_C is the structure function constant which depends on the characteristics of the turbulent kinetic energy spectrum, and typically takes values $2 \leqslant S_C \leqslant 2.5$. Since spatial homogeneity is assumed, the property of spatial average is equivalent to the probability (or ensemble) average. Making the assumption that the swimming velocities are independent of the turbulent velocity, Rothschild and Osborn (1988) replaced v_P and v_Z with $\sqrt{v_P^2 + w_{RO}^2}$ and $\sqrt{v_Z^2 + w_{RO}^2}$, respectively. Substituting into equation (5.1.1) provides an estimate for

the turbulent encouter rate,

$$CR_T = \frac{\pi \rho_{prey} R_{cont}^2 \left(v_P^2 + 3v_Z^2 + 4w_{RO}^2\right)}{3\sqrt{v_P^2 + w_{RO}^2}} \quad ; \quad v_Z \geqslant v_P. \tag{5.1.7}$$

5.1.2 Lewis and Pedley (2000) model

Lewis and Pedley (2000) highlight a number of problems with this model. In particular, it is unclear what is meant by the distance r in equation (5.1.6). In order to account for this they presented a better formulation of the turbulent encounter rate problem. Consider the predator and prey, as before, to be swimming in turbulence at positions $\boldsymbol{x}$ and $\boldsymbol{x} + \boldsymbol{r}$ respectively, at time t. The total velocities of the predator and prey are given by

$$\boldsymbol{V_Z}(\boldsymbol{x}, t) = \boldsymbol{v_Z}(\boldsymbol{x}, t) + \boldsymbol{w}(\boldsymbol{x}, t) \tag{5.1.8}$$

and

$$\boldsymbol{V_P}(\boldsymbol{x} + \boldsymbol{r}, t) = \boldsymbol{v_P}(\boldsymbol{x} + \boldsymbol{r}, t) + \boldsymbol{w}(\boldsymbol{x} + \boldsymbol{r}, t) \tag{5.1.9}$$

respectively. Here $\boldsymbol{w}$ represents the turbulent velocity vector. For simplicity they began by assuming that the predator has a spherical field of perception (figure 5.1a). On planktonic micro-scales $\sim 10^{-3}$ m, the flow field is homogeneous and isotropic (Gargett et al. 1984). In what follows it will also be assumed to be statistically stationary. Generally the planktonic length scales, r_Z and r_P, are smaller than the Kolmogorov length scale (η_K from equation (2.2.1)), which means they can be considered to be point particles that do not influence the characteristics of the flow. Finally, it is assumed that the swimming velocities are uncorrelated with the turbulent flow, although in practice fluid may exert a viscous torque onto the cell body which in turn may influence the cell's orientation and motion (Pedley and Kessler 1992, Alqarni and Bearon 2016).

The formulation of the model presented by Lewis and Pedley (2000) is similar to that of Gerritsen and Strickler (1977). Consider a coordinate system moving with the prey such that the predator has relative speed

$$\boldsymbol{U} = \boldsymbol{V_Z} - \boldsymbol{V_P} \tag{5.1.10}$$

to the prey, directed (linearly) along the z-axis, as before. The number of prey crossing into the contact sphere, at points between χ & $\chi + \delta\chi$ and ϕ & $\phi + \delta\phi$, where $\chi = \theta/2$, per unit time is given by

$$\frac{R_{cont}^2}{2}\left(\sin^2(\chi + \delta\chi) - \sin^2(\chi)\right)\delta\phi\rho_{prey}U(\boldsymbol{R_{cont}})P(\boldsymbol{V_Z}, \boldsymbol{V_P}|R_{cont})\,\mathrm{d}\boldsymbol{V_Z}\mathrm{d}\boldsymbol{V_P}. \tag{5.1.11}$$

Here $P(\boldsymbol{V_Z}, \boldsymbol{V_P}|R_{cont})$ represents the conditional joint probability density function of the velocities of predator and prey at a distance R_{cont} apart, and $U(\boldsymbol{R_{cont}})$ is the relative speed between the predator and prey at the surface of the perception sphere. Integrating over the

velocity and angle variables gives the total contact rate for a single predator

$$CR_T = \frac{\rho_{prey} R_{cont}^2}{4} \int_{\boldsymbol{V_Z}} \int_{\boldsymbol{V_P}} \int_0^{\pi} \int_0^{2\pi} U(\boldsymbol{R_{cont}}) P(\boldsymbol{V_Z}, \boldsymbol{V_P} | R_{cont}) \sin(\theta)\, \mathrm{d}\phi \mathrm{d}\theta \mathrm{d}\boldsymbol{V_P} \mathrm{d}\boldsymbol{V_Z}, \quad (5.1.12)$$

where $\theta = 2\chi$. Lewis and Pedley (2000) then employed a change of variables into $\boldsymbol{U}$ and $\boldsymbol{V}$,

$$\boldsymbol{U}(\boldsymbol{x}, \boldsymbol{r}, t) = \boldsymbol{V_Z}(\boldsymbol{x}, t) - \boldsymbol{V_P}(\boldsymbol{x} + \boldsymbol{r}, t), \quad (5.1.13)$$

$$\boldsymbol{V}(\boldsymbol{x}, \boldsymbol{r}, t) = \frac{\sigma_Z^2 \boldsymbol{V_P}(\boldsymbol{x} + \boldsymbol{r}, t) + \sigma_P^2 \boldsymbol{V_Z}(\boldsymbol{x}, t)}{\sigma_Z^2 + \sigma_P^2}, \quad (5.1.14)$$

where σ_i^2 is the ensemble average variance of the predator and prey velocities. This puts equation (5.1.12) in the form

$$CR_T = \frac{\rho_{prey} R_{cont}^2}{4} \int_{\boldsymbol{V}} \int_{\boldsymbol{U}} \int_0^{\pi} \int_0^{2\pi} U(\boldsymbol{R_{cont}}) P(\boldsymbol{U}, \boldsymbol{V} | R_{cont}) \sin(\theta)\, \mathrm{d}\phi \mathrm{d}\theta \mathrm{d}\boldsymbol{U} \mathrm{d}\boldsymbol{V}, \quad (5.1.15)$$

where $P(\boldsymbol{U}, \boldsymbol{V} | R_{cont})$ is the conditional joint distribution for $\boldsymbol{U}$ and $\boldsymbol{V}$ at vector separation $\boldsymbol{R_{cont}}$. Since $\boldsymbol{U}$ now appears explicitly in $P(\boldsymbol{U}, \boldsymbol{V} | R_{cont})$ this integral is somewhat easier to evaluate than equation (5.1.12).

5.1.3 Gaussian swimming

Equations (5.1.1) and (5.1.7) were formulated for microorganisms whose swimming velocities were constant, i.e. the swimming speed for all predators is v_Z. One simple improvement is to assume that instead the swimming velocities $\boldsymbol{v_Z}$ and $\boldsymbol{v_P}$ follow three-dimensional isotropic Gaussian distributions with zero means and standard deviations σ_Z and σ_P respectively. This is called Gaussian swimming, and this will be assumed in this work. Appendix A of Lewis and Pedley (2000) shows that in this case, equation (5.1.15) reduces to

$$CR_T = 4\rho_{prey} R_{cont}^2 \sqrt{\frac{\pi}{2}}\, \sigma_U(R_{cont}), \quad (5.1.16)$$

assuming a plausible functional form for $P(\boldsymbol{U}, \boldsymbol{V} | R_{cont})$, and that neither predator nor prey make any changes of direction. The problem now is to determine σ_U, the ensemble-average variance for $\boldsymbol{U}$, as a function of R_{cont}. This is defined by

$$\begin{aligned} \sigma_U^2(R_{cont}) &= \frac{\langle \boldsymbol{U} \cdot \boldsymbol{U} \rangle - \langle \boldsymbol{U} \rangle \cdot \langle \boldsymbol{U} \rangle}{3} \\ &= 2W^2 - \frac{2}{3} \langle \boldsymbol{w}(\boldsymbol{x}, t) \cdot \boldsymbol{w}(\boldsymbol{x} + \boldsymbol{R_{cont}}, t) \rangle + \frac{\langle \boldsymbol{v_P} \cdot \boldsymbol{v_P} \rangle}{3} + \frac{\langle \boldsymbol{v_Z} \cdot \boldsymbol{v_Z} \rangle}{3} - \frac{2 \langle \boldsymbol{v_P} \cdot \boldsymbol{v_Z} \rangle}{3}. \end{aligned} \quad (5.1.17)$$

For homogeneous, isotropic turbulence, the measure of turbulent intensity, $W^2 = \langle \boldsymbol{w}(\boldsymbol{x},t) \cdot \boldsymbol{w}(\boldsymbol{x},t) \rangle$ and the turbulent velocity correlation term, can be written as

$$2W^2 - \frac{2}{3}\langle \boldsymbol{w}(\boldsymbol{x},t) \cdot \boldsymbol{w}(\boldsymbol{x}+\boldsymbol{R_{cont}},t) \rangle = \frac{4}{3}\int_0^\infty E(k,t)\left(1 - \frac{\sin(kR_{cont})}{kR_{cont}}\right) \mathrm{d}k, \tag{5.1.18}$$

where k and $E(k,t)$ are the wavenumber and turbulent energy spectrum, see section 2.2.

Assuming that $R_{cont} \gg \eta_K$ (the contact radii considered here are $O(10^{-2}$ m), compared with $\eta_K = O(10^{-3})$ m, see table 5.1), and that the energy spectrum outside the inertial subrange makes little contribution to equation (5.1.18) then the well-known 5/3-rule of Kolmogorov (1941) (see equation (2.2.33)) can be used to find an approximation for equation (5.1.18). Assuming Gaussian swimming as described above and $\langle \boldsymbol{v_P} \cdot \boldsymbol{v_Z} \rangle = 0$ then

$$\sigma_U^2(R_{cont}) \approx \langle \varepsilon \rangle^{2/3} R_{cont}^{2/3}\left[S_C - \frac{3\eta_K^{2/3}}{R_{cont}^{2/3}} + 2\int_{R_{cont}/\eta_K}^\infty \frac{\sin(x)}{x^{8/3}}\,\mathrm{d}x\right] + \sigma_P^2 + \sigma_Z^2 = w_T^2 + \sigma_P^2 + \sigma_Z^2. \tag{5.1.19}$$

The Lewis and Pedley (2000) straight line turbulent contact rate is given by

$$CR_T = \pi \rho_{prey} R_{cont}^2 \left[\frac{8}{\pi} w_T^2 + v_P^2 + v_Z^2\right]^{1/2}, \tag{5.1.20}$$

where w_T is the turbulent velocity scale and $v_{P,Z} = \sqrt{8/\pi}\,\sigma_{P,Z}$.

5.1.4 Encounter rates incorporating changes of direction

Equation (5.1.20) gives an approximation for the encounter rate assuming the predators move in straight lines. In practice this is not the case and (5.1.20) actually overestimates the true value. It is important to consider why this is the case. The modelling ideas formulated above implicitly assume that as it swims through the flow, the predator "sweeps" out a search volume. For a straight line swimmer with speed $\langle U(R_{cont}) \rangle$ moving for a time T, this search volume is a cylinder of radius R_{cont} and height $\langle U(R_{cont}) \rangle T$. This volume is directly proportional to the number of contacts per unit time given by equation (5.1.17). Notice that in this case the predator never revisits part of the water column it has passed through before.

Now consider a predator that after some time $\tau < T$, changes its velocity and begins moving in a different direction. It is assumed that this has no effect on the ensemble average speeds and that $\langle U(R_{cont}) \rangle$ remains constant over al T. As the predator turns, some of the volume searched (mapped out) previously will be revisited. This small volume (Lewis and Pedley (2000) call it the "overlap volume") will be in the same state as before the turn (containing much the same number of prey encountered previously). This means that the contact rate is no longer proportional to the volume mapped out, in fact the number of contacts in time T wiill be less than $\pi \rho_{prey} R_{cont}^2 U(R_{cont}) T$. Removing the overlap volume gives a reduced overall volume, and the number of contacts is also reduced in proportion. To account for this Lewis and Pedley (2000) introduced a measure called the volume fraction,

f_V, which is defined as the ratio between the reduced volume and the straight-line volume, and for spherical perception fields $0 \leqslant f_V \leqslant 1$. The contact rate is then given by

$$CR_T = 4\rho_{prey} R_{cont}^2 \sqrt{\frac{\pi}{2}}\, \sigma_U(R_{cont}) \times f_V(U(R_{cont}), R_{cont}, n, \tau), \tag{5.1.21}$$

where n is the number of turns made during the simulation, i.e. $T = (n+1)\tau$. Assuming that the angle through which the predator turns, α_{sight}, is uniformly distributed on $[0, \pi]$, and the changes in direction are relatively infrequent so that $\tau > 2R_{cont}/U(R_{cont})$, then the average volume fraction can be estimated by

$$\langle f_V(U(R_{cont}), R_{cont}, n, \tau)\rangle = \frac{(n+1)[\pi R_{cont}^2 \langle U(R_{cont})\rangle \tau + 4\pi R_{cont}^2/3] - n\langle \text{overlap volume}\rangle}{(n+1)[\pi R_{cont}^2 \langle U(R_{cont})\rangle \tau + 4\pi R_{cont}^2/3]}. \tag{5.1.22}$$

In this case the volume overlapped can be calculated analytically for any $\alpha_{sight} \in [0, \pi]$ and averaged to give $\langle$overlap volume$\rangle$. If direction changes are relatively frequent, $\tau < 2R_{cont}/\langle U(R_{cont})\rangle$, i.e. the time the predator takes to move the length of its perception sphere, the predator is much more likely to revisit regions it has already passed through. This situation is much more complicated and cannot be calculated using equation (5.1.22). Instead Lewis and Pedley (2000) adopted a Monte Carlo technique to estimate $\langle f_V \rangle$. It will be assumed in this work that $\tau > 2R_{cont}/\langle U(R_{cont})\rangle$. All that remains is to find values for τ, which can be readily found in film studies (e.g. Bundy et al. (1998)).

5.1.5 Encounter rates for predators with a restricted perception field Lewis (2003*b*)

Up to this point it has been assumed that the predator has a spherical perception field, such as in figure 5.1a. However, the experimental results of Fields and Yen (1997), Bundy et al. (1998) indicate that this is highly unrealistic. In fact, particular copepods are far more sensitive to the presence of a predator, or prey, at certain orientations than others. Specifically, copepods are very sensitive to movements in the regions closely aligned with the direction of their antennae, akin to figure 5.1d. Such a restricted perception field means the encounter rate must also be far smaller than the estimates produced so far. A perception field like figure 5.1d will be too complicated to model here. So instead Lewis (2003*b*) assumed that the predator has a conical perception field of the form 5.1c, defined by contact radius R_{cont} and semi-vertex angle $\alpha_{sight} \in [0, \pi/2]$.

Hemispherical perception field

The simplest case is when $\alpha_{sight} = \pi/2$, which means the perception field is hemispherical (figure 5.1b). This is a good example to look at because it brings out the conceptual difficulties associated with estimating the encounter rate, without the very complicated mathematical

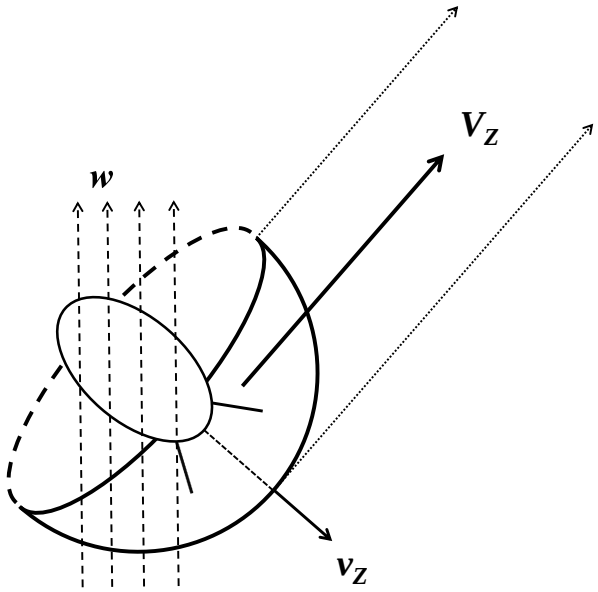

Figure 5.2: Schematic of a predator moving through a flow with velocity $\boldsymbol{V_Z}$, since the swimming direction $\boldsymbol{v_Z}$ is not aligned with the flow $\boldsymbol{w}$ the predator is not in an optimal orientation.

formulations necessary for $\alpha_{sight} < \pi/2$. Consider, as before, a coordinate system moving with the prey so that the predator has relative speed U (defined by equation (5.1.13)) directed along the z-axis. The predator's line of sight (i.e. its preferred swimming direction) lies, without loss of generality, in the y-z-plane at an angle γ to the z-axis. It is important to note that the swimming direction, $\boldsymbol{v_Z}$, is not the direction of motion ,$\boldsymbol{V_Z}$, which is determined by a combination of the swimming and turbulent velocities, $\boldsymbol{w}$, see figure 5.2. There are two cases to consider, $\gamma \leqslant \pi/2$ and $\gamma > \pi/2$, see figure 5.3. In the latter case, shown in figure 5.3b the "underside" of the predator's perception field is the leading edge. This means that encounters can now occur at distances $r < R_{cont}$ on the base of the hemisphere. Such encounters are defined as "close-encounters". These close-encounters occur because the predator no longer has all-round visibility. In both cases the predator can miss prey that pass in the predator's blind-side at distances $r < R_{cont}$.

For $\gamma \leqslant \pi/2$ as shown in figure 5.3a, the number of prey that pass into the predator's perception field per unit time is given by the projected surface area (or cross-sectional area) onto the x-y-plane. All encounters will occur at distance R_{cont}, if the contact occurs when $y < 0$ then the projected area is a semicircle or radius R_{cont}, for $y > 0$ it is half the ellipse $x^2 + y^2/\cos^2(\gamma) = R_{cont}^2$. The contact rate is then

$$\rho_{prey}\frac{\pi R_{cont}^2}{2}\int_{\boldsymbol{U}}\int_{\boldsymbol{V}}(1+\cos(\gamma))U(R_{cont})P(\boldsymbol{U},\boldsymbol{V}|R_{cont})\,\mathrm{d}\boldsymbol{U}\mathrm{d}\boldsymbol{V}\ \ ;\ \ \gamma \leqslant \pi/2, \tag{5.1.23}$$

where U and V are defined by equations (5.1.13) and (5.1.14), respectively.

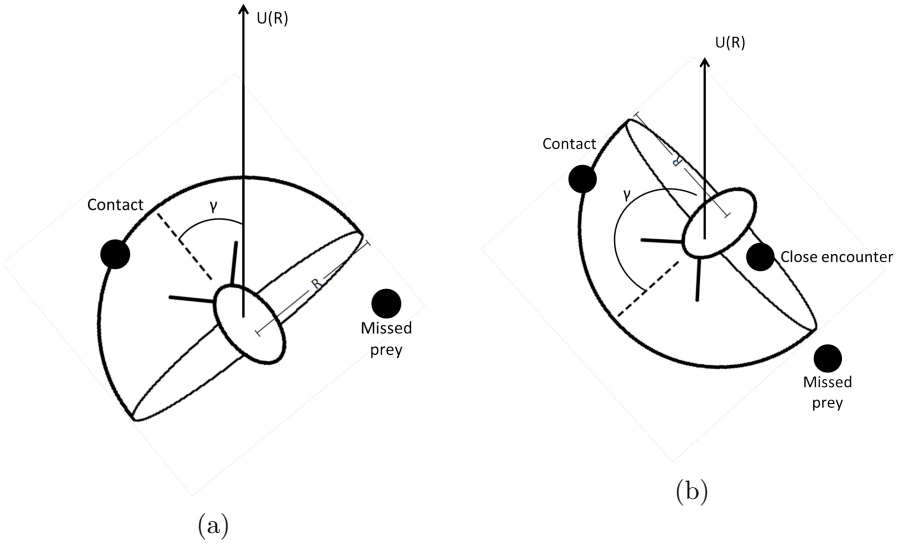

Figure 5.3: Schematic of types of encounters for a hemispherical perception field moving with relative velocity $\boldsymbol{U}$. (a) $\gamma < \pi/2$, (b) $\gamma > \pi/2$.

For the case of $\gamma > \pi/2$, the number of encounters at R_{cont} (standard encounters) is given by the small surface area of the curved hemisphere for $y < 0$. This is given by the area of the semicircle - area of half the ellipse $x^2 + y^2/\cos^2(\gamma) = R_{cont}^2$, which is $\pi R_{cont}^2(1 + \cos(\gamma))$ as before ($\cos(\gamma) < 0$ for $\gamma > \pi/2$). Close-encounters (at distance $r < R_{cont}$) occur when prey enter the area bounded by the ellipse $x^2 + y^2/\cos^2(\gamma) = R_{cont}^2$. For close encounters the relative velocity at $r < R_{cont}$ must also be included. Hence the total contact rate for this case is given by

$$\rho_{prey}\frac{\pi R_{cont}^2}{2}\int_{\boldsymbol{U}}\int_{\boldsymbol{V}}(1+\cos(\gamma))U(R_{cont})P(\boldsymbol{U},\boldsymbol{V}|R_{cont})\,\mathrm{d}\boldsymbol{U}\mathrm{d}\boldsymbol{V} + 2\pi\rho_{prey}\int_0^{R_{cont}}\int_{\boldsymbol{U}}\int_{\boldsymbol{V}}(-\cos(\gamma)r)U(r)P(\boldsymbol{U},\boldsymbol{V}|r)\,\mathrm{d}\boldsymbol{U}\mathrm{d}\boldsymbol{V}\mathrm{d}r \;\;;\;\; \pi/2 < \gamma < \pi. \quad (5.1.24)$$

For a predator with a conical perception zone, with $\alpha_{sight} < \pi/2$ the situation is more complex, the concepts are similar but there are a number of possible combinations of α_{sight} and γ that need to be considered. Lewis (2003*b*) presents the full contact rate for such a predator in appendix A of that work. The resulting integrals can be evaluated numerically for a suitable functional form of $P(\boldsymbol{U},\boldsymbol{V}|R_{cont})$ and $P(\boldsymbol{U},\boldsymbol{V}|r)$. Results of this kind of analysis form the basis of the ($T_R = 0$) predictions in tables 5.2–5.7

5.2 Numerical experiments

5.2.1 Kinematic simulations

Kinematic simulation is a technique for generating turbulent-like flows using a large number of Fourier nodes which vary randomly in time and space. It is advantageous since it removes the need to solve the full Navier-Stokes equations, and so the flow field can be gener-

ated much more rapidly. For modelling aspects of turbulence on small homogeneous scales, it is a very useful technique. The method was first developed by Kraichnan (1970) and modified by Drummond et al. (1984), Fung et al. (1992), Malik and Vassilicos (1999). It has been used for a variety of purposes, including turbulent dispersion (Thomson and Devenish 2005), to study the orientation of gyrotactic micro-organisms (Lewis 2003*a*), and the motion of bubbles (Spelt and Biesheuvel 1997) & fibres (Olson 2001) in homogeneous isotropic turbulence. Kinematic simulations are a standard means for studying the effects of turbulence on oceanic microorganisms, and have been previously used by Lewis and Pedley (2000, 2001), Lewis (2003*b*), Lewis and Bala (2006, 2008) to study encounter and capture rates in homogeneous isotropic turbulent flows. They have also been used by Visser and Jackson (2004) to examine the dispersion of chemical trails laid by copepods.

The methodology is as follows. The velocity field is represented by a superposition of N_K Fourier modes,

$$\boldsymbol{w}(\boldsymbol{x},t) = \sum_{n=1}^{N_K} [(\boldsymbol{a}^{(n)} \times \hat{\boldsymbol{k}}^{(n)}) \cos(\boldsymbol{k}^{(n)} \cdot \boldsymbol{x} + \omega^{(n)} t) + (\boldsymbol{b}^{(n)} \times \hat{\boldsymbol{k}}^{(n)}) \sin(\boldsymbol{k}^{(n)} \cdot \boldsymbol{x} + \omega^{(n)} t)]. \quad (5.2.1)$$

Here $\boldsymbol{k}^{(n)} = k^{(n)} \hat{\boldsymbol{k}}^{(n)}$ represent wave vectors (a measure of the reciprocal of the eddy length scales) and $\omega^{(n)}$ are the frequency modes, both of which depend upon the prescribed turbulent kinetic energy spectrum $E(k)$. The directions of unit wave vectors, $\hat{\boldsymbol{k}}^{(n)}$, are independent of the direction of the other wave modes. The random vectors $\boldsymbol{a}^{(n)}$ and $\boldsymbol{b}^{(n)}$ can be chosen to construct a simulated flow field which satisfies many of the kinematic properties of a real velocity field derived from the Navier-Stokes equations (2.1.12). So for example the vectors $\boldsymbol{a}^{(n)}$ and $\boldsymbol{b}^{(n)}$ are constrained by the requirement that they must be normal to $\hat{\boldsymbol{k}}^{(n)}$ to guarantee that the flow is incompressible. The magnitudes of $\boldsymbol{a}^{(n)}$ and $\boldsymbol{b}^{(n)}$ are equal and are prescribed to satisfy

$$\sum_{n=1}^{N_K} \left|\boldsymbol{a}^{(n)}\right|^2 = \sum_{n=1}^{N_K} \left|\boldsymbol{b}^{(n)}\right|^2 = \langle \boldsymbol{w}(\boldsymbol{x},t) \cdot \boldsymbol{w}(\boldsymbol{x},t) \rangle = 2 \int_0^\infty E(k) \mathrm{d}k. \quad (5.2.2)$$

In principle any suitable spectrum can be substituted into equation (5.2.2). The most pertinent here is one that models the inertial subrange correctly, since the contact radius, R_{cont}, lies in the length scales covered by that part of the spectrum. So in this work the spectrum function used is given by

$$E(k) = \begin{cases} 0, & k \in \left[0, \dfrac{\alpha}{L_e}\right] \\ \dfrac{3}{2}\beta \langle \varepsilon \rangle^{2/3} k^{-5/3}, & k \in \left[\dfrac{\alpha}{L_e}, \dfrac{1}{\eta_K}\right] \\ 0, & k > \dfrac{1}{\eta_K}, \end{cases} \quad (5.2.3)$$

where $\alpha = (3/2)^{3/2}$ and $\beta = [1 - 1.5(\eta_K/L_e)^{2/3}]^{-1}$. In the inertial subrange, the eddy turnover

time is proportional to $k^{2/3}$ (Leslie 1973). The frequency modes should therefore be chosen to satisfy

$$\omega^{(n)} = \gamma\sqrt{(k^{(n)})^3 E(k^{(n)})}\,, \tag{5.2.4}$$

where $\gamma = 0.4$. This choice of parameters is the same as in Lewis and Pedley (2000) and produces a flow whose Lagrangian statistics closely matched some direct numerical simulation data (Malik and Vassilicos 1999).

This method is suitable for this problem since it only requires knowledge of two-point velocity correlations over small scales. Many of the typical drawbacks of kinematic simulations, in particular the absence of an energy cascade described by section 2.2, should not influence the number of contacts significantly. The main benefit is the considerable reduction in computing time in comparison to direct numerical simulations (DNS).

5.2.2 A typical simulation set-up for calculating contact rates

A number of simulations were set-up using the flow fields generated by equations (5.2.1) and (5.2.3) over large cubic domain (box) sizes. Each set of simulations comprised 10 runs, each using a unique flow field based around a fixed ε value. The simulations consisted of tracking planktonic particles with a prescribed swimming velocity over a simulation time of $T = 400$ s. Particle trajectories were calculated by integrating

$$\frac{\mathrm{d}\boldsymbol{X}_{Z,P}(t)}{\mathrm{d}t} = \boldsymbol{w}\left[\boldsymbol{X}_{Z,P}(t), t\right] + \boldsymbol{v}_{Z,P}(t), \tag{5.2.5}$$

using a fourth-order Runge-Kutta method, with a time-step of $0.02\tau_K$. All the calculations were non-dimensionalised using the Kolmogorov scales, assuming $\nu = 10^{-6}$ m^2 s^{-1}. This means that the time-step decreases with ε in order to maintain accuracy with increased turbulent intensity. Each simulation used $N_K = 64$ wavenumber modes, except for the case of $\varepsilon = 5.53 \times 10^{-7}$ m^2 s^{-3}, when it was increased to $N_K = 96$ modes. When a designated prey particle moves to lie within a predator's perception field a "contact/encounter" is recorded. The number of such encounters over a fixed time interval gives the encounter rate.

Unlike DNS, or the full LES-NPZ model, it is not easy to impose periodic boundary conditions over a cubic domain in a kinematic simulation. For instance, if a predator or prey is advected outside the simulation domain, by crossing the boundary, it cannot simply be moved to the opposite boundary, since it could lead to erroneous contacts brought about by the boundary conditions. To counter this, any predators, or prey, that cross the boundary are relocated within the simulation domain away from any potential contacts. This means that all contacts are genuine, i.e. brought about by the flow. However, this procedure may still bias the number of contacts. In order to avoid this each simulation was repeated 6 times over increasingly large domains, whilst maintaining prey density. A simple, linear, least-squares fit was applied to the data to obtain the expected contact rate over an idealised infinite domain in which no re-locations would be necessary. Figure 5.4 demonstrates this procedure.

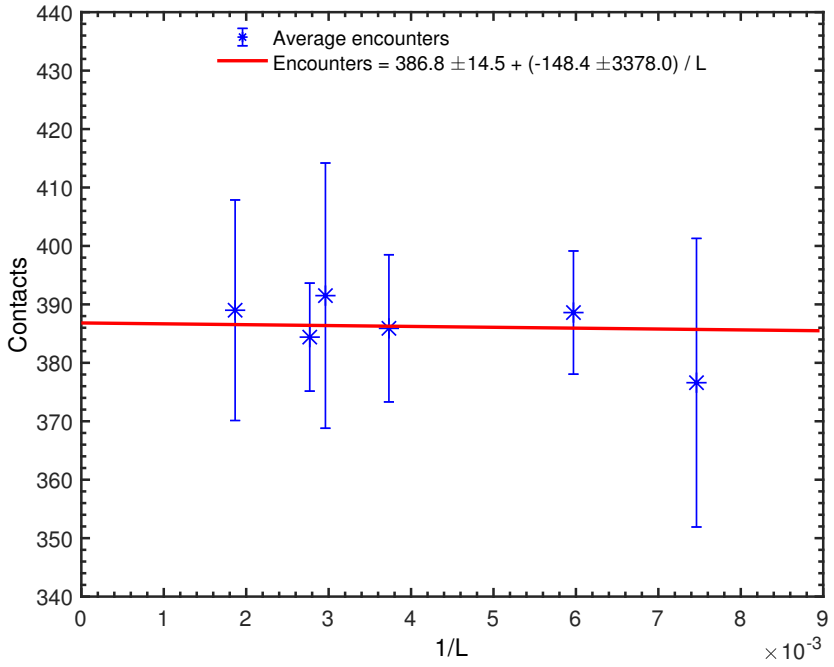

Figure 5.4: Example of simulation results demonstrating the linear fit to obtain the number of contacts in an infinite domain. $1/L$ is the inverse of the non-dimensionalised domain size. The solid line is the linear regression best fit..

Note that the x-axis represents the inverse of the domain length scale, normalised by the Kolmogorov length scale η_K.

5.2.3 Speeding up the counting of contacts

After each time step the number of new predator-prey encounters must be recorded. In principle this means checking every predator with every prey, an $N_Z \times N_P$ operational process. This is very slow and long-winded. Since each time step is small it is only necessary to check the relative positions of predator and prey in close vicinity on the previous step. To this end the large simulation domain is split into much smaller cells of size R_{cont}. At each time step each cell is checked for the presence of predator and/or prey. Cells containing a predator

Variable	Values
Zooplankton swimming speed S.D., σ_Z	2.726×10^{-4}, 5.452×10^{-4}, 8.178×10^{-4} m s^{-1}
Zooplankton contact radius, R_{cont}	1.173×10^{-2} m
Zooplankton sight angle, α_{sight}	$\frac{\pi}{12}$, $\frac{\pi}{6}$, $\frac{\pi}{4}$, $\frac{\pi}{3}$, $\frac{5\pi}{12}$, $\frac{\pi}{2}$ radians
Zooplankton change of direction time, τ_{sight}	2.7–400 s
Number of zooplankton particles, N_Z	512
Phytoplankton swimming speed S.D., σ_P	0 m s^{-1}
Phytoplankton density, ρ_{prey}	4.3154×10^3 cells m^{-3}
TKE dissipation rate, ε	2.27×10^{-9} – 5.53×10^{-7} m^2 s^{-3}
Kinematic viscosity, ν	10^{-6} m^2 s^{-1}

Table 5.1: Key biological and physical parameters for the kinematic simulations.

or prey are then noted. After all cells are checked, each of the cells containing a predator will be analysed. In this second stage, only a predator's own cell and its nine neighbouring cells are checked for the presence of prey. Distances and relative orientations between any such predator and prey in close proximity are calculated to determine whether the prey lies within the predator's perception field. If a contact has occurred, the encounter is counted and the prey is then removed from the simulation and repositioned away from any predators, in order to maintain the prey density and ensure that all contacts are brought about by the combination of the flow and/or the predator's swimming. The main benefit of this process is that it avoids the need to check each predator and prey individually to determine if a contact has occurred and drastically reduces the required computer time.

The contact rate can then be calculated from the number of contacts by

$$CR_{sim} = \frac{\text{Contacts} \times N_P}{T \times \text{Volume} \times N_Z} = \frac{\text{Contacts}}{400 \times 4.3154 \times 10^3 \times 512}. \tag{5.2.6}$$

5.3 Kinematic simulations of planktonic encounters and prediction results

This section will analyse the results of the kinematic simulations described in section 5.2.1 and compare with predicted encounter rate ($T_R = 0$) results presented in tables 5.2–5.7. These results will be used to help understand how the different variables influence the best possible encounter strategy for the predator in each scenario.

5.3.1 Turbulent intensity

The first set of simulations was designed to demonstrate the enhancement effect of small-scale turbulence on the encounter rate (equation (5.1.17)). Lewis and Pedley (2000) compared theoretical results to the still contact rate of Gerritsen and Strickler (1977). In these simulations the zooplankton predator, which had a hemispherical perception field of radius $R_{cont} = 1.173 \times 10^{-2}$ m, was subject to four levels of turbulence. The results are shown in figure 5.5 for three different zooplankton swimming speeds (table 5.1). For each of the three swimming speeds, the encounter rate is enhanced with increasing turbulent intensity. In particular consider the weak $\varepsilon = 5.53 \times 10^{-9}$ m^2 s^{-3}, and moderate $\varepsilon = 5.53 \times 10^{-8}$ m^2 s^{-3} results. These would correspond to levels in the thermocline and in the middle of the mixed layer respectively. Increasing the turbulent intensity has the effect of increasing the relative swimming speed of the predator, as can be seen by comparing the $U(R_{cont})$ results from tables 5.2 and 5.3. In the case of moderate turbulence ,$U(R_{cont})$ is higher than the corresponding weak turbulent case, which results in a larger volume swept out by the predator, and hence an increased contact rate. Consider in particular the swimming speed $\sigma_Z = 5.452 \times 10^{-4}$ m s^{-1} (central column of data points in figure 5.5). In each of these cases, the predicted contact rates (which are for $\sigma_Z = 5.0 \times 10^{-4}$ m s^{-1} from tables 5.2 & 5.3) provide a very good approxi-

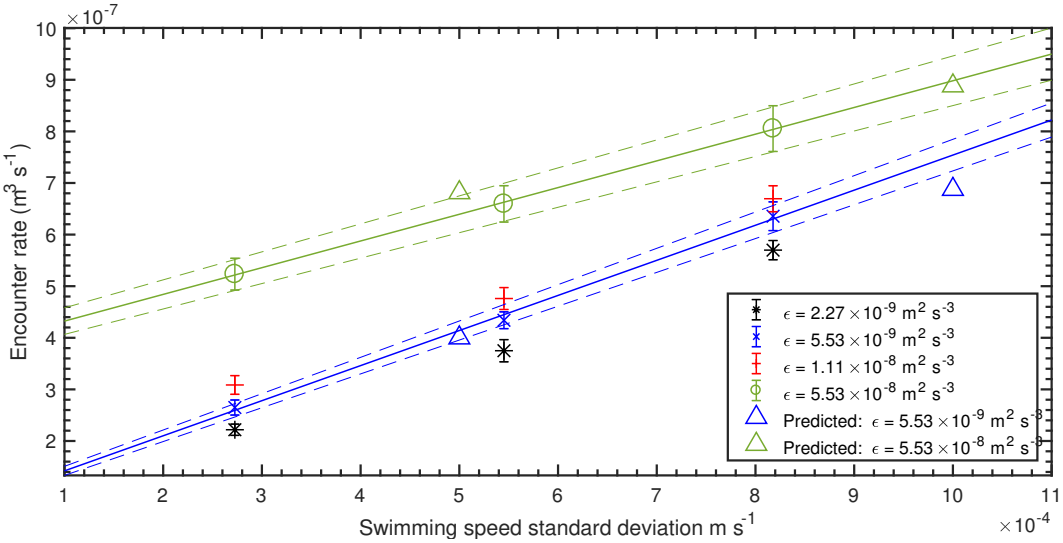

Figure 5.5: Encounter rate for predators with different swimming speed standard deviations, σ_Z in different simulated turbulent environments. Each predator is a straight line swimmer with a hemispherical contact volume ($\alpha_{sight} = 90°$) with radius, $R_{cont} = 1.173 \times 10^{-2}$ m. The predicted results are found using equations (5.1.23) & (5.1.24), and the values are shown in tables 5.2 and 5.3. Lines for the $\varepsilon = 5.53 \times 10^{-9}$ m^2 s^{-3} and $\varepsilon = 5.53 \times 10^{-8}$ m^2 s^{-3} indicated best fit to the results (solid) and bounds (dashed).

mation to the simulation result. The predicted results lie within, or are very close to, the best linear fit regions for the simulated results (including the error bounds). This demonstrates the predictive capability of the analysis surrounding equations (5.1.23) & (5.1.24).

5.3.2 Swimming speed

The simulation results shown in figure 5.5 also show how the encounter rate is influenced by the swimming speed. For all four turbulent intensities, it is clear that increasing the swimming speed increases the encounter rate. Higher values of σ_Z increase the relative swimming speed $U(R_{cont})$, as can be seen in table 5.2, which, much as before, increases the volume searched by the predator. Consider in particular the cases of weak $\varepsilon = 5.53 \times 10^{-9}$ m^2 s^{-3}, and moderate $\varepsilon = 5.53 \times 10^{-8}$ m^2 s^{-3} turbulence, indicated by the blue and green data respectively. A linear fit has been applied to each of these results, highlighting the trend of increasing encounters with swimming speed. As expected, the simulation results show that predators with a higher swimming speed will encounter more prey. The predicted results, detailed in tables 5.2–5.4 also show the same trend.

5.3.3 Sight angle

As discussed previously, copepods are often much more sensitive to prey located at specific orientations. Figure 5.6 shows the results of various sets of simulations in which the shape of predator's perception field was conical, characterised by different α_{sight} values (figure 5.1c). Consider the straight line swimmers first (black data points). In each of the turbulent environments, increasing the cone angle results in a higher encounter rate. This is expected

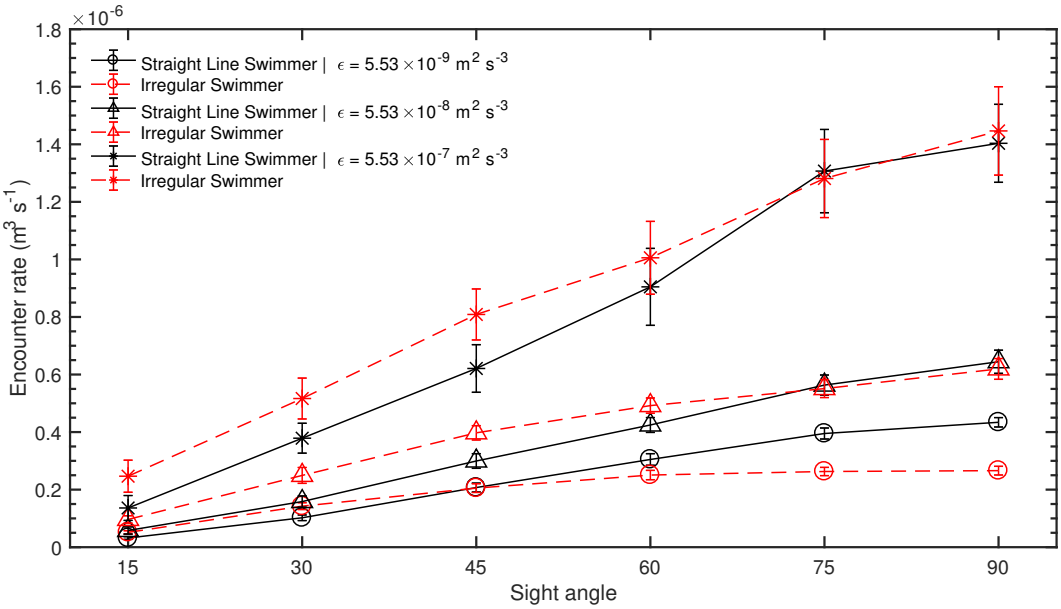

Figure 5.6: Encounter rate for predators with different sight angles in different simulated turbulent environments. Swimming speed, $\sigma_Z = 5.452 \times 10^{-4}$ m s^{-1}, contact radius, $R_{cont} = 1.173 \times 10^{-2}$ m. Irregular swimmer changes direction randomly every 2.7 s. Total simulation time is 400 s.

since a large cone angle means a larger perception volume, and hence a larger volume mapped out when swimming through the flow.

What is interesting, however, is that for cone angles of $< 60°$ the optimal encounter strategy changes. The red data points indicate the encounter rate for a predator which changes direction every 2.7 s. Since the predator's line of sight is not necessarily in the direction of $\boldsymbol{U}$, see figure 5.2, a straight-line swimmer may not be moving in an optimal orientation. A predator that changes direction regularly may be in a more optimal orientation for more of the time than its straight-line swimming equivalent. This becomes more acute for a predator with a cone angle $< 60°$. The cross section of the perception field perpendicular to the direction of travel will be larger in some orientations than others. If direction changes are sufficiently rapid this can have the effect of increasing the volume mapped out by the predator. Consequently, a predator with $\alpha_{sight} < \pi/2$ can enhance its volume fraction, $\langle f_V \rangle$, to a value greater than one. This explains why copepods typically follow very irregular, non-linear trajectories. By doing so they enhance their search volume and encounter rate. But they must swim relatively slowly compared to the flow for this encounter enhancement strategy to have its full effect (Lewis 2003*b*). They must also allow time for the flow to advect prey into their enhanced search volume. For example the optimal orientation for a predator with a hemispherical perception field is in its swimming direction $\boldsymbol{v_Z}$. For a predator with a conical perception field the optimal orientation is perpendicular to $\boldsymbol{v_Z}$ if the cone angle $\alpha_{sight} > \pi \sin^2(\alpha_{sight})$ (approximately 20°). However the optimal orientation may be somewhere between these two orientations.

5.3.4 Swimming style

Figure 5.7 shows the trajectories of some of the predators for each of the two swimming strategies in a weakly turbulent environment. The first case (figure 5.7a) shows the trajectories of the cells within the simulated domain. Two simulations were used to generate this figure. The predators in the first simulation were straight line swimmers (blue trajectories), the predators in the second simulation changed their swimming direction every 2.7 s (red trajectories). Each predator's initial position was the same between the two simulations. The blue paths, representing the straight line swimmer, are noticeably smoother, the only direction change is the external force of the flow, although this is weak in this case. The details of the individual paths can be seen more clearly in figure 5.7b, which shows the swimming trajectories relative to their initial position.

The problem is then to determine the optimal swimming strategy for a given sight angle. Figures 5.8a and 5.8b show how the encounter rate changes for different change of direction times, τ, for a predator with sight angles 30° and 60°, respectively. Consider first figure 5.8a. In this instance the predator encounters more prey more frequently if it changes direction rapidly. However, it is unrealistic for predators to change direction too frequently. Osborn et al. (1990) argue that copepods cannot typically reorient themselves in as short a time period as 0.27 s. In order to keep the predator from re-mapping areas it has previously searched, the minimum value of τ was chosen to be 2.7 s, following Yamazaki et al. (1991).

The relative advantage gained from regular orientation changes increases with turbulent intensity. As the speed of the flow increases, $\boldsymbol{w_T}$ becomes more dominant in the cell's motion. For a straight line swimmer this could mean that the cell is not in an optimal orientation for the entire simulation, for example in the case demonstrated in figure 5.2. However, if the cell can re-orient itself regularly it may be better orientated for longer periods. This can be seen in figure 5.8b for the 30° cone angle. In the more turbulent case (red data points) the best strategy is to make regular changes of direction, whereas in the weak turbulence (black data points) case it is better for the predator to swim in a straight line. The flow speed here is much slower ($W = \sqrt{\langle\varepsilon\rangle/\overline{\omega}} = \sqrt{\langle\varepsilon\rangle/0.01\ \mathrm{s}^{-1}} = 7.43 \times 10^{-4}\ \mathrm{m\,s^{-1}}$ for $\langle\varepsilon\rangle = 5.53 \times 10^{-9}\ \mathrm{m^2\,s^{-3}}$, compared to $2.35 \times 10^{-3}\ \mathrm{m\,s^{-1}}$ for $\langle\varepsilon\rangle = 5.53 \times 10^{-8}\ \mathrm{m^2\,s^{-3}}$, where $\overline{\omega}$ is the buoyancy frequency), and the predator's own swimming has a larger impact on $\boldsymbol{V_Z}$.

5.4 Planktonic captures

It is now important to investigate what happens after an encounter has occurred. Once a prey has been detected, the predator would be expected to make an attempt to capture the prey, for example, by making some form of ambush attack (Kiørboe et al. 2009, Kiørboe 2011). The actual biomechanics of the capture attempt will depend upon the specific abilities of the predator, as well as the flow conditions at that time. Modelling the complex interactions between the water motion, the predator and its prey during the capture attempt will be

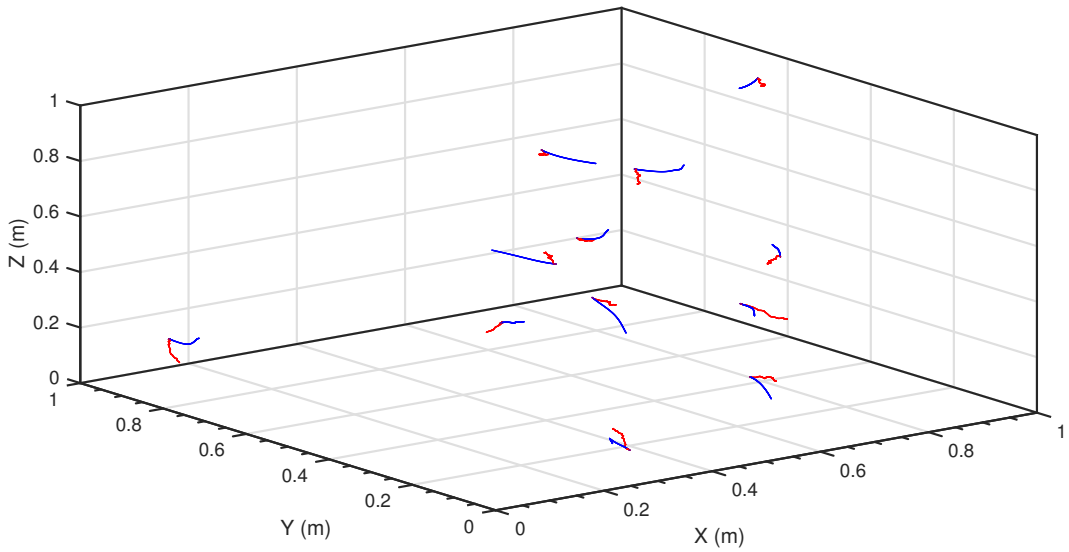

(a) Trajectories of swimming predators within the simulation domain

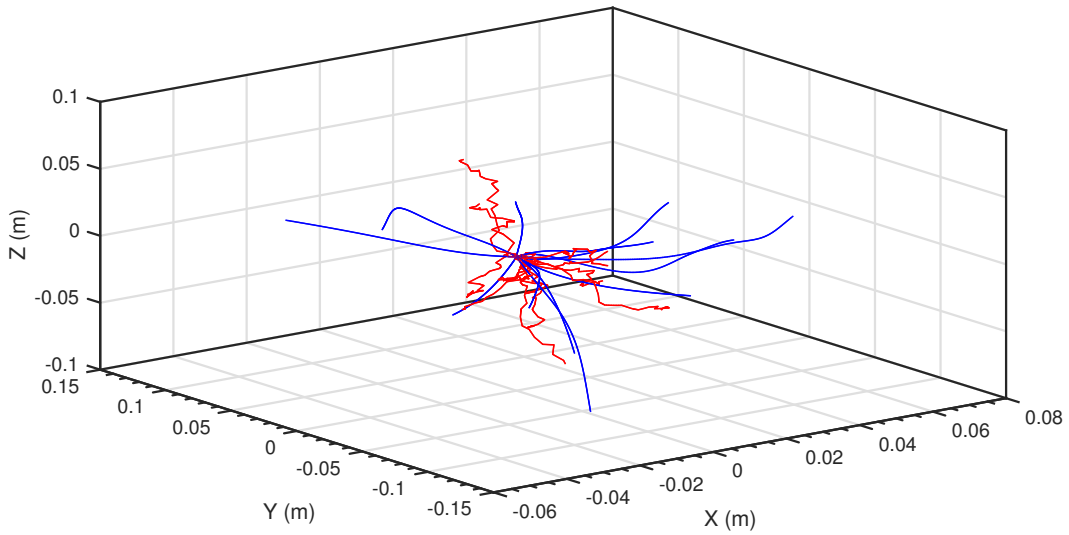

(b) Trajectories of swimming predators relative to initial position

Figure 5.7: Trajectories of swimming predators in a low turbulent environment, $\varepsilon = 5.53 \times 10^{-9}$ $\mathrm{m^2\,s^{-3}}$, over the simulated time of 60 s. Swimming speed, $\sigma_Z = 5.452 \times 10^{-4}$ $\mathrm{m\,s^{-1}}$. Blue curves indicate straight line swimmers, red curves indicate irregular swimmers changing direction every 2.7 s.

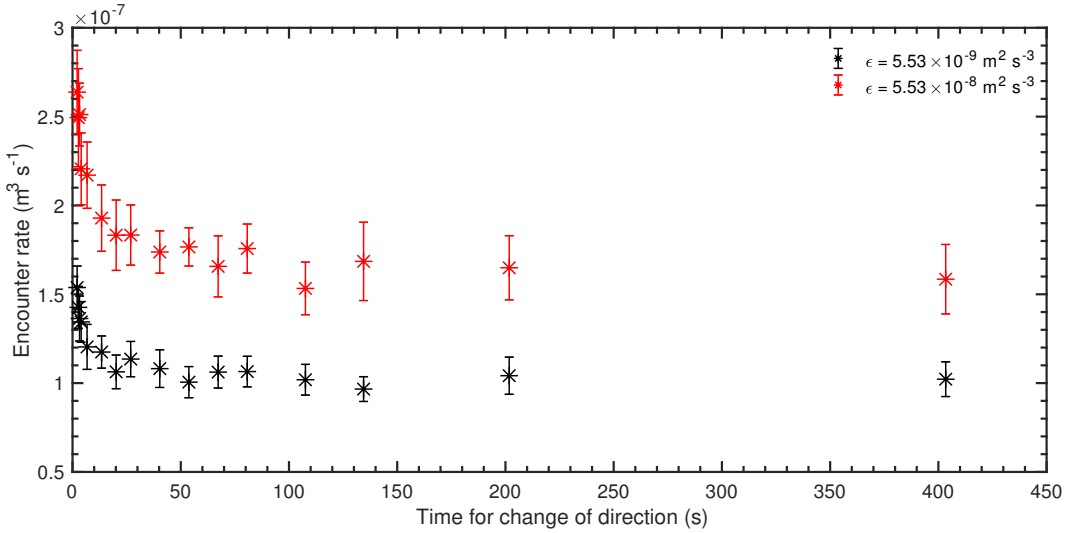

(a) Sight angle = 30°.

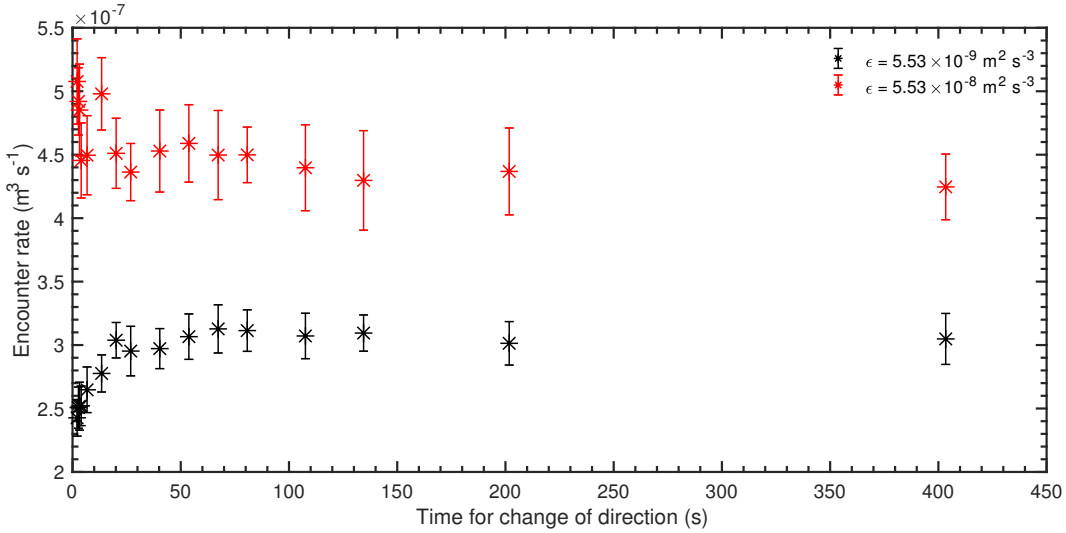

(b) Sight angle = 60°.

Figure 5.8: Encounter rates of swimming predators for different change of direction times, τ_{sight} subject to different simulated turbulent environments. Swimming speed, $\sigma_Z = 5.452 \times 10^{-4}$ m s^{-1}, contact radius, $R_{cont} = 1.173 \times 10^{-2}$ m. Predator sight angle (a) 30°, (b) 60°.

extremely difficult. In order to simplify the problem Lewis and Pedley (2001) introduce a relatively simple probabilistic measure P_{cap} in order to determine whether the outcome of any capture attempt was successful. Potentially P_{cap} could depend on many factors. Perhaps the most important factor is the time in which the prey stays within the perception field, which in turn can be related to the minimum distance between predator and prey during this time (the closest approach distance), denoted by r_M. It would also depend upon the predator's abilities to make a capture attempt.

5.4.1 The case of a predator with a spherical perception field Lewis and Pedley (2001)

The simplest case is for that of a predator with a spherical perception field of radius R_{cont}, such as in figure 5.1a. From equations (5.1.12) and (5.1.22) the number of prey entering the predator's perception field at a distance R_{cont}, at points lying between χ_R and $\chi_R + \mathrm{d}\chi_R$ and ϕ_R and $\phi_R + \mathrm{d}\phi_R$ (as in section 5.1.2), over a time T, is given by

$$\rho_{prey} T \langle f_V(U(R_{cont}), R_{cont}, n, \tau)\rangle R_{cont}^2 \sin(\theta_R) U(\boldsymbol{R}_{cont}) P(\boldsymbol{U}, \boldsymbol{V}|R_{cont})\, \mathrm{d}\phi_R \mathrm{d}\theta_R \mathrm{d}\boldsymbol{U} \mathrm{d}\boldsymbol{V}, \tag{5.4.1}$$

where $U(R_{cont})$ is the relative speed between the predator and prey (without loss of generality in the z-axis, as in section 5.1.2). U and V are the speeds defined by equations (5.1.13) and (5.1.14). Similarly, the number of prey that are perceived at any distance $r_M < R_{cont}$, over a time T, is given by

$$\rho_{prey} T \langle f_V(U(r_M), r_M, n, \tau)\rangle r_M^2 \sin(\theta_R) U(\boldsymbol{r}_M) P(\boldsymbol{U}, \boldsymbol{V}|r_M)\, \mathrm{d}\phi_R \mathrm{d}\theta_R \mathrm{d}\boldsymbol{U} \mathrm{d}\boldsymbol{V}. \tag{5.4.2}$$

If r_M is the distance of closest approach to the predator (i.e. the prey's path through the perception field brings it no closer than r_M), then the number of prey with this closest approach is the number of prey perceived at distance $r_M + \mathrm{d}r_M$ minus the number of prey perceived at distance r_M, over a time T, as $\mathrm{d}r_M \to 0$, i.e.

$$\begin{aligned}\big[\rho_{prey} T \langle f_V(U(r_M + \mathrm{d}r_M), r_M, +\mathrm{d}r_M n, \tau)\rangle (r_M^2 + 2 r_M \mathrm{d}r_M) \\ \times \sin(\theta_{r_M}) U(\boldsymbol{r}_M + \mathrm{d}\boldsymbol{r}_M) P(\boldsymbol{U}, \boldsymbol{V}|r_M)\, \mathrm{d}\phi_{r_M} \mathrm{d}\theta_{r_M} \mathrm{d}\boldsymbol{U} \mathrm{d}\boldsymbol{V}\big] \\ - \rho_{prey} T \langle f_V(U(r_M), r_M, n, \tau)\rangle r_M^2 \sin(\theta_R) U(\boldsymbol{r}_M) P(\boldsymbol{U}, \boldsymbol{V}|r_M)\, \mathrm{d}\phi_R \mathrm{d}\theta_R \mathrm{d}\boldsymbol{U} \mathrm{d}\boldsymbol{V}.\end{aligned} \tag{5.4.3}$$

Taking the limit as $\mathrm{d}r_M \to 0$, assuming that $\langle f_V \rangle$ and $P(\boldsymbol{U}, \boldsymbol{V}|r_M)$ are differentiable functions of r_M, gives

$$\rho_{prey} T \sin(\theta_{r_M}) \frac{\partial \left[\langle f_V \rangle r_M^2 U(r_M) P(\boldsymbol{U}, \boldsymbol{V}|r_M)\right]}{\partial r_M} \mathrm{d}r_M \mathrm{d}\phi_R \mathrm{d}\theta_R \mathrm{d}\boldsymbol{U} \mathrm{d}\boldsymbol{V}. \tag{5.4.4}$$

The number of prey likely to be consumed is then the number of prey that approach to r_M, multiplied by the probability of capture at r_M. Integrating the result over all possible r_M,

and all the angle and velocity variables, gives the total number likely to be consumed by the predator

$$N(T) = \rho_{prey} T \int_{\boldsymbol{V_Z}} \int_{\boldsymbol{V_P}} \int_0^{\pi} \int_0^{2\pi} \int_0^{R_{cont}} \sin(\theta_{r_M}) \times \frac{\partial \left[\langle f_V \rangle r_M^2 U(r_M) P(\boldsymbol{U}, \boldsymbol{V} | r_M) \right]}{\partial r_M} P_{cap}(r_M) \, \mathrm{d}r_M \mathrm{d}\phi_R \mathrm{d}\theta_R \mathrm{d}\boldsymbol{U} \mathrm{d}\boldsymbol{V}. \quad (5.4.5)$$

Assuming that predator will not capture any prey that do not enter the perception field, i.e. $P_{cap}(r_M = R_{cont}) = 0$, it is convenient to write equation (5.4.5) (using integration by parts) as

$$N(T) = \rho_{prey} T \int_{\boldsymbol{V_Z}} \int_{\boldsymbol{V_P}} \int_0^{\pi} \int_0^{2\pi} \int_0^{R_{cont}} \sin(\theta_{r_M}) \langle f_V(U(r_M), r_M, n, \tau) \rangle r_M^2 \sin(\theta_R) U(\boldsymbol{r}_M) P(\boldsymbol{U}, \boldsymbol{V} | r_M) \left[-\frac{\partial P_{cap}(r_M)}{\partial r_M} \right] \mathrm{d}r_M \mathrm{d}\phi_R \mathrm{d}\theta_R \mathrm{d}\boldsymbol{U} \mathrm{d}\boldsymbol{V}. \quad (5.4.6)$$

Lewis and Pedley (2001) show that for Gaussian swimmers (see section 5.1.3) this reduces to

$$N(T) = \rho_{prey} T 4 \sqrt{\frac{\pi}{2}} \int_0^{R_{cont}} \left[-\frac{\partial P_{cap}(r_M)}{\partial r_M} \right] r_M^2 \langle f_V(U(r_M), r_M, n, \tau) \rangle \sigma_U(r_M) \, \mathrm{d}r_M. \quad (5.4.7)$$

5.4.2 Probability of capture

The problem now is to find a suitable form for the capture probability term. This will largely depend on the predator's abilities, in particular, the specific technique capture technique it utilises (Kiørboe 2011).It would be very difficult to encapsulate all of the capture mechanisms described above with a single capture probability. To simplify things, Lewis and Pedley (2001) assumed that P_{cap} should depend upon $t_{r_M=T}$, the time taken for the prey to traverse the predator's perception field assuming the predator made no attempt to capture the prey. Consider the scenario presented in figure 5.9, where a prey cell has entered the predator's perception sphere moving with relative speed $U(r)$. If no capture attempt was made then the prey will have travelled through the perception field after a time t_{r_M}. Lewis and Pedley (2001) assumed that in order to make a capture the predator must be able to react and make an attempt within this timescale. This is most similar to the attack strategy of an active ambush predator described above. Assuming that, on average, the predator is able to detect and react to the presence of prey in a time T_R, Lewis and Pedley (2001) take an isotropic form of P_{cap} given by

$$P_{cap}(t_{r_M}) = \frac{\langle t_{r_M} \rangle^{\beta}}{\langle t_{r_M} \rangle^{\beta} + T_R^{\beta}}. \quad (5.4.8)$$

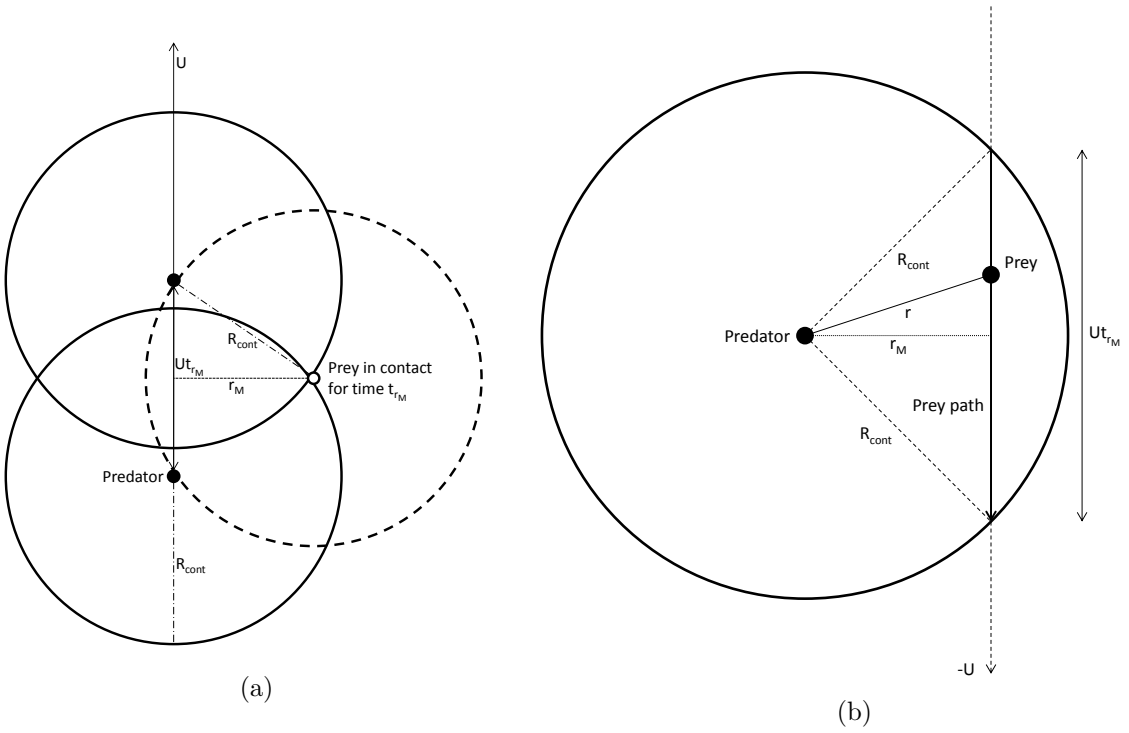

Figure 5.9: (a) Predator moving at relative speed U in contact with prey for time t_{r_M} with closest approach distance $r_M < R_{cont}$ from reference frame of prey with fixed position. (b) Predator-prey encounter from reference frame of predator with fixed position. Prey passes through spherical perception field with relative speed $-U(r)$ over a time t_{r_M} with closest approach distance $r_M < R_{cont}$. In both cases the predator or prey follow a simple straight line path.

Here β is a "shape" parameter which must be greater than 1 to ensure that $\mathrm{d}P_{cap}/\mathrm{d}t_{r_M} \to 0$ as $t_{r_M} \to 0$. As $\beta \to \infty$, the shape of P_{cap} tends to a step function. In this work β will be taken to be equal to 2. The advantage of a capture probability of this form is that measurements for typical predator reaction times are available (e.g. Kiørboe and MacKenzie (1995), Bundy et al. (1998)) The problem is now how to calculate t_{r_M} from r_M. It is logical to define t_{r_M} by the prey's path-length through the perception field of the predator. Assuming that the average distance moved by the prey before it changes direction is larger than the predator's contact radius ($R_{cont} < U(r)\tau(r)$), then the average time that a prey is in contact is given by

$$\langle t_{r_M} \rangle = \int \frac{\mathrm{d}s}{U(r(s))} = \left(\frac{2}{\pi}\right)^{1/2} \int \frac{\mathrm{d}s}{\sigma_U(r(s))}. \tag{5.4.9}$$

Here s parameterises the path of the prey crossing through the perception field. Equation (5.4.9) is relatively simple for straight-line trajectories as shown in figure 5.9, but it is much more complicated if $U(r)\tau(r)$ is small in comparison with R_{cont}. Since the resulting path across the perception field will be irregular, calculation of $\langle t_{r_M} \rangle$ will be much more difficult.

Two components of equation (5.4.7) remain. First it is necessary to understand how $\sigma_U(r)$ varies with distance r. From equations (5.1.17) and (5.1.18), the ensemble average variance of U in isotropic turbulence is given by

$$\sigma_U^2(r) = \frac{4}{3}\int_0^\infty E(k,t)\left(1 - \frac{\sin(rk)}{kr}\right)\mathrm{d}k + \sigma_P^2 + \sigma_Z^2 = w_T^2(r) + \sigma_P^2 + \sigma_Z^2. \tag{5.4.10}$$

The encounter rate required only knowledge of σ_U on the boundary of the perception field, i.e. at $r = R_{cont}$ for the spherical case. For captures it is necessary to estimate its value for all $r \in [0,\, R_{cont}]$. Monin and Yaglom (1975) suggest that for $r \ll \eta_K$, $w_T^2(r)$ is proportional to $\langle\varepsilon\rangle r^2/\nu$; whilst for $r \sim \eta_K$ it's proportional to $\langle\varepsilon\rangle^{2/3} r^{2/3}$. A simple model which is consistent with these two results is

$$\sigma_U^2(r) = \frac{c_1 r^2}{1 + c_2 r^{4/3}} + \sigma_P^2 + \sigma_Z^2, \tag{5.4.11}$$

where $c_1 \approx 1/9$ and

$$c_2 = \frac{(c_1 R_{cont}^2)/(\sigma_U^2(R_{cont}) - \sigma_P^2 - \sigma_Z^2) - 1}{R_{cont}^{4/3}}, \tag{5.4.12}$$

can be chosen to ensure that σ_U has the correct value at $r = R_{cont}$.

The only remaining term which needs to be considered is the average volume fraction $\langle f_V \rangle$. Previously this was only calculated for $r = R_{cont}$, and now needs to be computed for $r \leqslant R_{cont}$. Equation (5.1.22) gives an analytic result if the predator's direction changes less frequently than $\tau = 2R_{cont}/\langle U(R_{cont})\rangle$. For rapid changes of direction Monte Carlo methods were needed. Evaluating $\langle f_V(U(r_M), r_M, n, \tau)\rangle$ for all r_M would be very computationally expensive, especially if Monte Carlo methods have to be used. To get around this, Lewis and Pedley (2001) simply assumed that f_V varied linearly with r_M. Substituting values of

$\langle f_V \rangle = 1$ at $r_M = 0$ and $\langle f_V \rangle = 0$ at $r_M = R_{cont}$ gives

$$\langle f_V(U(r_M), r_M, n, \tau) \rangle = 1 + \frac{r_M}{R_{cont}} \left(\langle f_V(U(R_{cont}), R_{cont}, n, \tau) \rangle - 1 \right). \tag{5.4.13}$$

Equation (5.4.7) can now be rapidly computed using standard numerical integration techniques, such as a Gauss-Legendre quadrature method.

5.5 Kinematic simulations of planktonic captures

The kinematic simulations described in section 5.2.1 were adapted by Lewis and Pedley (2001) to study planktonic captures. When a predator and its prey are first deemed to be in contact by the procedure outlined in section 5.2.3, the time t spent in contact was monitored until the prey moved outside the predator's perception field. After which, equation (5.4.8) was used to make a decision on whether or not the prey had been captured. If a capture was deemed to have occurred, the prey was removed and relocated in a random position outside any perception fields of other predators. If not, the predator and prey continued on their trajectories, which could result in them encountering each other again.

The following sections detail some of the simulation results, and compares them with predicted capture rates shown in tables 5.2–5.7 (for $T_R > 0$). The results will be analysed to understand how the variables influence the optimal foraging strategy.

5.5.1 Reaction time

Figure 5.10 shows the results of a set of simulations for each of the six domains described in section 5.2.2 for a predator with swimming speed standard deviation $\sigma_Z = 5 \times 10^{-4}$ m s^{-1}, hemispherical perception field of radius $R_{cont} = 1.2 \times 10^{-2}$ m, subject to a low level of turbulence ($\varepsilon = 5.53 \times 10^{-9}$ m^2 s^{-3}). The 6 simulations were repeated to give the number of encounters, and the number of captures for four, increasing, reaction times. Predictably these results show that predators with slower reaction times will capture fewer prey, as would be expected. A larger reaction time means that the predator will be less likely to make captures, since fewer prey will remain in contact for that duration. The interception of the solid lines (when $1/L \to 0$) represent the expected number of contacts in an infinite domain, and is the value that is used to determine the capture rate, using equation (5.2.6).

Figure 5.11 compares the capture (and encounter) rate results from figure 5.10 with the predicted capture (and encounter) rates, shown in table 5.2. The predicted results are very good approximations to the simulated results for turbulent encounter rates, and for capture rates for fast reacting predators. For slow reacting predators, however, the predictions slightly underestimate the numerical results. These excellent predictions provide the basis for the formulation of the predation rate profiles across many different ε values, used in the much larger scale LES-NPZ simulations.

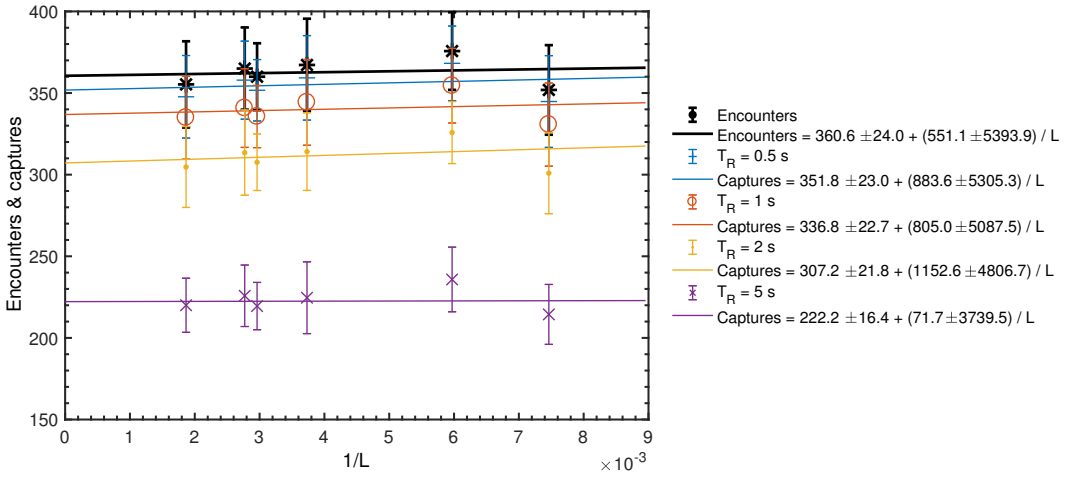

Figure 5.10: Number captures for four different predator reaction times T_R. Predator has a hemispherical perception field, $\sigma_Z = 5 \times 10^{-4}$ m s^{-1}, $R_{cont} = 1.2 \times 10^{-2}$ m, $\varepsilon = 5.53 \times 10^{-9}$ m^2 s^{-3}. Solid lines represent the linear regression best fit. Bolder black points (and line) are the equivalent number of encounters (and linear regression).

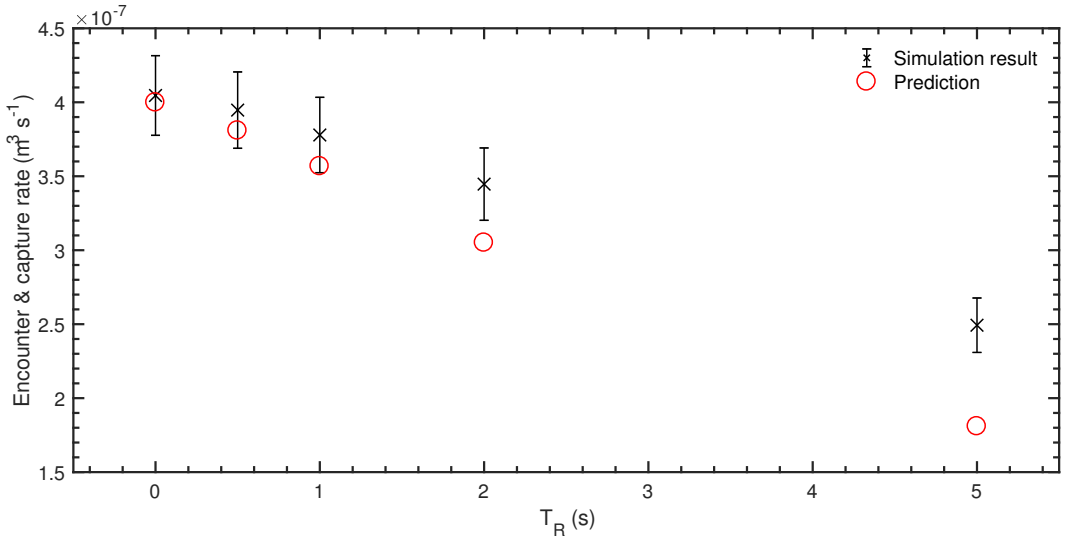

Figure 5.11: Comparison of simulated and predicted contact and capture rates (from table 5.2) for four different predator reaction times T_R. Predator has a hemispherical perception field, $\sigma_Z = 5 \times 10^{-4}$ m s^{-1}, $R_{cont} = 1.2 \times 10^{-2}$ m, $\varepsilon = 5.53 \times 10^{-9}$ m^2 s^{-3}. $T_R = 0$ represents the encounter rate.

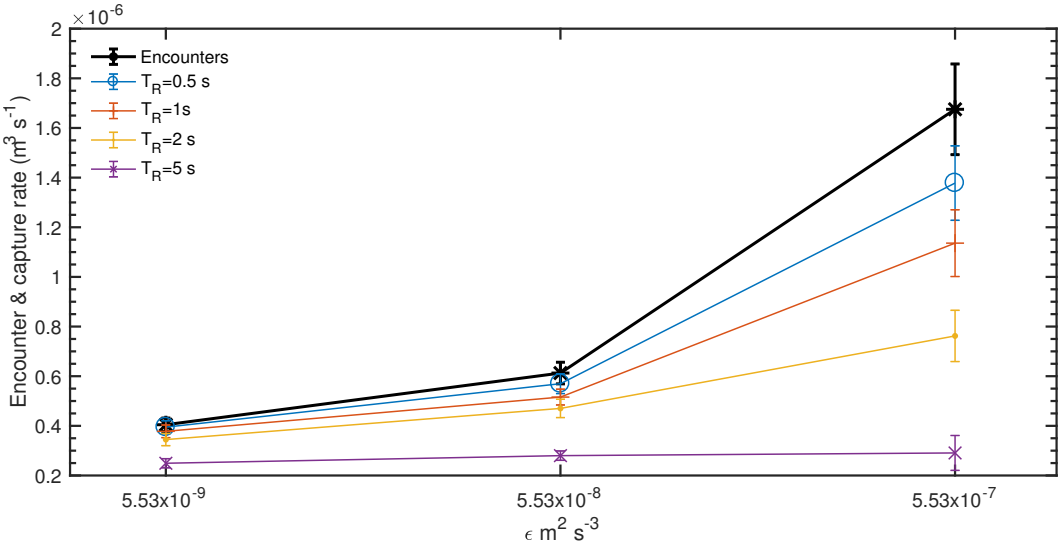

Figure 5.12: Contact and capture rates for four different predator reaction times T_R, for different levels of ε. Predator has a hemispherical perception field, $\sigma_Z = 5 \times 10^{-4}$ m s^{-1}, $R_{cont} = 1.2 \times 10^{-2}$ m. Bold black data and line represents the encounter rate.

5.5.2 Turbulent intensity

Another group of simulations was set-up to investigate the difference between the encounter rate and capture rates for different T_R when subject to different levels of turbulence. Figure 5.12 shows the results of these simulations for a straight-line swimming predator with $\sigma_Z = 5 \times 10^{-4}$ m s^{-1}, and hemispherical perception field defined by $R_{cont} = 1.2 \times 10^{-2}$ m. As discussed in section 5.3.1, increasing the turbulence results in a higher encounter rate, since the volume mapped out is larger. If the predator can react fast enough, in this case $T_R \leqslant 2$ s, the predator is able to take advantage of increases in turbulent intensity by increasing its capture rate. However, as can be seen the predator with the slowest reaction time, $T_R = 5$ s, has a capture rate that remains relatively stable at $\approx 2.5 \times 10^{-7}$ m^3 s^{-1}, even for higher levels of turbulence. The increased turbulence has the effect of increasing V_Z and U, this means that the prey traverses the perception field far too quickly for the predator to respond. So the increase in volume mapped out by the more turbulent flow is offset by the increasing difficulty in making a capture. Hence it is vital for any planktonic predator to be able to react quickly to any prey in its vicinity, if it wants to take advantage of increases in its encounter rate brought about by turbulence.

5.5.3 Swimming speed

Similar results are seen when the predator's swimming speed is varied. Figure 5.13a shows the results of a set of simulations for different values of σ_Z, under a low level of turbulence ($\varepsilon = 5.53 \times 10^{-9}$ m^2 s^{-3}). The other biological parameters were kept as in the previous case. Increasing σ_Z results in a higher contact rate. The effect of T_R restricting the predation rate is clearer here, since the predators with the slower reaction times, $T_R \geqslant 1$ s,

receive significantly less of an enhancement to the capture rate for higher σ_Z. Figure 5.13b shows the results for the same predators, but now subject to an increased level of turbulence ($\varepsilon = 5.53 \times 10^{-7}$ m^2 s^{-3}). In this case it is clear that even the fastest reacting predator ($T_R = 0.5$ s) is beginning to be restricted by its reaction time. In both figures this predator attains a maximum capture rate of 2.5–3.0 $\times 10^{-6}$ m^3 s^{-1}, even with the increased U for $\varepsilon = 5.53 \times 10^{-7}$ m^2 s^{-3}.

5.5.4 Sight angle

Figure 5.14 shows the encounter and capture rates for predators with different conical perception fields (defined by radius $R_{cont} = 1.2 \times 10^{-2}$ m). In this case the straight line swimming predators with speed $\sigma_Z = 5 \times 10^{-4}$ m s^{-1} are subject to a low level of turbulence ($\varepsilon = 5.53 \times 10^{-7}$ m^2 s^{-3}). These simulations show that increasing the cone angle results in a higher capture rate, which is expected since this will result in a larger volume swept out by the predator. This increase is demonstrated by all four predators.

5.5.5 Swimming style

Figures 5.6 and 5.8 demonstrated that a predator with a conical perception field may enhance their encounter rate by changing its swimming direction at regular intervals. This enhancement depended upon the cone angle α_{sight} and relative velocity U. Figure 5.15 demonstrates how this effects the corresponding predation rate when the predator's reaction time is taken into account. In this case the predator swims at $\sigma_Z = 5 \times 10^{-4}$ m s^{-1} and is subject to a turbulent flow characterised by $\varepsilon = 5.53 \times 10^{-9}$ m^2 s^{-3}. For a narrow cone angle $\alpha_{sight} \leqslant 45°$ the faster reacting predator will gain an enhancement by utilising an irregular swimming strategy (dashed line). A predator with $\alpha_{sight} < 90°$ can increase its capture rate by making regular changes in direction, if it can react fast enough to the presence of prey. However, this is not the case for the slower reacting predator ($T_R = 2$ s, yellow lines and data points) who does not receive this enhancement. It does better to swim in a straight line, because it reacts too slowly to benefit form the enhanced encounter rate it experiences by changing direction rapidly.

This result is interesting since it demonstrates a significant difference between the encounter and capture rates and suggests that the optimal encounter strategy is not necessarily the optimal predation strategy. The enhancement in encounters comes about as a consequence of the cell's orientation giving a larger projection of the leading surface area. However, when the predator is in an optimal orientation for encounters it may not be optimal for captures. When reaction times are being taken into account it is more important to consider the prey's path length through the perception field. The path through a predators optimal encounter orientation may be, on average, too short for the predator to react in time to make a capture, whereas an orientation that is less optimal for encounters may result in longer prey paths, meaning it can make more captures.

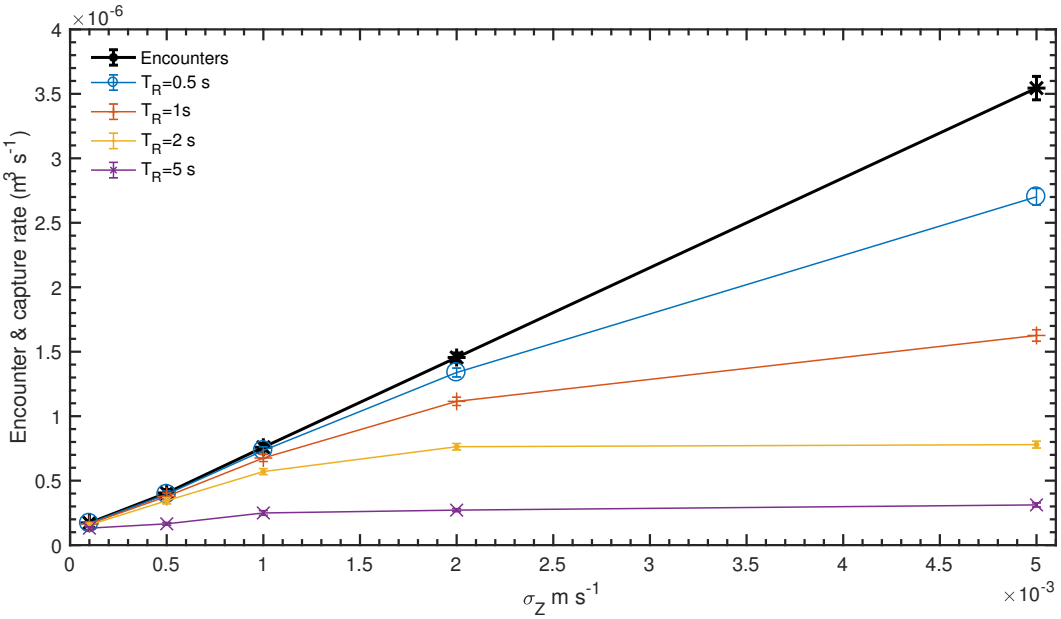

(a) $\varepsilon = 5.53 \times 10^{-9}$ m^2 s^{-3}

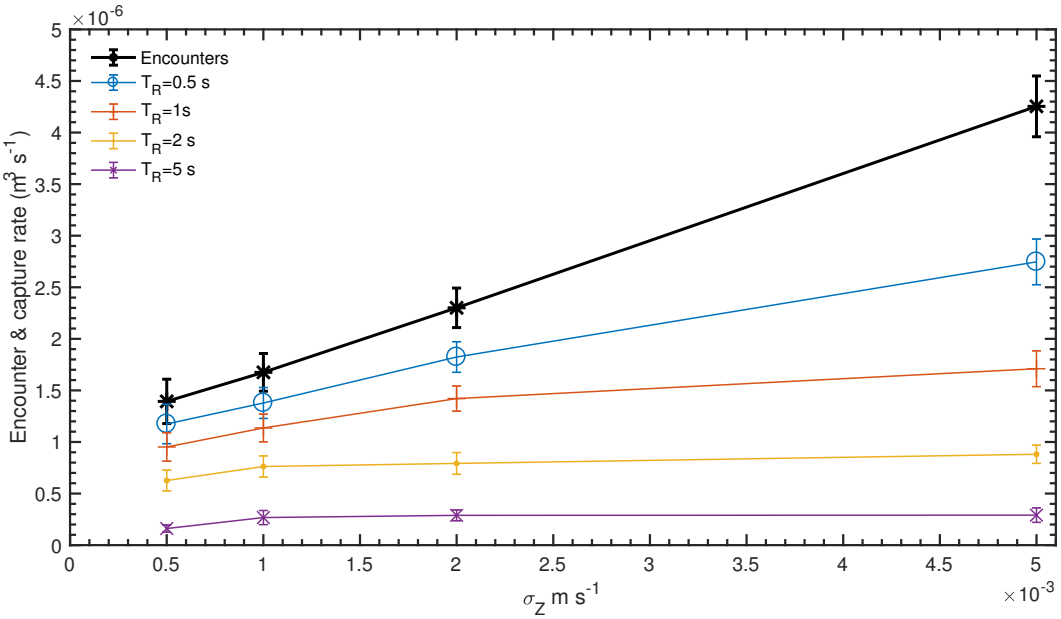

(b) $\varepsilon = 5.53 \times 10^{-7}$ m^2 s^{-3}

Figure 5.13: Contact and capture rates for four different predator reaction times T_R, for different values of σ_Z. Predator has a hemispherical perception field, $R_{cont} = 1.2 \times 10^{-2}$ m. (a) $\varepsilon = 5.53 \times 10^{-9}$ m^2 s^{-3}, (b) $\varepsilon = 5.53 \times 10^{-7}$ m^2 s^{-3}. Bold black data and lines represents the encounter rate.

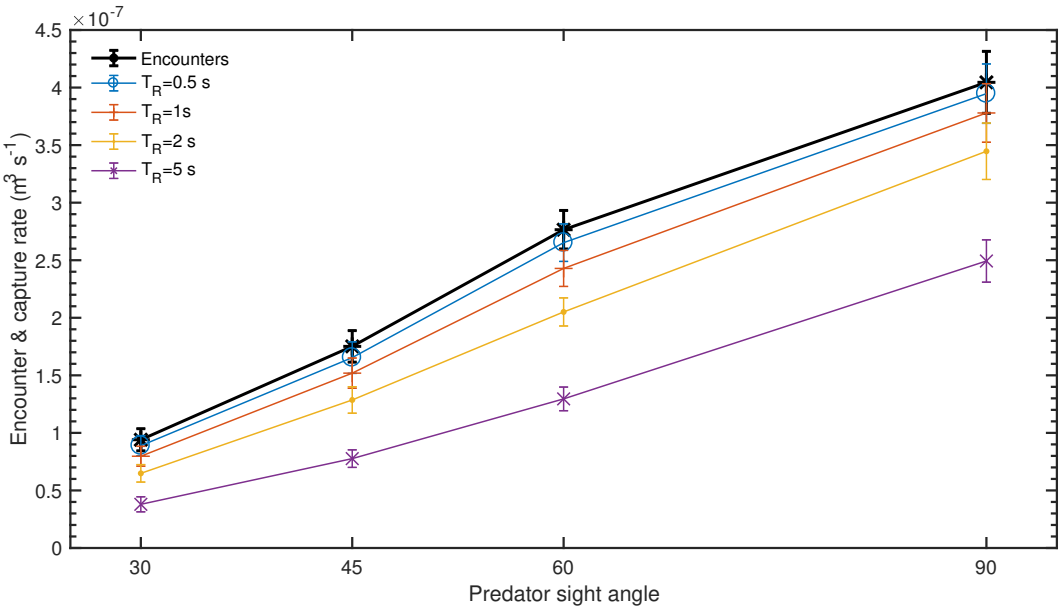

Figure 5.14: Contact and capture rates for four different predator reaction times T_R, for different values of conical angle α_{sight}. $\sigma_Z = 5 \times 10^{-4}$ m s^{-1}, $R_{cont} = 1.2 \times 10^{-2}$ m, subject to $\varepsilon = 5.53 \times 10^{-9}$ m^2 s^{-3}. Bold black data and line represents the encounter rate.

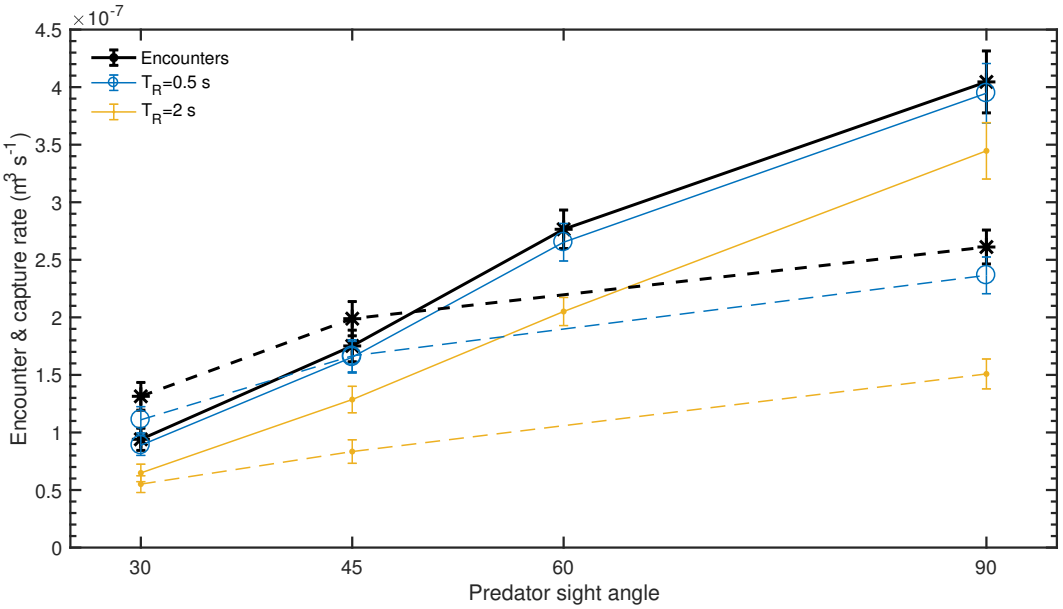

Figure 5.15: Contact and capture rates for two different predator reaction times T_R, for different values of conical angle α_{sight}. $\sigma_Z = 5 \times 10^{-4}$ m s^{-1}, $R_{cont} = 1.2 \times 10^{-2}$ m, subject to $\varepsilon = 5.53 \times 10^{-9}$ m^2 s^{-3}. Straight line swimmer (solid lines), Irregular swimmer with $\tau_S = 2.7$ s (dashed lines). Bold black data and lines represents the encounter rate.

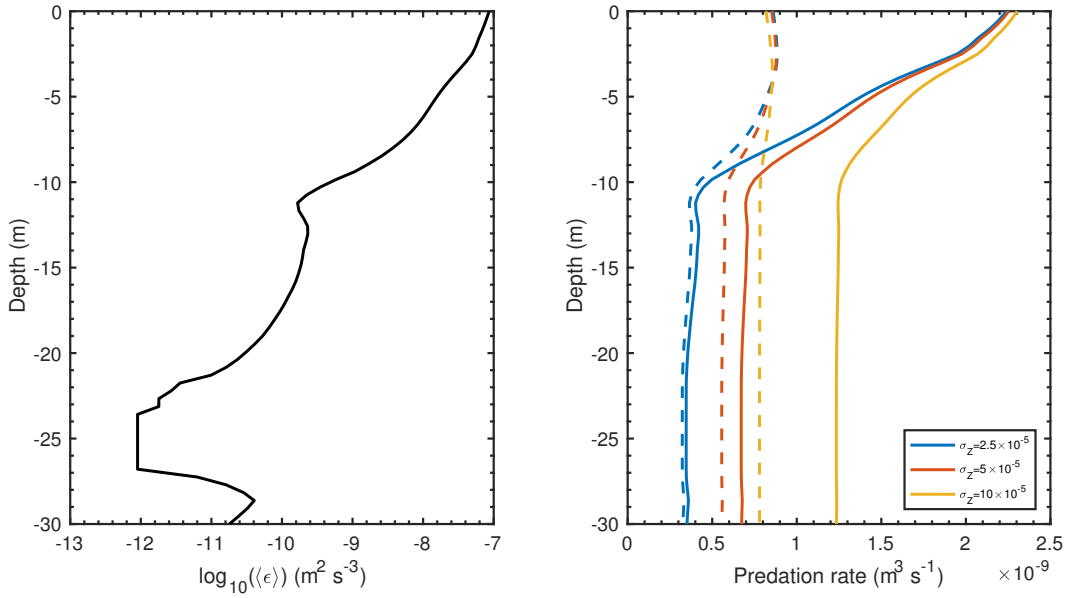

Figure 5.16: Turbulent kinetic energy dissipation rate (left) and various predation rates (right) for a full LES-NPZ simulation with $U_* = 3.0 \times 10^{-3}$ m s^{-1}, $U_S = 3.3 \times 10^{-2}$ m s^{-1} Predation rates: solid lines represent predators with reaction time $T_R = 5$ s, dashed $T_R = 15$ s.

5.6 Application to the LES-NPZ model

Incorporating these ideas into the full LES-NPZ model requires some simplifying assumptions, for computational efficiency. It is assumed throughout that the predator is a straight line swimmer and has a hemispherical perception field. This makes computation of the volume fraction, $\langle f_V \rangle$, relatively simple. Once the LES-NPZ simulation has "spun-up" (see section 3.6), the predation rate, based upon a prescribed T_R value, is calculated at each depth from the kinetic energy dissipation rate profile before the biological fields are introduced.

Examples of predation profiles for a typical LES-NPZ simulation of a wind driven Ekman-Stokes boundary layer with friction velocity $U_* = 3.0 \times 10^{-3}$ m s^{-1}, and Stokes drift velocity $U_S = 3.3 \times 10^{-2}$ m s^{-1} are shown in figure 5.16. Within the first 10 m of the boundary layer the turbulent intensity (as measured by ε) is relatively high, which results in an enhanced predation rate. However, the slower reacting predator appears to reach a limit on its predation rate at -5 m as the increase in ε is offset by the difficulty in capturing prey. How such predation rates influence the vertical distribution of the phytoplankton prey is one of the main subjects of chapter 6

T_R s	σ_Z m s^{-1}	0.5×10^{-3}	1.0×10^{-3}	2.0×10^{-3}	5.0×10^{-3}
0.0	Contact Rate $r \leqslant R$	3.998×10^{-7}	6.876×10^{-7}	1.358×10^{-6}	3.429×10^{-6}
	$U(R_{cont})$	8.3173×10^{-4}	1.5407×10^{-3}	3.1306×10^{-3}	7.9273×10^{-3}
0.5	Capture Rate $r \leqslant R$	3.808×10^{-7}	6.255×10^{-7}	1.086×10^{-6}	1.632×10^{-6}
	$U(R_{cont})$	7.9082×10^{-4}	1.4044×10^{-3}	2.5034×10^{-3}	3.7714×10^{-3}
1.0	Capture Rate $r \leqslant R$	3.567×10^{-7}	5.445×10^{-7}	7.755×10^{-7}	7.1×10^{-7}
	$U(R_{cont})$	7.4174×10^{-4}	1.2217×10^{-3}	1.7889×10^{-3}	1.6416×10^{-3}
2.0	Capture Rate $r \leqslant R$	3.05×10^{-7}	3.894×10^{-7}	3.894×10^{-7}	2.188×10^{-7}
	$U(R_{cont})$	6.3539×10^{-4}	8.7263×10^{-4}	8.9718×10^{-4}	5.0722×10^{-4}
5.0	Capture Rate $r \leqslant R$	1.809×10^{-7}	1.499×10^{-7}	9.116×10^{-8}	3.791×10^{-8}
	$U(R_{cont})$	3.7632×10^{-4}	3.3542×10^{-4}	2.0970×10^{-4}	8.7536×10^{-5}

Table 5.2: Predicted contact ($T_R = 0$) and capture rates ($T_R > 0$), (m^3 s^{-1}), for a straight line swimming predator with sight angle = 90°, subject to flow field characterised by $\varepsilon = 5.53 \times 10^{-9}$ m^2 s^{-3}. $U_{R_{cont}}$ is the relative velocity of the predator to the prey.

T_R s	σ_Z m s^{-1}	0.5×10^{-3}	1.0×10^{-3}	2.0×10^{-3}	5.0×10^{-3}
0.0	Contact Rate $r \leqslant R$	6.812×10^{-7}	8.882×10^{-7}	1.428×10^{-6}	3.373×10^{-6}
	$U(R_{cont})$	1.3093×10^{-3}	1.7555×10^{-3}	3.0357×10^{-3}	7.7153×10^{-3}
0.5	Capture Rate $r \leqslant R$	6.212×10^{-7}	7.793×10^{-7}	1.117×10^{-6}	1.613×10^{-6}
	$U(R_{cont})$	1.1978×10^{-3}	1.5469×10^{-3}	2.3810×10^{-3}	3.8358×10^{-3}
1.0	Capture Rate $r \leqslant R$	5.558×10^{-7}	6.594×10^{-7}	8.065×10^{-7}	7.248×10^{-7}
	$U(R_{cont})$	1.0669×10^{-3}	1.3045×10^{-3}	1.7118×10^{-3}	1.6585×10^{-3}
2.0	Capture Rate $r \leqslant R$	4.321×10^{-7}	4.539×10^{-7}	4.18×10^{-7}	2.327×10^{-7}
	$U(R_{cont})$	8.3408×10^{-4}	9.0197×10^{-4}	8.8743×10^{-4}	5.2858×10^{-4}
5.0	Capture Rate $r \leqslant R$	2.093×10^{-7}	1.673×10^{-7}	1.03×10^{-7}	4.06×10^{-8}
	$U(R_{cont})$	4.0492×10^{-4}	3.3024×10^{-4}	2.1676×10^{-4}	9.2622×10^{-5}

Table 5.3: Predicted contact ($T_R = 0$) and capture rates ($T_R > 0$), (m^3 s^{-1}), for a straight line swimming predator with sight angle = 90°, subject to flow field characterised by $\varepsilon = 5.53 \times 10^{-8}$ m^2 s^{-3}. $U_{R_{cont}}$ is the relative velocity of the predator to the prey.

T_R s	σ_Z m s^{-1}	0.5×10^{-3}	1.0×10^{-3}	2.0×10^{-3}	5.0×10^{-3}
0.0	Contact Rate $r \leqslant R$	1.465×10^{-6}	1.573×10^{-6}	1.947×10^{-6}	3.55×10^{-6}
	$U(R_{cont})$	2.7509×10^{-3}	2.9665×10^{-3}	3.7340×10^{-3}	7.3817×10^{-3}
0.5	Capture Rate $r \leqslant R$	1.167×10^{-6}	1.225×10^{-6}	1.396×10^{-6}	1.689×10^{-6}
	$U(R_{cont})$	2.2076×10^{-3}	2.3197×10^{-3}	2.6819×10^{-3}	3.5011×10^{-3}
1.0	Capture Rate $r \leqslant R$	8.926×10^{-7}	9.081×10^{-7}	9.305×10^{-7}	7.772×10^{-7}
	$U(R_{cont})$	1.6988×10^{-3}	1.7247×10^{-3}	1.7937×10^{-3}	1.6040×10^{-3}
2.0	Capture Rate $r \leqslant R$	5.359×10^{-7}	5.118×10^{-7}	4.446×10^{-7}	2.568×10^{-7}
	$U(R_{cont})$	1.0176×10^{-3}	9.7445×10^{-4}	8.5545×10^{-4}	5.2776×10^{-4}
5.0	Capture Rate $r \leqslant R$	1.647×10^{-7}	1.423×10^{-7}	1.02×10^{-7}	4.567×10^{-8}
	$U(R_{cont})$	3.1562×10^{-4}	2.7250×10^{-4}	1.9661×10^{-4}	9.3996×10^{-5}

Table 5.4: Predicted contact ($T_R = 0$) and capture rates ($T_R > 0$), (m^3 s^{-1}), for a straight line swimming predator with sight angle = 90°, subject to flow field characterised by $\varepsilon = 5.53 \times 10^{-7}$ m^2 s^{-3}. $U_{R_{cont}}$ is the relative velocity of the predator to the prey.

T_R s	σ_Z m s^{-1}	0.5×10^{-3}	1.0×10^{-3}	2.0×10^{-3}	5.0×10^{-3}
0.0	Contact Rate $r \leqslant R$	9.995×10^{-8}	1.713×10^{-7}	3.326×10^{-7}	8.53×10^{-7}
	$U(R_{cont})$	7.1719×10^{-4}	1.4180×10^{-3}	3.0351×10^{-3}	7.8837×10^{-3}
0.5	Capture Rate $r \leqslant R$	8.599×10^{-8}	1.27×10^{-7}	1.792×10^{-7}	1.999×10^{-7}
	$U(R_{cont})$	6.0539×10^{-4}	1.0363×10^{-3}	1.6253×10^{-3}	1.8462×10^{-3}
1.0	Capture Rate $r \leqslant R$	7.375×10^{-8}	9.495×10^{-8}	1.036×10^{-7}	7.358×10^{-8}
	$U(R_{cont})$	5.1267×10^{-4}	7.6901×10^{-4}	9.3808×10^{-4}	6.7902×10^{-4}
2.0	Capture Rate $r \leqslant R$	7.375×10^{-8}	9.495×10^{-8}	1.036×10^{-7}	7.358×10^{-8}
	$U(R_{cont})$	3.7360×10^{-4}	4.4177×10^{-4}	3.8178×10^{-4}	1.9362×10^{-4}
5.0	Capture Rate $r \leqslant R$	2.378×10^{-8}	1.582×10^{-8}	8.564×10^{-9}	3.533×10^{-9}
	$U(R_{cont})$	1.6089×10^{-4}	1.2544×10^{-4}	7.6355×10^{-5}	3.2724×10^{-5}

Table 5.5: Predicted contact ($T_R = 0$) and capture rates ($T_R > 0$), (m^3 s^{-1}), for a straight line swimming predator with sight angle = 30°, subject to flow field characterised by $\varepsilon = 5.53 \times 10^{-9}$ m^2 s^{-3}. $U_{R_{cont}}$ is the relative velocity of the predator to the prey.

T_R s	σ_Z m s^{-1}	0.5×10^{-3}	1.0×10^{-3}	2.0×10^{-3}	5.0×10^{-3}
0.0	Contact Rate $r \leqslant R$	1.657×10^{-7}	2.218×10^{-7}	3.629×10^{-7}	8.283×10^{-7}
	$U(R_{cont})$	1.0523×10^{-3}	1.4742×10^{-3}	2.7059×10^{-3}	7.3952×10^{-3}
0.5	Capture Rate $r \leqslant R$	1.319×10^{-7}	1.608×10^{-7}	2.027×10^{-7}	2.022×10^{-7}
	$U(R_{cont})$	8.0984×10^{-4}	1.0281×10^{-3}	1.4548×10^{-3}	1.7797×10^{-3}
1.0	Capture Rate $r \leqslant R$	1.046×10^{-7}	1.166×10^{-7}	1.177×10^{-7}	7.52×10^{-8}
	$U(R_{cont})$	6.3526×10^{-4}	7.3225×10^{-4}	8.3408×10^{-4}	6.5951×10^{-4}
2.0	Capture Rate $r \leqslant R$	6.757×10^{-8}	9.373×10^{-8}	4.812×10^{-8}	2.174×10^{-8}
	$U(R_{cont})$	4.0249×10^{-4}	3.9764×10^{-4}	3.3945×10^{-4}	1.8912×10^{-4}
5.0	Capture Rate $r \leqslant R$	2.316×10^{-8}	1.695×10^{-8}	9.645×10^{-9}	3.646×10^{-9}
	$U(R_{cont})$	1.3578×10^{-4}	1.0669×10^{-4}	6.7891×10^{-5}	3.3945×10^{-5}

Table 5.6: Predicted contact ($T_R = 0$) and capture rates ($T_R > 0$), (m^3 s^{-1}), for a straight line swimming predator with sight angle = 30°, subject to flow field characterised by $\varepsilon = 5.53 \times 10^{-8}$ m^2 s^{-3}. $U_{R_{cont}}$ is the relative velocity of the predator to the prey.

T_R s	σ_Z m s^{-1}	0.5×10^{-3}	1.0×10^{-3}	2.0×10^{-3}	5.0×10^{-3}
0.0	Contact Rate $r \leqslant R$	3.55×10^{-7}	3.843×10^{-7}	4.877×10^{-7}	9.133×10^{-7}
	$U(R_{cont})$	2.1559×10^{-3}	2.3542×10^{-3}	3.0699×10^{-3}	6.5280×10^{-3}
0.5	Capture Rate $r \leqslant R$	2.171×10^{-7}	2.24×10^{-7}	2.413×10^{-7}	2.309×10^{-7}
	$U(R_{cont})$	1.2504×10^{-3}	1.3021×10^{-3}	1.4401×10^{-3}	1.5608×10^{-3}
1.0	Capture Rate $r \leqslant R$	1.365×10^{-7}	1.348×10^{-7}	1.265×10^{-7}	8.461×10^{-8}
	$U(R_{cont})$	7.7697×10^{-4}	7.7180×10^{-4}	7.4593×10^{-4}	5.6742×10^{-4}
2.0	Capture Rate $r \leqslant R$	6.273×10^{-8}	5.79×10^{-8}	4.67×10^{-8}	2.43×10^{-8}
	$U(R_{cont})$	3.5615×10^{-4}	3.3200×10^{-4}	2.7509×10^{-4}	1.6298×10^{-4}
5.0	Capture Rate $r \leqslant R$	1.408×10^{-8}	1.215×10^{-8}	8.788×10^{-9}	4.067×10^{-9}
	$U(R_{cont})$	8.1060×10^{-5}	6.9850×10^{-5}	5.1741×10^{-5}	2.7595×10^{-5}

Table 5.7: Predicted contact ($T_R = 0$) and capture rates ($T_R > 0$), (m^3 s^{-1}), for a straight line swimming predator with sight angle = 30°, subject to flow field characterised by $\varepsilon = 5.53 \times 10^{-7}$ m^2 s^{-3}. $U_{R_{cont}}$ is the relative velocity of the predator to the prey.

Chapter 6

Deep chlorophyll maxima: the role of planktonic predation

6.1 Introduction

A ubiquitous feature of aquatic and marine ecosystems throughout the world is the presence of significant sub-surface primary production (phytoplankton growth), observed in vertical fluorescence profiles. Such features are known as deep chlorophyll maxima (DCM) or deep biological maxima (DBM). These are described as a broad region ($O(10\text{ m})$) of relatively high chlorophyll concentration, often found below the mixing layer, a region of high mixing. Garratt (1994) suggests that the mixing layer depth is $z_{ML} \approx 0.2\text{-}0.4 z_{TD}$, where $z_{TD} = U_*/f$ is the mixed layer depth. DCM have been observed in many oceanic environments (Cullen and Eppley 1981, Cullen 1982, Furuya and Marumo 1983, Takahashi et al. 1989, Letelier et al. 2004, Macías et al. 2008, Cullen 2015), as well as a number of limnic (inland water) systems (Burnett et al. 2006, White and Matsumoto 2012, Simmonds et al. 2015).

The question of exactly what processes drive the formation of DCM remains an open problem (Cullen 2015). One of the earliest hypotheses is that DCM form as a consequence of concentrations of organic particles along density gradients (Jerlov 1953). Simmonds et al. (2015) suggests that the presence of the nutricline, brought about by thermal stratification, leads to an increase in the phytoplankton growth rate. Klausmeier and Litchman (2001) inferred that DCM would form at depths corresponding to equal light and nutrient limitation in weak turbulence. Letelier et al. (2004) found that the increase of PAR (photosynthetically available radiation) during the summer induced an increase in the phytoplankton biomass around the deep chlorophyll maxima depth at a location north of O'ahu. They also found that the DCM depth increased between winter and summer due to seasonal variation in the nutricline depth, and the water column PAR attenuation rate.

Many studies indicate that turbulent mixing plays an important role in the formation of DCM. Vertical heterogeneity in phytoplankton populations is typically associated with poorly mixed regions of the water column (Venrick et al. 1973, Klausmeier and Litchman

2001, Huisman et al. 2006, Wang and Goodman 2010, Macías et al. 2013). One of the most relevant studies to this work is that of Venrick et al. (1973). The authors observed a DCM in the Pacific Ocean that resulted from wind-driven turbulence. DCM often form when the mixing of the water column is restricted by either a density gradient, or by low turbulent kinetic energy Lindholm (1992), Reynolds (1992), Macías et al. (2013). The observations of Macías et al. (2013) are of particular interest to this work, since they display a strong anti-correlation between the kinetic energy dissipation rate and fluorescence. Results of this nature are very important and show that turbulence has both a creative and destructive capacity with regard to particle vertical structure. Macías et al. (2013) results provide motivational and empirical support for the analysis and results of this chapter.

This raises a question, can the physical drivers controlling DCM formation and persistence be related to a biological process? The experimental results of Pannard et al. (2015) suggest that depth dependent zooplankton grazing may promote the persistence of a DCM in a stratified lake. They hypothesised that grazing removed phytoplankton biomass in the upper region (epilimnion) of the stratified lake. This increased the availability of light in the metalimnion (thermocline). They argued that oxygen sensitive zooplankton species were not able to reach the DCM which was close to the anoxic layer. The results agreed with similar studies of Pilati and Wurtsbaugh (2003), Sawatzky (2006). Fennel and Boss (2003) define what they call the "general compensation depth", which is the depth at which the attained phytoplankton growth rate is balanced out by losses due to zooplankton predation and sinking. These studies highlight the importance of zooplankton predation on the vertical distribution of phytoplankton. In a wind driven ocean boundary layer, high levels of turbulent mixing near the surface leads to an enhanced predation rate. High predation near the surface will restrict growth in this region. Lower levels of turbulence below the mixing layer depth results in reduced predation pressure and the phytoplankton can grow relatively unabated. The work of this chapter seeks to test the hypothesis that a turbulent dependent predation pressure can result in DBM similar to the results of Macías et al. (2013). The LES-NPZ model described in this work, incorporating the predation model of chapter 5, is an ideal tool for testing the ideas described above.

6.2 Macías data

This section provides a brief summary of the observations of DCM recorded in the sub-surface upper ocean discussed by Macías et al. (2013) (subsequently denoted by M13), which provided the motivation for the studies in this chapter and the work of Lewis et al. (2017).

M13 describes the results of measurements taken at four different marine environments, specifically the Alboran Sea (a coastal upwelling region off the Spanish east coast), the tidally dominated Strait of Gibraltar, a region of open ocean in the North Atlantic (at $\sim$ 34°30' N, 8°30' W) and a site just off the tip of the Antarctic Peninsula. The measurements were recorded using a TurboMAP-L fast sampling (512 Hz) probe (Doubell et al. 2009), an

implement which can be used to measure conductivity, temperature, shear, and fluorescence to a high resolution scale of the order centimetres. In the experiments the probe was allowed to free-fall from the surface to a typical depth of 150 m. The choice of 150 m captures the effects of both the wind driven upper mixed layer as well as the weakly stratified lower part of the water column. With the exception of the North Atlantic site (where measurements took place in the spring), the measurements were taken during the summer months, at a time when DCM are very prevalent in the polar and temperate latitudes. At this time of year the levels of turbulent mixing are relatively low, which leads to nutrient depletion and low phytoplankton growth in the upper mixed layer (Holm-Hansen et al. 2005).

Estimates of the average energy dissipation rate profiles, $\langle \varepsilon(z) \rangle_T$ were calculated from the measurements of vertical shear using the relation

$$\langle \varepsilon(z) \rangle_T = \frac{15}{2} \nu \langle \frac{\partial u}{\partial z} \rangle_T^2 \tag{6.2.1}$$

(c.f equation (2.2.24)) where ν is the kinematic viscosity. The authors acknowledge that the results from the highly turbulent near surface region may be unrealistic, since the probe needs to be free-falling through the water column, and typically this condition is only achieved some $10-15$ m below the surface. The prevailing vertical stratification conditions were summarised by an average buoyancy frequency $\overline{\omega}(z)$, also known as the Brunt-Väisälä frequency, given by

$$\overline{\omega}^2(z) = -\frac{g}{\rho} \langle \frac{\partial \rho}{\partial z} \rangle_T. \tag{6.2.2}$$

Figure 6.1 shows four vertical profiles, one for each of the locations, comparing the energy dissipation rate and fluorescence (measured in relative fluorescent units) fitted to standard Gaussian curves. These profiles are reproduced from M13.

From these datasets, the most important feature relevant to this study is the relative position of the deep chlorophyll maximum, $\text{DCM}_{\text{depth}}$, to the depth at with the energy dissipation rate achieves its maximum, $\text{peak}_{\text{depth}}$. Of the 73% profiles that featured a subsurface $\text{peak}_{\text{depth}}$, approximately two thirds (31/46) exhibited a $\text{DCM}_{\text{depth}}$ situated below, but within one standard deviation of $\text{peak}_{\text{depth}}$. M13 found that the maximum fluorescence measurements were significantly correlated with negative $\varepsilon(z)$ gradients within the upper mixed layer, with the average $\text{DCM}_{\text{depth}}$ occurring 18 m below the corresponding $\text{peak}_{\text{depth}}$ value. This correlation was not found in the remaining 15 profiles where there was a higher degree of stratification ($\overline{\omega}^2 = 3.21 \times 10^{-3} \pm 1.82 \times 10^{-3}$ s^{-2}) relative to the "matching" profiles ($\overline{\omega}^2 = 1.1 \times 10^{-3} \pm 1.2 \times 10^{-3}$ s^{-2}). The results of M13 are very important because they present experimental evidence of intense DCM (of the order of $2-6$ times the background level) in absence of strong stratification, conditions that are typically considered to be a prerequisite for biological aggregations, especially thin layers (Durham et al. 2009, Hoecker-Martínez and Smyth 2012, Shroyer et al. 2014).

Figure 6.2 shows the location of the $\text{DCM}_{\text{depth}}$ relative to the $\text{peak}_{\text{depth}}$ for each of the 31

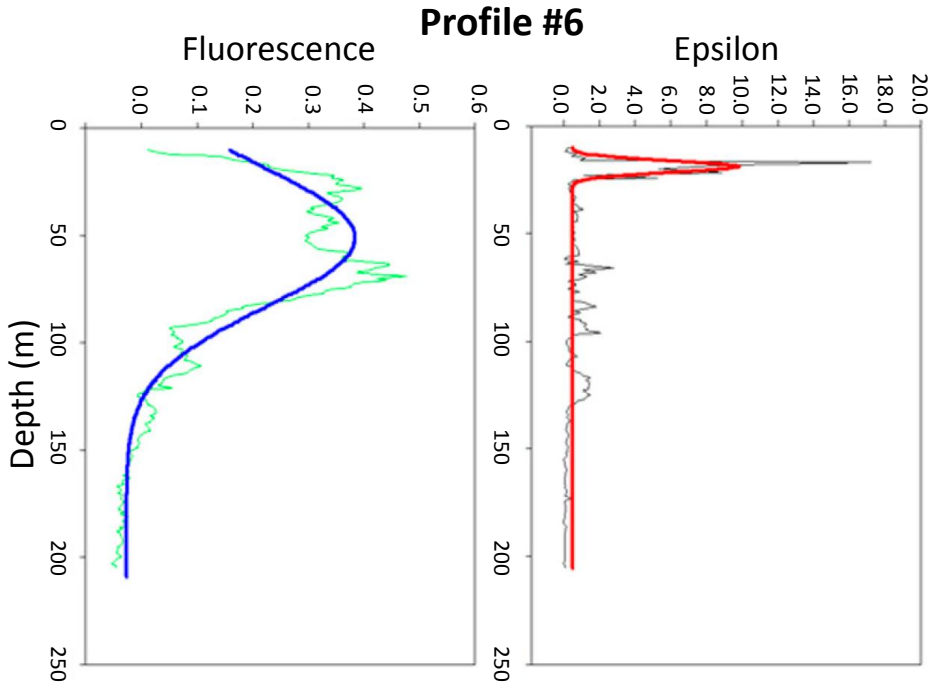
Profile #6
Fluorescence
Epsilon
Depth (m)
0.0
0.1
0.2
0.3
0.4
0.5
0.6
0.0
2.0
4.0
6.0
8.0
10.0
12.0
14.0
16.0
18.0
20.0
0
50
100
150
200
250

(a)

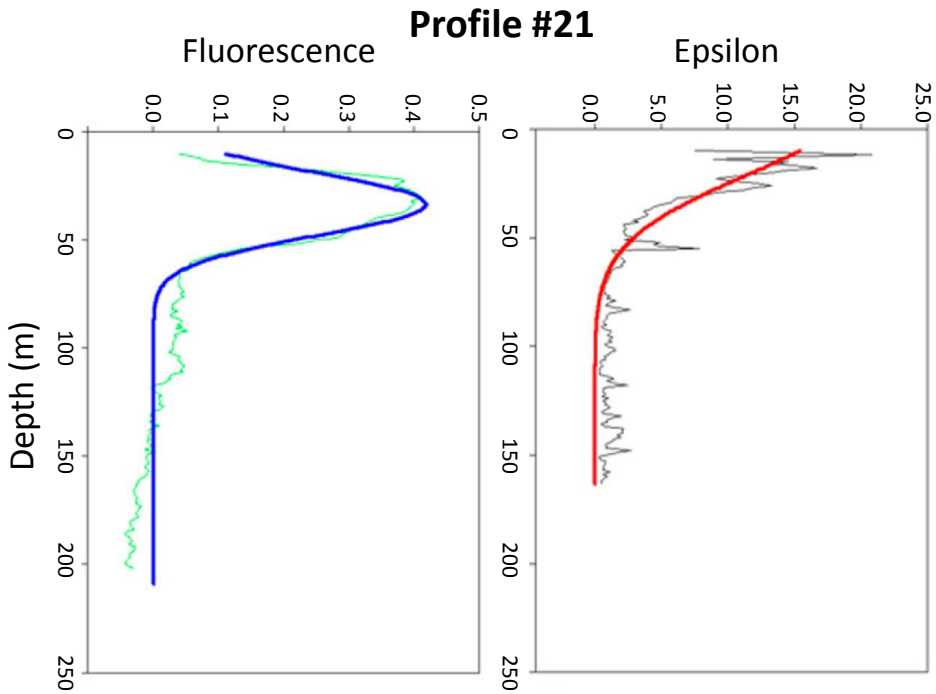
Profile #21
Fluorescence
Epsilon
Depth (m)
0.0
0.1
0.2
0.3
0.4
0.5
0.0
5.0
10.0
15.0
20.0
25.0
0
50
100
150
200
250

(b)

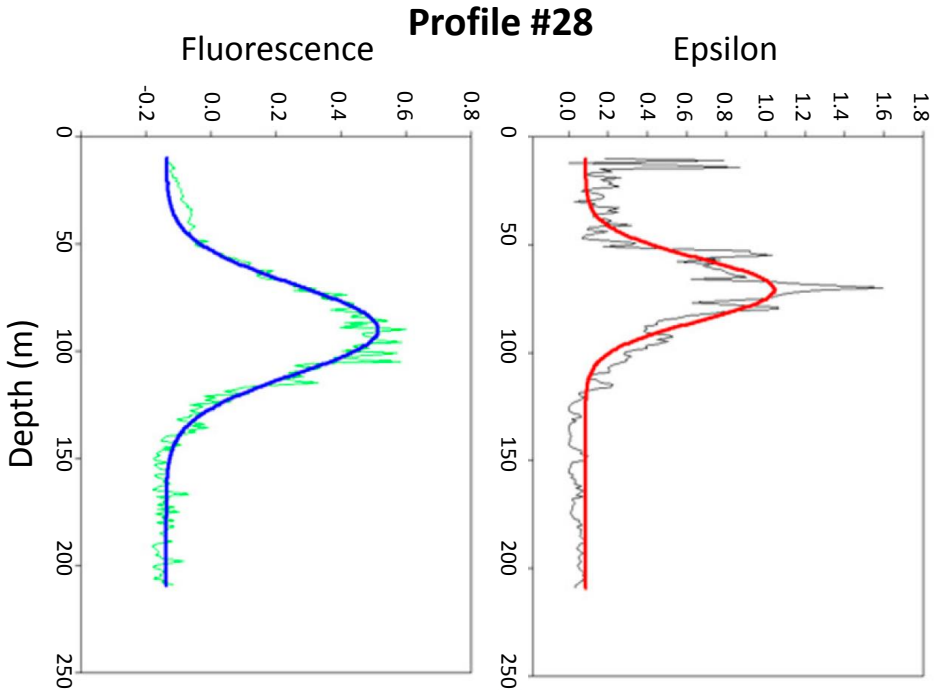

(c)

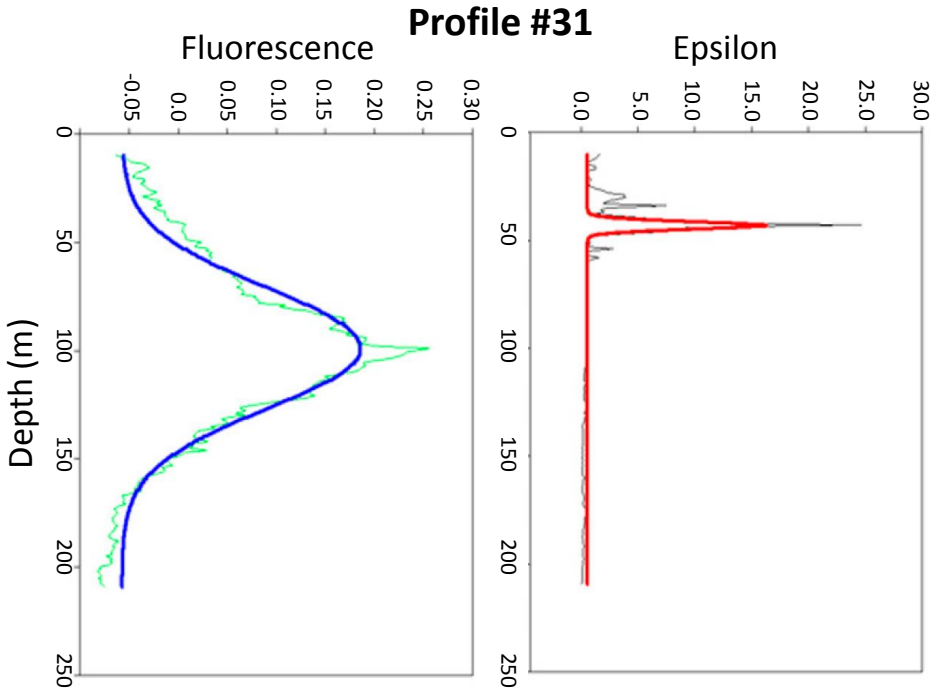

(d)

Figure 6.1: Four illustrative fluorescence (left) and energy dissipation rate (right) profiles taken from Fig. S1 of Macías et al. (2013), showing how DCM are to be found just below $z = \text{peak}_{\text{depth}}$, where $\varepsilon(\times 10^{-7}\ \text{m}^2\,\text{s}^{-3})$ achieves its maximum value. (a) is from the Alboran Sea, (b) is from the Strait of Gibraltar, (c) is near the Antarctic Peninsula and (d) is from the North Atlantic. Further similar profiles are presented in Macías et al. (2013).

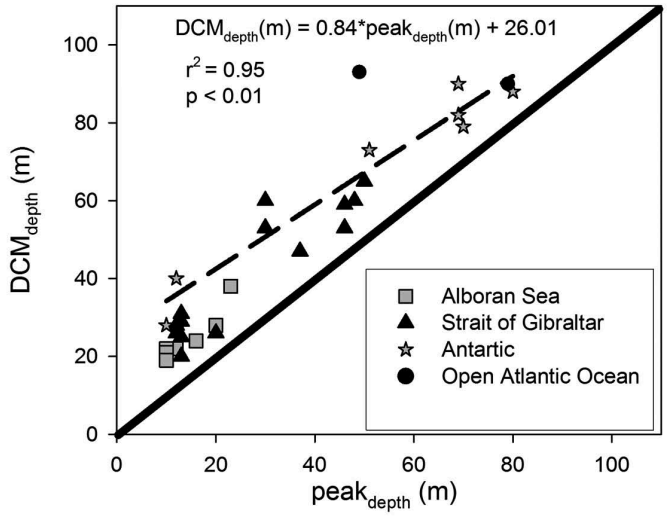

Figure 6.2: Location of $\mathrm{DCM}_{\mathrm{depth}}$ compared to $\mathrm{peak}_{\mathrm{depth}}$ for each of the 31 profiles from Macías et al. (2013) classified as "matching". The dashed line represents the linear fit to the data. The figure is taken from Macías et al. (2013) figure 3a.

profiles classified as matching, i.e. $\mathrm{DCM}_{\mathrm{depth}} \in [\mathrm{peak}_{\mathrm{depth}} - \mathrm{peak}_{\mathrm{width}}, \mathrm{peak}_{\mathrm{depth}} + \mathrm{peak}_{\mathrm{width}}]$. This demonstrates the statistically significant relationship between $\mathrm{DCM}_{\mathrm{depth}}$ and the sub-surface $\mathrm{peak}_{\mathrm{depth}}$. A further negative correlation was found between $\mathrm{DCM}_{\mathrm{depth}}$ and ε near $\mathrm{DCM}_{\mathrm{depth}} \pm \mathrm{DCM}_{\mathrm{thick}}$, which indicates that high fluorescence values are associated with low levels of turbulence within the upper mixing layer. It is important to note that the matching criteria is applied to the measured levels of fluorescence and ε, rather than the Gaussian approximations. This can be seen in figures 6.1a and 6.1d where the approximation to the DCM appears to lie outside of the matching criteria, whereas the data (green plot on the figure) lies within the required region to be a match. Figure 6.3 shows the depth of the Gaussian approximations to $\mathrm{DCM}_{\mathrm{depth}}$ and associated approximation to $\mathrm{peak}_{\mathrm{depth}} \pm \mathrm{peak}_{\mathrm{width}}$, for each of the profiles denoted as "matching" by M13. The black $*$ and bounds represent the matching criteria, as measured by the Gaussian approximation to ε (the peaks and half-widths for ε and fluorescence are presented in the appendix of M13). In each case the location of the approximated fluorescence peak lies either within, or below, the matching criteria. With only a few exceptions, this is below the ε $\mathrm{peak}_{\mathrm{depth}}$. This demonstrates a strong anti-correlation between turbulent intensity and fluorescence. The dissociation between the actual measurements, used to classify the results, and the Gaussian approximations is illustrated in the differences between figures 6.2 and 6.3. Differences are particularly evident for the results from the North Atlantic site.

These aren't the first results that demonstrate a relationship between DCM and regions of low turbulence, see for example Cullen and Eppley (1981), Estrada et al. (1993), Yamazaki et al. (2010). However, most of the previous works have approximated the level of turbulence by vertical eddy diffusion. M13 is to the best of the authors' knowledge the first paper to describe the existence of a consistent relationship between DCM and ε in a wide variety of ocean environments.

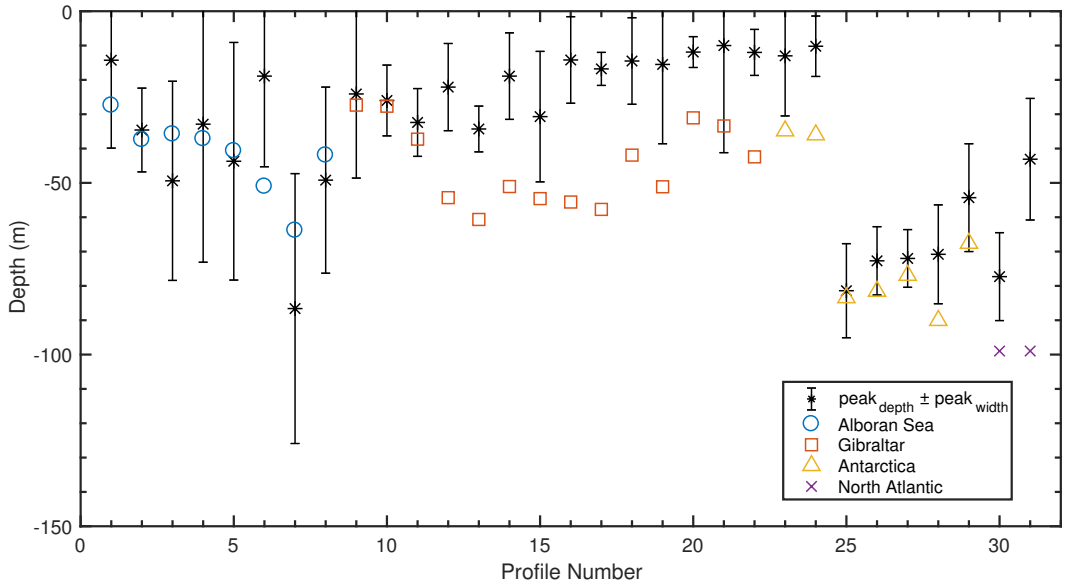

Figure 6.3: Location of the Gaussian fit for $\mathrm{DCM_{depth}}$ relative to the fit for the $\mathrm{peak_{depth}}$ and matching criteria $\mathrm{DCM_{depth}} \in [\mathrm{peak_{depth}} - \mathrm{peak_{width}}, \mathrm{peak_{depth}} + \mathrm{peak_{width}}]$ for each of the 31 "matching" profiles from Macías et al. (2013). The ✻ data points and bounds correspond to the location and half-widths (respectively) of the Gaussian band for the $\mathrm{peak_{depth}}$ in each profile (see appendix of M13). The location of the Gaussian band peak for fluorescence is shown by the data points indicated in the legend.

The location of the DBM (deep biological maxima) relative to its associated DCM is typically assumed to correlate exactly. However, because the chlorophyll-to-carbon ratio is not constant and increases with depth (and can vary widely with species) there is some experimental evidence that the location of the DBM can lie deeper than the observed DCM (Longhurst and Harrison 1989, Pérez et al. 2006, Cullen 2015, Mojica et al. 2015). This displacement typically occurs in relatively stable boundary layers, such as those found in tropical waters; however these conditions do pertain for the locations studied by M13. Hence it is assumed that the DCM is equivalent to the DBM in these cases. M13 point out that the later-summer and early-autumn DCM location coincides with a net rate of carbon accumulation (Macías et al. 2008), similarly, in the sampling location of the Antarctic Peninsula it was found that the chlorophyll concentration was highly correlated with total microbial biomass throughout the austral summer (Karl et al. 1991). A dissociation between DCM and DBM occurred most often at the North Atlantic site. In that instance the DCM appeared below 80 m, and M13 argued that at such depths light is a limiting factor which explains why the results from this region differ substantially from the other three locations.

M13 hypothesise that these observations of DCM in absence of stratification occur when appropriate physical and biological conditions exist, namely the juxtaposition of two vertically opposing gradients of resources - light and nutrients (Longhurst and Harrison 1989). The two vertically opposing gradients of light and nutrients form an optimal window for DCM formation. This seems to be a plausible hypothesis, although it is likely to be modulated by other factors. For example the action of turbulent motions continually acts to redistribute any accumulation of planktonic particles. So the observation of a DCM implies that there must

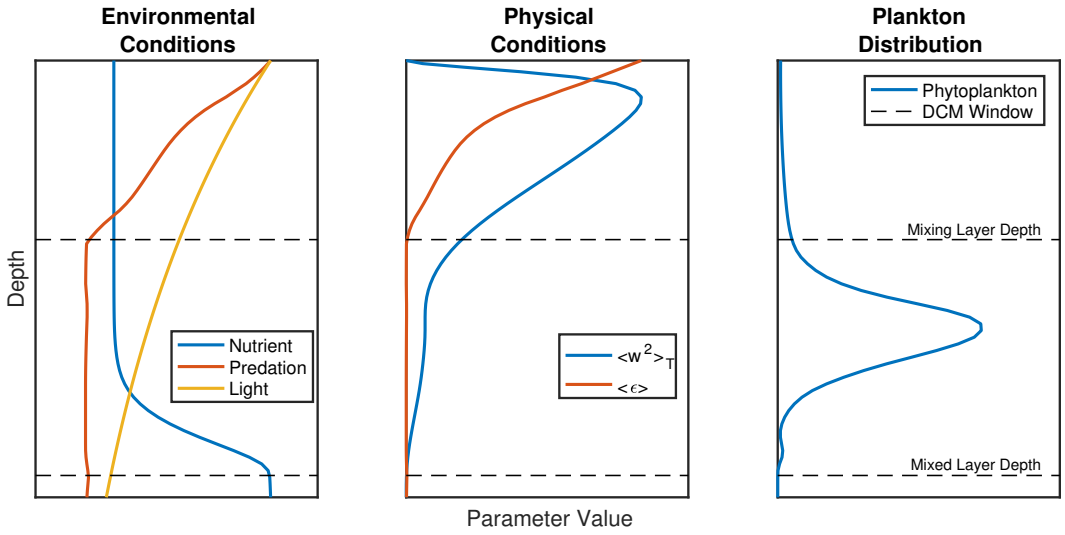

Figure 6.4: Illustration of the suitable region for DCM formation. The intensity and exact position of the DCM is determined by a combination of the favourable physical (low mixing) and environmental (high nutrient and light resources) conditions. The region between the mixing layer depth and the mixed layer depth is the DCM window.

be some mechanism underlying its formation which overcomes this natural mixing process. Figure 6.4 illustrates this idea of an optimal window for DCM formation. The top layer is referred to as the mixing layer and is a region of high mixing (indicated by the topmost dashed line), the second dashed line is the depth of the mixed layer. The intensity and position of the DCM within the region of the mixed layer below the mixing layer depth is determined by a combination of the environmental factors and hydrological conditions. In the profiles in which the a subsurface ε maxima that did not meet the "matching" criteria, M13 observed that the ε-peak was located near a stratified region of the water-column whereas the DCM-peak was located in a region of weaker stratification within the mixed layer. This suggests that discontinuities within the water column, such as the thermocline or pycnocline, can hinder the turbulent redistribution of planktonic matter. M13 also highlight the role of cells sinking faster out of high turbulence zones and accumulating in regions of low vorticity below $\text{peak}_{\text{depth}}$, which is supported experimentally by Ruiz et al. (2004).

Another regulatory important factor is the predation of zooplankton on phytoplankton, summarised in chapter 5. The gradient of this predation is known to be strongly dependent on the level of background turbulence (Rothschild and Osborn 1988, Lewis and Pedley 2000, 2001, Lewis et al. 2017). So in a sense it can be classified as both an environmental and physical factor (figure 6.4) that influences the DCM window. Understanding the role played by planktonic predation in regulating DCM formation and persistence is one of the main goals of this work.

6.3 Intensity/aggregation statistics

In order to establish the connection between the level of turbulence and biological subsurface maxima it is helpful to introduce an intensity measure of the form

$$I_P(z,t) = \begin{cases} \dfrac{\langle P'^2 \rangle_I}{\langle P \rangle_I^2} & \text{if } \langle P \rangle_I \geqslant 0.1 \\ 0 & \text{otherwise} \end{cases} \tag{6.3.1}$$

from Lewis (2005), Brereton (2013), Brereton et al. (2018). Here $P = \langle P \rangle_I + P'$, where the triangular brackets represent a horizontal average, and the primed quantity denotes a fluctuation from the horizontal mean. If $\langle P \rangle_I$ is very small then the fraction $\langle P'^2 \rangle_I / \langle P \rangle_I^2$ will be large by definition, since this is of little interest the value of I_P is set to zero for $\langle P \rangle_I < 0.1$ in equation (6.3.1). This measure is typically used to establish the existence of horizontal planktonic patchiness. However, it can also be used to determine the depth at which turbulent mixing is low enough to facilitate the formation of a DBM. If I_P is small then the population is homogeneous and well mixed, whilst high values of I_P indicated a more heterogeneous population indicative of reduced levels of background turbulence. When there is a higher level of heterogeneity in the phytoplankton field this indicates that the planktonic growth is, to some extent, able to overcome the homogenising tendencies of the turbulent mixing. In this low mixing scenario there will also be fewer predator-prey interactions, resulting in a lower predation rate. This will stimulate higher growth rates leading to patches of higher phytoplankton concentrations.

The time-evolution of the maximum value of $I_P(z,t)$ for a simulation with $(U_*, U_S) = (3.0, 3.3)$ is shown in figure 6.5a. The level of heterogeneity is not consistent over time, the peaks and troughs are aligned with the growth cycles of the phytoplankton. The corresponding depth at which the maximum value occurs is shown in figure 6.5b. In order to get a clearer idea as to the level of heterogeneity it is often more convenient to consider the time average of $I_P(z,t)$, this is given by

$$I_{P\,av}(z) = \frac{1}{T_{sim}} \int_0^{T_{sim}} I_P \, \mathrm{d}t \tag{6.3.2}$$

where T_{sim} is the simulation time. The depth at which $I_{P\,av}(z)$ takes its maximum is denoted as z_{opt}. The time-evolution of $I_P(z_{opt}, t)$ is plotted as dashed lines in figure 6.5a. The evolution closely matches that of $\max_z(I_P(z,t))$ and indicates that z_{opt} is a good approximation to the depth at which there is the highest level of heterogeneity. This depth, z_{opt}, is indicated by the dashed line on figure 6.5b. Profiles of $I_{P\,av}$ for simulations at $(U_*, U_S) = (3.0, 3.3)$ over a depth of $z_S = 30$ m with a base (and surface) flux of nutrients are shown in figures 6.6a (and 6.6b respectively). Profiles of I_P at various times are plotted in the finer dashed lines. Whilst the maximum level of heterogeneity does change significantly over time, the average of the measure does provide useful information on the overall heterogeneity of the phytoplankton

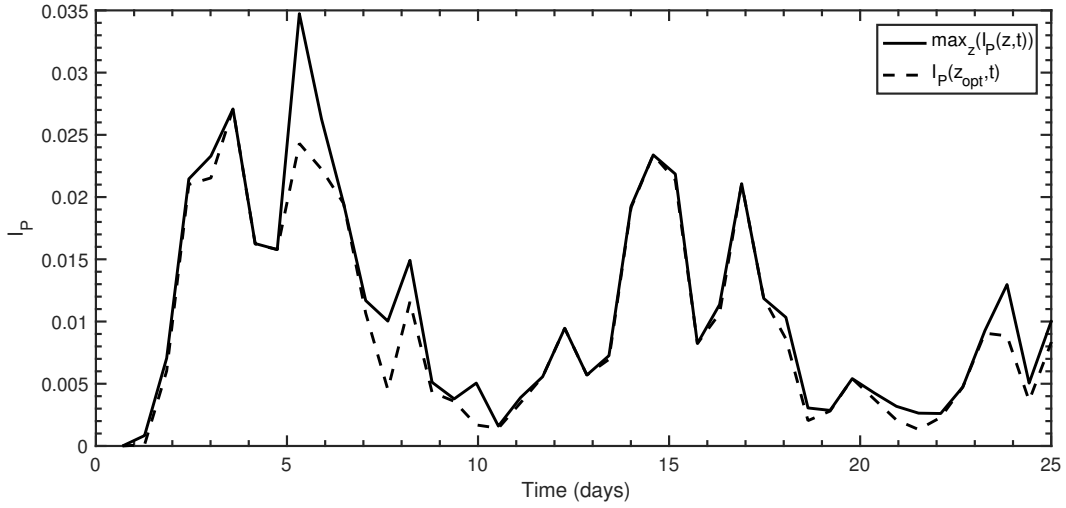

(a)

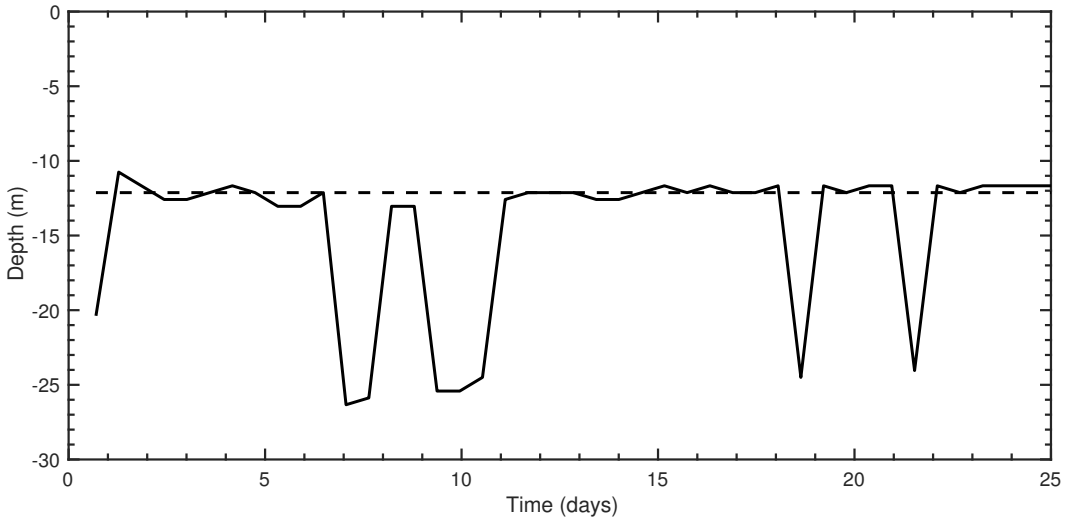

(b)

Figure 6.5: Time evolution of (a) $\max_z(I_P(z,t))$ and $I_P(z_{opt},t)$, (b) Depth of $\max_z(I_P(z,t))$. Taken from a LES-NPZ simulation for $(U_*, U_S) = (3.0, 3.3)$ over a depth of $z_S = 30$ m with the nutrient flux at the base of the simulation layer $z = z_S$. The dashed line in (b) is the line $z = z_{opt}$.

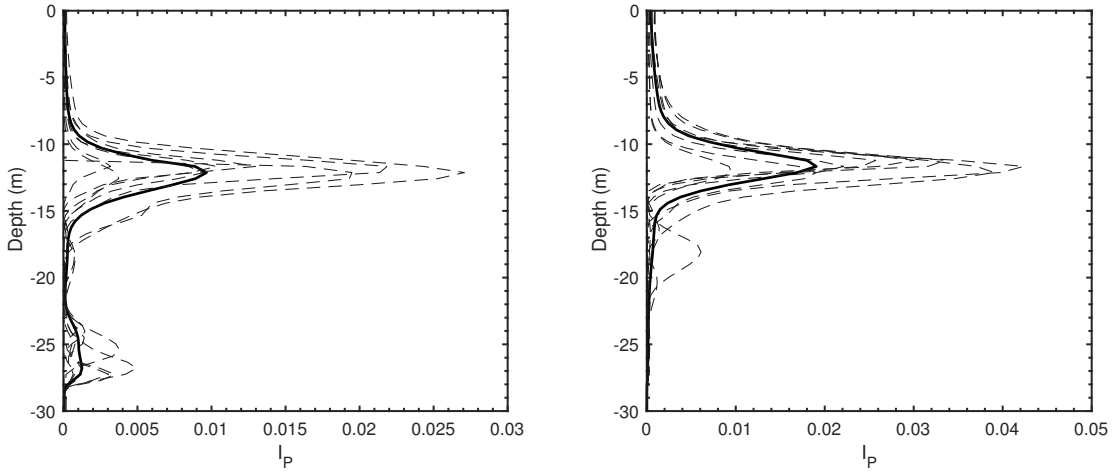

Figure 6.6: $I_{P\,av}(z)$ for a LES-NPZ simulation for $(U_*, U_S) = (3.0, 3.3)$ over a depth of $z_S = 30$ m with nutrient flux at the (a) base $z = z_S$, (b) surface $z = 0$. Finer dashed lines are $I_P(z,t)$ at different times.

population within the boundary layer. The first 10 m of the boundary layer are highly turbulent, and well mixed, as indicated by the low values of $I_{P\,av}$. In both cases, there is a subsurface peak in $I_{P\,av}$ at 12 m, which means that the level of turbulence has subsided, and the P field is more heterogeneous as a result. Below this peak, the phytoplankton population starts to increase, and a DBM forms (this is shown in figure 6.7). In this region, the phytoplankton population is relatively high, and dominates the fraction (6.3.1), which means I_P is low as result. It is important to note that high I_P does not necessarily correlate with high $\langle P \rangle_I$, however a subsurface peak can given an indication that the level of turbulence has declined and the P population is becoming more heterogeneous.

A similar measure for the nutrient will be used in section 6.6 in passive tracer (LES + Nutrient only) simulations in order to determine the mixing depth z_{ML} of the boundary layer.

6.4 Nitrate boundary conditions

In all of the simulations that have been considered so far the flux of nutrients into the boundary layer has been located at the base of the simulated boundary layer, at $z = z_S$. However, in the instances where $z_S \gg z_{TD}$, this is not very useful, since there is little or no mixing at this depth. Consequently the nutrients may not reach z_{TD} during a typical simulation time. To overcome this problem, additional simulations were conducted in which an inward flux of nutrients was imposed at the *surface*, $z = 0$, with the flux at $z = z_S$ set to *zero*. Mathematically this boundary condition is given by

$$\left.\frac{\mathrm{d}N}{\mathrm{d}z}\right|_{z=0} = -\langle wN \rangle \;\; ; \;\; \left.\frac{\mathrm{d}N}{\mathrm{d}z}\right|_{z=z_S} = 0, \tag{6.4.1}$$

where $\langle wN \rangle = -2.8 \times 10^{-10}\ \mathrm{kg\,m^{-2}\,s^{-1}}$. Such a surface flux of nutrients could be attributed to a significant river run-off event (Varela et al. 2005), ash from a volcanic eruption (Frogner et al. 2001), or even by agricultural or industrial pollution (Smith 1998, Carpenter et al. 1998). Whilst some of these processes, in particular those involving pollutants, have many adverse affects to lakes, rivers and coastal waters caused by eutrophication, they can result in increased biomass of phytoplankton and zooplankton. This surface replenishment of nutrient will be used to investigate what changes (if any) occur to the DCM/DBM characteristics under different turbulent regimes when the nutrient source is changed. It will help to analyse whether the DCM occurs directly as a consequence of the nutricline or whether there are additional drivers (physical or biological) behind the formation of DCM/DBM. In the absence of any uptake by phytoplankton, the nutrient can be considered a passive tracer within the water column. This means that when the surface boundary condition is imposed, nutrients should become well-mixed down to the mixing layer depth, before slowly diffusing into the lower layers. As a consequence this will create a gradient at the mixing layer boundary, giving an indication of the turbulent depth.

Figure 6.7 shows the time-averaged profiles of $\langle N \rangle_T$ and $\langle P \rangle_T$ from two simulations with intermediate wind forcing, $(U_*, U_S) = (3.0, 3.3)$ for each of the nutrient (base and surface) boundary conditions. The simulations demonstrate that a DBM does indeed form in the surface flux regime. Nutriclines form for both boundary conditions; bottom-up (base flux) and top-down (surface flux). In both cases this leads to the formation of a DBM at or around the mixing depth near where the nutricline is located. Figure 6.8 shows the evolution of the normalised horizontally averaged instantaneous phytoplankton population, $\langle P \rangle_I$, for each of the two nutrient boundary conditions described above. The DBM exhibit the typical oscillatory behaviour of the NPZ system, detailed in section 3.3. These oscillations appear as a consequence of the growth and predation cycles of the P and Z fields respectively. These results look very similar to the experimental datasets of M13, displaying a clear DBM peak at 25 m (base flux) and 23 m (surface flux). The question arises as to why the DBM still forms at the nutricline in the surface flux case. When the nutrient flux is located at the surface, it would be intuitively expected that phytoplankton would grow near the surface where there is an abundance of nutrients and high light levels. However, something is inhibiting surface growth, forcing the phytoplankton to grow at deeper, less optimal, depths. The main hypothesis of this work is that zooplankton predation acts to restrict surface growth, and consequently plays a very important role in DBM formation.

6.5 Studies of DCM/DBM using the LES-NPZ model - Lewis et al. (2017)

In what follows the roles of turbulent mixing, predation pressure, nutrient resources and the correlations between them will be systematically examined with a view to obtaining a better understanding of how DBM, such as those shown in the M13 datasets, can come

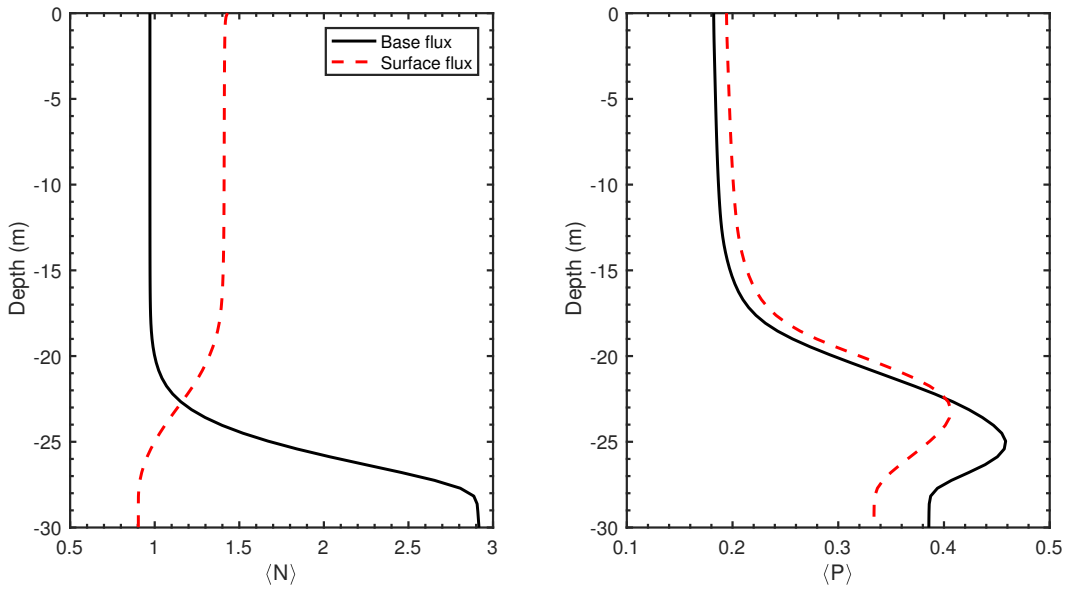

Figure 6.7: Time averaged $\langle N \rangle_T$ (left) and $\langle P \rangle_T$ (right) profiles for the two nutrient boundary conditions, base (solid, black) and surface (dashed, red) flux of nutrient into boundary layer. Taken from a LES-NPZ simulatio for $(U_*, U_S) = (3.0, 3.3)$ (intermediate wind forcing), with the normalised (N, P, Z) fields starting from initial values (1.0, 0.5 and 0.5) respectively.

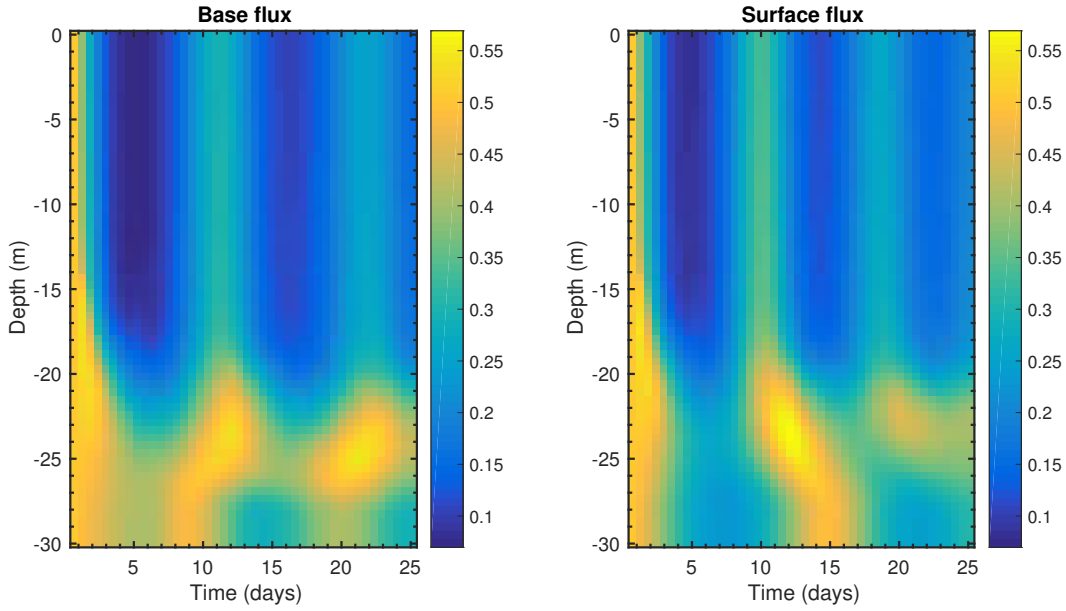

Figure 6.8: Evolution of phytoplankton ($\langle P \rangle_I$) for the two nutrient boundary conditions, base (left) and surface (right) flux of nutrient into boundary layer. Taken from a LES-NPZ simulation for $(U_*, U_S) = (3.0, 3.3)$ (intermediate wind forcing), with the normalised (N, P, Z) fields starting from initial values (1.0, 0.5 and 0.5) respectively.

about. The LES-NPZ model presented in chapters 2 and 3 along with the boundary conditions described above is an ideal tool for analysing the various physical and biological drivers of DBM formation. Each boundary layer is generated by a fixed wind forcing summarised by the U_* and U_S parameters. These simulations will be characterised by notation of the form (U_*, U_S), such that a boundary layer with $U_* = 3.5 \times 10^{-3}$ m s^{-1} and $U_S = 3.9 \times 10^{-2}$ m s^{-1} will be denoted by $(U_*, U_S) = (3.5, 3.9)$. The boundary layers are generated using the procedures outlined in section 3.6.

6.5.1 Sensitivity to wind forcing

The first set of simulations were designed to investigate the sensitivity of DCM/DBM formation to wind forcing. To achieve this, three different wind driven, Stokes-Ekman boundary layers (each with a simulation depth $z_S = -50$ m) were spun up, with parameter settings $(U_*, U_S) = (2.0, 2.2)$, $(3.0, 3.3)$, and $(4.0, 4.4)$, corresponding to "low", "intermediate", and "strong" wind forcing regimes, respectively (the terminology "strong" is only comparative, since it represents a windspeed of only around 4 m s^{-1}). Figure 6.9a-6.9c show the energy dissipation rate profiles for each of the three boundary layers in turn, alongside the corresponding profiles of zooplankton predation. Derived from the initial spin up run, these average profiles remain fixed throughout the subsequent biological simulation. The dissipation profiles show a progressive increase in the near surface maximum dissipation rates (0.65×10^{-7}–2.0×10^{-7} m^2 s^{-3}) with wind forcing, and a corresponding deepening of the mixing layer. In each case, the dissipation rate falls to (almost) zero around about half the turbulent depth $z_{TD}/2$, equivalent to 10 m, 15 m, and 20 m, respectively. The predation rate profiles are calculated for a relatively small predator length scale $r_Z = 5 \times 10^{-5}$ m, possessing a spherical perception field of radius $R = 2 \times 10^{-3}$ m, with an average swimming speed $\sigma_Z = 5 \times 10^{-5}$ m s^{-1}, with a reaction time $T_R = 5$ s (see Table 3.2). These profiles are all fairly similar near the surface (as the reaction time limits the number of possible captures, despite the increase in predator-prey contacts as a consequence of higher dissipation rates), falling away at different rates, before levelling off at $\sim 10^{-9}$ m^3 s^{-1} near $z_{TD}/2$. Since $\varepsilon(z < z_{TD}/2) \approx 0$ and the flow is relatively quiescent, the predator is forced to rely on its swimming capabilities alone in order to find prey. This means the predation rate is almost constant for $z < z_{TD}/2$.

Figures 6.10a–6.10c show the corresponding evolution of the biological $(\langle N \rangle_I, \langle P \rangle_I, \langle Z \rangle_I)$ profiles over the simulation time T_{sim}, assuming a maximum phytoplankton growth rate of $\mu_P^{\max} = 5 \times 10^{-5}$ s^{-1}. Here the triangular brackets, $\langle \cdot \rangle_I$, refer to an instantaneous 2d (horizontal) average. In these simulations, nutrient supplies are constantly replenished by a uniform flux into the boundary layer at the base, $z = z_S$, of the simulation domain, described by equation (3.4.9). This nutrient replenishment outweighs the losses through phytoplankton growth, the result is the steady formation of a nutricline, with significantly higher nutrient concentrations at the base of the domain compared to the surface. Consider the low wind,

$(U_*, U_S) = (2.0, 2.2)$, case in figure 6.10a first. The mixing layer of $z_{ML} = z_{TD}/2 = 10$ m is relatively shallow, insufficient to mix the additional nutrients from the base of the domain towards the surface region, so these nutrients simply accumulate in the lower regions, very slowly diffusing further into the layer. Nonetheless, the initial nutrient level $N = 1.0$ is already sufficient to support immediate P growth. However, this initial growth is not uniformly distributed across the boundary layer. Instead a DBM forms from a depth $z = 8$–15 m, in the region of the point $z_{ML} \approx z_{TD}/2$ where $\varepsilon(z) \approx 0$. The numerical DBM is a transient feature, lasting about 2-3 days or so because, just as in the simplified model illustrated in section 3.3, the growth in the P concentration promotes a response from the zooplankton population. This DBM is somewhat similar to those presented by M13 (figure 6.1). A numerical DZM forms at a similar depth and with similar structure but somewhat after the DBM, consuming the latter before itself dies off. This restores the biological fields to a uniform (not the initial) state at around 8-10 days, the oscillation timescale, from section 3.3, for this system is approximately 6 days.However, This is not the full story, a little later a second DBM forms and extends deeper into the boundary layer, with decreasing magnitude and subject to some time dilation due to decreasing light levels. This results in intense phytoplankton growth at 45–50 m at the base of the domain, where the nutricline is forming, on a similar timescale. This DBM is apparently not subject to the time dilation that occurs in the regions above. This is because the increased nutrient presence effectively counters the reduction in the attained phytoplankton growth rate due to the lower light levels. Mathematically, increasing (or decreasing) the light, or nutrient, levels, whilst keeping the other constant, has the effect of increasing (or decreasing) the phytoplankton growth rate (equation (3.2.19)). At this depth, the light levels are low, which means that the growth rate declines. However, the nutrients are relatively abundant here, which increases the growth rate. These two effects combined with the low level of predation (figure 6.9a) allow this magnitude of population on a timescale similar to that achieved at the surface. As in the previous cycle, this phytoplankton growth initiates a response from the zooplankton, which forms two deep zooplankton maxima of similar structure to that of the phytoplankton. The formation of this deeper DBM supports the idea that the presence of the nutricline is a driver in DBM formation. However, this does not account for the initial DBM at $z = z_M$, the location and form of this DBM is similar to those recorded in the experimental datasets shown in figure 6.1 (which are for DCM). This illustrates that the results of M13 are important, since most other observational reports on DCM do not include any corresponding measure of turbulent mixing. This numerical modelling work supports M13's observations that the two are correlated.

For the moderate wind, $(U_*, U_S) = (3.0, 3.3)$, simulation shown in figure 6.10b, the results are broadly similar. Again the inital phytoplankton growth occurs in the region of $z_{ML} = z_{TD}/2 = 15$ m which is still too shallow for much of the replenishment nutrient added at $z_S = 50$ m to be mixed into the surface region. As before this initial DBM forms and persists for about 5 days, before being consumed by the zooplankton, which itself dies out through lack of food after about 10 days. After 12 days a second DBM forms just below z_{ML} and

extends deeper into the boundary layer before increasing in intensity in the region of the nutricline. The growth in the region between $0.6z_{TD}$ and z_{TD} is most interesting because it forms well above the nutricline. The DBM increases with intensity deeper in the mixed layer as the increased nutrient concentration compensates for the reduced light availability.

In the strongest wind case, (figure 6.10c) the DBM only forms below z_{TD}, in the region dominated by the nutricline after 12 days. In the region above, the predator is strong enough to prevent any significant growth from the phytoplankton population and the growth is uniform throughout this region. The most interesting feature of figures 6.10a and 6.10b are that a DBM forms in the regions well above the nutricline.

6.5.2 Sensitivity to nutrient boundary conditions

Figures 6.11a–6.11c shows the evolution of the biological (N, P, Z) profiles for the same three boundary layers as before, only this time the replenishing nutrient flux is applied at the surface rather than the base (equation (6.4.1)). So unlike in the previous examples, this extra nutrient is mixed throughout the mixing layer, eventually reaching depths close to z_{TD} for the highest wind case of $(U_*, U_S) = (4.0, 4.4)$. Although a surface flux is a somewhat unrepresentative of how nutrient replenishment typically occurs within ocean mixing layers, it provides a means, within the model constraints, of making the extra nourishment readily available to the biological populations in those regions of the water column where DBM formed previously. In all three cases, the initial behaviour is similar to before, however the initial DBM of the low and intermediate wind simulations are of larger magnitude. In the low wind case (figure 6.11a) a second DBM forms after 8-10 days in a similar fashion to figure 6.10a. However, the relative absence of nutrients at the base of the layer means that the DBM in this region occurs much later and appears as a time-dilated extension of the DBM at z_{ML}, unlike the significant growth seen in this region in figure 6.10a. The main effect of adding nutrients to the surface of the boundary layer is to stimulate an additional DBM cycle at z_{ML}. The increase in nutrients in this region has the effect of increasing the (attained) phytoplankton growth rate, allowing for the fourth DBM within the simulation time.

In the intermediate wind case, shown in figure 6.11b, the general behaviour is similar. A second DBM forms after 8 days at just below z_{ML} and extends to the base of the simulation zone, subject to the time-dilation caused by decreased light levels. Similarly to the low wind case, the additional nutrients near the surface has increased the attained growth rate of the phytoplankton, which has allowed for the third predator-prey cycle to be completed, whereas in the equivalent case of figure 6.10b this has cycle only just begun.

This high wind case (figure 6.11c) is very similar to that of figure 6.10c. However, the DBM that forms below z_{TD} occurs much later and is less intense due to the absence of nutrients in this region. The phytoplankton are unable to grow as rapidly and do not reach a similar population before the zooplankton responds. Similarly, the additional nutrient in the surface region above z_{TD} initiates an additional oscillation in this region compared to the

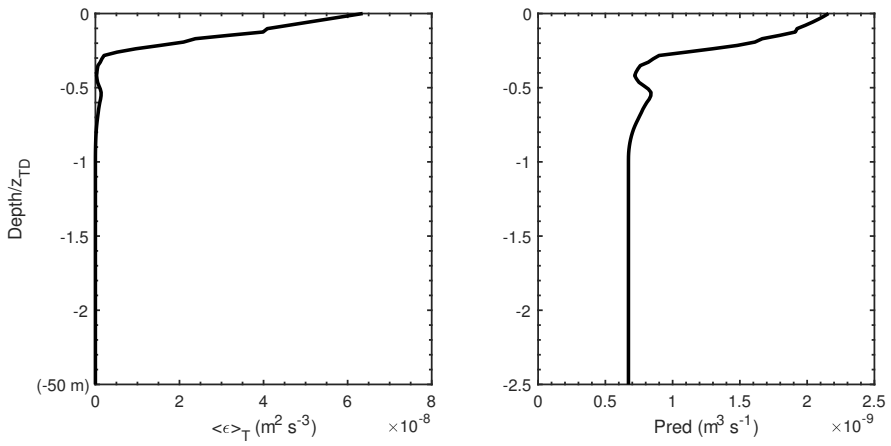

(a)

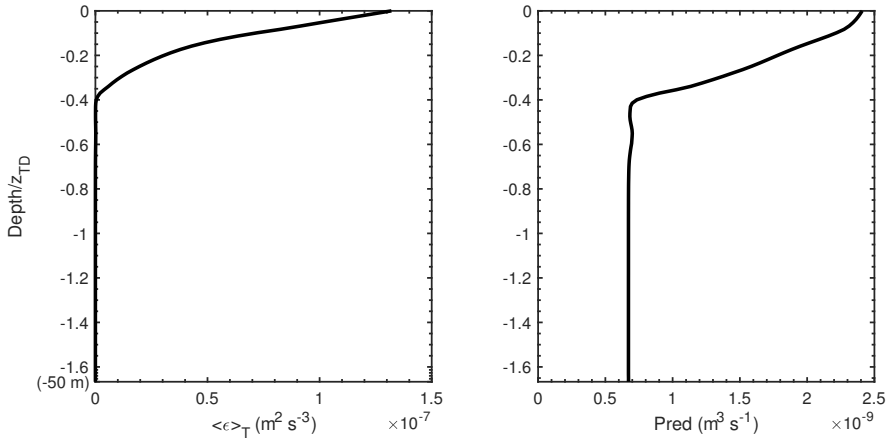

(b)

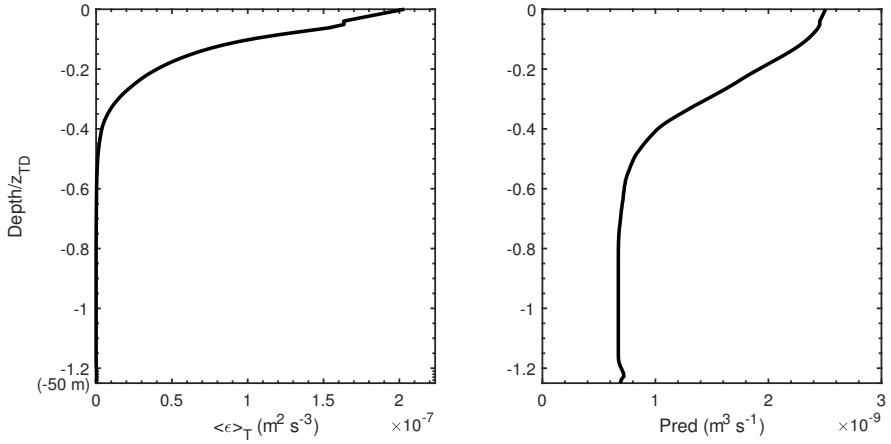

(c)

Figure 6.9: Energy dissipation profiles (left) and the corresponding zooplankton predation rate profiles (right) for the small predator (Table 6.1) taken from three LES-NPZ simulations subject to (a) $(U_*, U_S) = (2.0, 2.2)$, (b) $(U_*, U_S) = (3.0, 3.3)$, and (c) $(U_*, U_S) = (4.0, 4.4)$.

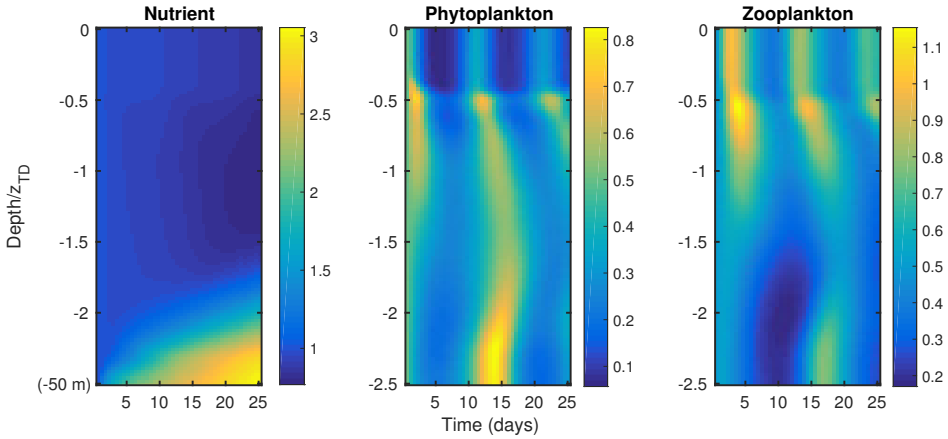

(a)

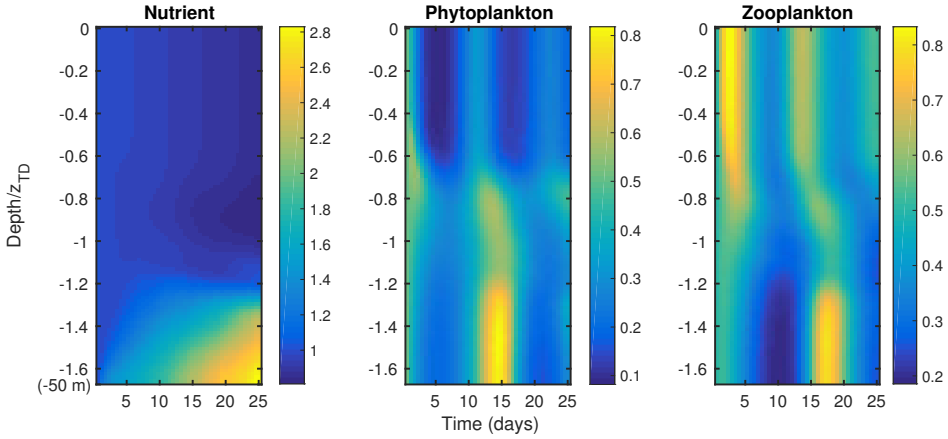

(b)

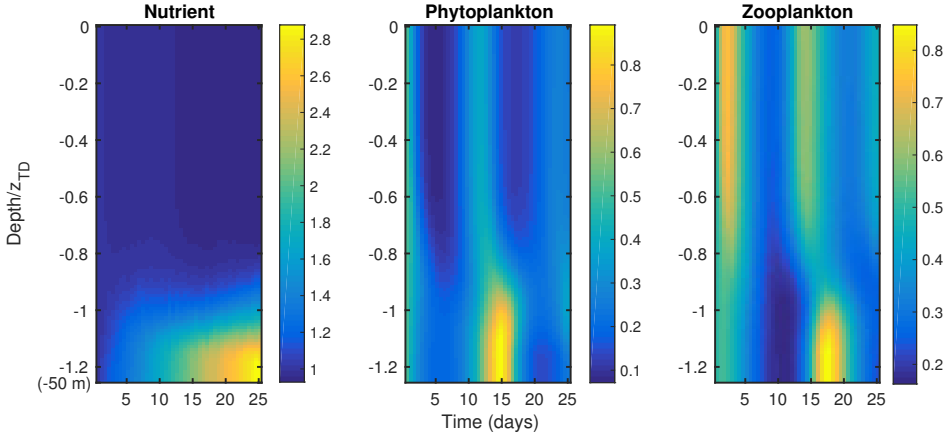

(c)

Figure 6.10: Evolution profiles of the normalised $(\langle N\rangle_I, \langle P\rangle_I, \langle Z\rangle_I)$ concentrations, starting from initial conditions $(1.0, 0.5, 0.5)$ subject to (U_*, U_S) = (a) $(2.0, 2.2)$, (b) $(3.0, 3.3)$, and (c) $(4.0, 4.4)$. An inward flux of nutrients is imposed at the base $z_S = -50$ m. Biological data from table 3.2, incorporating the small predator.

equivalent base flux simulation.

The interesting feature of these simulations is that significant phytoplankton growth occurs below the region of high nutrient, in the same location as the equivalent base flux simulation. Additionally, the zooplankton response is strongest in the near surface regions. This demonstratesthat DBM formation is clearly a fairly robust process and operates independently of changes in the nutrient distribution within the boundary layer. Provided there is sufficient nutrient to support growth, DBM are likely to form in the regions of reduced mixing. It might be expected that the phytoplankton would reside in the surface regions, where nutrient is most abundant, however this is not the case, since the high levels of predation pressure restricts the growth near the surface.

6.5.3 Sensitivity to predation pressure

Further simulations were designed to test how the predation pressure influences the formation of DBM. Firstly, the same set of simulations as in section 6.5.1 were initiated with the relatively small predator replaced with a larger zooplankton species. The key biological parameters for this larger predator are presented in table 6.1, where the formulae used in calculating growth rates, etc., follow table 3.2.

Parameter	Small predator	Large Predator
Background Z concentration Z_0	2×10^4 cells m^{-3}	1×10^2 cells m^{-3}
Z cell radius r_Z	5×10^{-5} m	3×10^{-4} m
Z maximum growth rate $\mu_Z^{\max}$	1×10^{-5} s^{-1}	2.9×10^{-6} s^{-1}
Z death rate $\mu_{Z\,\mathrm{death}}$	4×10^{-6} s^{-1}	1.2×10^{-6} s^{-1}
Z swimming speed σ_Z	5×10^{-5} m s^{-1}	2×10^{-4} m s^{-1}
Contact radius R_{cont}	2×10^{-3} m	1.2×10^{-2} m
Yield Y	3.3×10^{-3}	1.2×10^{-5}

Table 6.1: Key predation parameters for LES-NPZ simulations. Values calculated from the formulae in table 3.2. Background concentration for the large predator calculated to maintain zooplankton bio-volume compared with the small predator.

Figures 6.12a–6.12c show the energy dissipation rate profiles, and corresponding predation rate profiles for each of the three wind speeds used previously. Note that the energy dissipation rate profiles are the same as in figure 6.9. Similarly the predation rates have very similar vertical structure to their small predator counterparts. However, the predation rate of the larger predator is two orders of magnitude stronger than the smaller predator. The predation rate is higher near the surface as the predator benefits from the increase in predator-prey interactions brought about by the highest dissipation rates. In this case the predation rates level off to approximately 10^{-7} $\mathrm{m}^3\,\mathrm{s}^{-1}$ near $z_{TD}/2$. The faster swimming speed allows the larger predator to maintain a significantly higher predation rate than the smaller zooplankton in these lower regions. It is not clear how the background population level for this larger

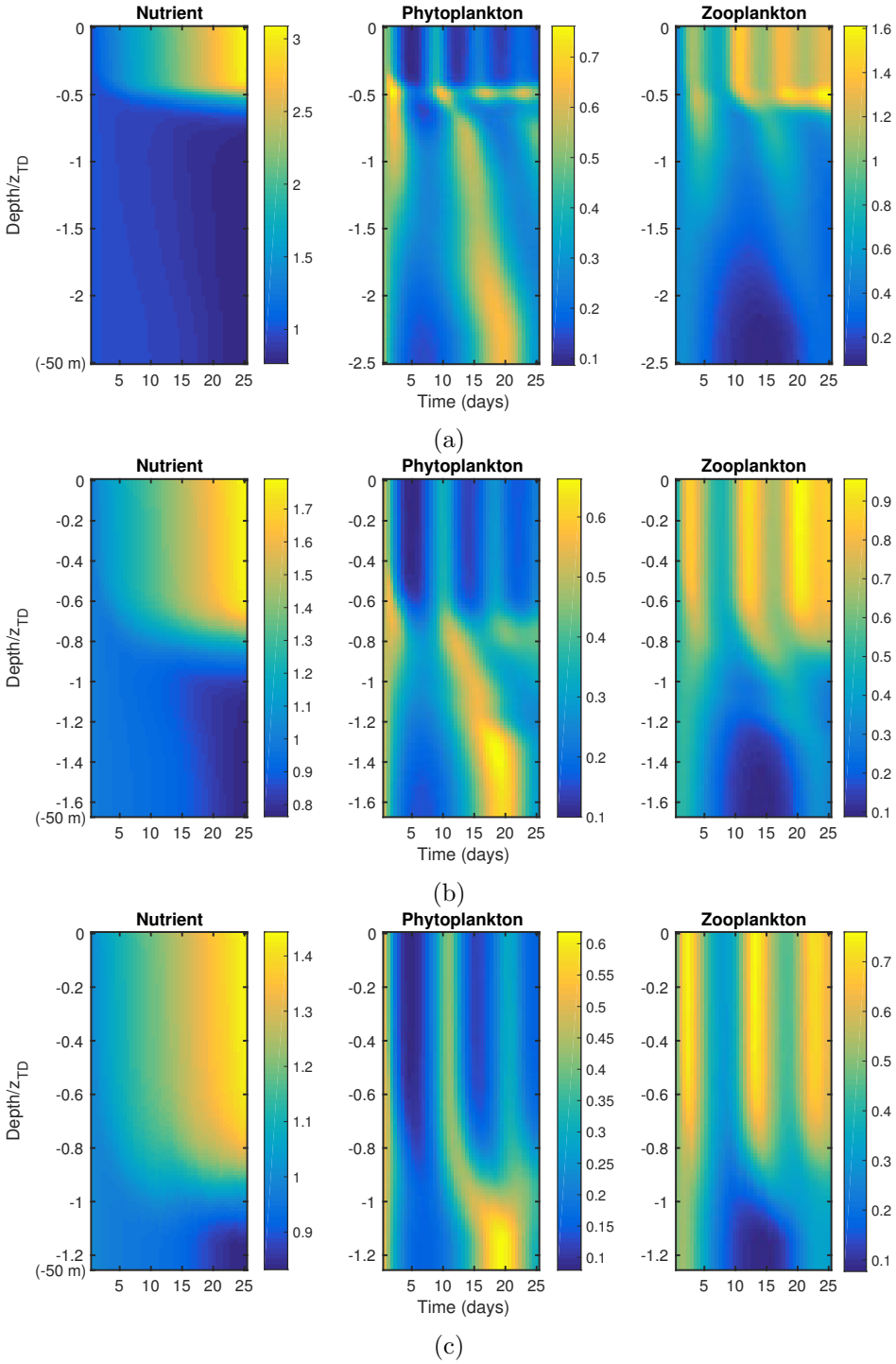

Figure 6.11: Evolution profiles of the normalised $(\langle N\rangle_I, \langle P\rangle_I, \langle Z\rangle_I)$ concentrations, starting from initial conditions $(1.0, 0.5, 0.5)$ subject to $(U_*, U_S) =$ (a) $(2.0, 2.2)$, (b) $(3.0, 3.3)$, and (c) $(4.0, 4.4)$. An inward flux of nutrients is imposed at the surface $z = 0$ m. Biological data from table 3.2, incorporating the small predator.

predator should be chosen in order to keep the two sets of simulations equivalent. There is a natural tendency for there to be larger numbers of small predators. In this case, the initial and background zooplankton populations were calculated to maintain initial and background zooplankton bio-volume. The background concentration is reduced to $Z_0 = 10^2$ cells m^{-3} for the large predator, compared to 2×10^4 cells m^{-3} for the small predator, this significantly offsets the increase in predation rate.

Figures 6.13a–6.13c show the corresponding evolution of the biological $\langle N \rangle_I, \langle P \rangle_I, \langle Z \rangle_I)$ profiles over the simulation time T_{sim}. All other biological parameters, such as the maximum phytoplankton growth rate, are the same as before (from table 3.2). In this set of simulations the nutrient is replenished at the base, $z = z_S$, of the simulation layer. The most obvious difference between figures 6.13 and 6.10 is that only one instance of a DBM forms in each of the large predator simulations. This is because the zooplankton die away at a much slower rate than the smaller predator and so are present for longer. This in turn drives the phytoplankton into near extinction dynamics. Additionally, the phytoplankton reach a higher population level before the zooplankton are able to respond. The result of this is that the minimum oscillation timescale (based on the maximum phytoplankton growth rate) in this case is now 11 days. In the low and medium wind cases (figures 6.13a and 6.13b respectively) the DBM forms at approximately $z_{TD}/2$ as before. However, no such DBM forms in the high wind case. It is worth looking at the high wind cases in more detail. It might be expected that a somewhat less intense maxima should form in the region of $z_{ML} = 25$ m. However, this is not the case, for either large or small predator. Indeed, the DBM forms at around 45 m in the small predator simulations. Consider the normalised horizontally averaged vertical velocity variance profiles, $\langle w^2 \rangle_T$, shown in figure 6.14a–6.14c. For the low and intermediate wind cases these profiles have similar structure to the equivalent $\varepsilon(z)$ profiles. The $\langle w^2 \rangle_T$ profiles are strongest for $z < z_{ML}$, indicating a high level of vertical mixing in this region. In the low wind case this then decays quickly to 0 above z_{TD}, this decay is much slower in the intermediate case. There is a small amount of vertical mixing between z_{ML} and z_{TD} in this case, hence why the DBM is seen slightly lower than $z_{TD}/2$ for $(U_*, U_S) = (3.0, 3.3)$. This is even more pronounced in the high wind case, and the $\langle w^2 \rangle_T$ profile (figure 6.14c) is quite different to the corresponding dissipation rate profile (figure 6.12c). This additional mixing below z_{ML} extends almost to the base of simulation domain and demonstrates that the energy dissipation rate profiles tend to underestimate the level of mixing lower in the boundary layer. The mixing in this region has the effect of mixing zooplankton into this region, despite the lower predation rate, restricting phytoplankton growth. This behaviour is also a feature of other LES ocean boundary layer codes (e.g., McWilliams et al. (1997), Pearson et al. (2015)) which incorporate Langmuir circulations. The inclusion of wave effects characterised by the Stokes drift term has the effect of increasing vertical transport associated with the downwelling jets, carrying fluid lower below z_{ML}, as far as the turbulent depth z_{TD} (Polton and Belcher 2007). This is also evident from the dissipation rate profiles of M13, in particular those from the Antarctic and North Atlantic sites where strong sub-surface peaks

were recorded. In the strong wind case this enhanced mixing extends to $z_{TD} = 40$ m, meaning the DBM forms below this, or not at all (as in the case of the large predator which is strong enough to prevent growth at this depth).

The evolution of the $\langle N\rangle_I, \langle P\rangle_I, \langle Z\rangle_I)$ fields with the large predator subject to a surface replenishment of nutrients, for the three wind speeds, are shown in figures 6.15a–6.15c. As in the small predator case the main difference between figures 6.13 and 6.15 is that the surface flux of nutrients leads to a second oscillation of the (P, Z) growth cycles in the low and medium wind conditions. This is because the increased presence of nutrients in the upper regions of the boundary layer increases the effective phytoplankton growth rate. For the small predator this growth extended to depths below the mixing layer, z_{ML}, of the simulation layer (figure 6.11a). However, this is not the case when the large predator is present. The absence of nutrients means that the effective phytoplankton growth rate at these depths is not enough to overcome the increased predation pressure at $z < z_{ML}$ due to the superior predation capabilities of the larger predator. For the strong wind $(4.0, 4.4)$ simulation, the extra vertical mixing prevents the formation of either a primary or secondary DBM, much as before.

The case of a non-swimming predator

Figures 6.16a–6.16b show the evolution of the normalised $\langle N\rangle_I, \langle P\rangle_I, \langle Z\rangle_I)$ fields subject to $(U_*, U_S) = (3.0, 3.3)$. In this case the small predator is non-swimming, i.e. $\sigma_Z = 0$. The result of this is that the predation rate rapidly decays to 0 below $z = z_{ML}$, as can be seen in figure 6.17. Meanwhile the non-swimming predator attains a similar level of predation to its swimming counterpart (figure 6.9b) near the surface. In the absence of any significant fluid motion ($z < z_{ML}$) the swimming predator is still able to encounter prey (notice that this level of predation is very similar for all three cases in figure 6.9, approximately 0.7×10^{-9} m^3 s^{-1}) at depths $z < z_{ML}$, whereas the non-swimmer cannot. This means that any phytoplankton residing, or growing, in the deeper regions are subject to little or no predation, allowing them to grow unabated. Indeed, the phytoplankton growth below $0.8z_{TD}$ is so strong that it quickly depletes the available nutrients. By contrast no zooplankton are found at these depths because they cannot find food. In figure 6.16a the nutrients are replenished at the base of the simulation layer, $z_S = 50$ m, this inwards flux of nutrients allows for more significant growth below $1.2z_{TD}$ compared to figure 6.16b. However, the increased presence of nutrients close to the surface in figure 6.16b initiates a second DCM at z_{ML} after 20 days, whereas only one complete P, Z-oscillation has occurred at this depth in figure 6.16a. The level of phytoplankton growth in these simulations is unrealistic. The absence of predation means that P grows to $16 - 18$ times the background level, well above what is typically observed.

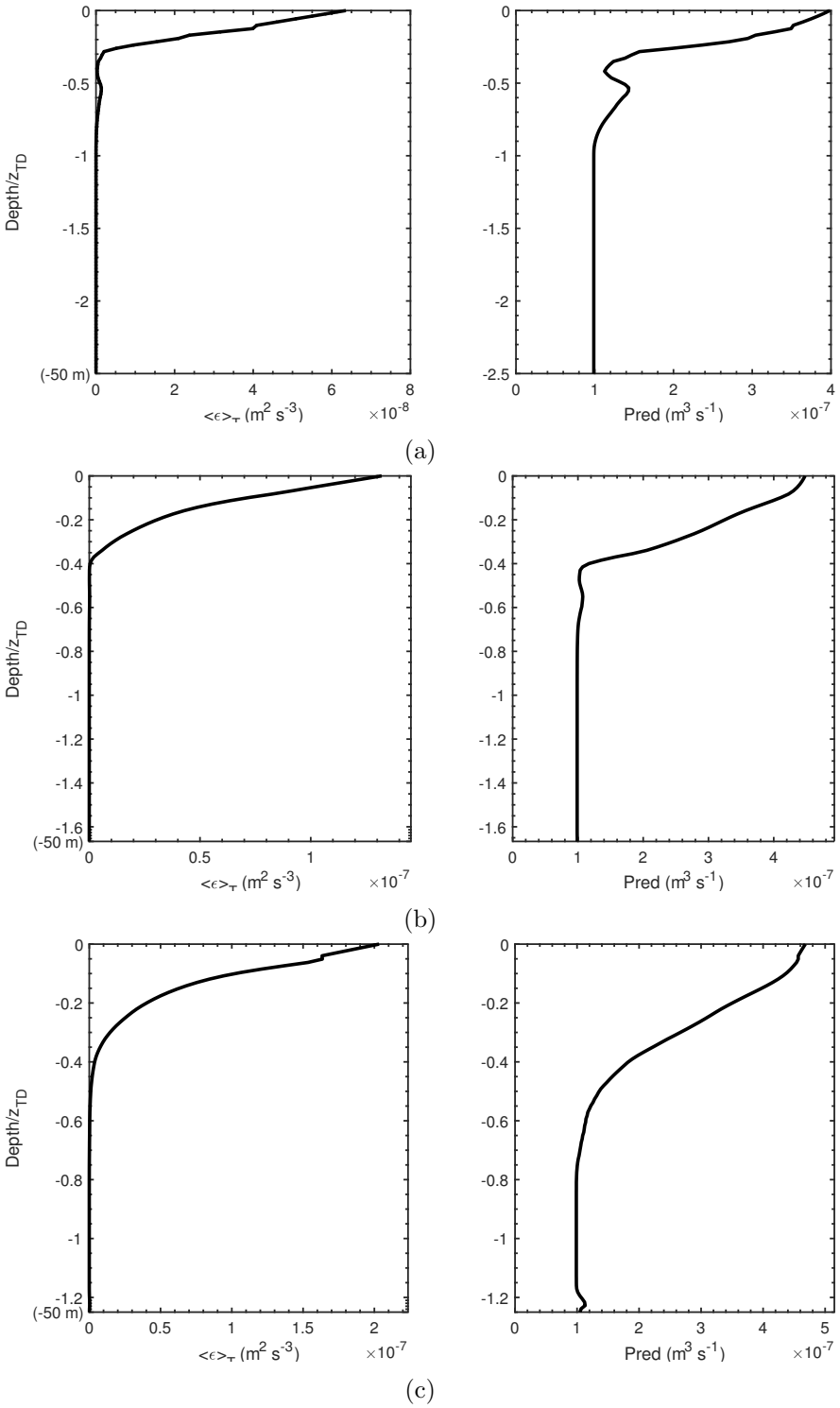

Figure 6.12: Energy dissipation profiles (left) and the corresponding zooplankton predation rate profiles (right) for the large predator (Table 6.1) taken from three LES-NPZ simulations subject to (a) $(U_*, U_S) = (2.0, 2.2)$, (b) $(U_*, U_S) = (3.0, 3.3)$, and (c) $(U_*, U_S) = (4.0, 4.4)$.

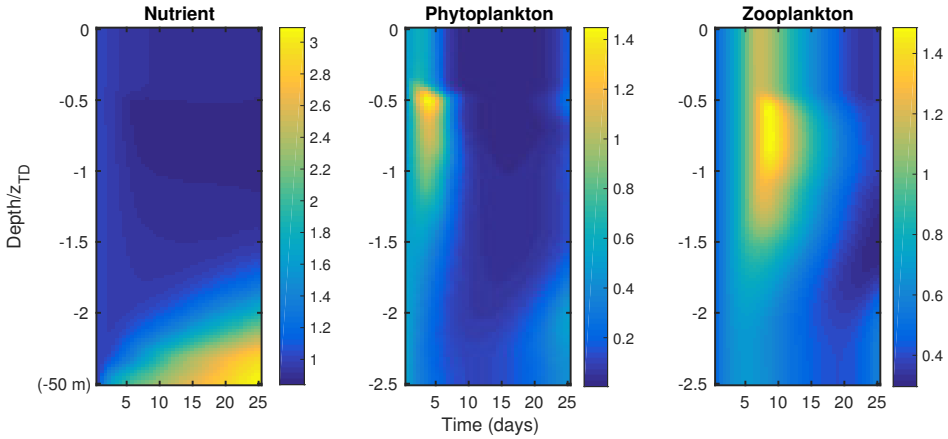

(a)

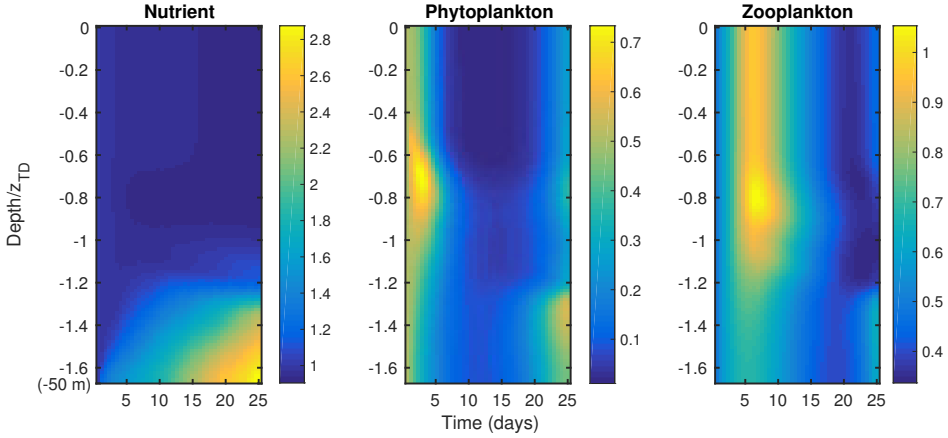

(b)

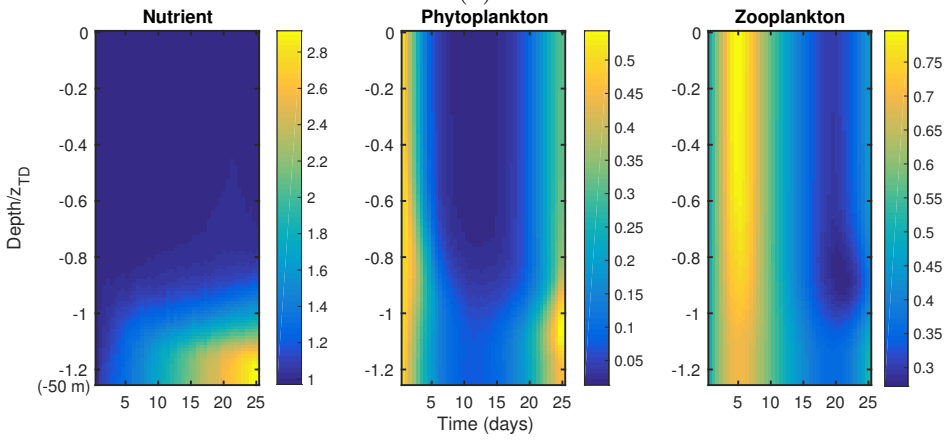

(c)

Figure 6.13: Evolution profiles of the normalised $(\langle N\rangle_I, \langle P\rangle_I, \langle Z\rangle_I)$ concentrations, starting from initial conditions $(1.0, 0.5, 0.5)$ subject to (U_*, U_S) = (a) $(2.0, 2.2)$, (b) $(3.0, 3.3)$, and (c) $(4.0, 4.4)$. An inward flux of nutrients is imposed at the base $z_S = -50$ m. Biological data from table 3.2, incorporating the large predator (table 6.1).

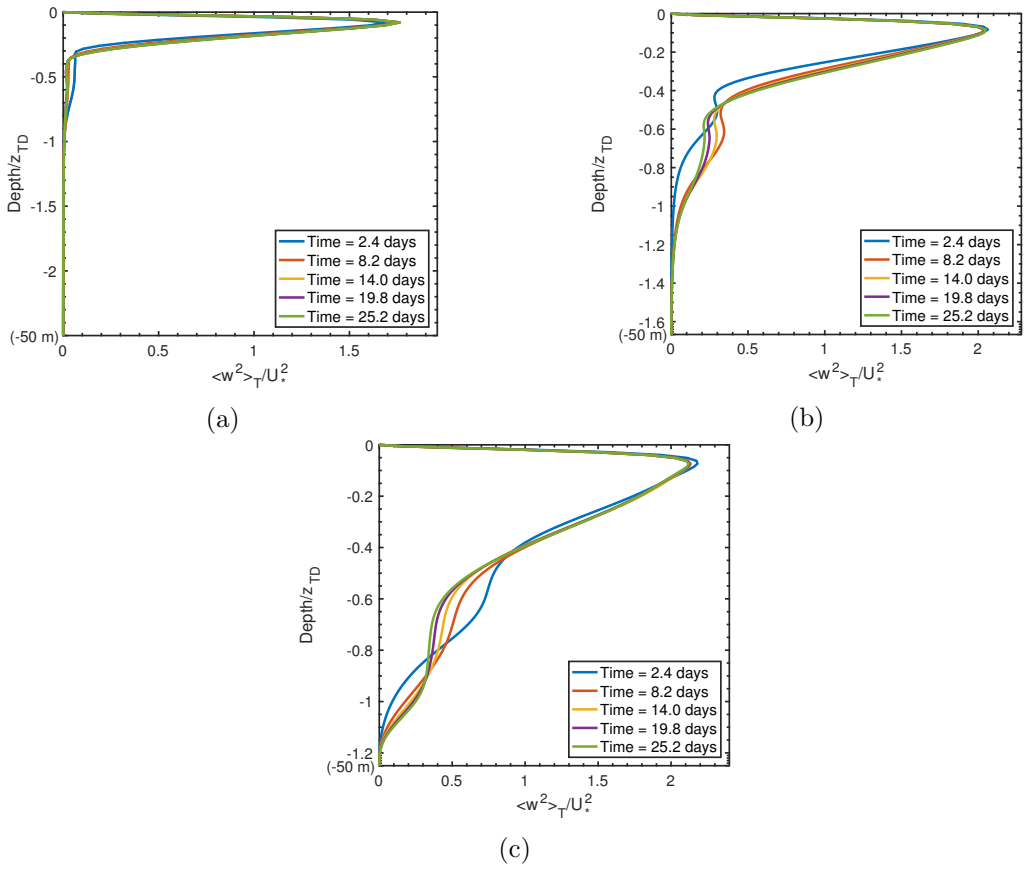

Figure 6.14: Evolution of the normalised, time and horizontally averaged, vertical velocity variance $\langle w^2 \rangle_T$ profile recorded during different stages of a typical set of simulations with (a) $(U_*, U_S) = (2.0, 2.2)$, (b) $(U_*, U_S) = (3.0, 3.3)$, and (c) $(U_*, U_S) = (4.0, 4.4)$.

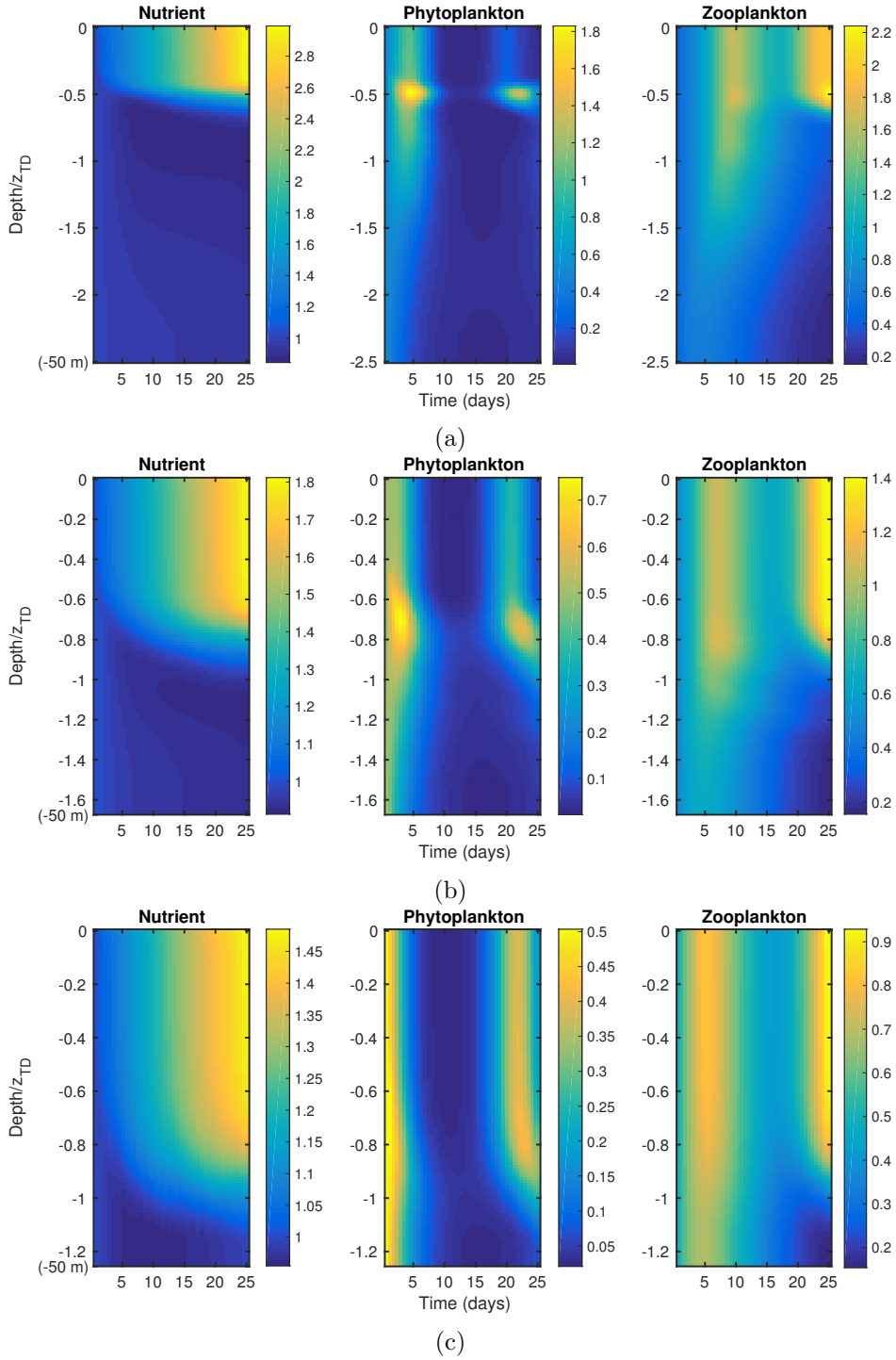

Figure 6.15: Evolution profiles of the normalised $(\langle N\rangle_I, \langle P\rangle_I, \langle Z\rangle_I)$ concentrations, starting from initial conditions $(1.0, 0.5, 0.5)$ subject to $(U_*, U_S) =$ (a) $(2.0, 2.2)$, (b) $(3.0, 3.3)$, and (c) $(4.0, 4.4)$. An inward flux of nutrients is imposed at the surface $z = 0$ m. Biological data from table 3.2, incorporating the large predator (table 6.1).

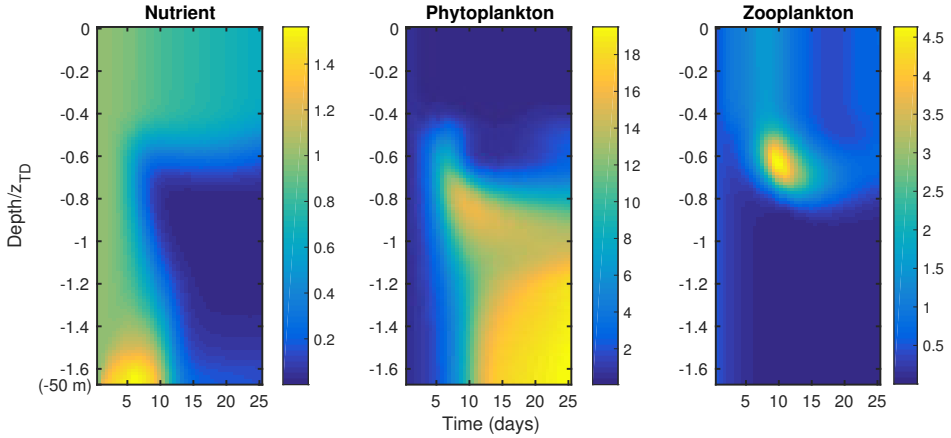

(a)

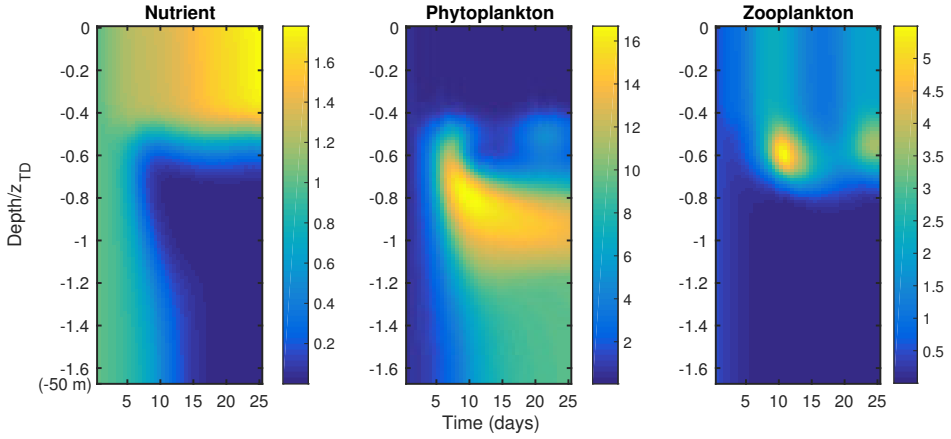

(b)

Figure 6.16: Evolution profiles of the normalised $(\langle N\rangle_I, \langle P\rangle_I, \langle Z\rangle_I)$ concentrations, starting from initial conditions $(1.0, 0.5, 0.5)$ subject to $(U_*, U_S) = (3.0, 3.3)$. Nutrients are replenished at the (a) base of the simulation layer $z = z_S = 50$ m , (b) surface $z = 0$ m. Biological data from table 3.2, incorporating a non-swimming small predator with $\sigma_Z = 0.0\,\mathrm{m\,s^{-1}}$.

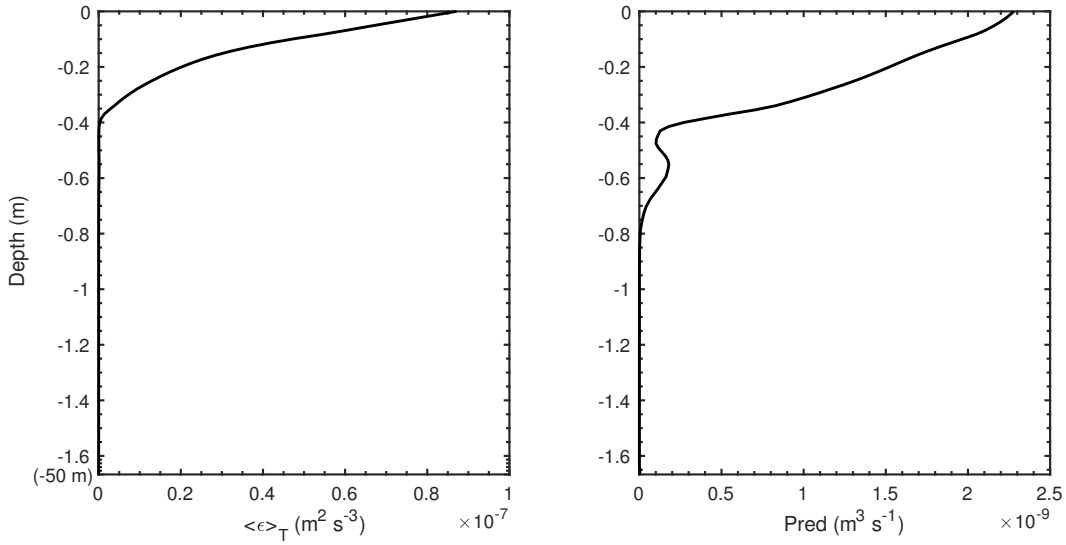

Figure 6.17: Energy dissipation rate (left) and predation rate (right) profiles for the small non-swimming predator. Biological data from table 3.2 with $\sigma_Z = 0.0$.

No predation

So far all these simulations (with the exception of figure 6.15c) have demonstrated significant subsurface phytoplankton growth approximated at the depth at which mixing levels go into decline, causing predation pressure to ease. These results support the hypothesis that the predation rate is a key driver in the formation of DBM. High predation near the surface restricts the growth of the phytoplankton despite the abundance of light and nutrient resources. To test this further figures 6.18a–6.18b show what happens in the scenario where the predation term is switched off (equations (3.2.22) and (3.2.23) set to 0). Starting from a low nutrient $(N, P, Z)_{t=0} = (0.1, 0.5, 0.5)$ initial profile, the zooplankton population starves and quickly dies out. Unrestrained by predation, the phytoplankton population grows rapidly to very high concentrations, almost uniformly, across those regions of the boundary layer where there is sufficient nutrient to support the excess growth (below $z_{TD} = 25$ m for the base flux, figure 6.18a; in the top layers for the surface flux 6.18b). Note in particular that the decline in light levels cannot disrupt the near uniform growth across the boundary layer. The turbulent mixing ensures most phytoplankton cells are circulated around the entire mixing layer and are on average exposed to the same amount of light. It is the presence of predation pressure enhanced by the high ε values at the surface, which is the key driver of the characteristic DBM seen in the observations of M13.

6.5.4 Sensitivity to nutrient initial conditions

In all the previous set of simulations the initial nutrient concentration is large enough to support rapid initial phytoplankton growth. It is worth investigating how the dynamics described in the previous sections change in a nutrient-limited environment. Figures 6.19a–6.19b show the evolution of the normalised $\langle N\rangle_I, \langle P\rangle_I, \langle Z\rangle_I)$ concentrations commencing from a very low nutrient environment, $(N, P, Z)_{t=0} = (0.1, 0.5, 0.5)$, under a moderate wind stress. Nutrient is added at the base and surface of the simulation domain respectively, as before. Initially there is not enough nutrient to support phytoplankton growth, so the phytoplankton population is quickly consumed by the swimming (small) predator. At this point the zooplankton population then starves and dies off quickly. As the nutrient levels are slowly replenished the phytoplankton population recovers, much quicker in the surface flux regime (figure 6.19b), despite a lower maximum nutrient concentration. The phytoplankton are able to respond faster in this environment due to the higher availability of light at the surface, allowing a full P, Z-oscillation. When the nutrient is replenished at the base of the simulation layer ($z_S = 50$ m), the phytoplankton respond much slower in the deeper light-limited region. Similar to the results with no predation, the phytoplankton grow only in the regions where there is enough nutrient. This implies that whilst earlier analysis supports the conclusions that the non-uniform predation restricts growth near the surface (which can result in a DBM), a DBM can only form if there is enough nutrient to support growth.

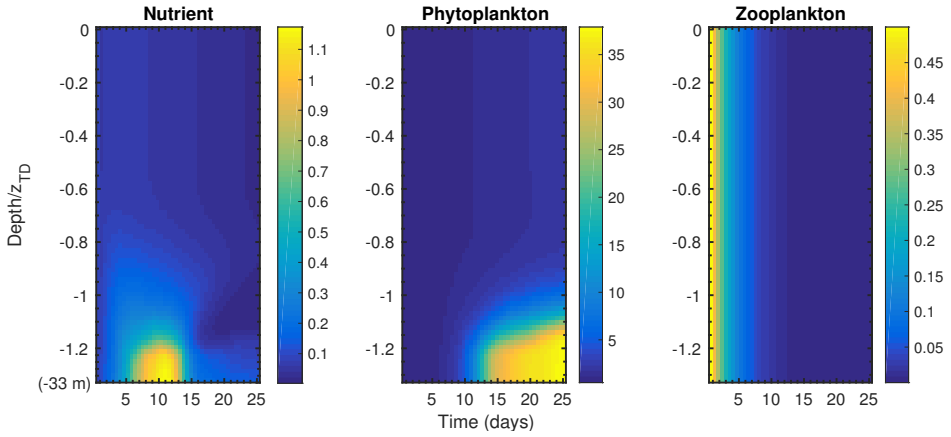

(a)

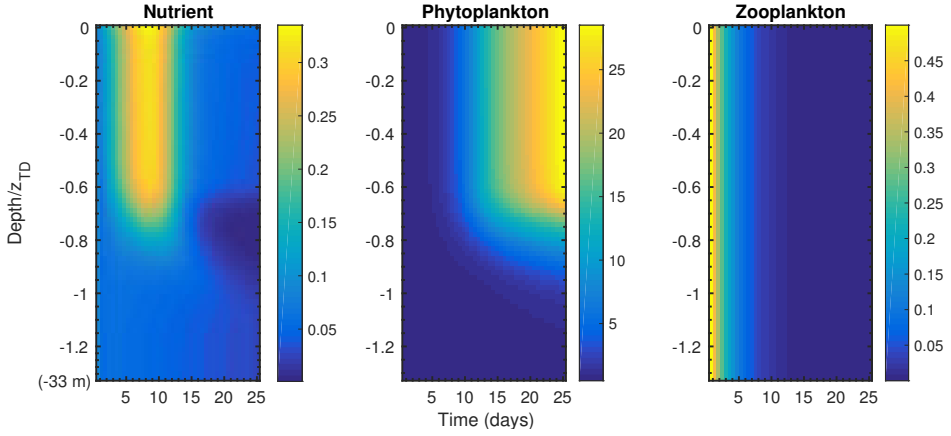

(b)

Figure 6.18: Evolution profiles of the normalised $(\langle N\rangle_I, \langle P\rangle_I, \langle Z\rangle_I)$ concentrations, starting from initial conditions $(0.1, 0.5, 0.5)$ subject to $(U_*, U_S) = (2.5, 2.8)$. Nutrients are replenished at the (a) base of the simulation layer $z = z_S = 33$ m , (b) surface $z = 0$ m. Biological data from table 3.2, with predation term turned off (set to $0\ \forall\ z$).

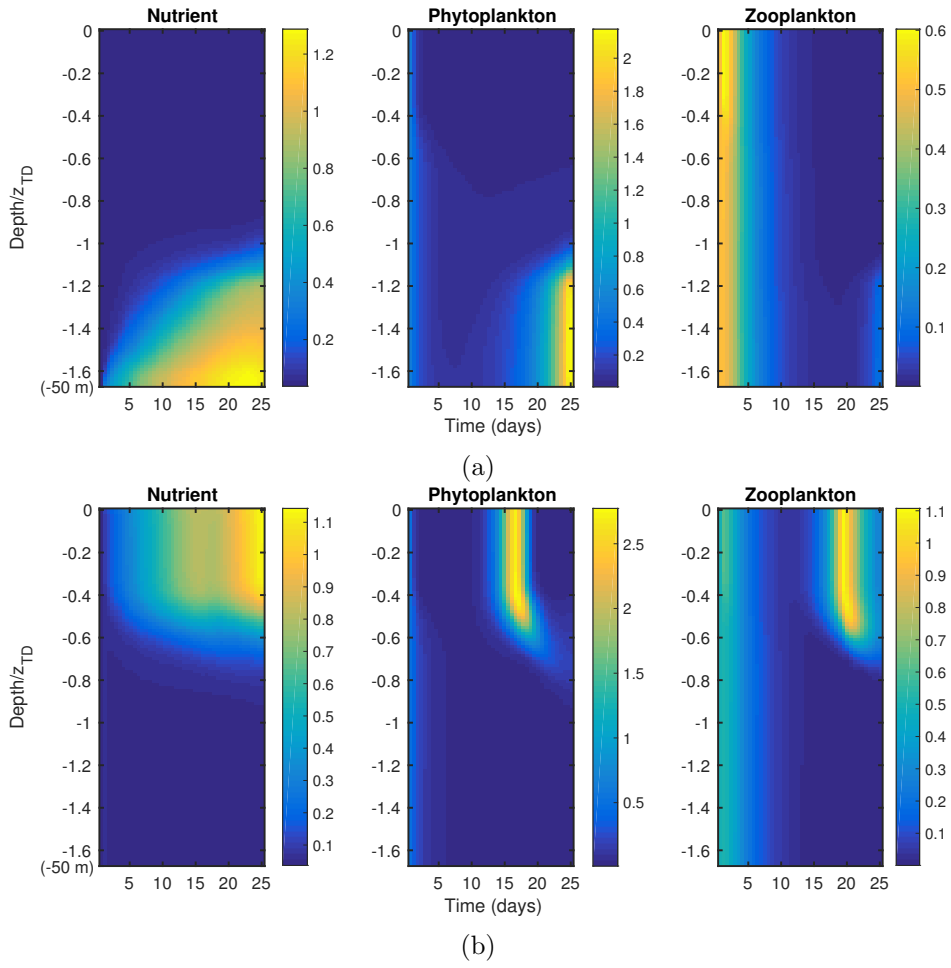

Figure 6.19: Evolution profiles of the normalised $(\langle N\rangle_I, \langle P\rangle_I, \langle Z\rangle_I)$ concentrations, starting from initial conditions $(0.1, 0.5, 0.5)$ subject to $(U_*, U_S) = (3.0, 3.3)$. Nutrients are replenished at the (a) base of the simulation layer $z = z_S = 50$ m , (b) surface $z = 0$ m. Biological data from table 3.2, incorporating the small (swimming) predator.

6.6 Mixing depth

The results and analysis of the previous sections indicate that DBM often form in regions of low turbulent intensity, regions in which the reduced predation rate allows for increased phytoplankton growth. It is very important to try to establish the depth, for any given wind stress, (U_*, U_S), at which the turbulent intensity is expected to start to decay rapidly. The problem of determining the mixing layer depth is an active area of research (for example Brainerd and Gregg (1995), Thomson and Fine (2003), de Boyer Montégut et al. (2004)), and a wide variety of criteria have been used. One typical method is to determine the depth at which some variable, for example temperature, θ, varies from its surface value, $\theta(0)$, by some preset amount, $\Delta\theta$. However, even within such a criterion, definitions for the mixing depth vary (Kara et al. 2000). In a Stokes-Ekman boundary layer (as described by the LES model presented here) it would be expected that the mixing layer depth would be related to the depth at which the effects of the wind and Stokes drift penetrate. Previously, the turbulent (mixed layer) depth has been defined as $z_{TD} = U_*/f = \delta_E$, which is defined as the Ekman depth (Coleman et al. 1990). Up-to now the mixing layer depth has been related to the turbulent depth z_{TD} by (Garratt 1994) $z_{ML} \approx 0.2$–$0.4 z_{TD}$ (Garratt 1994). The value of 0.2–0.4 is directly linked to von Kármán's universal constant $k \approx 0.4$. Lewis et al. (2017) then assumed that the inclusion of the Stokes drift would increase the depth of the mixing layer, so a rough equivalence would be $z_{ML} \approx 0.5 z_{TD}$ (Lewis et al. 2017).

6.6.1 Stokes drift depth scale

First it is important to try to establish the impact of the Stokes drift on the mixing layer depth. The Stokes drift depth scale is defined as $\delta_S = 1/(2k)$ (Polton et al. 2005), and this is the depth over which the wave effects manifest themselves directly. The problem is now to determine the wavenumber, k, for a given Stokes drift velocity scale, U_S. Komen et al. (1994) published a series of equations of wave growth equations, summarising the results of a number of independent experimental trials, which recorded sea state, significant wave heights, etc. Lewis and Belcher (2004) considered two cases from the Komen et al. (1994). The first of these assumed that the wave growth was fetch (or distance to windward shore) limited, in which case the non-dimensional wave height, $H_S = 2a$ and peak frequency can be expressed as a function of the non-dimensional fetch, Γ^*, in the form

$$\frac{g^2 H_S^2}{16 U^4} = A_1 \Gamma^{*A_2}, \tag{6.6.1}$$

and

$$\frac{\sigma U}{g} = B_1 \Gamma^{*B_2}. \tag{6.6.2}$$

Here, U is a reference wind velocity and $\Gamma^* = g\Gamma/U^2$. Hwang (2006) lists a summary of the coefficients A_1, A_2, B_1 and B_2 from different proposed functions. In the second case it was

assumed that the waves were fully developed, in which case the following relations for the non-dimensional H_S and σ can be employed (equations (6.71a,b) from Komen et al. (1994))

$$\frac{g^2 H_S^2}{16U^4} = 1.1 \times 10^3, \tag{6.6.3}$$

and

$$\frac{\sigma U}{g} = 2\pi \times 5.6 \times 10^{-3}. \tag{6.6.4}$$

From equations (6.6.3) and (6.6.4) it is possible to obtain a relation between the wave amplitude and frequency. Rearranging the equations and cancelling out the velocity scale, U gives

$$a = \frac{0.08212g}{\sigma^2}. \tag{6.6.5}$$

From section 2.3.1, the wave frequency can be written as $\sigma = \sqrt{gk}$, which gives the following relationship between amplitude a and the wavenumber, k,

$$a = \frac{0.08212}{k}. \tag{6.6.6}$$

Using (6.6.6) and the relation between σ and k, the Stokes drift velocity scale, U_S can then be rewritten as a function of the wavenumber only

$$U_S = 0.0067434\sqrt{\frac{g}{k}} \approx 6.7 \times 10^{-3}\sqrt{\frac{g}{k}}. \tag{6.6.7}$$

Hence the Stokes drift depth scale $\delta_S = 1/(2k)$ can then be written in terms of the velocity scale

$$\delta_S = \frac{U_S^2}{2g \times (6.7 \times 10^{-3})^2} = \left(\frac{U_S}{\sigma}\right) \times \frac{1}{2 \times 6.7 \times 10^{-3}}. \tag{6.6.8}$$

This equation shows that the Stokes drift depth scale can be written as a velocity scale divided by frequency, which is analogous in form to the Ekman depth scale, δ_E. The mixing depth might then be expected to take the form

$$z_{ML} = A\delta_E + B\delta_S, \tag{6.6.9}$$

where A and B are dimensionless.

6.6.2 Passive tracer simulations

One of the most interesting features about the LES-NPZ simulations which incorporated a surface nutrient replenishment boundary condition was that the DBM usually formed just below the depth at which the nutrient concentration starts to decline. This decline in nutrient concentration gives an indication to the depth at which the turbulent advection (or mixing) no longer dominates the flow. As such, any model of the mixing layer depth in a Stokes-Ekman boundary layer should be able to predict the depth at which the nutrient mixing

ceases.

To facilitate such model development, the LES-NPZ code was modified to remove both the phytoplankton and zooplankton, reducing the system to a LES-N model. The source and sink terms for the nutrient equation were also removed, rendering the nutrient a passive tracer within the boundary layer. The boundary conditions for the nutrient (described in section 6.4) are retained, allowing for a flux of nutrients at the surface ($z = 0$) of the simulation layer. The idea is that, after some time, the initial (uniform) nutrient concentration will separate into two layers, the upper layer containing a higher concentration extending to the depth at which the effects of the wind stress and Stokes drift penetrate, i.e. the mixing layer depth z_{ML}. One possibility is to define this depth as the point at which the vertical nutrient gradient achieves its maximum,

$$\left.\frac{\partial N}{\partial z}\right|_{z_{ML}} = \max_z \left(\frac{\partial N(z)}{\partial z}\right). \tag{6.6.10}$$

These results provide data that can be used to estimate values of A and B in equation (6.6.9). The full set of U_* and U_S values for the various LES-N simulations are presented in table 6.2. Six values of the Langmuir number, La, were used for each value of U_*. A larger Langmuir number indicates that energy production is primarily driven by turbulent shear and the mixing depth will be dominated by the Ekman depth scale. For small Langmuir numbers the Stokes production dominates and δ_S will be the relevant depth scale (Grant and Belcher 2009). The chosen range of (U_*, U_S) values should therefore provide a wide range of environments in which to investigate how the shear and Stokes drift impact the mixing depth. For each simulation the depth of the simulated boundary layer was set to $z_S = z_{TD} = \delta_E$, since the results of section 6.5 indicated that a DBM typically begin to form in the region of $z_{ML} = z_{TD}/2$. The mixing layer depth, z_{ML}, defined by equation (6.6.10) for each of

$La \setminus U_*$	**0.0015**	**0.002**	**0.0025**	**0.003**	**0.0035**	**0.004**	**0.0045**	**0.005**
0.6	0.0042	0.0056	0.0069	0.0083	0.0097	0.011	0.012	0.014
0.42	0.0083	0.011	0.014	0.017	0.019	0.022	0.025	0.028
0.37	0.011	0.015	0.019	0.022	0.026	0.03	0.033	0.037
0.3	0.017	0.022	0.028	0.033	0.039	0.044	0.05	0.056
0.24	0.025	0.033	0.042	0.05	0.058	0.067	0.075	0.083
0.21	0.033	0.044	0.056	0.067	0.078	0.089	0.1	0.11
z_S (m)	15	20	25	30	35	40	45	50

Table 6.2: U_S ($\mathrm{m\,s^{-1}}$) values used for each U_* ($\mathrm{m\,s^{-1}}$) with corresponding Langmuir number La for each of the LES-N simulations in section 6.6.2. Depth for each simulation is $z_S = z_{TD} = U_*/f$.

the 48 simulations detailed in table 6.2 is shown in figure 6.20 as the solid black line. Each column of table 6.2 is shown as the 'blocks' along the x-axis, indicated by the U_* value and dashed vertical line on the left edge, with U_S indicated by the tick marks, increasing towards

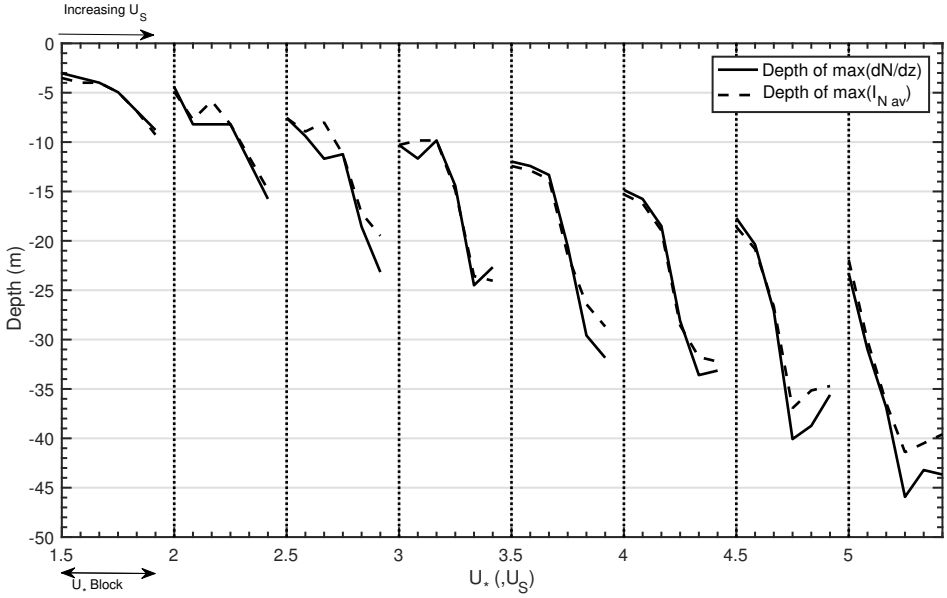

Figure 6.20: Mixing depth as measured by depth of $\max(\mathrm{d}N/\mathrm{d}z)$ (solid black), depth of $\max(I_{N\,av})$ (dashed black) for the simulations detailed in table 6.2. Results for each of the columns in table 6.2 are plotted along x-axis, each block (indicated by the vertical dashed lines) represents each U_* value with increasing U_S (decreasing La from 0.6, on dashed line, to 0.21) rightwards, indicated by the x-axis minor ticks.

to the right along the block. For each fixed U_* value the mixing depth typically decreases with increasing U_S, with U_S having a larger impact on the mixing layer depth for $La < 0.37$. This demonstrates that increasing the Stokes drift velocity an (indirect) effect of mixing the nutrients supplied at the surface further into the boundary layer. So the influence of surface waves goes very much deeper than their direct penetration depth δ_S. Similarly, increasing the surface friction velocity, U_*, also increases the mixing depth. Another possible measure that could be used to define z_{ML} is the depth that the intensity of the nutrients, measured by $(I_{N\,av})$, reaches its maximum, given by

$$I_{Nav}(z_{ML}) = \max_z \left(\frac{1}{T_{sim}} \int_0^{T_{sim}} \frac{\langle N'^2 \rangle_I}{\langle N \rangle_I^2} \, \mathrm{d}t \right). \tag{6.6.11}$$

This is shown as the dashed line in figure 6.20. This depth very closely matches that given by equation (6.6.10) and indicates that the intensity measure also gives a very good indication to the depth to which the turbulent mixing penetrates. Similarly to equation (6.3.2), $I_{N\,av}$ gives a measure of the horizontal homogeneity of the nutrient, the nutrient distribution becomes more heterogeneous as the impact of the turbulent mixing declines. The simulations with the highest (U_*, U_S) pairing (i.e. $La \leqslant 0.24$ for $U_* \geqslant 4 \times 10^{-3}\ \mathrm{m\,s^{-1}}$), resulted in almost uniform nutrient distributions throughout the layer, consequently the values of $I_{N\,av}$ and $\mathrm{d}N/\mathrm{d}z$ are very small throughout the layer. As a result the mixing layer depth is very close to z_S. In these cases a deeper simulation domain would be needed to achieve an accurate prediction for z_{ML}.

6.6.3 Mixing layer depth prediction

To produce a predictive tool for DBM depth, the results of the passive tracer simulations of section 6.6.2 were subject to a 3D linear fit in terms of, first, the velocity scales U_* and U_S, and second the length scales δ_E and δ_S. The variables were fitted to the data using a standard least squares minimisation technique for two variables (see for example Press (2007)).

(U_*, U_S) model

For the first approximation to the mixing layer depth, based upon the definition (6.6.10), the variables U_* and U_S were employed alongside simulation data to find the best fit equation of the form $z_{ML} = AU_* + BU_S$. Here, A and B are time scales related to the Ekman and Stokes layers respectively. The first regression analysis gave rise to

$$z_{ML} \approx (-3495 \pm 757) \times U_* + (-252.4 \pm 59) \times U_S, \tag{6.6.12}$$

where the coefficients are given with the 95% confidence bounds, and the R^2 value is 0.855 indicating a strong fit to the data. Figure 6.21 shows equation (6.6.12) plotted as the solid red curve against the depth of the maximum of $\mathrm{d}N/\mathrm{d}z$ which is plotted in solid black. The model parameters show a good fit to the data and captures the structure of each U_* "block" described previously. The model underestimates the data for large (U_*, U_S). However, as mentioned above, the simulation results were very homogeneous in this case, and it is probable that z_{ML} was too deep to be fully captured by the simulation depth z_S.

It is difficult to assign real physical meaning to the parameters A and B in this model. In particular, the timescale associated with the Stokes drift depends upon the velocity scale, since σ can be expressed in terms of U_S. However, AU_* can be related to δ_E by setting $AU_* = 0.3495 \times U_*/f$, which fits the prediction of Garratt (1994).

δ_E, δ_S model

The second model takes the form $z_{ML} = A\delta_E + B\delta_S$, as formulated in section 6.6.1. In this case the variables are the depth scales associated with the Ekman and Stokes layers respectively. The coefficients are both dimensionless parameters. The regression analysis was carried out using the same methodology as equation (6.6.12). The resulting best fit satisfied

$$z_{ML} \approx (-0.4801 \pm 0.0576) \times \delta_E + (-1.969 \pm 0.524) \times \delta_S, \tag{6.6.13}$$

where the coefficients are given with the associated 95% confidence bounds and the $R^2 = 0.831$ in this case. This approximation is shown as the dashed red curves in figure 6.20. The fit is very similar to that of equation (6.6.12) and maintains the behaviour expected when U_S increases for fixed U_*.

Based on the R^2 value, this approximation is not quite as good as equation (6.6.12).

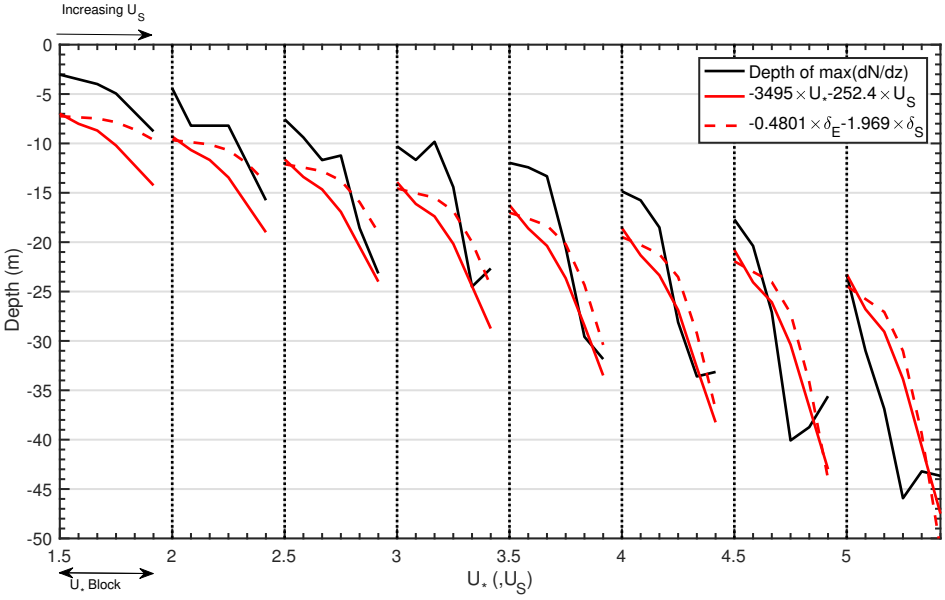

Figure 6.21: Mixing depth as measured by depth of max(dN/dz) (solid black), fit to max(dN/dz) from equation (6.6.12) (solid red), and fit to max(dN/dz) from equation (6.6.13) (dashed red). For the simulations detailed in table 6.2. Results for each of the columns in table 6.2 are plotted along x-axis, each block (indicated by the vertical dashed lines) represents U_* value with increasing U_S (decreasing La from 0.6, on dashed line, to 0.21) rightwards, indicated by the minor ticks on the x-axis.

However, the coefficients and variables provide more insight from a physical standpoint. In this case $A \approx 0.5$ as suggested by Lewis et al. (2017), and $B\delta_S \approx 2\delta_S = 1/k$ is approximately the wavelength of the surface waves associated with Stokes drift. These results suggest that in wind driven turbulent boundary layers in which surface waves are a factor (a very common scenario) the mixing layer depth can be estimated by the very simple equation

$$z_{ML} \approx \frac{1}{2}\delta_E + 2\delta_S, \tag{6.6.14}$$

to a first order of magnitude.

6.6.4 Comparison with results from LES-NPZ simulations

A selection of the simulations carried out in section 6.6.2 were repeated for the full LES-NPZ model in order to test the mixing layer hypothesis. The (U_*, U_S) pairings are presented in table 6.3. Each simulation was repeated for both nutrient boundary conditions, the plankton parameters are given by table 3.2 for the small (swimming) predator. The evolution of the normalised phytoplankton population for each of the simulations are shown in figures 6.22 and 6.23 for the base and surface replenishment of nutrients respectively. Each of the simulations, with the exceptions of $(U_*, U_S) = (3.0, 6.7)$ and $(4.0, 8.9)$, exhibit a DBM at or just below z_{ML} defined by equation (6.6.10) which is indicated by the solid red line. This supports the idea that DBM will form at, or just below, the mixing layer depth as a consequence of rapid decline in predation associated with the reduction in turbulent mixing. In the region above,

$La \setminus U_*$	$\mathbf{2 \times 10^{-3}\ m\,s^{-1}}$	$\mathbf{3 \times 10^{-3}\ m\,s^{-1}}$	$\mathbf{4 \times 10^{-3}\ m\,s^{-1}}$
0.42	$1.1 \times 10^{-2}\ \mathrm{m\,s^{-1}}$	$1.7 \times 10^{-2}\ \mathrm{m\,s^{-1}}$	$2.2 \times 10^{-2}\ \mathrm{m\,s^{-1}}$
0.3	$2.2 \times 10^{-2}\ \mathrm{m\,s^{-1}}$	$3.3 \times 10^{-2}\ \mathrm{m\,s^{-1}}$	$4.4 \times 10^{-2}\ \mathrm{m\,s^{-1}}$
0.21	$4.4 \times 10^{-2}\ \mathrm{m\,s^{-1}}$	$6.7 \times 10^{-2}\ \mathrm{m\,s^{-1}}$	$8.9 \times 10^{-2}\ \mathrm{m\,s^{-1}}$

Table 6.3: U_S ($\mathrm{m\,s^{-1}}$) values used for each U_* ($\mathrm{m\,s^{-1}}$) with corresponding Langmuir number La for each of the LES-NPZ simulations in section 6.6.4. Depth for each simulation is $z_{TD} = U_*/f$.

the predation rate will be too strong for any significant phytoplankton growth.

The predictions of the mixing depth, equations (6.6.12) and (6.6.13) are indicated by the solid and dashed lines respectively on figures 6.22 and 6.23. As anticipated both models provide a very good approximation to the depth at which the DBM form. Equation (6.6.13) appears to provide the better estimation of the DBM depth. This can be seen in figure 6.24, which shows the time averaged $\langle P \rangle_I$ profiles for each of the 18 simulations. The depth predicted by equation (6.6.13) (including the bounds) provides a very good approximation to the DBM depth. This means that knowing the friction and Stokes drift velocity scales can provide a very good indication to where a DBM might form in a Stokes-Ekman boundary layer. One of the most interesting details about this result is that the equation has a physical interpretation, and the coefficients match the physical predictions of Garratt (1994), Lewis et al. (2017). The DBM region can be predicted from the depth scales associated with the Ekman spiral and Stokes drift.

6.7 Conclusion

The results of this chapter strongly support the recent observations of M13. Assuming that the phytoplankton were neither nutrient nor light limited, and that the wind forcing was not too strong, a DBM would form at, or just below, $z = z_{TD}/2$. The location of the simulated DBM, relative to the turbulent intensity (measured by $\langle \varepsilon \rangle$), is very similar to the DCM observations of M13. Klausmeier and Litchman (2001) suggest that DCM will form in a window of optimal light conditions *and* nutrient supply. When nutrients are replenished at the surface, the optimal location for P growth would be at the surface. The results here (e.g. figure 6.11) suggest that this is not necessarily the case. Instead, the results demonstrate that predation pressure is a key component of DBM formation. Near the surface, predation pressure will be high due to the high levels of turbulence. This acts to enhance the number of interactions between the predator and prey, increasing the predation rate. The high predation pressure restricts phytoplankton growth near the surface. As the levels of turbulence decline, the number of predator-prey encounters also declines. Consequently, the lower predation rate will allow the phytoplankton population to grow more freely than in the water above. These results support the results of Pannard et al. (2015), although they suggest that high predation near the surface allows more light to reach phytoplankton in the thermocline. The importance

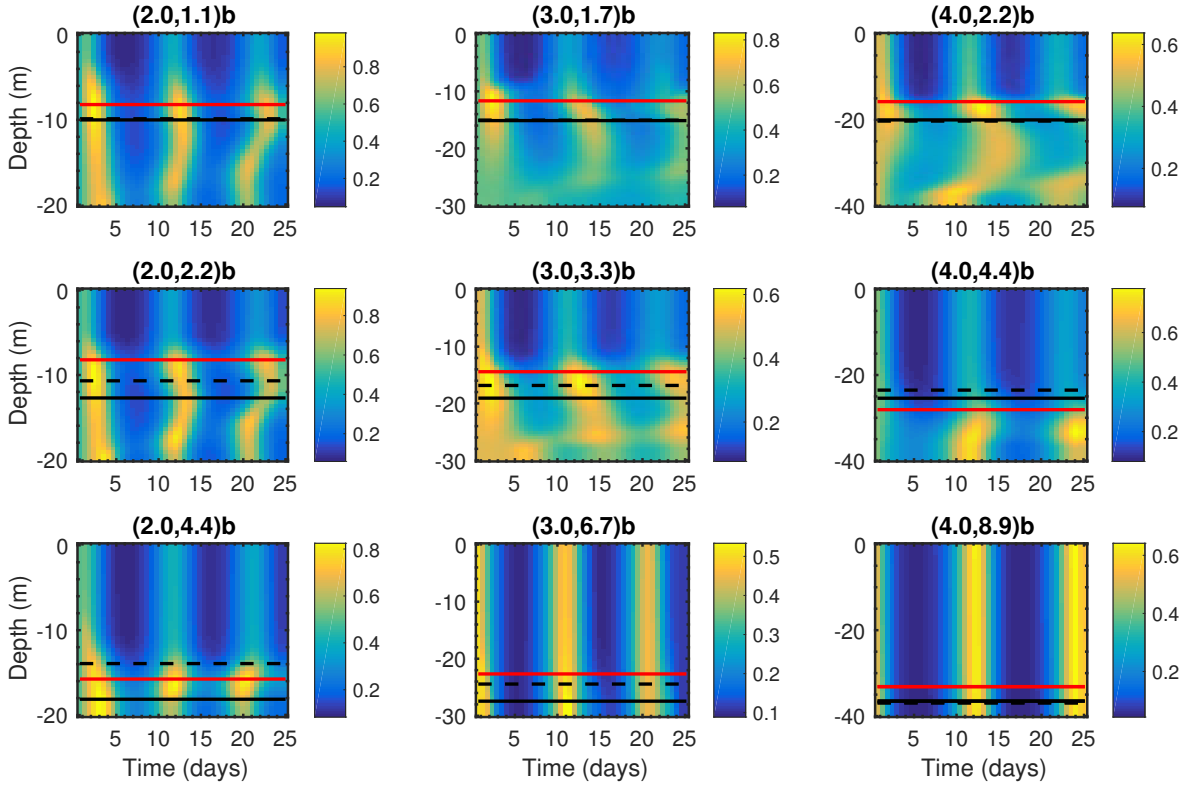

Figure 6.22: Evolution of the normalised $\langle P \rangle_I$ field subject to a replenishment of nutrients at the base z_S of the simulation domain, for (U_*, U_S) from table 6.3. NPZ parameters from table 3.2 for the small predator. The solid red line indicates the mixing depth defined by equation (6.6.10). The depth predicted by equation (6.6.12) is indicated by the solid black line, the depth predicted by equation (6.6.13) is indicated by the dashed black line.

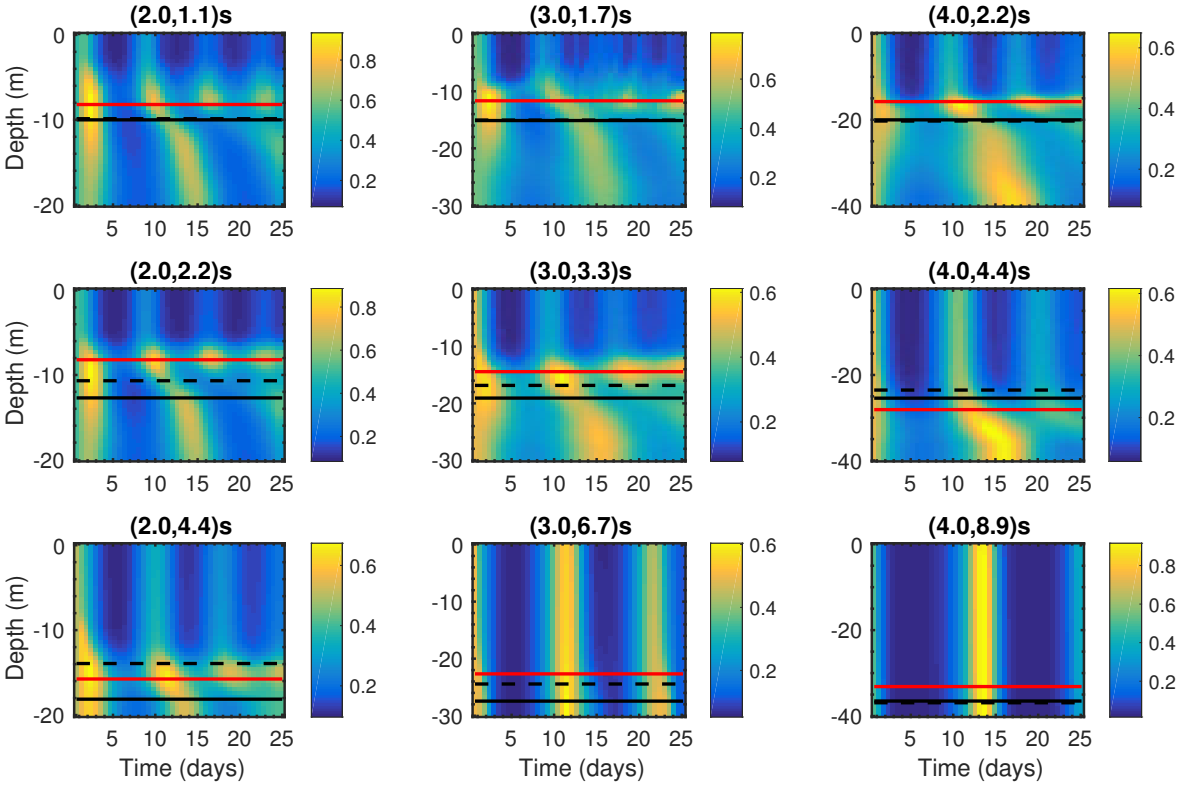

Figure 6.23: Evolution of the normalised $\langle P \rangle_I$ field subject to a surface replenishment of nutrients, for (U_*, U_S) from table 6.3. NPZ parameters from table 3.2 for the small predator. The solid red line indicates the mixing depth defined by equation (6.6.10). The depth predicted by equation (6.6.12) is indicated by the solid black line, the depth predicted by equation (6.6.13) is indicated by the dashed black line.

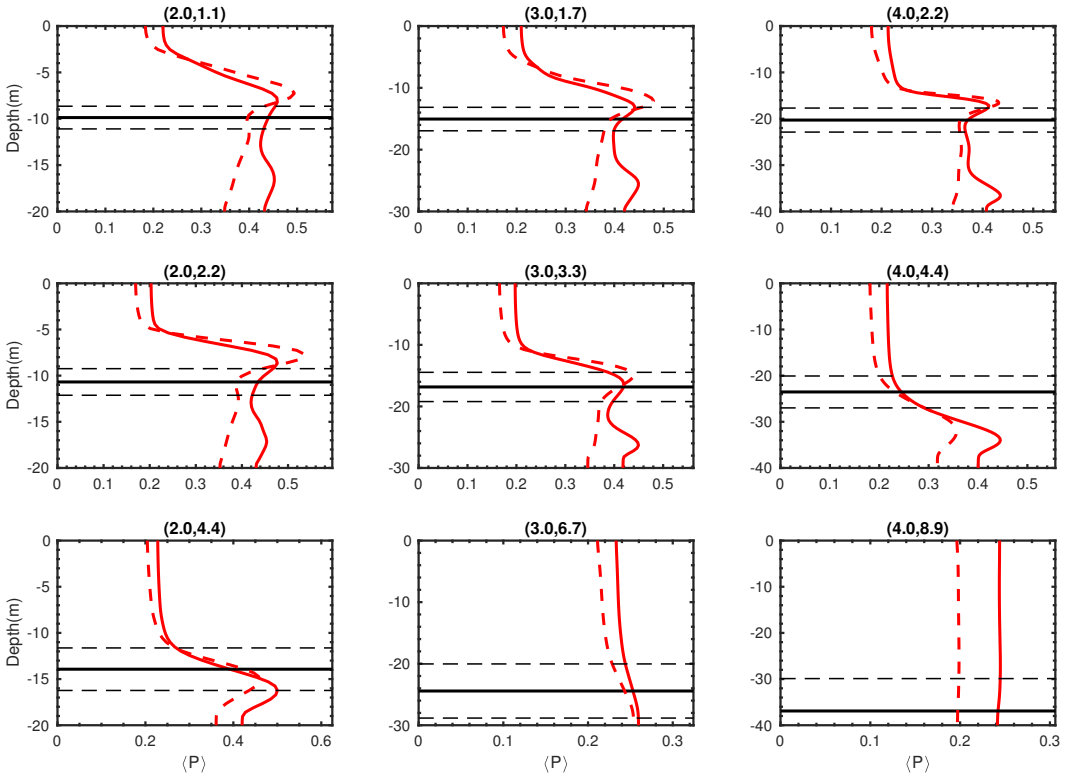

Figure 6.24: Time averaged $\langle P \rangle_I$ profile for base flux of nutrients (solid red), surface flux of nutrients (dashed red) for the simulations computed in section 6.6.4. The depth predicted by equation (6.6.13) is plotted in the solid black line with the bounds (finer dashed black).

of predation is further supported by the simulations containing the large predator. It is very significant that DBM formed for both predators, and further supports the conclusions of Fennel and Boss (2003).

When the phytoplankton are nutrient limited, as in figure 6.19, they tend to grow only in the regions where the nutrients are being replenished. In these results, the initial nutrient concentration is too low to support any initial P growth. As a consequence, the zooplankton starve due to a lack of food. As the nutrient concentration begins to rise, the phytoplankton are able to grow in a relatively predator free environment.

Combined, the results suggest that a DBM will form in a window of sufficient light levels and nutrient concentration, and *low* predation pressure. The DCM will form at the depth where the *balanced* phytoplankton growth rate (from reduced light levels but high nutrient concentration in the nutricline) is greater than the predation rate. The conclusions are very important since they demonstrate an example of the physics driving the biology and vice-versa. This biological-physical coupling demonstrates the power of the LES-NPZ model described here.

Chapter 7

Summary

7.1 Discussion

The fully coupled LES-NPZ model formulated in chapters 2 and 3 provides a means for studying the vertical heterogeneity of planktonic populations. Since this problem is both inherently physical and biological in nature, it is essential to understand how the interactions of the physical and biological parameters will influence the populations. From the analysis of the model and results of simulations, four parameters were identified as being important in driving the population's vertical structure.

1. **Nutrient concentration:** In order to test the importance of the nutricline several simulations were conducted with the nutrient source located at the surface, rather than the base (as would form in a traditional surface mixed layer), of the simulation layer. In a nutrient limited environment it was found that the phytoplankton growth was located close to the location of the source in each case. Initially nutrient concentrations were not sufficient for phytoplankton growth, which meant that the zooplankton population died off through starvation. As the nutrient levels were replenished, the phytoplankton population was able to grow close to the surface, in absence of predation in the surface flux regime. However, if the boundary layer was initially nutrient rich, so that zooplankton predation was always prevalent, then a DBM formed at or just below the mixing layer depth, z_{ML}, irrespective of the source of the nutrient flux.

2. **Light levels:** The results of the one-dimensional PZ-q model (z and t) were very interesting, and demonstrated how the light levels interact with the other drivers of DCM/DBM formation. In very clear waters, the highest phytoplankton populations were seen towards the base of the boundary layer, aligned with the nutricline. Here, the combination of the light levels and nutrient concentrations resulted in the highest growth rate. In slightly darker waters the amount of light reaching the nutricline was not sufficient for significant growth. Instead a DBM would form at or just below the mixing layer depth, due to the restrictions imposed by zooplankton grazing in the surface layers. As light levels were reduced further, predation pressure ceased to be

the main driver fixing the position of the DBM. Rather the phytoplankton maxima shifted towards the surface, as light levels became too low for phytoplankton growth. Eventually light levels became so low (less than 1% of the surface level (Pannard et al. 2015, Letelier et al. 2017)) that DBM formation became impossible, and phytoplankton growth was restricted to the surface layers only.

3. **Predation rate:** Assuming that the phytoplankton were neither nutrient nor light limited, DBM formation at or just below the mixing depth was a robust feature of the simulations. These results mirrored the observational data of M13. The importance of the predation pressure in DBM formation is readily apparent from the simulations where the nutrient replenishment occurred at the surface. The enhanced growth rate was still not able to overcome the predation pressure, and a DBM continued to form at the mixing layer depth, rather than at the surface.

4. **Wind and wave forcing:** The results of chapter 6 show that increasing the level of turbulence (by increasing the strength of the wind or wave effects) deepened the the level of the mixing depth and consequently the position of the DBM. Since increasing (U_*, U_S) has the effect of increasing the mixing layer depth, z_{ML}, it is important both physically and biologically (given its established correlation with DBM formation), to predicts its position. Using a combination of simulation results and scaling arguments it was shown that the mixing layer depth could be approximated by δ_E and δ_S, the depth scales of wind forcing and Stokes drift respectively. The results supported the very simple approximation

$$z_{ML} = -0.5\delta_E - 2\delta_S.$$

This is interesting as it shows that surface waves influence not only the physical structure of the boundary layer, but its biological characteristics deep below the surface. It seems likely (Lewis et al. 2017) that the breakdown of Langmuir cell structure and the consequent increase in horizontal as opposed to vertical nutrient flux levels is the mechanism (along with the corresponding reduction in predation pressure) that drives increased biological aggregations.

These four drivers all have an impact on the vertical structure of the phytoplankton community, in particular the formation and maintenance of any DBM. The results show that a DBM can form in a window of sufficient nutrient concentration, sufficient light levels, and low enough predation. The predation pressure is perhaps the most important driver, since it has the effect of restricting surface growth. Without this restriction, a DBM would be unlikely to form in clear, nutrient rich waters. The other drivers are still important, and manifest themselves under specialised limiting conditions, when for whatever reason, surface predation pressure is relatively low.

7.2 Future work

There are a number of relatively simple refinements and developments that would enhance the features of the LES-NPZ model. These include

1. There are other factors which affect the phytoplankton growth rate, for example temperature, salinity. The LES code does not currently model these parameters, so it would be interesting to consider how the temperature would influence the populations. A thermocline could then be directly included in the model.

2. For simplicity, the only nutrients considered in this work were nitrates. In reality, there are a number of nutrients that affect phytoplankton growth, in different ways. Each of these would be limited by various factors. In particular, oxygen would be important to consider, Pannard et al. (2015) suggested that zooplankton were unable to surface in the lake's metalimnion due to hypoxia.

3. The NPZ-q model incorporates a simple formulation for phytoplankton self-shading. During a seasonal bloom, light available for growth beneath would be significantly reduced. In the context of a DBM this may have the effect of reducing the DBM thickness.

4. The approximation of the mixing layer depth assumes that U_* and U_S are independent. In reality this may not be the case. Values for U_* and U_S may not necessarily be known, it is more common that the only parameter available might be La. It would be more useful then, to try to find a scaling effect of changing La, so that the mixing layer depth can be approximated by

$$z_{ML} = -AU_*/f\,(1 + g(La))$$

for some function g.

5. When approximating z_{ML}, the simulation depth was chosen to be $z_{TD} = U_*/f$, for a number of simulations this was not deep enough for the mixing layer to properly develop. Better theoretical predictions of z_{ML} could be used to determine a more suitable simulation depth, to encompass all of the key aspects of the boundary layer environment (such as in 4. above). This would allow nutrients replenished at the base of the simulation layer to begin to diffuse into the mixing layer immediately, replicating much more closely the true workings of nutrient distribution in real surface mixed layers.

Acknowledgements

I would like to thank my supervisor, Dr David Lewis, for his continued support and advice throughout this project. I would also like to thank Dr Ashley Brereton for his advice and help with computational difficulties, as well as technical advice related to the LES. I also thank Dr. Vasiev and Dr. Bearon for their advice on the structure and content of this thesis. Finally, I wish to thank my family and friends for all their support.

Bibliography

Ahn, Y.-H. & Shanmugam, P. (2006), 'Detecting the red tide algal blooms from satellite ocean color observations in optically complex northeast-asia coastal waters', *Remote Sensing of Environment* **103**(4), 419–437.

Alqarni, M. S. & Bearon, R. N. (2016), 'Transport of helical gyrotactic swimmers in channels', *Physics of Fluids* **28**(7), 071904.

Anderson, L. A. & Sarmiento, J. L. (1994), 'Redfield ratios of remineralization determined by nutrient data analysis', *Global biogeochemical cycles* **8**(1), 65–80.

Arismendez, S. S., Kim, H.-C., Brenner, J. & Montagna, P. A. (2009), 'Application of watershed analyses and ecosystem modeling to investigate land–water nutrient coupling processes in the guadalupe estuary, texas', *Ecological Informatics* **4**(4), 243–253.

Baird, M. E. & Emsley, S. M. (1999), 'Towards a mechanistic model of plankton population dynamics', *J.Plankton Res.* **21**, 85–126.

Baird, M. E., Emsley, S. M. & McGlade, J. M. (2001), 'Modelling the interacting effects of nutrient uptake, light capture and temperature on phytoplankton growth', *J.Plankton Res.* **23**(8), 829–840.

Barstow, S. F. (1983), 'The ecology of Langmuir circulation: a review', *Marine Environmental Research* **9**(4), 211–236.

Bataille, F., Rubinstein, R. & Hussaini, M. Y. (2005), 'Eddy viscosity and diffusivity modeling', *Phys. letters A* **346**, 168–173.

Batchelor, G. K. (1953), *The theory of homogeneous turbulence*, Cambridge university press.

Batchelor, G. K. (1967), *An introduction to fluid dynamics*, Cambridge university press.

Batchelor, G. K. (1980), 'Mass transfer from small particles suspended in turbulent fluid', *Journal of Fluid Mechanics* **98**(03), 609–623.

Beer, A. (1852), 'Bestimmung der absorption des rothen lichts in farbigen flüssigkeiten', *Ann.Phys.Chem.* **86**, 78–88.

Bees, M. A., Mezic, I. & McGlade, J. (1998), 'Planktonic interactions and chaotic advection in langmuir circulation', *Mathematics and Computers in Simulation* **44**(6), 527–544.

Berg, H. C. (1993), *Random walks in biology*, Princeton University Press.

Bouguer, P. (1729), *Essai d'optique sur la gradation de la lumière*, Jombert, Paris.

Brainerd, K. E. & Gregg, M. C. (1995), 'Surface mixed and mixing layer depths', *Deep Sea Research Part I: Oceanographic Research Papers* **42**(9), 1521–1543.

Brereton, A. (2013), Phytoplankton Aggregations in a Turbulent Boundary Layer, PhD thesis, Univeristy of Liverpool.

Brereton, A., Siddons, J. T. & Lewis, D. M. (2018), 'Large eddy simulation of subsurface plankton patchiness: a Goldilocks zone for chlorophyll aggregations induced by langmuir circulations', *(accepted) Marine Ecol. Prog. Series* .

Bricaud, A., Morel, A. & Prieur, L. (1981), 'Absorption by dissolved organic matter of the sea (yellow substance) in the uv and visible domains', *Limnol.Oceanogr.* **26**, 43–53.

Buiteveld, H., Hakvoort, J. H. M. & Donze, M. (1994), Optical properties of pure water, *in* 'Ocean Optics XII', International Society for Optics and Photonics, pp. 174–183.

Bundy, M. H., Gross, T. F., Vanderploeg, H. A. & Strickler, R. J. (1998), 'Perception of inert particles by calanoid copepods: behavioral observations and a numerical model', *Journal of Plankton Research* **20**(11), 2129–2152.

Burnett, L., Moorhead, D., Hawes, I. & Howard-Williams, C. (2006), 'Environmental factors associated with deep chlorophyll maxima in dry valley lakes, south victoria land, antarctica', *Arctic, Antarctic, and Alpine Research* **38**(2), 179–189.

Carpenter, S. R., Caraco, N. F., Correll, D. L., Howarth, R. W., Sharpley, A. N. & Smith, V. H. (1998), 'Nonpoint pollution of surface waters with phosphorus and nitrogen', *Ecological applications* **8**(3), 559–568.

Chakraborty, K., Das, K. & Kar, T. K. (2015), 'Modeling and analysis of a marine plankton system with nutrient recycling and diffusion', *Complexity* **21**(1), 229–241.

Chen, Y.-S. & Kim, S.-W. (1987), 'Computation of turbulent flows using an extended k-epsilon turbulence closure model'.

Chereskin, T. K. (1995), 'Direct evidence for an Ekman balance in the California current', *J.Geophys.Res.* **100**, 18261–18269.

Ciotti, A. M., Cullen, J. M. & Lewis, M. R. (1999), 'A semi-analytical model of the influence of phytoplankton community structure on the relationship between light attenuation and ocean color', *J.Geophys.Res.* **104**(C1), 1559–1578.

Coleman, G. N., Ferziger, J. H. & Spalart, P. R. (1990), 'A numerical study of the turbulent Ekman layer', *Journal of Fluid Mechanics* **213**, 313–348.

Craik, A. D. D. & Leibovich, S. (1976), 'A rational model for Langmuir circulations', *J.Fluid Mech.* **73**, 401–426.

Cullen, J. J. (1982), 'The deep chlorophyll maximum: comparing vertical profiles of chlorophyll a', *Can.J.Fish.Aquat.Sci.* **39**, 791–803.

Cullen, J. J. (2015), 'Subsurface chlorophyll maximum layers: enduring enigma or mystery solved?', *Annu.Rev.Marine Sci.* **7**, 207–239.

Cullen, J. J. & Eppley, R. W. (1981), 'Chlorophyll maximum layers of the southern-California bight and possible mechanisms of their formation and maintenance', *Oceanologica Acta* **4**(1), 23–32.

Davidson, P. (2015), *Turbulence: an introduction for scientists and engineers*, Oxford University Press.

de Boyer Montégut, C., Madec, G., Fischer, A. S., Lazar, A. & Iudicone, D. (2004), 'Mixed layer depth over the global ocean: An examination of profile data and a profile-based climatology', *Journal of Geophysical Research: Oceans* **109**(C12).

Deardorff, J. W. (1970), 'A numerical study of three-dimensional turbulent channel flow at large Reynolds numbers', *Journal of Fluid Mechanics* **41**(02), 453–480.

Denman, K. L. & Gargett, A. E. (1995), 'Biological-physical interactions in the upper ocean: the role of vertical and small scale transport processes', *Annual Review of Fluid Mechanics* **27**, 225–255.

Doubell, M. J., Yamazaki, H., Li, H. & Kokubu, Y. (2009), 'An advanced laser-based fluorescence microstructure profiler (TurboMAP-L) for measuring bio-physical coupling in aquatic systems', *Journal of plankton research* **31**(12), 1441–1452.

Drummond, I. T., Duane, S. & Horgan, R. R. (1984), 'Scalar diffusion in simulated helical turbulence with molecular diffusivity', *Journal of Fluid Mechanics* **138**, 75–91.

Durham, W. M., Kessler, J. O. & Stocker, R. (2009), 'Disruption of vertical motility by shear triggers formation of thin phytoplankton layers', *science* **323**(5917), 1067–1070.

Duysens, L. N. M. (1956), 'The flattening of the absorption sectrum of suspensions, as compared to that of solutions', *Biochim. Biophys. Acta* **19**.

Edwards, A. M. & Brindley, J. (1996), 'Oscillatory behaviour in a three-component plankton population model', *Dynamics and stability of Systems* **11**(4), 347–370.

Ekman, V. W. (1905), 'On the influence of earth's rotation in ocean currents', *Arch. Math. Astron. Phys.* **2**, 1–52.

Emlet, R. B.and Strathman, R. R. (1985), 'Gravity, drag, and feeding currents of small zooplankton', *Science* **228**(4702), 1016–1017.

Estrada, M., Marrase, C., Latasa, M., Berdalet, E., Delgado, M. & Riera, T. (1993), 'Variability of deep chlorophyll maximum characteristics in the northwestern Mediterranean', *Marine Ecology-Progress Series* **92**, 289–289.

Falkowski, P., Scholes, R. J., Boyle, E. E. A., Canadell, J., Canfield, D., Elser, J., Gruber, N., Hibbard, K., Högberg, P., Linder, S. et al. (2000), 'The global carbon cycle: a test of our knowledge of earth as a system', *science* **290**(5490), 291–296.

Fasham, M. J. R., Ducklow, H. W. & McKelvie, S. M. (1990), 'A nitrogen-based model of plankton dynamics in the oceanic mixed layer', *Journal of Marine Research* **48**(3), 591–639.

Fenchel, T. & Juel Hansen, P. (2006), 'Motile behaviour of the bloom-forming ciliate mesodinium rubrum', *Marine Biology Research* **2**(01), 33–40.

Fennel, K. & Boss, E. (2003), 'Subsurface maxima of phytoplankton and chlorophyll: Steady-state solutions from a simple model', *Limnol.Oceanogr.* **48**(4), 1521–1534.

Fick, A. (1855), ''Uber diffusion (in german)', *Annalen der Physik* **170**(1), 59–86.

Fields, D. M. & Yen, J. (1997), 'Implications of the feeding current structure of euchaeta rimana, a carnivorous pelagic copepod, on the spatial orientation of their prey', *Journal of plankton research* **19**(1), 79–95.

Franks, P. J. S. (2002), 'NPZ models of plankton dynamics: their construction, coupling to physics and application', *J.Oceanogr.* **58**, 379–387.

Franks, P. J. S., Wroblewski, J. S. & Flierl, G. R. (1986), 'Behavior of a simple plankton model with food-level acclimation by herbivores', *Marine Biology* **91**(1), 121–129.

Frogner, P., Gíslason, S. R. & Óskarsson, N. (2001), 'Fertilizing potential of volcanic ash in ocean surface water', *Geology* **29**(6), 487–490.

Fung, J. C. H., Hunt, J. C. R., Malik, N. A. & Perkins, R. J. (1992), 'Kinematic simulation of homogeneous turbulence by unsteady random Fourier modes', *Journal of Fluid Mechanics* **236**, 281–318.

Furuya, K. & Marumo, R. (1983), 'The structure of the phytoplankton community in the subsurface chlorophyll maxima in the western north pacific ocean', *Journal of Plankton Research* **5**(3), 393–406.

Gallager, S. M., Yamazaki, H. & Davis, C. S. (2004), 'Contribution of fine-scale vertical structure and swimming behavior to formation of plankton layers on georges bank', *Marine Ecology Progress Series* **267**, 27–43.

Gallagher, J. C. (1980), 'Population genetics of skeletonema costatum (bacillariophyceae) in Narragansett bay', *Journal of phycology* **16**(3), 464–474.

Gargett, A. E. (1984), 'Vertical eddy diffusivity in the ocean interior', *Journal of Marine Research* **42**(2), 359–393.

Gargett, A. E., Osborn, T. R. & Nasmyth, P. W. (1984), 'Local isotropy and the decay of turbulence in a stratified fluid', *Journal of Fluid Mechanics* **144**, 231–280.

Garratt, J. R. (1994), 'The atmospheric boundary layer', *Earth-Science Reviews* **37**(1-2), 89–134.

Gerritsen, J. & Strickler, J. R. (1977), 'Encounter probabilities and community structure in zooplankton: a mathematical model', *Journal of the Fisheries Board of Canada* **34**(1), 73–82.

Grant, A. L. M. & Belcher, S. E. (2009), 'Characteristics of Langmuir turbulence in the ocean mixed layer', *J.Phys.Oceanogr.* **39**, 1871–1887.

Grant, H. L., Stewart, R. W. & Moilliet, A. (1962), 'Turbulence spectra from a tidal channel', *Journal of Fluid Mechanics* **12**(02), 241–268.

Hansen, B. W., Bjørnsen, P. K. & Hansen, B. W. (1997), 'Zooplankton grazing and growth: Scaling within the 2-2,000-˜ iii body size range', *Limnol. Oceanogr* **42**, 687–704.

Harris, G. (2012), *Phytoplankton ecology: structure, function and fluctuation*, Springer Science & Business Media.

He, G., Guo, Y. & Hsu, A. T. (1999), 'The effect of Schmidt number on turbulent scalar mixing in a jet-in-crossflow', *International Journal of Heat and Mass Transfer* **42**(20), 3727–3738.

Hernández-Carrasco, I., Rossi, V., Hernández-García, E., Garçon, V. & López, C. (2014), 'The reduction of plankton biomass induced by mesoscale stirring: A modeling study in the benguela upwelling', *Deep Sea Research Part I: Oceanographic Research Papers* **83**, 65–80.

Herron, J. A., Kim, J., Upadhye, A. A., Huber, G. W. & Maravelias, C. T. (2015), 'A general framework for the assessment of solar fuel technologies', *Energy Environ. Sci.* **8**, 126–157.

Hinze, J. O. (1959), 'Turbulence: An introduction to its mechanisms and theory', *Mechanical Engineering* .

Hoecker-Martínez, M. S. & Smyth, W. D. (2012), 'Trapping of gyrotactic organisms in an unstable shear layer', *Continental Shelf Research* **36**, 8–18.

Hoepffner, N. & Sathyendranath, S. (1991), 'Effect of pigment composition on absorption properties of phytoplankton', *Mar.Ecol.Prog.Ser.* **73**, 11–23.

Holling, C. S. (1959), 'Some characteristics of simple types of predation and parasitism', *The Canadian Entomologist* **91**(07), 385–398.

Holm-Hansen, O., Kahru, M. & Hewes, C. D. (2005), 'Deep chlorophyll a maxima (dcms) in pelagic Antarctic waters. ii. relation to bathymetric features and dissolved iron concentrations', *Marine Ecology Progress Series* **297**, 71–81.

Horvath, H. (1993), 'Atmospheric light absorption - a review', *Atmos.Env.* **27A**(3), 293–317.

Hsu, S.-B. & Lou, Y. (2010), 'Single phytoplankton species growth with light and advection in a water column', *SIAM Journal on Applied Mathematics* **70**(8), 2942–2974.

Hughes, L. (2000), 'Biological consequences of global warming: is the signal already apparent?', *Trends in ecology & evolution* **15**(2), 56–61.

Huisman, J., Thi, N. N. P., Karl, D. M. & Sommeijer, B. (2006), 'Reduced mixing generates oscillations and chaos in the oceanic deep chlorophyll maximum', *Nature* **439**(7074), 322–325.

Hutchings, L., Pitcher, G. C., Probyn, T. A. & Bailey, G. W. (1995), 'The chemical and biological consequences of coastal upwelling', *Environmental Sciences Research Report Es* **18**, 65–82.

Hwang, P. A. (2006), 'Duration- and fetch-limited growth functions of wave-generated waves parameterized with three different scaling wind velocities', *J. Geophys. Res.* **111**.

Iqbal, M. (2012), *An introduction to solar radiation*, Elsevier.

Jerlov, N. G. (1953), 'Maxima in the vertical distribution of particles in the sea', *Deep Sea Res.* **5**(2–4), 173–184.

Jiang, H., Meneveau, C. & R Osborn, T. (1999), 'Numerical study of the feeding current around a copepod.', *Journal of plankton research* **21**(8).

Johnson, K. A. & Goody, R. S. (2011), 'The original Michaelis constant: translation of the 1913 Michaelis–Menten paper', *Biochemistry* **50**(39), 8264–8269.

Jones, W. P. & Launder, B. E. (1972), 'The prediction of laminarization with a two-equation model of turbulence', *International journal of heat and mass transfer* **15**(2), 301–314.

Juzeniene, A., Brekke, P., Dahlback, A., Andersson-Engels, S., Reichrath, J., Moan, K., Holick, M. F., Grant, W. B. & Moan, J. (2011), 'Solar radiation and human health', *Reports on Progress in Physics* **74**(6), 066701.

Kara, A. B., Rochford, P. A. & Hurlburt, H. E. (2000), 'An optimal definition for ocean mixed layer depth', *Journal of Geophysical Research: Oceans* **105**(C7), 16803–16821.

Karl, D. M., Holm-Hansen, O., Taylor, G. T., Tien, G. & Bird, D. F. (1991), 'Microbial biomass and productivity in the western Bransfield strait, Antarctica during the 1986–87 austral summer', *Deep Sea Research Part A. Oceanographic Research Papers* **38**(8-9), 1029–1055.

Karp-Boss, L., Boss, E., Jumars, P. A. et al. (1996), 'Nutrient fluxes to planktonic osmotrophs in the presence of fluid motion', *Oceanography and Marine Biology* **34**, 71–108.

Kiørboe, T. (2008), *A mechanistic approach to plankton ecology*, Princeton University Press.

Kiørboe, T. (2011), 'How zooplankton feed: mechanisms, traits and trade-offs', *Biological Reviews* **86**(2), 311–339.

Kiørboe, T., Andersen, A., Langlois, V. J., Jakobsen, H. H. & Bohr, T. (2009), 'Mechanisms and feasibility of prey capture in ambush-feeding zooplankton', *Proceedings of the National Academy of Sciences* **106**(30), 12394–12399.

Kiørboe, T. & MacKenzie, B. (1995), 'Turbulence-enhanced prey encounter rates in larval fish: effects of spatial scale, larval behaviour and size', *Journal of Plankton Research* **17**(12), 2319–2331.

Kirk, J. T. O. (1975), 'A theoretical analysis of the contribution of algal cells to the attenuation of light within natural waters: ii. spherical cells', *New Phytol.* **75**, 21–36.

Kirk, J. T. O. (1976*a*), 'A theoretical analysis of the contribution of algal cells to the attenuation of light within natural waters: iii. cylindrical and spheroidal cells', *New Phytol.* **77**, 341–358.

Kirk, J. T. O. (1976*b*), 'Yellow substance (gelbstoff) and its contribution to the attenuation of photosynthetically active radiation in some inland and coastal south-eastern australian waters', *Marine and Freshwater Research* **27**(1), 61–71.

Kirk, J. T. O. (1994), *Light and photosynthesis in aquatic ecosystems*, 2 edn, Cambridge University Press.

Klausmeier, C. A. & Litchman, E. (2001), 'Algal games: the vertical distribution of phytoplankton in poorly mixed water columns', *Limnol. Oceanogr.* **48**(6), 1998–2007.

Kloosterman, M., Campbell, S. A. & Poulin, F. J. (2014), 'A closed NPZ model with delayed nutrient recycling', *Journal of mathematical biology* **68**(4), 815–850.

Koller, L. R. (1965), *Ultraviolet radiation*, 2 edn, John Wiley and Sons, NY.

Kolmogorov, A. N. (1936), 'Sulla teoria di Volterra della lotta per lesistenza', *Giornale Instituto Ital. Attuari* **7**, 74–80.

Kolmogorov, A. N. (1941), 'Dissipation of energy in locally isotropic turbulence', **32**(1), 16–18.

Komen, G. J., Cavaleri, L., Donelan, M., Hasselmann, K., Hasselmann, S. & Janssen, P. A. E. M. (1994), *Dynamics and modelling of ocean waves*, Cambridge University Press.

Kraichnan, R. H. (1970), 'Diffusion by a random velocity field', *The physics of fluids* **13**(1), 22–31.

Kraichnan, R. H. (1987), 'Eddy viscosity and diffusivity: exact formulas and approximations', *Complex Systems* **1**(4-6), 805–820.

Lambers, H., Chapin III, F. S. & Pons, T. L. (2008), *Plant physiological ecology*, 2 edn, Springer.

Lambert, J. H. (1760), *Photometria sive de mensura et gradibus luminis colorum et umbrae*, Klett, Eberhard.

Langmuir, I. (1938), 'Surface motion of water induced by wind', *Science* **87**(2250), 119–123.

Launder, B. E. & Spalding, D. B. (1974), 'The numerical computation of turbulent flows', *Computer methods in applied mechanics and engineering* **3**(2), 269–289.

Lees, B. J. (1981), 'Relationship between eddy viscosity of seawater and eddy diffusivity of suspended particles', *Geo-Marine Letters* **1**(3-4), 249–254.

Leibovich, S. (1980), 'On wave-current interaction theories of langmuir circulations', *Journal of Fluid Mechanics* **99**(04), 715–724.

Lesieur, M. (1997), *Turbulence in fluids*, 3 edn, Kluwer Academic Publishers.

Lesieur, M. (2008), 'Turbulence in fluids, fluid mechanics and its applications'.

Leslie, D. C. (1973), *Developments in the theory of turbulence*, Clarendon Press, Oxford.

Letelier, R. M., Karl, D. M., Abbott, M. R. & Bidigare, R. R. (2004), 'Light driven seasonal patterns of chlorophyll and nitrate in the lower euphotic zone of the north pacific subtropical gyre', *Limnology and Oceanography* **49**(2), 508–519.

Letelier, R. M., White, A. E., Bidigare, R. R., Barone, B., Church, M. J. & Karl, D. M. (2017), 'Light absorption by phytoplankton in the north Pacific subtropical gyre', *Limnology and Oceanography* .

Lévy, M. (2015), 'Exploration of the critical depth hypothesis with a simple NPZ model', *ICES Journal of Marine Science: Journal du Conseil* **72**(6), 1916–1925.

Lewis, D. M. (2003*a*), 'The orientation of gyrotactic spheroidal micro-organisms in a homogeneous isotropic turbulent flow', **459**(2033), 1293–1323.

Lewis, D. M. (2003*b*), 'Planktonic encounter rates in homogeneous isotropic turbulence: the case of predators with limited fields of sensory perception', *Journal of theoretical biology* **222**(1), 73–97.

Lewis, D. M. (2005), 'A simple model of plankton population dynamics coupled with a LES of the surface mixed layer', *J.Theor.Biol.* **234**, 565–591.

Lewis, D. M. & Bala, S. I. (2006), 'Plankton predation rates in turbulence: a study of the limitations imposed on a predator with a non-spherical field of sensory perception', *Journal of theoretical biology* **242**(1), 44–61.

Lewis, D. M. & Bala, S. I. (2008), 'An examination of saltatory predation strategies employed by fish larvae foraging in a variety of different turbulent regimes', *Marine Ecology Progress Series* **359**, 261–274.

Lewis, D. M. & Belcher, S. E. (2004), 'Time-dependent, coupled, Ekman boundary layer solutions incorporating Stokes drift', *J.Dyn.Atmos.Oceans.* **37**, 313–351.

Lewis, D. M., Brereton, A. & Siddons, J. T. (2017), 'A large eddy simulation study in the formation of deep chlorophyll/biological maxima in un-stratified mixed layers: the roles of turbulent mixing and predation pressure (accepted)', *Limnology and Oceanography* **62**(5), 2277–2307.

Lewis, D. M. & Pedley, T. J. (2000), 'Planktonic contact rates in homogeneous isotropic turbulence: theoretical predictions and kinematic simulations', *J.Theor.Biol.* **205**, 377–408.

Lewis, D. M. & Pedley, T. J. (2001), 'The influence of turbulence on plankton predation strategies', *J.Theor.Biol.* **210**, 347–365.

Lewis, M. R., Harrison, W. G., Oakey, N. S., Herbert, D. & Platt, T. (1986), 'Vertical nitrate fluxes in the oligotrophic ocean.', *Science(Washington)* **234**(4778), 870–872.

Li, M. & Garrett, C. (1995), 'Is Langmuir circulation driven by surface waves or surface cooling', *J.Phys.Oceanogr.* **25**, 64–76.

Li, S.-X., Liu, F.-J., Zheng, F.-Y., Zuo, Y.-G. & Huang, X.-G. (2013), 'Effects of nitrate addition and iron speciation on trace element transfer in coastal food webs under phosphate and iron enrichment', *Chemosphere* **91**(11), 1486–1494.

Lindholm, T. (1992), 'Ecological role of depth maxima of phytoplankton', *Arch. Hydrobiol. Beih. Ergebn. Limnol* **35**, 33–45.

Long, S. P., Ainsworth, E. A., Rogers, A. & Ort, D. R. (2004), 'Rising atmospheric carbon dioxide: plants face the future', *Annu. Rev. Plant Biol.* **55**, 591–628.

Longhurst, A. R. & Harrison, W. G. (1989), 'The biological pump: profiles of plankton production and consumption in the upper ocean', *Progress in Oceanography* **22**(1), 47–123.

Lotka, A. J. (1920), 'Undamped oscillations derived from the law of mass action', *Journal of American Chemical Society* **42**, 1595–1599.

Macías, D., Lubián, L. M., Echevarría, F., Huertas, I. E. & García, C. M. (2008), 'Chlorophyll maxima and water mass interfaces: tidally induced dynamics in the strait of gibraltar', *Deep Sea Research Part I: Oceanographic Research Papers* **55**(7), 832–846.

Macías, D., Rodríguez-Santana, A., Ramírex-Romero, E., Bruno, M., Pelegrí, J. P., Sangrà, P., Aguiar-González, B. & García, C. M. (2013), 'Turbulence as a driver for vertical plankton distribution in the subsurface upper ocean', *Scientia Marina* **77**(4), 541–549.

MacKenzie, B. R. & Leggett, W. C. (1991), 'Quantifying the contribution of small-scale turbulence to the encounter rates between larval fish and their zooplankton prey: effects of wind and tide', *Marine Ecology Progress Series* pp. 149–160.

Madsen, O. S. (1977), 'A realistic model of the wind-induced Ekman boundary layer', *Journal of Physical Oceanography* **7**(2), 248–255.

Malik, N. A. & Vassilicos, J. C. (1999), 'A Lagrangian model for turbulent dispersion with turbulent-like flow structure: Comparison with direct numerical simulation for two-particle statistics', *Physics of fluids* **11**(6), 1572–1580.

Malkiel, E., Sheng, J., Katz, J. & Strickler, J. R. (2003), 'The three-dimensional flow field generated by a feeding calanoid copepod measured using digital holography', *Journal of Experimental Biology* **206**(20), 3657–3666.

Marlatt, S., Waggy, S. & Biringen, S. (2010), 'Direct numerical simulation of the turbulent Ekman layer: turbulent energy budgets', *J.Thermop. and Heat Trans.* **24**, 544–555.

Marlatt, S., Waggy, S. & Biringen, S. (2011), 'Direct numerical simulation of the turbulent Ekman layer: evaluation of closure models', *J.Atmos.Science* **69**, 1106–1117.

Martin, A. P. (2003), 'Phytoplankton patchiness: the role of lateral stirring and mixing', *Prog.in Oceanogr.* **57**, 125–174.

Maurer, J., Tabeling, P. & Zocchi, G. (1994), 'Statistics of turbulence between two counter-rotating disks in low-temperature helium gas', *EPL (Europhysics Letters)* **26**(1), 31.

McKiver, W. J. & Neufeld, Z. (2009), 'Influence of turbulent advection on a phytoplankton ecosystem with nonuniform carrying capacity', *Physical Review E* **79**(6), 061902.

McWilliams, J. C. & Huckle, E. (2006), 'Ekman layer rectification', *J.Phys.Oceanogr.* **36**, 1646–1659.

McWilliams, J. C., Sullivan, P. P. & Moeng, C. H. (1997), 'Langmuir turbulence in the ocean', *J.Fluid Mech.* **334**, 1–30.

Mecherikunnel, A. T. & Richmond, J. (1980), 'Spectral distribution of solar radiation', *NASA Tech. Mem.* **82021**.

Michaelis, L. & Menten, M. L. (1913), 'Die kinetik der invertinwirkung', *Biochem. z* **49**(333-369), 352.

Moeng, C.-H. & Sullivan, P. P. (2002), 'Large-eddy simulation', *Encyclopedia of Atmospheric Sciences* **1140**, 1150.

Mohammadi, B. & Pironneau, O. (1993), *Analysis of the k-epsilon turbulence model*, France: Editions MASSON.

Mojica, K. D. A., van de Poll, W. H., Kehoe, M., Huisman, J., Timmermans, K. R., Buma, A. G. J., van der Woerd, H. J., Hahn-Woernle, L., Dijkstra, H. A. & Brussaard, C. P. D. (2015), 'Phytoplankton community structure in relation to vertical stratification along a north-south gradient in the northeast Atlantic ocean', *Limnology and Oceanography* **60**(5), 1498–1521.

Monin, A. S. & Yaglom, A. M. (1975), 'Mechanics of turbulence', *Statistical fluid mechanics* **2**.

Moss, B. R. (2009), *Ecology of fresh waters: man and medium, past to future*, John Wiley & Sons.

Muelbert, J. H., Lewis, M. R. & Kelley, D. E. (1994), 'The importance of small-scale turbulence in the feeding of herring larvae', *Journal of plankton research* **16**(8), 927–944.

Murray, A. G. & Parslow, J. S. (1999), 'The analysis of alternative formulations in a simple model of a coastal ecosystem', *Ecological Modelling* **119**(2), 149–166.

Murray, J. D. (2002), *Mathematical biology: An introduction*, 3 edn, Springer.

Murray, J. D. (2003), *Mathematical Biology. II Spatial Models and Biomedical Applications*, 3 edn, Springer-Verlag New York Incorporated.

Navier, C. L. M. H. (1823), 'Mémoire sur les lois du mouvement des fluides', *Mem. Acad. Sci. Inst. Fr* **6**(1823), 389–416.

Nelson, J. et al. (2003), *The physics of solar cells*, Vol. 1, Imperial College Press.

Okubo, A. (1980), *Diffusion and ecological problems: mathematical Models*, Vol. 10, Springer-Verlag Berlin.

Okubo, A. & Levin, S. A. (2013), *Diffusion and ecological problems: modern perspectives*, Vol. 14, Springer Science & Business Media.

Olson, J. A. (2001), 'The motion of fibres in turbulent flow, stochastic simulation of isotropic homogeneous turbulence', *International Journal of Multiphase Flow* **27**(12), 2083–2103.

Osborn, T. R., Yamazaki, H. & Squires, K. (1990), 'Direct simulation of the effect of turbulence on planktonic contact rates', *Large patterns marine processes ecosystems and yields. Am. Assoc. Adv. Sc* .

Pacanowski, R. C. & Philander, S. G. H. (1981), 'Parameterization of vertical mixing in numerical models of tropical oceans', *Journal of Physical Oceanography* **11**(11), 1443–1451.

Pannard, A., Planas, D. & Beisner, B. E. (2015), 'Macrozooplankton and the persistence of the deep chlorophyll maxima in a stratified lake', *Freshwarer biology* **60**(8), 1717–1733.

Parmesan, C. (2006), 'Ecological and evolutionary responses to recent climate change', *Annu. Rev. Ecol. Evol. Syst.* **37**, 637–669.

Pearson, B. C., Grant, A. L. M., Polton, J. A. & Belcher, S. E. (2015), 'Langmuir turbulence and surface heating in the ocean surface boundary layer', *Journal of Physical Oceanography* **45**(12), 2897–2911.

Pécseli, H. L., Trulsen, J. K. & Fiksen, Ø. (2014), 'Predator–prey encounter and capture rates in turbulent environments', *Limnology and Oceanography: Fluids and Environments* **4**(1), 85–105.

Pedley, T. J. & Kessler, J. O. (1992), 'Hydrodynamic phenomena in suspensions of swimming microorganisms', *Annual Review of Fluid Mechanics* **24**(1), 313–358.

Pérez, V., Fernández, E., Marañón, E., Morán, X. A. G. & Zubkov, M. V. (2006), 'Vertical distribution of phytoplankton biomass, production and growth in the Atlantic subtropical gyres', *Deep Sea Research Part I: Oceanographic Research Papers* **53**(10), 1616–1634.

Philips, O. M. (1977), *The dynamics of the upper ocean*, Cambridge University Press.

Pilati, A. & Wurtsbaugh, W. A. (2003), 'Importance of zooplankton for the persistence of a deep chlorophyll layer: a limnocorral experiment', *Limnol. Oceanogr.* **48**, 249–260.

Planas, D., Agustí, S., Duarte, C. M., Granata, T. C. & Merino, M. (1999), 'Nitrate uptake and diffusive nitrate supply in the central Atlantic', *Limnology and Oceanography* **44**(1), 116–126.

Polton, J. A. & Belcher, S. E. (2007), 'Langmuir turbulence and deeply penetrating jets in an unstratified mixed layer', *Journal of Geophysical Research: Oceans* **112**(C9).

Polton, J. A., Lewis, D. M. & Belcher, S. E. (2005), 'The role of wave-induced Coriolis-Stokes forcing on the wind-driven mixed layer', *J.Phys.Oceanogr.* **35**, 444–457.

Prentice, I. C., Farquhar, G. D., Fasham, M. J. R., Goulden, M. L., Heiman, M., Jaramilo, V. J., Kheshgi, H. S., LeQuéré, C., Scholes, R. J. & Wallace, D. W. R. (2001), 'The carbon cycle and atmospheric carbon dioxide', *Cambridge Univ Press* .

Press, W. H. (2007), *Numerical recipes: the art of scientific computing*, 3rd edn, Cambridge Univ Press.

Price, J. F. & Sundermeyer, M. A. (1999), 'Stratified Ekman layers', *J.Geophys.Res.* **104**, 20467–20494.

Price, J. F., Weller, R. A. & Schudlich, R. R. (1987), 'Wind-driven ocean currents and Ekman transport', *Science* **238**, 1534–1538.

Reynolds, C. (1992), 'Dynamics, selection and composition of phytoplankton in relation to vertical structure in lakes', *Arch. Hydrobiol. Beihefte Ergebnisse der Limnologie* **35**, 13–31.

Reynolds, O. (1894), 'On the dynamical theory of incompressible viscous fluids and the determination of the criterion.', *Proceedings of the Royal Society of London* **56**(336-339), 40–45.

Richardson, L. F. (1921), 'Some measurements of atmospheric turbulence', *Philosophical Transactions of the Royal Society of London. Series A, Containing Papers of a Mathematical or Physical Character* **221**, 1–28.

Rothschild, B. J. & Osborn, T. R. (1988), 'Small-scale turbulence and plankton contact rates', *J.Plank.Res.* **10**(3), 465–474.

Ruiz, J., Macías, D. & Peters, F. (2004), 'Turbulence increases the average settling velocity of phytoplankton cells', *Proceedings of the National academy of Sciences of the United States of America* **101**(51), 17720–17724.

Ryabov, A. B. & Blasius, B. (2008), 'Population growth and persistence in a heterogeneous environment: the role of diffusion and advection', *Mathematical Modelling of Natural Phenomena* **3**(3), 42–86.

Sagaut, P. (2006), *Large eddy simulation for incompressible flows: an introduction*, Springer Science & Business Media.

Saha, T. & Bandyopadhyay, M. (2009), 'Dynamical analysis of toxin producing phytoplankton–zooplankton interactions', *Nonlinear Analysis: Real World Applications* **10**(1), 314–332.

Saiz, E., Alcaraz, M. & Paffenhöfer, G.-A. (1992), 'Effects of small-scale turbulence on feeding rate and gross-growth efficiency of three acartia species (copepoda: Calanoida)', *Journal of Plankton Research* **14**(8), 1085–1097.

Saiz, E. & Kiørboe, T. (1995), 'Predatory and suspension feeding of the copepod acartia tonsa in turbulent environments', *Marine Ecology Progress Series* pp. 147–158.

Sawatzky, C. L. (2006), 'The spatial and temporal dynamics of deep chlorophyll layers in high-mountain layers: effects of nutrients, grazing and herbovore nutrient recycling as growth determinants', *J. Plankton Res* **28**, 65–86.

Schmitt, F. G. (2007), 'About Boussinesq's turbulent viscosity hypothesis: historical remarks and a direct evaluation of its validity', *Comptes Rendus Mécanique* **335**(9-10), 617–627.

Schulten, H. R., Plage, B. & Schnitzer, M. (1991), 'A chemical structure for humic substances', *Naturwissenschaften* **78**(7), 311–312.

Schulten, H. R. & Schnitzer, M. (1997), 'The chemistry of soil organic nitrogen: a review', *Biology and Fertility of Soils* **26**(1), 1–15.

Sekerci, Y. & Petrovskii, S. (2015), 'Mathematical modelling of plankton–oxygen dynamics under the climate change', *Bulletin of mathematical biology* **77**(12), 2325–2353.

Shroyer, E. L., Benoit-Bird, K. J., Nash, J. D. & Moum, J. N. (2014), 'Stratification and mixing regimes in biological thin layers over the mid-Atlantic bight', *Limnology and Oceanography* **59**(4), 1349–1363.

Simmonds, B., Wood, S. A., Özkundakci, D. & Hamilton, D. P. (2015), 'Phytoplankton succession and the formation of a deep chlorophyll maximum in a hypertrophic volcanic lake', *Hydrobiologia* **745**(1), 297–312.

Smagorinksy, J. (1963), 'General circulation experiments with the primitive equations, i: the basic experiment', *Mon. Weathe Rev.* **91**, 99–164.

Smith, J. A. (1992), 'Observed growth of Langmuir circulation', *Journal of Geophysical Research: Oceans* **97**(C4), 5651–5664.

Smith, R. C. & Baker, K. S. (1981), 'Optical properties of the clearest natural waters (200–800 nm)', *Applied optics* **20**(2), 177–184.

Smith, V. H. (1998), Cultural eutrophication of inland, estuarine, and coastal waters, *in* 'Successes, limitations, and frontiers in ecosystem science', Springer, pp. 7–49.

Spelt, P. D. M. & Biesheuvel, A. (1997), 'On the motion of gas bubbles in homogeneous isotropic turbulence', *Journal of fluid Mechanics* **336**, 221–244.

Steele, J. H. & Henderson, E. W. (1981), 'A simple plankton model', *The American Naturalist* **117**(5), 676–691.

Straile, D. (1997), 'Gross growth efficiencies of protozoan and metazoan zooplankton and their dependence on food concentration, predator-prey weight ratio, and taxonomic group', *Limnology and Oceanography* **42**(6), 1375–1385.

Strickler, J. R. (1982), 'Calanoid copepods, feeding currents, and the role of gravity', *Science* **218**(4568), 158–160.

Sullivan, P. P., McWilliams, J. C. & Moeng, C.-H. (1994), 'A subgrid-scale model for large-eddy simulation of planetary boundary-layer flows', *Boundary-Layer Meteorology* **71**(3), 247–276.

Sundby, S., Ellertsen, B. & Fossum, P. (1994), Encounter rates bctwecn first-feeding cod larvae and their prey during moderate to strong turbulent mixing, *in* 'ICES Marine Science Symposia', Vol. 198, Copenhagen, Denmark: International Council for the Exploration of the Sea, 1991-, pp. 393–405.

Sundby, S. & Fossum, P. (1990), 'Feeding conditions of Arcto-Norwegian cod larvae compared with the Rothschild–Osborn theory on small-scale turbulence and plankton contact rates', *Journal of Plankton Research* **12**(6), 1153–1162.

Sybesma, C. & Olson, J. M. (1963), 'Transfer of chlorophyll excitation energy in green photosynthetic bacteria', *Proceedings of the National Academy of Sciences* **49**(2), 248–253.

Takahashi, M., Ichimura, S., Kishino, M. & Okami, N. (1989), 'Shade and chromatic adaptation of phytoplankton photosynthesis in a thermally stratified sea', *Marine Biology* **100**(3), 401–409.

Teixeira, M. A. C. & Belcher, S. E. (2002), 'On the distortion of turbulence by a progressive surface wave', *Journal of Fluid Mechanics* **458**, 229–267.

Tennekes, H. & Lumley, J. L. (1972), *A first course in turbulence*, MIT Press.

Terray, E. A., Donelan, M. A., Agrawal, Y. C., Drennan, W. M., Kahma, K. K., Williams, A. J., Hwang, P. A. & Kitaigorodskii, S. A. (1996), 'Estimates of kinetic energy dissipation under breaking waves', *Journal of Physical Oceanography* **26**(5), 792–807.

Thomson, D. J. & Devenish, B. J. (2005), 'Particle pair separation in kinematic simulations', *Journal of Fluid Mechanics* **526**, 277–302.

Thomson, R. E. & Fine, I. V. (2003), 'Estimating mixed layer depth from oceanic profile data', *Journal of Atmospheric and Oceanic Technology* **20**(2), 319–329.

Varela, M., Prego, R., Pazos, Y. & Moroño, Á. (2005), 'Influence of upwelling and river runoff interaction on phytoplankton assemblages in a middle Galician ria and comparison with northern and southern rias (nw iberian peninsula)', *Estuarine, Coastal and Shelf Science* **64**(4), 721–737.

Venrick, E. L., McGowan, J. A. & Mantyla, A. W. (1973), 'Deep maxima of photosynthetic chlorophyll in the Pacific ocean', *US Natl Mar Fish Serv Fish Bull* .

Visser, A. W. & Jackson, G. A. (2004), 'Characteristics of the chemical plume behind a sinking particle in a turbulent water column', *Marine Ecology Progress Series* **283**, 55–71.

Volterra, V. (1926), 'Fluctuations in the abundance of a species considered mathematically', *Nature* **118**(2972), 558–560.

Wang, M. & Shi, W. (2008), 'Satellite-observed algae blooms in China's lake Taihu', *Eos, Transactions American Geophysical Union* **89**(22), 201–202.

Wang, Z. & Goodman, L. (2010), 'The evolution of a thin phytoplankton layer in strong turbulence', *Continental Shelf Research* **30**(1), 104–118.

White, B. & Matsumoto, K. (2012), 'Causal mechanisms of the deep chlorophyll maximum in lake Superior: A numerical modeling investigation', *Journal of Great Lakes Research* **38**(3), 504–513.

Wijffels, S., Firing, E. & Bryden, H. (1994), 'Direct observations of Ekman balance at 10N in the Pacific', *J.Phys.Oceanogr.* **24**, 1666–1679.

Williams, R. G. & Follows, M. J. (1998), 'The ekman transfer of nutrients and maintenance of new production over the north Atlantic', *Deep-Sea Res.* **I 45**, 461–489.

Yamazaki, H., Honma, H., Nagai, T., Doubell, M. J., Amakasu, K. & Kumagai, M. (2010), 'Multilayer biological structure and mixing in the upper water column of lake Biwa during summer 2008', *Limnology* **11**(1), 63–70.

Yamazaki, H., Mackas, D. L. & Denman, K. L. (2002), 'Coupling small-scale physical processes with biology', *The sea* **12**, 51–112.

Yamazaki, H., Osborn, T. R. & Squires, K. D. (1991), 'Direct numerical simulation of planktonic contact in turbulent flow', *Journal of Plankton Research* **13**(3), 629–643.

Yeung, P. K., Xu, S. & Sreenivasan, K. R. (2002), 'Schmidt number effects on turbulent transport with uniform mean scalar gradient', *Physics of Fluids* **14**(12), 4178–4191.